The Ages, Speeds and Offspring of Pulsars

Thesis by

Bradley Miles Stougaard Hansen

In Partial Fulfillment of the Requirements

for the Degree of

Doctor of Philosophy

California Institute of Technology

Pasadena, California

1996

(Submitted May 23 1996)

Acknowledgements

The past five years in Southern California have been some of the happiest of my life. There are a number of people to thank for this.

Firstly, I should thank my Housemates, the Johns, Ushma and Chris. Whether it be the road trips sans destination, the silly arguments till 4 a.m., or the awful puns, I shall definitely miss the people at 344 South Allen Ave. I would also like to thank CP, not the least for adding some breadth to my diversions in the past year and a half.

Of course, I also did some work in the last few years! I would like to thank my advisor, Sterl Phinney, for leading by example and for always treating even my stupidest questions (no small subset) with a gravity they did not deserve. YanQin Wu and Marten van Kerkwijk also provided a lot of useful insight while helping to nurture the study of white dwarfs in these dark days of rampant cosmology (my apologies, CP)! The happily egalitarian nature of the TAPIR group is in no small part due to the unselfish efforts of the tapirim as a whole, and I thank them for that, en masse.

I would also like to thank the many friends I made among the astronomy students and faculty. Todd, Angela, Peter, Jagmit, Brad, Andrew and many others were responsible for ski trips and soccer games that helped maintain my sanity between long bouts in front of the computer. Wal and Todd deserve special mention as a vital support group in this remote corner of the soccer universe.

Finally, I would like to thank my parents, Beryl and Bent, and my sister Bronwyn, for their distance-independent support and encouragement.

Abstract

We investigate the cooling of low mass white dwarfs with helium cores. We construct a detailed numerical model using the most modern input physics, including our own calculations of low temperature hydrogen opacities. We use our models to constrain the ages of binary millisecond pulsars from the optical observations of their white dwarf companions. We use this to place limits on the initial spin periods, magnetic field decay times and accretion histories of the millisecond pulsars. Our models can also be used along with observations of spectroscopic gravities and radial velocities to place interesting constraints on the neutron star equation of state. We provide grids of temperature and luminosity as a function of age for various white dwarf masses and surface compositions to facilitate future analyses.

We have investigated the effect of the pulsar wind on the atmospheric composition of binary companions. The spallation of atmospheric helium to hydrogen increases the cooling age of the white dwarf. We find that all white dwarf companions in binaries with orbital period < 300 days should cool as DA (hydrogen surface layer) white dwarfs, irrespective of their original hydrogen content. We investigate the effect of various wind compositions and note that, if almost all the hydrogen on the surface of a pulsar companion is the result of spallation of an ionic wind, then the D/H ratio is large.

We investigate the processes by which planets might form around a millisecond pulsar such as PSR B1257+12. We study the evolution of accretion disks of different mass, angular momentum and composition, corresponding to various proposed formation scenarios. We find that most formation scenarios require a high efficiency of conversion of metal-rich material into planets if they are to produce the observed parameters of the 1257+12 planetary system.

We have studied the distribution of pulsar proper motions in the light of the recent analysis of Lyne & Lorimer (1994). Using a simulation of the selection effects of the various surveys, and treating the censored data using survival statistics, we arrive at an estimate of the characteristic pulsar birth velocity ~ 300 km.s^{-1}, 2/3 that of Lyne & Lorimer. We also show that the older pulsar population shows the effects of the asymmetric drift, indicating that it must be dynamically old.

Summary

In a general sense, all of the calculations described in this thesis are intended to study some aspect of pulsars. Nevertheless, we cover a fairly eclectic range of fields in the forthcoming pages.

The major part of this thesis is devoted to the study of the cooling of low mass Helium white dwarfs such as are found in binaries with millisecond pulsars. We describe in detail the construction of a numerical model to calculate accurate cooling ages for these stars, using the most recent input physics available. We may use the cooling ages we infer to determine the age of the millisecond pulsar, which in turn allows us to place constraints on the initial spin periods and accretion history of the neutron star. chapters 2 through 4 deal with this calculation.

The choice of atmospheric composition is quite important in studying the white dwarf cooling. The opacity of the atmosphere has a dramatic effect and thus the relative amounts of Hydrogen and Helium in the atmosphere is important, especially at low temperatures ($T_{eff} < 10\ 000$ K). The proximity of a pulsar with a relativistic wind of particles emanating from it can cause a change in the atmospheric composition of a Helium atmosphere companion. We study the spallation of atmospheric Helium by the pulsar wind in chapter 5.

The presence of planetary mass companions around PSR B1257+12 prompts questions about the formation scenarios of such objects. In chapter 6 we study the planet formation probabilities for the class of formation scenarios that form planets after the creation of the neutron star. All of these models result in a protoplanetary disk of varying mass, angular momentum and composition. We examine the efficiency required by each scenario to produce the observed planetary system and rank the various schemes accordingly.

The final chapter (chapter 7) deals with the velocity distribution of young pulsars. We present a statistical analysis of the pulsar proper motion distribution, including a discussion of the selection effects of the relevant pulsar surveys as well as a proper statistical treatment of those pulsars with only upper limits on their proper motion. We examine the consequences of our results and also demonstrate that the class of pulsars with spin-down ages $> 10^7$ years is dynamically old, because they show evidence for the asymmetric drift.

Of the material in the forthcoming chapters, chapter 2 and Appendices A and B describe the details of the numerical calculations of the input physics and stellar model for our cooling code. The calculations in these chapters are based on material in the literature and included for completeness. chapters 3, 4, 5 and 7 are original work and will be submitted to various scientific journals in the forthcoming months. chapter 6 has appeared in *Planets Around Pulsars*, ed. J.A. Phillips, S.E. Thorsett & S.R. Kulkarni, Volume 36 of the Astronomical Society of the Pacific Conference Series. Sections 6.1, 6.2, 6.3 and 6.7 of this chapter are primarily the work of E.S. Phinney.

Contents

Chapter 1 Introduction

When a star nears the end of its lifetime as a cosmic nuclear reactor, it begins to contract under the effects of its own gravity. Without the energy release from nuclear burning to support it, the star will collapse until the internal pressures of its constituents are strong enough to resist further contraction. For objects of stellar masses and composition, these forces are due to the degeneracy pressure of the Fermi gases that comprise the stellar cores under such conditions. For cores of mass less than $\sim 1.4\,M_\odot$, the core is composed of a gas of degenerate electrons and non-degenerate ions supported by the degeneracy pressure of the electrons. For cores of mass between $\sim 1.4 - 3.0\,M_\odot$, the core is composed primarily of a degenerate neutron superfluid, which provides the degeneracy pressure in this case. For masses greater than $\sim 3\,M_\odot$, the gravitational attraction is stronger than even the nuclear repulsion and the object is thought to collapse to a black hole. The values given for the boundaries in each of these cases are somewhat uncertain due to uncertainties in our knowledge of the equations of state at such densities and pressures as well as the effects of rotation in these objects. Nevertheless, it is expected that all stars will eventually end their lives (neglecting catastrophic events such as deflagration supernovae or stellar merging) in one of three degenerate configurations, either a white dwarf (lowest masses), a neutron star (intermediate masses) or a black hole (highest masses).

The correspondence between the original main sequence mass of a star and the mass of its final degenerate configuration is determined by the evolutionary history of the star and the circumstances under which it exists. Isolated stars undergo significant mass loss in their shell burning giant phases, and stars in binaries can lose even more through mass transfer to their companions. It appears that the division between main sequence white dwarf and neutron star progenitors lies between 6 and 8 $M_\odot$ (D'Antona & Mazzitelli (1990)), while the division between neutron star and black hole is somewhat uncertain, lying at $> 20\,M_\odot$ (Timmes et al. (1996)).

These degenerate remnants are among the oldest objects in our galaxy, and thus offer useful information about our local environment, as well as a possibility for investigating the physics of matter at densities well above that which we can obtain in the laboratory. The

following sections 1.1 and 1.2 offer a brief description of the basic physics of each of these classes of objects as a prelude to the more detailed models we shall require later.

1.1 Pulsars

Although postulated by Landau (1932) and Baade & Zwicky (1934) in the 1930s, neutron stars were not directly observed until Hewish et al. (1968) discovered the first radio pulsars, which were soon identified as rapidly rotating, magnetized neutron stars, generating observable periodic radio emission from the loss of their spin-down energy (Gold (1968)). From the measurement of the period P and its derivative, one may infer a characteristic spin-down age $t_p = P/2\dot{P}$ for each pulsar and the spin-down luminosity $\dot{E} = I\Omega\dot{\Omega}$, where $\Omega = 2\pi/P$ is the angular frequency of the pulsar rotation and P is the rotation period. In Figure 1.1 we show the known pulsar distribution in terms of P and $\dot{E}$.

The very high brightness temperatures of the observed radio emission imply that the emission comes from a large number of particles emitting coherently (e.g. Melrose (1992)). Goldreich and Julian (1969) demonstrated that the immediate surroundings of a spinning, magnetized neutron star must contain a magnetosphere, consisting of a large number of charged particles. This plasma can remain tied to the field lines as long as the distance from the star remains less than the light cylinder radius. Field lines that penetrate outside of the light cylinder cannot close, and the plasma on these field lines escapes in a relativistic wind, composed of electrons, positrons and possibly ions as well.

1.1.1 Magnetic Fields

Observations of the spin-down rate, combined with the assumption that magnetic dipole radiation is responsible for the energy loss, implies a magnetic field strength $B \sim 10^{12}$ G. Ostriker & Gunn (1969) and Gunn and Ostriker (1970) found evidence for the decay of this magnetic field[1] on the basis of the scatter in the P-$\dot{P}$ diagram. However, this was later discounted by Lyne et al. (1975), who showed that the decay signal was an artifact of the greater range of observed period derivatives. Further evidence in favour of magnetic field decay was advanced by Lyne et al. (1982) on the basis of proper motion measurements.

[1] One should note that when we say field decay, we refer to the decay of the quantity $B \sin\alpha$, where α is the angle between the dipole magnetic field axis and the rotation axis, so that we include alignment of the field and rotation axes in this definition.

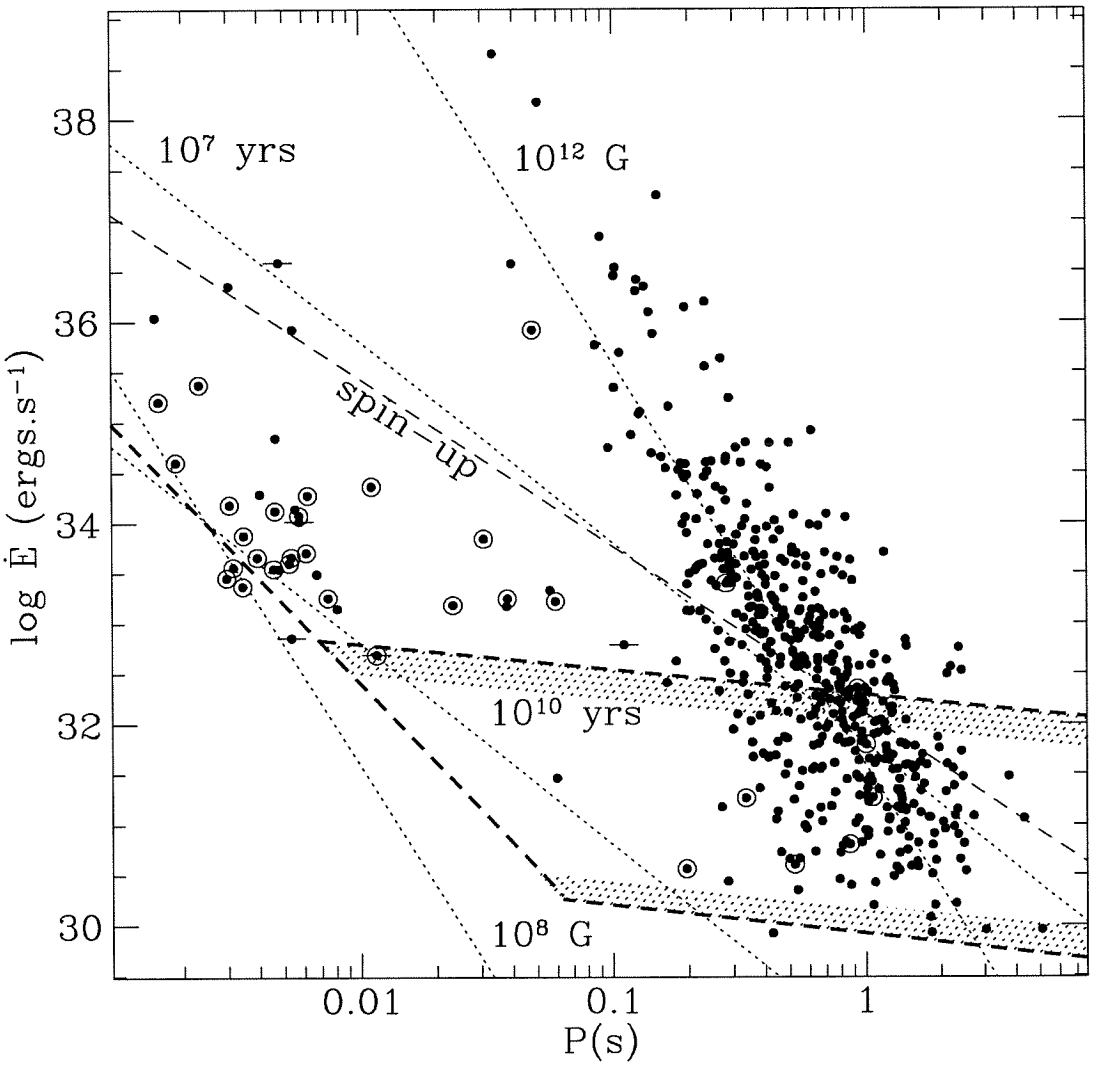

Figure 1.1: **The Known Pulsar Population:** The circled points indicate pulsars in binary systems. The points with horizontal lines through them have negative $\dot{P}$ and are situated in globular clusters, where $\dot{P}$ is dominated by the acceleration due to the local gravitational field (see Phinney (1993)). The dotted lines indicate spin-down ages and magnetic dipole field values. The thin dashed line is the canonical spin-up line for accretion of material onto a neutron star with a dipole magnetic field. The heavy dashed lines indicate various 'death-lines' from Chen & Ruderman (1993) and Phinney & Kulkarni (1994). The shaded regions enclose the 'death valley' of Chen & Ruderman.

Using the measured height of the pulsar above the galactic plane z and the component of the measured proper motion perpendicular to the plane (which yields the vertical velocity V_z, shown in Figure 1.2 for the latest data), they calculated the 'kinetic age' $t_k = z/V_z$. Comparison of the kinetic age with the measured spin-down age $t_p = P/2\dot{P}$ indicates that $t_k \sim t_p$ for $t_p \leq 10^7$ years, but that $t_k < t_p$ for $t_p > 10^7$ years. The claim was that t_p was not a good age estimate for the older pulsars, and that most pulsars had ages of order 10^7 years or less. The increased t_p was interpreted as evidence for field decay. However, the veracity of the kinetic age determinations are somewhat suspect. In Figure 1.2 we show the vertical velocity as a function of t_p. The filled squares indicate pulsars moving away from the plane, and open squares indicate pulsars moving towards the plane. The heavy solid lines show the turn around age at which a pulsar born with initial vertical velocity V_z at z=0 will turn around and come back towards the plane, as estimated using the potential of Kuijken & Gilmore (1989). Also shown is the model of Narayan and Ostriker (1990). This calculation is one-dimensional and thus of limited validity and intended to merely illustrate the appropriate orders of magnitude. Nevertheless, it is striking to note that 7 of the 12 returning pulsars have ages longer than their model 'turn around' time. In fact the number of pulsars travelling towards and away from the plane is approximately equal for pulsars to the right of the heavy solid line, as would be expected for a population which has reached a steady state. On the other hand, 85% (28/33) of pulsars to the left of the line are leaving the plane. We should note that these data are based only on proper motions and thus some of the returning pulsars could have velocities directed away from the plane by a suitable choice of radial component. However, in many cases this value would be uncomfortably large.

Figure 1.3 shows the problem from another perspective. The left panel shows the comparison of t_{kin} and t_p a la Lyne et al., for those pulsars moving away from the Galactic plane. The turnover at $t_p \sim 10^7$ years is obvious. However, the right hand panel shows the same diagram for pulsars approaching the galactic plane (ignoring the sign of the velocity in t_k). Although the number of pulsars is smaller, the same flattening is seen in the range $t_p > 10^7$ years. This suggests that we see the influence of selection effects rather than the influence of a physical effect.

In recent years, more detailed phenomenological and theoretical studies have addressed this question. Narayan and Ostriker (1990), following Narayan (1987), used monte carlo

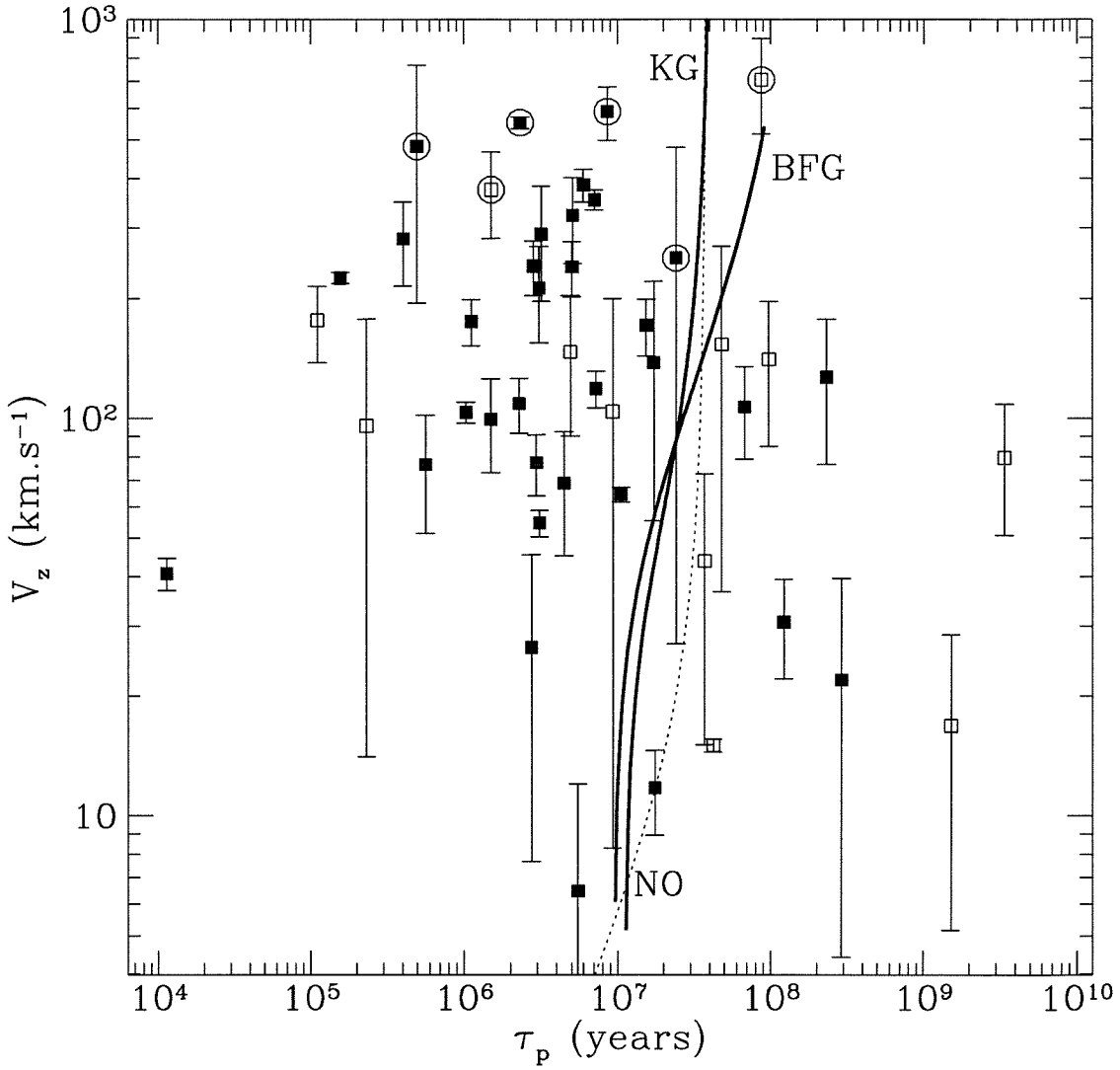

Figure 1.2: **The Vertical Motion of Pulsars:** The filled squares with error bars represent those pulsars that are moving away from the plane of the galaxy. The open squares are those pulsars that are moving back towards the plane of the galaxy. The heavy solid lines are the turn around times as calculated using the vertical potential model of Kuijken & Gilmore (1989), first with the original parameterisation and then with the later numbers of Bahcall, Flynn and Gould (1992). The dotted line indicates a similar calculation for the vertical potential of Narayan and Ostriker (1990). The circled pulsars have $z > 1.5$ kpc, i.e., they lie outside the electron layer and so the magnitudes of their velocities are only lower limits.

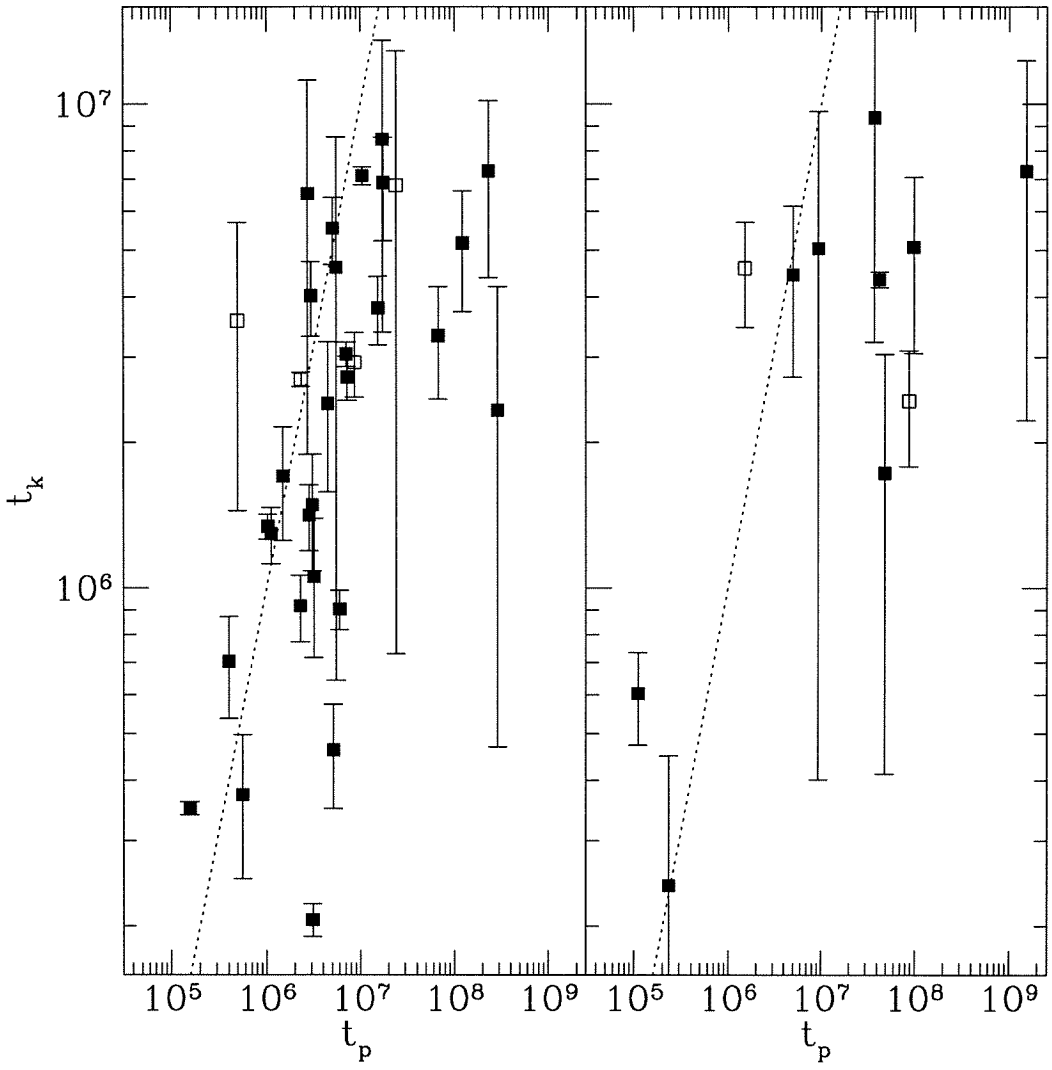

Figure 1.3: **The Kinetic Age Argument:** The left panel shows the kinetic and spin-down ages for those pulsars which are leaving the galactic plane, i.e., $z \times V_z > 0$. The open squares indicate those pulsars with $z > 1.5$kpc. The right panel shows the same diagram but for those pulsars approaching the galactic plane. The dotted line indicates $t_p = t_k$.

simulations and the known selection effects of the published pulsar surveys to examine the properties of the pulsar population as a whole. They concluded that magnetic field decay on timescales of $\sim 10^7$ years is required, a result consistent with the results of Lyne et al. However, Bhattacharya et al. (1992) performed a similar calculation and concluded that there was little evidence for magnetic field decay. Thus, the question of magnetic field decay is still open to discussion.

1.1.2 Pulsar Velocities

An important component of the above statistical analyses is the velocity distribution of the pulsar population. Shortly after their discovery, it was realized that pulsars have velocities significantly larger than those of their putative progenitors (Gunn & Ostriker (1970), Lyne, Anderson & Salter (1982)). Only transverse motions have been observed for pulsars, whether in the form of proper motions (Lyne, Anderson & Salter (1982), Harrison, Lyne & Anderson (1993)), scintillation measurements (Cordes (1986)) or inferences based on supernova remnant associations (Frail, Goss & Whiteoak (1995)). Recently, Lyne & Lorimer (1994) have reanalyzed the pulsar velocity data in the light of a recent revision of the dispersion measure distance scale (Taylor & Cordes (1993)). They infer a mean three-dimensional velocity of $\sim 450\,\mathrm{km.s^{-1}}$. This has important implications for binary survival fractions (Brandt & Podsiadlowski (1995)), Globular Cluster retention fractions (Drukier (1995), Phinney (1993)) and the origin of pulsar velocities (Burrows & Hayes (1996)). However, the analysis omits important selection effects and statistical biases. We shall address these shortcomings in Chapter 7.

1.1.3 Millisecond Pulsars

'Normal' pulsars have spin periods $\sim$ 0.1-3 seconds, and period derivatives $\sim 10^{-14} - 10^{-16}$, leading to inferred magnetic fields $\sim 10^{12}$ G, and hence spin-down ages $\sim 10^6 - 10^7$ years. However, Backer et al. (1982) discovered the first of a class of pulsars with much shorter spin periods, of the order of milliseconds. Since then searches at Arecibo, Parkes and Jodrell Bank have revealed many more. These pulsars have magnetic fields of order 10^8 G and spin-down ages $>$ Gigayears. Millisecond pulsars are also preferentially found in binaries, leading to the proposal that they are 'recycled' pulsars, which are spun up to high rotation speeds by the accretion of matter from their binary companions (Smarr & Blandford (1976)). It

has also been proposed that their low fields may be the result of the accretion episode, either due to the mass accreted (Taam & van den Heuvel (1986), Blondin & Freese (1988), Romani (1990)) or from the accretion-induced spin-down (Ruderman (1995)). The distribution of inferred magnetic field appears to be largely bimodal, prompting Kulkarni (1992) to suggest the presence of a magnetic field gap between $10^9 - 10^{10}$ G. However, this may be the result of selection effects if the magnetic field structure of recycled pulsars is primarily dipolar. This subject has already been discussed by Arons (1993), who concludes that higher order multipoles account for less than 40% of the millisecond pulsar magnetic fields. The upper boundary of the Chen and Ruderman 'death valley' shown in Figure 1.1 is the boundary for a purely dipole magnetic field. Neutron stars with significant non-dipolar components can still be seen as pulsars at longer periods down to the lower death line in Figure 1.1. A significant fraction of isolated pulsars can be seen to have non-dipolar magnetic fields in this interpretation. However, the shorter period pulsars lie above the dipole death line. Thus, a spun-up pulsar with initial spin-period of 20 ms and dipolar field $\sim 2 \times 10^{10}$ G will shine as a pulsar for only a few $\times 10^8$ years. Hence such pulsars are expected to be far more scarce than pulsars spun up to $\sim$ 5 ms, which take $\sim 10^{10}$ years to reach their death line, which is determined by the radiation reaction of the curvature photons rather than the polar cap potential difference (Phinney & Kulkarni (1994)).

The hypothesis that millisecond pulsars are the result of an accretion episode requires a progenitor population of neutron stars accreting from a companion. Thus, the Low Mass X-ray Binaries (LMXB) are a natural progenitor population for the Low Mass Binary Pulsars (LMBP). However, there is some uncertainty about whether the LMXB birthrate is sufficient to explain the LMBP birthrate (Kulkarni & Narayan (1988), van den Heuvel (1995)). The LMBP birthrate is $\sim$ number in galaxy/pulsar lifetime. Estimating the number of LMBP in the galaxy requires an estimate of the galactic volume efficiently covered by the pulsar searches. Stokes et al. (1986) claim that about 10% of detected pulsars are millisecond pulsars, which leads to an estimate of $\sim 3 \times 10^4$ millisecond pulsars in the galaxy. With lifetimes $\sim$ the age of the galaxy, we use 1.5×10^{10} years to yield a millisecond pulsar birth rate of $2 \times 10^{-6}\mathrm{yr}^{-1}$. The estimate of the LMXB birthrate is somewhat more complicated because the duration of the X-ray phase depends on the nature of the accretion process and the evolutionary state of the system. Furthermore, the final fate of the LMXB will depend on the initial orbital period, because this determines at what evolutionary stage the

companion will overflow its Roche Lobe, which in turn affects the response of the companion to mass loss.

The LMBP systems with orbital periods > 10 days can be explained by the following evolutionary scenario. If we have a neutron star in a binary with a companion $\sim 1 M_\odot$, mass transfer from the secondary to the primary (neutron star) will result in an expansion of the orbit. Hence the mass transfer will cease unless the secondary continues to expand in response to the mass loss. For a low mass giant, burning Hydrogen in a shell around a Helium core, this expansion will be driven by the nuclear evolution of the star. This timescale is long and the mass transfer is stable. For stars less massive than 2.3 $M_\odot$, there is a unique (i.e., independent of the total mass) relation between the core mass and the radius of the giant. The condition for mass transfer is that the giant must fill its Roche Lobe. Hence, setting the giant radius equal to the Roche lobe radius, we obtain a unique core mass - orbital period relation (Refsdal & Weigert (1971), Joss, Rappaport & Lewis (1987), Rappaport et al. (1995)). The final orbital separation of the LMBP system is determined when the opacity of the secondary envelope is no longer large enough to support convection any longer and the companion shrinks from giant dimensions towards the white dwarf sequence. However, this evolutionary scenario results in the expansion of the orbital period, so that even initial periods ~ 0.5 days will result in final orbital periods ≥ 15 days. Some LMBP have orbital periods much shorter than this.

For binaries with small initial separation, the secondary will overflow its Roche lobe before it becomes a giant. In this case the atmosphere is primarily radiative and the star will shrink in response to mass loss, thus shutting off further mass transfer. For such systems further evolution requires that there be an additional angular momentum loss (AML) mechanism in operation. This could be gravitational radiation (for very short period systems) or magnetic braking (e.g., Rappaport et al. (1983)). For systems in which the secondary is losing mass, the AML will act to counteract the expansion of the orbit, leading to either spiral in or a slow expansion of the orbit (Pylyser & Savonije (1988), Coté & Pylyser (1989)).

The aforementioned birthrate problem arises from the fact that the X-ray lifetimes of these systems is $\sim 10^8$ years. There are ~ 130 LMXB in the galaxy of which $\sim 40\%$ have orbital periods such that they are likely LMBP progenitors, yielding a birthrate of $\sim 5 \times 10^{-7} \mathrm{yr}^{-1}$ (four times too small). The solution may be that systems where the companion

is more massive have shorter X-ray lifetimes because the mass transfer is super-Eddington (van den Heuvel (1995)). van den Heuvel suggests Her X-1 may represent this short-lived class of pulsars with X-ray lifetimes $\sim 10^5$ years (Savonije (1983)) and a corresponding birthrate of $10^{-5}\mathrm{yr}^{-1}$ (enough to explain the discrepancy). Another recent analysis by Lorimer (1995) derives lower values for both the LMBP and LMXB birthrates which are comparable to one another.

Determining the ages of millisecond pulsars can teach us much about both their evolution and their structure. The use of the white dwarf companions as independent chronometers can allow us to estimate the age of the binary system and hence the age of the millisecond pulsar, completely independently of the spin-down of the pulsar. The determination of the age by this method is the subject of Chapters 2, 3 and 4.

1.1.4 Pulsar Winds

Ostriker and Gunn (1969) first discussed the mechanism for rotational energy loss in terms of magnetic dipole radiation in vacuum. The vacuum assumption was shown to be invalid by Goldreich & Julian (1969), who demonstrated that the large potential differences induced by the combination of the neutron star magnetic field and rotation would result in a charged magnetosphere. Furthermore, the braking index $\mathrm{n} = \Omega\ddot{\Omega}/\dot{\Omega}^2 = 3$ for a magnetic dipole while measured values are < 3 (Groth (1975a,b), Manchester et al. (1985), Michel (1991)).

Pair production in the high electric field regions of the magnetosphere will lead to the formation of a magnetohydrodynamic electron-positron wind, with a possible ionic component as well. The radial flow of this particle wind will also contribute to the spin-down torque of the star. Models of the Crab pulsar nebula (Rees & Gunn (1974), Kennel & Coriniti (1984a,b), Hoshino et al. (1992), Gallant & Arons (1994)) indicate that, far outside the light cylinder, the energy outflow is dominated by the particle component ($\sigma \sim$ Poynting Flux/Kinetic Flux $\sim 10^{-3}$).

The effects of the pulsar wind on the surroundings have been considered in a number of scenarios, such as the Crab nebula, the Vela pulsar (Bietenholz et al. (1991)), eclipsing close companions (e.g., Phinney et al. (1988), Johnston et al. (1994)) and Hα nebulae (e.g., Bell et al. (1993), Cordes et al. (1993)). In Chapter 5 we consider the effect of the wind and its composition on the atmospheric composition of white dwarf companions. Spallation of atmospheric Helium can yield a substantial Hydrogen blanket on the surface

of the white dwarf. This has important implications for the white dwarf cooling calculations in Chapters 3 and 4.

1.1.5 Pulsar Planets

Possibly the most esoteric pulsar known is PSR 1257+12, discovered by Wolszczan (1991). Further timing observations indicated the presence of two planetary mass companions (Wolszczan & Frail (1992)), making this the first (or longest surviving[2]) extrasolar planetary system detection. Further searches in radio and infra-red around pulsars have not located any other such systems (Phillips & Thorsett (1994), Foster & Fischer (1996)). Formation scenarios for such a system (see Podsiadlowski (1992)) differ markedly from those proposed for normal planetary systems and can be roughly divided into two classes, those in which the planets formed before the supernova and somehow survived it (termed 'Salamander' scenarios) and those in which the planets formed after the supernova from the debris (termed 'Memnonides' scenarios). The first class of models are fairly heterogeneous and have to be considered on individual merit. The second class all lead to the formation of circumpulsar disks of varying mass, angular momentum and composition. The subsequent planetary formation can be analysed solely in terms of these three parameters. This is the subject of Chapter 6.

1.2 White Dwarfs

After a star has shed the remnants of its envelope and contracted to form a white dwarf, it shines primarily by virtue of the residual thermal reservoir in its core. The heat is retained in the non-degenerate ions in the core of the white dwarf which is supported by electron degeneracy pressure. The degenerate electrons conduct heat very efficiently so that the strongly degenerate parts of the star remain almost isothermal throughout the white dwarf cooling lifetime. At the very edge of the star, the material is less degenerate and energy transport occurs via radiative diffusion and convection. These mechanisms are less efficient than the conduction in the core and thus the cooling rate is determined by the thermal 'bottleneck' in the thin, non-degenerate outer layers of the star.

[2]See the preface to *Planets around Pulsars*, ed. J.A. Phillips, S.E. Thorsett & S.R. Kulkarni, for a review of previous ill-fated reports of planetary companions to pulsars!

The basic cooling theory of white dwarfs was first discussed by Mestel (1952), using a simple picture much like the one above. The evolution can be reproduced using the following simple scalings. The radiative opacity is assumed to be of the Kramers form $\kappa \sim \kappa_0 \rho T^{-7/2}$, and thus the structure of the non-degenerate atmosphere is described by the power law

$$P \sim 1.05 \times 10^{17} \left(\frac{M}{M_\odot} \frac{L_\odot}{L} \right)^{1/2} T_7^{17/4} \tag{1.1}$$

where M and L are the mass and luminosity and T_7 is the temperature in units of 10^7 K. This holds until the region where the gas becomes degenerate, i.e., the Fermi energy of the electrons E_f is of order 10 kT. This implies the condition $P \propto T^{5/2}$, and thus matching the two conditions implies

$$L \sim 1.1 \times 10^{-4} L_\odot M_\odot T_7^{7/2} \tag{1.2}$$

where we have assumed that the degenerate electron fluid is infinitely conductive so that the degenerate core is isothermal. This luminosity law implies that the age and luminosity of a white dwarf are related by

$$L \sim 4 \times 10^{-3} L_\odot M_3 t_9^{-7/5} \tag{1.3}$$

where t_9 is the age in Gigayears and M_3 is the mass in units of 0.3 $M_\odot$.

This is the simple Mestel cooling law and it is the basic underpinning for all subsequent and more sophisticated cooling models. The essential point is that there is a correlation between the age and luminosity of a white dwarf and thus we may derive the age of a given white dwarf from its luminosity, given a sufficiently accurate model to describe the cooling processes.

Of course, to obtain more accurate cooling ages, one has to go beyond simple theory and consider all sources and sinks of energy that might play a role in the white dwarf cooling. Chapter 2 will discuss the various microphysical processes in some detail, but the following is a short list of the more important processes.

1. Proper radiative opacities do not conform to the Kramers law, and deviations can be large in regions of partial ionization. Also, for some cool white dwarfs, pressure ionization becomes important. A similar complication is that real electron conductivities are not infinite and these need to be accurately calculated as well. The opacities can

also vary somewhat depending on the atmospheric composition.

2. As white dwarfs cool, their atmospheres become convective. This affects the cooling and also the surface abundances, since it is possible to dredge up material that sank out under influence of the strong gravity of the white dwarf.

3. In the early stages of the white dwarf lifetime, the cooling due to neutrino emission can be important, leading to a loss from the thermal reservoir that does not manifest itself in the observed luminosity.

4. There can also be a contribution from residual Hydrogen shell burning if the remnant Hydrogen envelope is thick enough.

5. As the star cools the central temperature may reach a value where the ion gas begins to crystallize. The release of latent heat serves as an additional energy source and the heat capacity of the core drops sharply once the temperature reaches the Debye temperature of the coulomb lattice.

Iben & Tutukov (1984) studied the cooling of a representative white dwarf model using detailed microphysics. They concluded that, although the assumptions made by Mestel were drastic simplifications at all stages of the white dwarf evolution, the detailed cooling calculation was well represented by the scaling obtained by Mestel. There have been a number of subsequent detailed calculations of white dwarf cooling histories for a variety of masses and surface compositions (Iben & Tutukov (1984), Koester & Schonberner (1986), D'Antona & Mazzitelli (1989), Wood (1992)) although all of them considered a core mass composed of Carbon and Oxygen (or sometime Magnesium). The determination of ages using white dwarf cooling calculations has been applied to the galactic disk (Winget et al. (1987), Wood (1992)), the galactic halo (Tamahana et al. (1991)) and, most recently, globular clusters (Richer et al. (1995)).

Most white dwarfs result from the evolution of isolated stars, which go through a sequence of burning successive nuclear fuels until they can no longer muster the internal pressures to burn any of the core fuel, at which point they contract to the cooling sequence. At various stages during this evolutionary cycle, such stars can attain dimensions of hundreds to thousands of stellar radii. While this is no impediment for single stars, stars in close enough binaries will overflow their Roche lobes at this stage and mass loss will result. If sufficient mass is lost (and hence internal pressures lifted), the evolution of the star may be truncated and the star may proceed onto the cooling sequence sooner that it would have as an isolated star. In particular, this mechanism has been proposed to explain the low mass white dwarfs in binary systems (Kippenhahn et al. (1967)).

The important point to note about these binary white dwarfs is their low mass. The criterion for core helium ignition in a red giant is $M_{core} \sim 0.5\,M_{\odot}$ (Sweigart & Gross (1978), Mazzitelli (1989)). Thus, any star with mass less than this must be composed of helium. Most of the binary pulsar companions have mass estimates significantly below this, although a few do have masses consistent with a carbon-oxygen core white dwarf. Thus, to study the evolution of these systems, we require an extensive grid of white dwarf models for helium core white dwarfs. Previous work on this subject has been limited. Webbink (1975) investigated the cooling of low mass stars with thick hydrogen envelopes and found that their luminosity was maintained by hydrogen burning for the entire white dwarf lifetime. However, Iben & Tutukov (1986) showed that a solar metallicity star with such a thick hydrogen layer will undergo CNO shell flashes while at the top of the white dwarf cooling sequence, resulting in the burning of much of the Hydrogen envelope. Thus, the Hydrogen content is self-limiting at $\sim$ few $\times 10^{-4} M_{\odot}$. Other investigations by Chin & Stothers (1971) and D'Antona, Magni and Mazzitelli (1972) addressed the basic physics of such objects, but none of the results were of sufficient generality to be used to determine accurate cooling ages. The construction of a grid of models to address these issues will be the subject of Chapter 2. The application of these models to the LMBP will be discussed in Chapters 3 and 4.

REFERENCES

Arons, J., 1993, ApJ, **408**, 160.

Baade, W. & Zwicky, F., 1934, Proc. Natl. Acad. Sci. **20**, 254.

Backer, D.C., Kulkarni, S.R., Heiles, C., Davis, M.M. & Goss, W.M., 1982, *Nature*, **300**, 615.

Bahcall, J.N., Flynn, C. & Gould, A., 1992, ApJ, **389**, 234.

Bell, J.F., Bailes, M. & Bessel, M.S., 1993, *Nature*, **364**, 603.

Bhattacharya, D., Wijers, R.A.M.J., Hartman, J.W. & Verbunt, F., 1992, A&A, **254**, 198.

Bietenholz, M.F., Frail, D.A. & Hankins, T.H., 1991, ApJ, **376**, L41.

Blondin, J.M. & Freese, K., 1988, *Nature*, **323**, 786.

Brandt, N. & Podsiadlowski, P., 1995, MNRAS, **274**, 461.

Burrows, A. & Hayes, J., 1996, Phys.Rev.Lett, **76**, 352.

Chen, K.Y., & Ruderman,M.A., 1993, ApJ, **402**, 264.

Chin, C. & Stothers, R., 1971, ApJ, **163**, 555.

Cordes, J.M., 1986, ApJ, **311**, 183.

Cordes, J.M., Romani, R.W., Lundgren, S.C., 1993, *Nature*, **362**, 133.

Coté, J. & Pylyser, E.H.P., 1989, A&A, **218**, 131.

D'Antona, F., Magni, G. & Mazzitelli, I., 1972, Ap&SS, **19**, 151.

D'Antona, F. & Mazzitelli, I., 1989, ApJ, **347**, 934.

D'Antona, F. & Mazzitelli, I., 1990, ARA&A, **28**, 139.

Drukier, G.A., 1995, preprint

Foster, R.S. & Fischer, J., 1996, ApJ, **460**, 902.

Frail, D.A., Goss, W.M. & Whiteoak, J.B.Z., 1994, ApJ, **437**, 781.

Gallant, Y.A. & Arons, J., 1994, ApJ, **435**, 230.

Gold, T., 1968, *Nature*, **218**, 731.

Goldreich, P. & Julian, W.H., 1969, ApJ, **157**, 869.

Groth, E.J., 1975a, ApJ, **200**, 278.

Groth, E.J., 1975b, ApJS, **29**, 453.

Gunn, J.E. & Ostriker, J.P., 1970, ApJ, **160**, 979.

Harrison, P.A., Lyne, A.G. & Anderson, B., 1993, MNRAS, **261**, 113.

Hewish, A., Bell, S.J., Pilkington, J.D.H., Scott, P.F. & Collins, R.A., 1968, *Nature*, **217**, 709.

Hoshino, M., Arons, J., Gallant, Y.A. & Langdon, A.B., 1992, ApJ, **390**, 454.

Iben, I. & Tutukov, A.V., 1984, ApJ, **282**, 615.

Iben, I. & Tutukov, A.V., 1986, ApJ, **311**, 742.

Johnston, S., Manchester, R.N., Lyne, A.G., Nicastro, L. & Spyromilio, J., 1994, MNRAS, **268**, 430.

Joss, P.C., Rappaport, S. & Lewis, W., 1987, ApJ, **319**, 180.

Kennel, C.F. & Coroniti, F.V., 1984a, ApJ, **283**, 694.

Kennel, C.F. & Coroniti, F.V., 1984b, ApJ, **283**, 710.

Kippenhahn, R., Kohl, K. & Weigert, A., 1967, ZAp, **66**, 58.

Koester, D. & Schonberner, D., 1986, A&A, **154**, 125.

Kuijken, K. & Gilmore, G., 1989, MNRAS, **239**, 571,605.

Kulkarni, S.R. & Narayan, R., 1988, ApJ, **335**, 755.

Kulkarni, S.R., 1992, Phil. Trans. R. Soc. London Ser. A, **341**, 77.

Landau, L.D., 1932, private communication to L.Rosenfeld, referred to by Rosenfeld in Proc. of 16th Solvay Conf. on Physics, Univ. of Brussels Press, 1974

Lorimer, D.R., 1995, MNRAS, **274**, 300.

Lyne, A.G., Anderson, B. & Salter, M.J., 1982, ApJ, **201**, 503.

Lyne, A.G. & Lorimer, D.R., 1994, *Nature*, **369**, 127.

Lyne, A.G., Ritchings, R.T. & Smith, F.G., 1975, MNRAS, **171**, 579.

Manchester, R.N., Durdin, J.M. & Newton, L.M., 1985, *Nature*, **313**, 374.

Mazzitelli, I., 1989, ApJ, **340**, 249.

Melrose, D.B., 1992, Phil. Trans. R. Soc. Lond. A (1992), **341**, 105.

Mestel, L., 1952, MNRAS, **112**, 583.

Michel, F.C., 1991, *Theory of Neutron Star Magnetospheres*, Chicago: Chicago University Press

Narayan, R., 1987, ApJ, **319**, 162.

Narayan, R. & Ostriker, J.P., 1990, ApJ, **352**, 222.

Ostriker, J.P. & Gunn, J.E., 1969, ApJ, **157**, 1395.

Phillips,J.A. & Thorsett, S.E., 1994, Ap&SS, **212**, 91.

Phinney, E.S., Evans, C.R., Blandford, R.D. & Kulkarni, S.R., 1988, *Nature*, **333**, 832.

Phinney, E.S. & Kulkarni, S.R., 1994, ARA&A, **32**, 591.

Phinney, E.S., 1993, in *Structure & Dynamics of Globular Clusters*, ed. S.G. Djorgovski & G. Meylan, pp 141, Astr.Soc.Pac.

Podsiadlowski, P., 1993, in *Planets Around Pulsars*, ed. J.A. Phillips, S.E. Thorsett & S.R. Kulkarni, pp 149, Astr.Soc.Pac.

Pylyser, E.H.P. & Savonije, G.J., 1988, A&A, **191**, 57.

Rappaport, S., Verbunt, F. & Joss, P., 1983, ApJ, **275**, 713.

Rappaport, S., Podsiadlowski, P., Joss, P.C., Di Stefano, R. & Han, Z., 1995, ApJ, **273**, 731.

Rees, M.J. & Gunn, J.E., 1974, MNRAS, **167**, 1.

Refsdal, S. & Weigert, A., 1971, A&A, **13**, 367.

Richer, H.B. et al., 1995, ApJ, **451**, L17.

Romani, R.W., 1990, *Nature*, **347**, 741.

Ruderman, M., 1995, J.Ap.Astr., **16**, 207.

Smarr, L.L. & Blandford, R.D., 1976, ApJ, **207**, 574.

Sweigart, A.V. & Gross, P.G., 1978, ApJS, **36**, 405.

Taam, R.E. & van den Heuvel, E.P.J., 1986, ApJ, **305**, 235.

Tamahana, C.M., Silk, J., Wood, M.A. & Winget, D.E., 1990, ApJ, **358**, 164.

Timmes, F.X., Woosley, S.E. & Weaver, T.A., 1996, ApJ, **457**, 834.

van den Heuvel, E.P.J., 1995, J. Ap. Astr., **16**, 255.

Winget, D.E., Hansen, C.J., Liebert, J., Van Horn, H.M., Fontaine, G., Nather, R.E., Kepler, S.O. & Lamb, D.Q., 1987, ApJ, **315**, L77.

Webbink, R.F., 1975, MNRAS, **171**, 555.

Wolszczan, A., 1991, *Nature*, **350**, 688.

Wolszczan, A. & Frail, D.A., 1992, *Nature*, **355**, 145.

Wood, M.A., 1992, ApJ, **386**, 539.

Chapter 2 The White Dwarf Model

This chapter describes the details of the white dwarf model construction. Although most of the material in this chapter is probably not original, an exposition is necessary to demonstrate the features and limitations of the models we will use in the next chapter.

2.1 Numerical Algorithm

Our task in this chapter, in purely mathematical terms, is to solve the four stellar structure equations

$$\frac{dP}{dr} = -\rho\frac{GM(r)}{r^2} \tag{2.1}$$

$$\frac{dM}{dr} = 4\pi r^2\rho \tag{2.2}$$

$$\frac{dL}{dr} = 4\pi r^2\rho\epsilon \tag{2.3}$$

$$\frac{dT}{dP} = \frac{T}{P}\nabla \tag{2.4}$$

where we have written the last equation in a form that applies for both radiative and convective transport. In the case of radiative transport,

$$\nabla = \frac{3}{16\pi ac}\frac{\kappa}{T^3}\frac{L(r)}{GM(r)} \tag{2.5}$$

where κ is the opacity and L(r) and M(r) are the luminosity and mass interior to radius r respectively. ρ is the density and ϵ is the emissivity of the stellar material, including the thermal and gravitational contraction terms (see section 2.5). Although most stellar structure problems are concerned with the solution of these four equations, the rich variety of physical inputs that enter via functions ρ, κ and ϵ, plus the, as yet unspecified, boundary conditions mean that this is not a trivial exercise.

Our first step will be to transform the above equations to a form more amenable to numerical computation. The first matter is normalization. We shall normalize the radius

variable r to a characteristic stellar length scale

$$x = R/10^{11}cm. \tag{2.6}$$

We will also remove constants from the luminosity, pressure and temperature as well as transforming the last two to logarithmic variables,

$$\ell = L/L_0 \tag{2.7}$$

$$\pi = \ln P/P_0 \tag{2.8}$$

$$\theta = \ln T/T_0. \tag{2.9}$$

We will do the same to the density, which will be determined from the equation of state and P and T,

$$\phi = \ln \rho/\rho_0. \tag{2.10}$$

Since much of the interesting structure in a white dwarf occurs in a very thin shell on the outer edge of the star, we choose a mass variable ξ such that

$$m = M/M_0 = f(\xi). \tag{2.11}$$

where

$$f(\xi) = 1 - e^{-\xi}. \tag{2.12}$$

We also convert the equations to a form in which ξ is the independent variable rather than x.

We use the various normalization constants to set coefficients in the transformed stellar structure equations to unity. This determines P_0, T_0 and ρ_0 in terms of L_0 and M_0. Our stellar structure equations (2.1)-(2.4) are then

$$\frac{dx}{d\xi} = f'(\xi)\frac{e^{-\phi}}{x^2} \tag{2.13}$$

$$\frac{d\ell}{d\xi} = f'(\xi)\bar{\epsilon} \tag{2.14}$$

$$\frac{d\pi}{d\xi} = -f'(\xi)f(\xi)\frac{e^{-\pi}}{x^4} \tag{2.15}$$

$$\frac{d\theta}{d\xi} = -f'(\xi)f(\xi)\frac{e^{-\pi}}{x^4}\nabla. \tag{2.16}$$

In the second equation we have normalized the emissivity

$$\epsilon = \frac{\epsilon_0 M_0}{L_0}\bar{\epsilon}$$

We also use the radiative gradient (2.5) to determine the normalization, resulting in the expression

$$\nabla_{\rm rad} = \frac{\bar{\kappa}e^{\pi-4\theta}\ell}{f(\xi)} \tag{2.17}$$

The constants are thus

$$P_0 = 2.123\times 10^{14}\,{\rm dyn.cm^{-2}}\left(\frac{M_0}{M_\odot}\right)^2 \tag{2.18}$$

$$\rho_0 = 0.15915\,{\rm g.cm^{-3}}\frac{M_0}{M_\odot} \tag{2.19}$$

$$T_0 = 3.568\times 10^6{\rm K}\left(\frac{M_0}{M_\odot}\frac{L_0}{L_\odot}\right)^{1/4} \tag{2.20}$$

where the opacity has been normalized by 100 $\rm cm^2.g^{-1}$, i.e., $\kappa = 10^2\bar{\kappa}$.

The equations (2.13)-(2.16) are the equations we will solve. The method we use is that due to Henyey et al. (1959, 1964), although we followed the approach laid out in Kippenhahn et al. (1967). We define a grid in our independent variable ξ and use finite differences to express the equations on this grid. This defines a set of vectors A^i_j where i is the equation index and j is the grid point index. This also defines a set of dependent variables y^k_j where the k is the variable index and j is still the grid point index. A solution to the problem is a 4N- vector

$$y = \left(y^1_1, y^2_1, \cdots, y^3_N, y^4_N\right) \tag{2.21}$$

which yields

$$A^i_j(y) = 0 \tag{2.22}$$

for all i and j. Before we can solve the equations, we have to specify our boundary conditions. With four variables and four equations, we need four boundary conditions. There are two boundary conditions to be specified at r=0 (corresponding to m=0 and $\xi = 0$) and two at

the outer edge. At r=0, the physical boundary conditions are that mass and luminosity must vanish as $r \to 0$. The simple nature of these boundary conditions allows us to expand our four variables in Taylor series about the origin to get the values at the first grid point (which has $\xi > 0$). We also have to specify two conditions on the boundary at the outer edge. These are determined by matching a stellar atmosphere calculation to our solution at some point $\xi = \xi_{out}$. The full system to be solved is the following, with the assignments $y^1 = x$, $y^2 = \ell$, $y^3 = \pi$ and $y^4 = \theta$.

$$C^i(y_0^3, y_0^4, \bar{y}_1) = 0, (i = 1, 4) \tag{2.23}$$

$$A_j^i(\bar{y}_j, \bar{y}_{j+1}) = 0, (i = 1, 4; j = 1, N-1) \tag{2.24}$$

$$B^i(\bar{y}_N) = 0, (i = 1, 2) \tag{2.25}$$

where the C vectors are the inner boundary conditions determined by the Taylor series at the first grid point, the B vectors are the outer boundary conditions and the A vectors are the equations on the intermediate grid points. We also use the notation $\bar{y}$ to denote the four-vector of four dependent variables at a single grid point. This is a system of 4 + 4 (N-1) +2 = 4 N + 2 equations with 2 + 4 N variables, so it is solvable.

To solve the above system we do the following. Given an initial solution y_0, which, in general, does not satisfy the above equations, we calculate the linear perturbations necessary to satisfy said equations, i.e., we calculate δy such that

$$A_j^i(y_0) + \left.\frac{\partial A_j^i}{\partial y}\right|_0 \delta y = 0 \tag{2.26}$$

Since we can calculate $A_j^i(y_0)$ and $\left.\frac{\partial A_j^i}{\partial y}\right|_0$, we can solve the matrix equation

$$\mathbf{H}.\delta y = -\mathbf{A} \tag{2.27}$$

where $\mathbf{H}$ is the Henyey matrix, the matrix formed by the various derivatives. The structure of the stellar structure equations are such that the Henyey matrix is band diagonal, and can thus be solved in O(N) operations.

We collect all the equations as follows:

$$C^3 = y_1^3 - y_0^3 + \frac{3}{2}3^{-4/3}g(0)^{2/3}e^{4/3\phi_0 - y_0^3}\xi^{2/3} = 0 \quad (2.28)$$

$$C^4 = y_1^4 - y_0^4 + \frac{3}{2}3^{-4/3}g(0)^{2/3}e^{4/3\phi_0 - y_0^3}\nabla_0\xi^{2/3} = 0 \quad (2.29)$$

$$C^1 = y_1^1 - (3g(0))^{1/3}e^{-\phi_0/3}\xi^{1/3} = 0 \quad (2.30)$$

$$C^2 = y_1^2 - g(0)\bar{\epsilon}(0)\xi = 0 \quad (2.31)$$

$$A_j^1 = y_{j+1}^1 - y_j^1 - (\xi_{j+1} - \xi_j)\, g(\frac{1}{2}(\xi_j + \xi_{j+1}))\frac{\exp(-\frac{1}{2}(\phi_j + \phi_{j+1}))}{\left[\frac{1}{2}\left(y_j^1 + y_{j+1}^1\right)\right]^2} = 0 \quad (2.32)$$

$$A_j^2 = y_{j+1}^2 - y_j^2 - (\xi_{j+1} - \xi_j)\, \bar{\epsilon}(\frac{1}{2}(y_{j+1}^3 + y_j^3), \frac{1}{2}(y_{j+1}^4 + y_j^4)) = 0 \quad (2.33)$$

$$A_j^3 = y_{j+1}^3 - y_j^3 - (\xi_{j+1} - \xi_j)\, g(\frac{1}{2}(\xi_j + \xi_{j+1}))\, f(\frac{1}{2}(\xi_j + \xi_{j+1})) \times \frac{\exp(-\frac{1}{2}(y_{j+1}^3 + y_j^3))}{\left[\frac{1}{2}\left(y_j^1 + y_{j+1}^1\right)\right]^4} = 0 \quad (2.34)$$

$$A_j^4 = y_{j+1}^4 - y_j^4 - (\xi_{j+1} - \xi_j)\, g(\frac{1}{2}(\xi_j + \xi_{j+1}))\, f(\frac{1}{2}(\xi_j + \xi_{j+1})) \times \frac{\exp(-\frac{1}{2}(y_{j+1}^3 + y_j^3))}{\left[\frac{1}{2}\left(y_j^1 + y_{j+1}^1\right)\right]^4}\frac{1}{2}(\nabla_j + \nabla_{j+1}) = 0 \quad (2.35)$$

$$B^1 = y_N^3 - F^1(y_N^1, y_N^2) = 0 \quad (2.36)$$

$$B^2 = y_N^4 - F^2(y_N^1, y_N^2) = 0 \quad (2.37)$$

where $g(\xi) = f'(\xi)$ and F^1 and F^2 are determined from the atmosphere calculations.

We use the Press et al. (1992) subroutines **bandec** and **banbks** to solve the band-diagonal matrix equation (2.27). The corrections are applied to yield the new solution and iterated again. The iteration is stopped when the maximum change in the solution at any grid point is less than a given amount, i.e.,

$$\max(\Delta y_j^i; i = 1, 4; j = 1, N) \leq 10^{-4} \quad (2.38)$$

This method of solution is efficient for calculating sequences of models because each solution provides a good approximation for the next model in the sequence and thus con-

vergence is rapid (unlike shooting methods which start from scratch each time). This is the basic algorithm, common to many codes. The interesting part of the problem is the microphysical inputs.

2.2 Opacities

The most important aspect of the microphysics from the point of view of the cooling is the opacity. This determines the rate of energy transport at any point in the star (unless the region is convective, in which case the equation of state plays the dominant role). Figure 2.1 shows the temperature-density plane and the regions where various different opacity sources dominate. These will be explained below.

2.2.1 Radiative Opacities

While the gas is non-degenerate, the primary mechanism for energy transport will be radiative diffusion. The basis for our radiative opacity table is the calculation of the OPAL group at Lawrence Livermore (Rogers & Iglesias (1992)). This calculation is based on the so-called physical model for calculating the state of a Coulomb plasma. This approach has the advantage that it calculates a model using the fundamental constituents of ions and electrons, and the aggregates we know as atoms and molecules are accounted for self-consistently using the interatomic forces (Rogers (1981)). However, this method does require that the many body effects be treated in a perturbation expansion (Rogers & de Witt (1973)), so that it is limited to low density plasmas. This is not a severe restriction over much of the phase diagram because electron conduction becomes the dominant transport mechanism at high densities anyway. However, although molecules are accounted for in the underlying equation of state calculations, the opacities do not include any molecular contributions, which means that they do not extend to very low temperatures.

In order to avoid the time expended in calling the OPAL subroutine every time we want to calculate the opacity, we decided to fit the OPAL table by a series of spline fits first and to use this information in our calculation. The fitting is best performed not in $\rho - \mathrm{T}$ space, but rather $\mathrm{R} - \mathrm{T}$ space, where $\mathrm{R} = \rho/\mathrm{T}_6^3$ and $\mathrm{T}_6 = \mathrm{T}/10^6\mathrm{K}$. The OPAL region runs from $\mathrm{T}_6 = 0.006$ to $\mathrm{T}_6 = 500$ and from $\mathrm{R} = 10^{-7}$ to $\mathrm{R} = 10$ (although a small portion of this region is also excluded by the subroutine, which is not mentioned in the documentation).

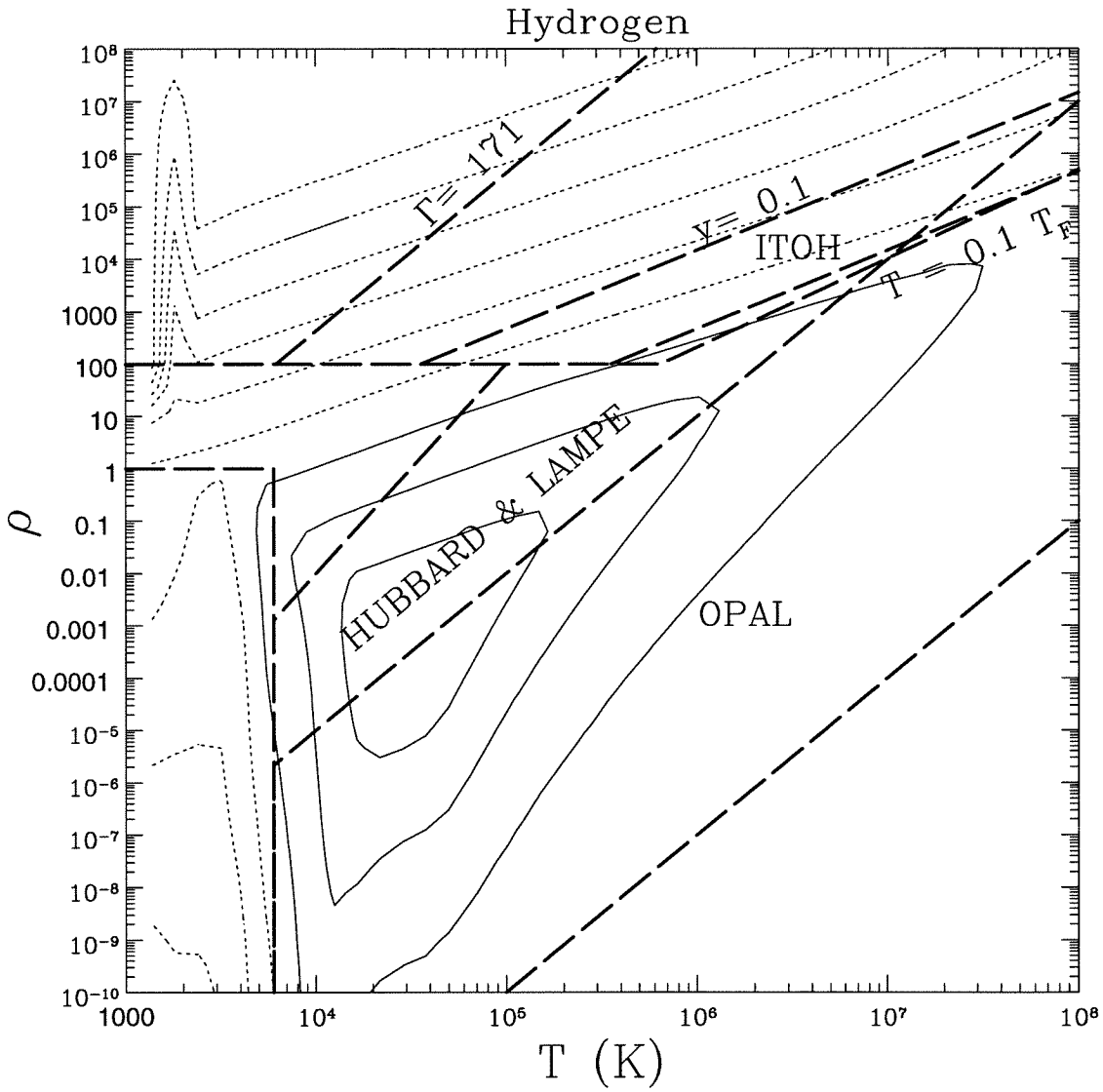

Figure 2.1: **The Hydrogen Phase Diagram:** We show here the contours of constant log κ, where κ is the Rosseland mean opacity in $cm^2.g^{-1}$. Solid contours have values 0,2 and 4, while the dotted contours have values, -2, -4, etc. down to -12. The thick dashed lines denote the boundaries between various regions of dominant opacities.

For 25 equally spaced values of log R between -7 and 1, we fit natural splines over the range of T, each spline consisting of 100 points, equally spaced in log T. We note that points which fall within the 'allowed' region but which satisfy

$$\log T_6 > -0.6116 \log R + 1.4758$$

will also not yield values in the OPAL subroutine. For splines which pass through this region, we retain the spacing in log T, but lower the number of grid points when fitting the spline. The calculation of the derivatives required in the Henyey matrix follows a similar route. We have checked that the derivatives from the spline are in good agreement with those obtained from the OPAL subroutines. We calculate the derivatives in the R-T plane rather than the ρ-T plane, so that we have to transform the opal derivatives

$$\left(\frac{\partial \log \kappa_r}{\partial \log T}\right)_\rho = \left(\frac{\partial \log \kappa_r}{\partial \log T}\right)_R - 3\left(\frac{\partial \log \kappa_r}{\partial R}\right)_T \tag{2.39}$$

$$\left(\frac{\partial \log \kappa_r}{\partial \log \rho}\right)_T = \left(\frac{\partial \log \kappa_r}{\partial R}\right)_T \tag{2.40}$$

However, the OPAL opacity calculations only go down to temperatures of 6000 K; they are not sufficient to address the properties of white dwarfs down to temperatures of 4000 K. Since no tables of sufficient generality exist for such temperatures, we performed the calculations ourselves, using physical parameters mostly from Lenzuni, Chernoff and Salpeter (1991). Since this represents the only truly original work in this chapter, it requires a more extended exposition, given in Appendix A.

2.2.2 Conductive Opacity

For high densities, the energy transport is not governed by the radiation, but rather by electron conduction. We can cast the conductivity in the form of a 'conductive opacity' and combine it with the radiative opacity to obtain a smooth transition. Recall that opacities add harmonically

$$\frac{1}{\kappa} = \frac{1}{\kappa_1} + \frac{1}{\kappa_2}.$$

For the conductive opacity at high density, we use the classical regime calculations of Itoh et al. (1983) and the extensions to semi-classical ions of Mitake et al. (1984). We

convert the thermal conductivity into an opacity as follows. We note that the heat flux can be represented in two ways:

$$F = -K_c \nabla T = -\frac{4ac}{3\kappa\rho} T^3 \nabla T \tag{2.41}$$

so that the equivalent opacity is

$$\kappa_c = \frac{4ac}{3K_c\rho} T^3 \tag{2.42}$$

or

$$\log \kappa_c = -3.519 + 3\log T - \log \rho - \log K_c \tag{2.43}$$

and thus the derivatives are

$$\left(\frac{\partial \log \kappa_c}{\partial \log \rho}\right)_T = -1 - \left(\frac{\partial \log K_c}{\partial \log \rho}\right)_T \tag{2.44}$$

$$\left(\frac{\partial \log \kappa_c}{\partial \log T}\right)_\rho = 3 - \left(\frac{\partial \log K_c}{\partial \log T}\right)_\rho \tag{2.45}$$

The range of validity of the above expressions is determined by the following conditions.

1. The electrons are degenerate. This requires that the temperature be less than the Fermi Temperature

$$T < T_F = 5.93 \times 10^9 \left[\left[1 + 0.641\rho_6^{2/3}\right]^{1/2} - 1\right]. \tag{2.46}$$

2. The ions form a Coulomb liquid, i.e.,

$$\Gamma = 0.5733 \frac{\rho_6^{1/3}}{T_8} < 171 \tag{2.47}$$

3. The state of the ionic system is described by the parameter

$$y = 2.608 \times 10^{-3} \frac{\rho_6^{2/3}}{T_8} \tag{2.48}$$

which measures the ratio of electron Fermi momentum to Ion thermal momentum. The Itoh calculations apply to the regime $y \ll 1$ where the electron Fermi energy is negligible. The Mitake results extend the analysis to $y \leq 0.1$.

The calculations of the Japanese group do not extend to densities lower than $10^2 g.cm^{-3}$. At densities lower than this, we use the conductivities of Hubbard and Lampe (1969). The primary improvement of the former calculations are the treatment of the ion-ion correlations at values of the Coulomb coupling parameter (see next section) $\Gamma > 1$, which leads to a more accurate electron-ion scattering cross-section.

2.3 Equation of State

Since we consider mostly Hydrogen and Helium, our primary equation of state is that of Saumon et al. (1995) (or SCV). At densities above the limits of their calculations, we extended the equation of state using a Thomas-Fermi model calculation of our own, outlined in Appendix B. When we have calculated Carbon composition cores, we have used the results of Fontaine, Graboske and Van Horn (1977).

Figure 2.2 delineates the important regions of the phase diagram. Also shown are the location of the centre and photosphere for a 0.3 $M_\odot$ stellar model with a Helium core and $3 \times 10^{-4} M_\odot$ of Hydrogen in the envelope. The dotted lines indicate the position where n(HI) $\sim$ n(HII) and n(HI) $\sim$ n(H2). Thus, we see that, when the dominant atmospheric constituent is neutral atomic Hydrogen, the opacity drops and hence the photospheric density (and hence pressure) increases. This trend is only reversed with the formation of molecular Hydrogen, when the opacity again increases.

The upper panel shows the Helium core. The thin solid line is the degeneracy boundary, defined by the relation $\eta = E_F/kT = 10$. We see that the core of the White dwarf is degenerate over all of the white dwarf sequence. We also note that, unlike Carbon/Oxygen white dwarfs, crystallization is not important, since the core takes longer than a Hubble time to reach the crystallization boundary. This is because the Coulomb coupling parameter $\Gamma = Ze^2/ak_BT \propto Z/A^{1/3}$ (where a=interatomic separation), which means it is 40% smaller for Helium than Carbon.

Figure 2.3 demonstrates the matching between the SCV equation of state and our supplementary Thomas-Fermi calculations described in B. We also see that the equation of state is well described by an ideal gas at all temperatures as long as $\rho < 10^{-2} g.cm^{-3}$.

Our high density equation of state includes the Thomas-Fermi correction but neglects the higher order corrections discussed by Salpeter (1961). To estimate the effect of neglecting

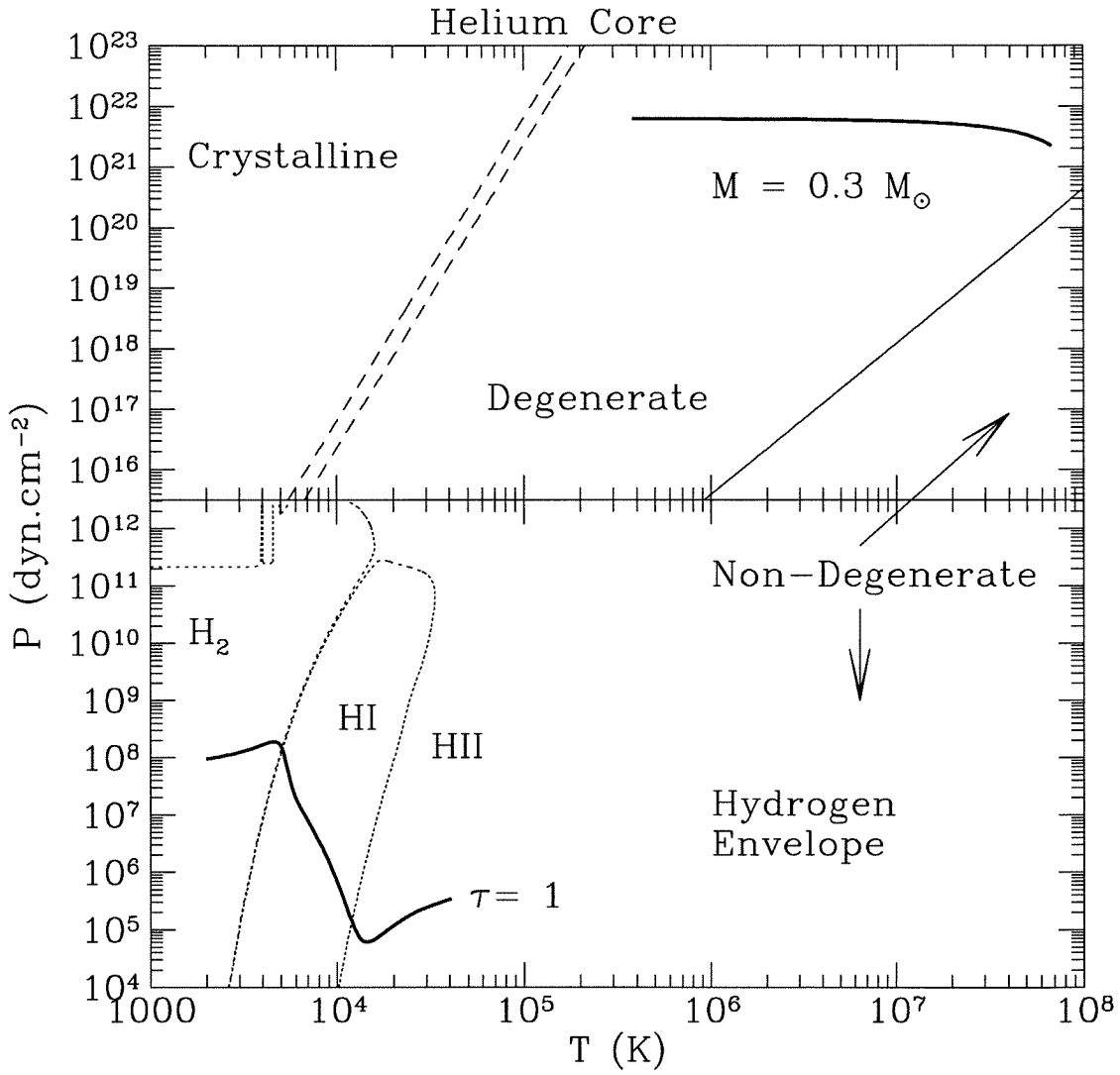

Figure 2.2: **The Most Important Regions of the Phase Diagram:** The lower panel shows the phase diagram for Hydrogen at low densities. The dotted lines indicate the transitions from a plasma dominated by ionized Hydrogen, to neutral Hydrogen and then to molecular Hydrogen. The heavy solid line denotes the location of the photosphere for a $0.3\,M_\odot$ model with Helium core and Hydrogen envelope. The upper panel shows the high density phase diagram for Helium, where the thin solid line indicates the degeneracy boundary for Helium and the dashed lines indicate the transition from an ionic gas/liquid to ionic glass and then to ionic crystal. The heavy solid line indicates the central values for the same $0.3\ M_\odot$ model as before.

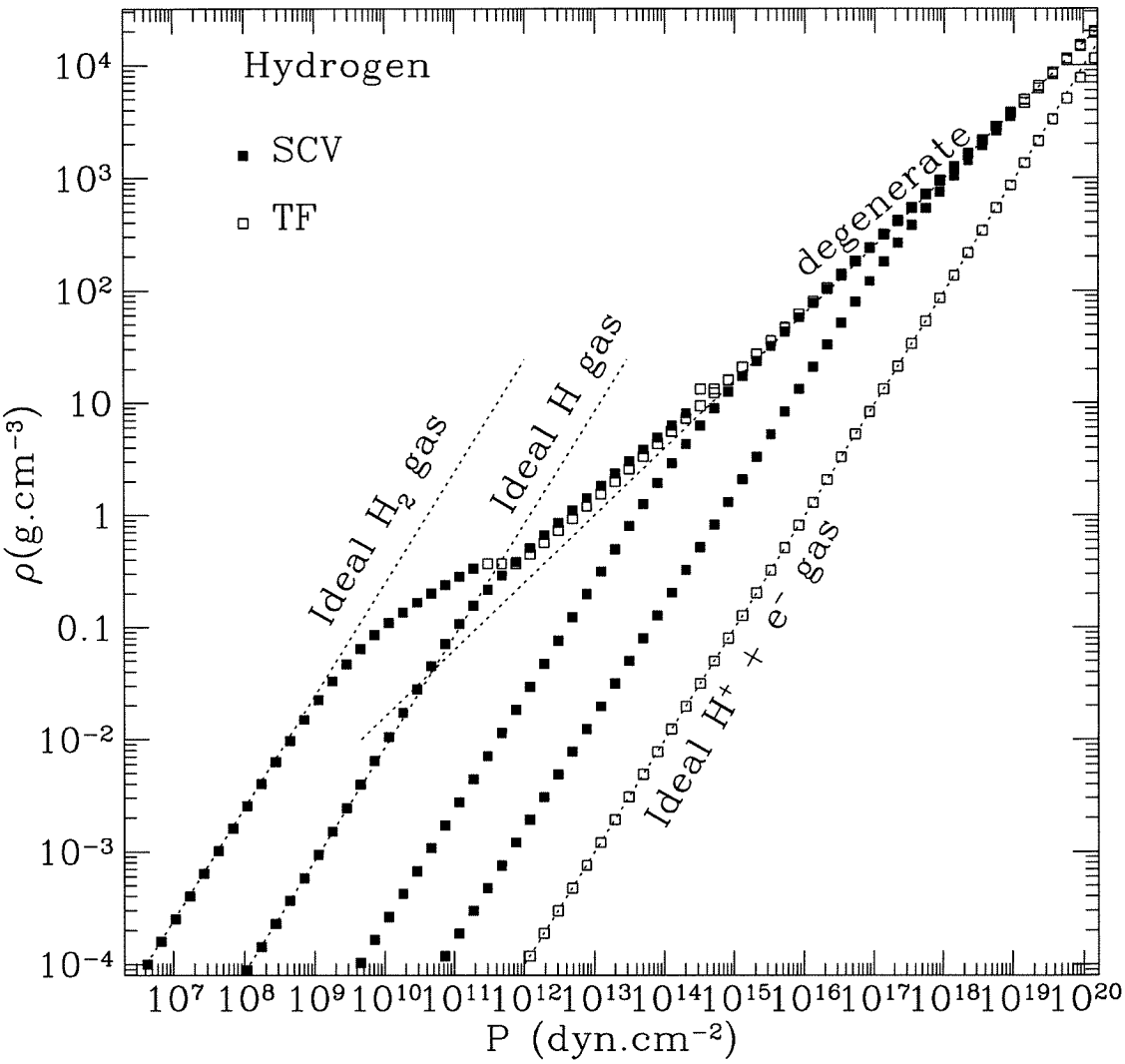

Figure 2.3: **The Equation of State for Hydrogen:** The solid squares are from the calculations of Saumon et al. (1995). The open squares are the result of our Thomas-Fermi calculation. The various curves are each at constant temperature, ranging from 10^3 K on the far left (so that the dominant low density species is molecular hydrogen) to 10^8 K on the far right (which is too high for the SCV equation of state and so is determined entirely from our calculation). The various dotted lines indicate the different simplified limiting cases as labelled.

the exchange energy correction (the next higher term), we compare the relative contributions to the internal energy as calculated by Salpeter. At the densities which we are interested in ($\rho \sim 10^5 - 10^6\,\mathrm{g.cm^{-3}}$), the exchange energy represents a correction $\sim 2\%$.

The most uncertain part of the equation of state table is that where the plasma is both partially ionised and partially degenerate ($\rho \sim 0.1 - 1\,\mathrm{g.cm^{-3}}$, $\mathrm{T} \sim 10^5\,\mathrm{K}$). All published equation of state calculations treat this region by interpolating between the various high and low density regions. SCV compare the various determinations in the literature and estimate that the density (as a function of pressure and temperature) is uncertain by a factor ~ 2. The most likely influence of this uncertainty is a change in the depth of the convection zone for stars where the base of the convection zone lies within this region. We have tested our models for this uncertainty in cases where it might be important and have found little important variation in any global parameters of the stellar models (see 4.3.4).

The effects of this uncertainty are small, as is shown in Figure 2.4. We see that the entropy is conserved to within 1 % in the convective region, as expected. This is despite the fact that the composition in this particular case is 75 % Helium and 25 % Hydrogen (due to convective dredge-up). The slight error in matching between the atmosphere and interior grid is due to the interpolation procedure used to determine the matching between interior and exterior solution. This error is even smaller for the cases when the atmosphere is of pure composition (because the variation due to changing composition from time-step to time-step is responsible for some of the mismatch in Figure 2.4).

2.4 Convection

Once we have our equation of state and thus ∇_{ad}, we need to include a prescription for calculating convection. We do so using the standard mixing length formalism outlined in Kippenhahn & Weigert (1991) (see also Mihalas (1980)). Convection sets in when the Schwarzschild criterion $\nabla_{\mathrm{rad}} > \nabla_{\mathrm{ad}}$ is satisfied.

The basic picture in mixing length theory is energy transport by turbulent fluid elements which possess an excess of energy relative to the surrounding medium. After travelling some characteristic distance (the mixing length), these fluid elements dissolve smoothly into the background, resulting in a direct transport of energy and enforcing a lower temperature gradient than would exist if the only method of energy transport were through radiation.

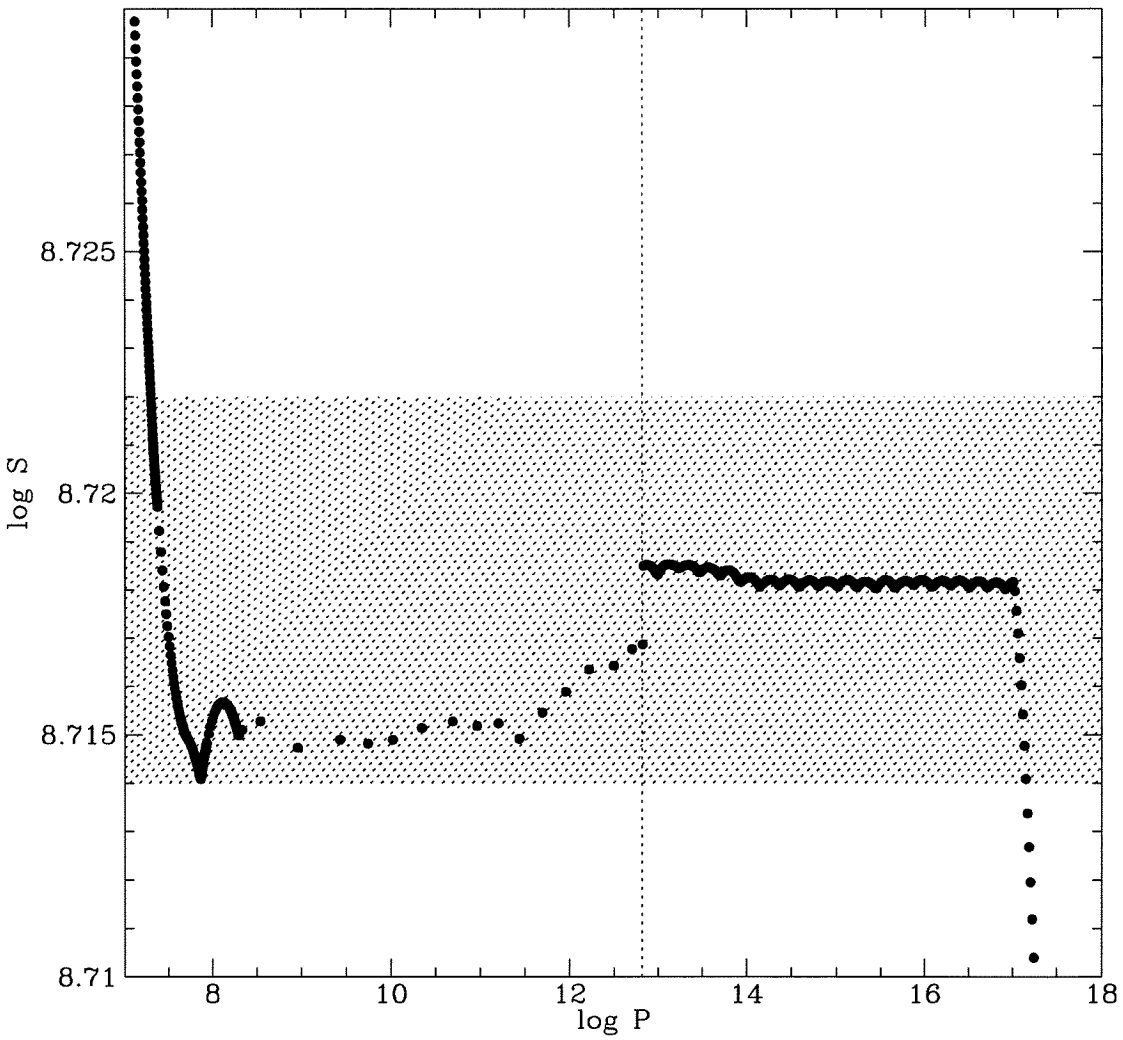

Figure 2.4: **Model Entropy Profile:** The profile shown here is the entropy for a 0.12 $M_\odot$ model with 10^{-4} $M_\odot$ of Hydrogen on the surface. The shaded area encloses a 1 % variation in the entropy determined from the base of the convection zone. We see that the entire convection zone, including the uncertain regions discussed above, lie within this range. The vertical dotted line indicates the matching between the central grid and the atmosphere calculation.

We need to define a number of different temperature gradients:

$\nabla_{\rm rad}$ = gradient if radiation were the only transport mechanism.

$\nabla_{\rm ad}$ = adiabatic gradient (i.e., fluid elements with this background are neutrally bouyant)

$\nabla_{\rm E}$ = gradient of convective elements

∇ = gradient of the background.

In general, we have

$$\nabla_{\rm rad} \geq \nabla \geq \nabla_{\rm E} \geq \nabla_{\rm ad}. \tag{2.49}$$

A rising fluid element which has travelled a distance Δr contains an excess heat relative to the surroundings $\sim \rho C_p \delta T$, because of the differenece in temperature gradients in fluid element and background ($\delta T \sim \Delta r \left(\partial T/\partial r - \partial T/\partial r|_E\right)$). Thus, for elements travelling with speed $\bar{v}$, we have an energy flux due to convection of

$$\pi F_{\rm conv} = \rho C_p \bar{v} \delta T = \rho C_p \bar{v} \left[-\frac{\partial T}{\partial r} + \left.\frac{\partial T}{\partial r}\right|_E \right] \Delta r \tag{2.50}$$

If we average over all fluid elements at any particular point, we approximate $\Delta r \sim \frac{1}{2}\ell_m$, where ℓ_m is the mixing length. This is usually cast in terms of the pressure scale height $H_p = -P\frac{\partial r}{\partial P} = \frac{P}{g\rho}$. Thus, we have

$$\pi F_{\rm conv} = \frac{P\bar{v}C_p}{g} \left[-\frac{\partial T}{\partial r} + \left.\frac{\partial T}{\partial r}\right|_E \right] \frac{\ell_m}{2H_p} = \frac{1}{2}\rho C_p \bar{v} T \left(\nabla - \nabla_E\right) \frac{\ell_m}{H_p} \tag{2.51}$$

To estimate $\bar{v}$, we need to consider the work done on an element by the buoyancy forces. The force (per unit volume) is $-g\delta\rho$, where $\delta\rho$ is the density difference between an element and the surroundings. In pressure equilibrium, we may relate the density difference to a temperature difference $\delta\rho = \frac{\rho}{T}\left(\frac{\partial \ln \rho}{\partial \ln T}\right)_P \delta T = -\frac{Q\rho}{T}\delta T$, and thus the work done is

$$W = \int_0^{\ell_m/2} f(\Delta r) d(\Delta r) = \frac{gQ\rho}{8} H_p \left(\nabla - \nabla_E\right) \left(\frac{\ell_m}{H_p}\right)^2 \tag{2.52}$$

If we assume that half of this energy is expended on pushing aside the background and half

goes into providing kinetic energy of the fluid element, then $\frac{1}{2}W = \frac{1}{2}\rho\bar{v}^2$, and thus

$$\pi F_{conv} = \left(\frac{gQH_p}{32}\right)^{1/2} \rho C_p T (\nabla - \nabla_E)^{3/2} \left(\frac{\ell_m}{H_p}\right)^2 \tag{2.53}$$

This expression is correct for the ML1 mixing length prescription (Böhm-Vitense (1958)) following the terminology of Fontaine, Villeneuve & Wilson (1981). The general mixing length expression is

$$\pi F_{conv} = b\rho C_p T (aQH_p)^{1/2} (\nabla - \nabla_E)^{3/2} \left(\frac{\ell_m}{H_p}\right)^2 \tag{2.54}$$

where a and b have the values 1/8 and 1/2 respectively in the ML1 theory.

We also need to consider the efficiency of the convective transport, expressed by the parameter

$$\gamma = \frac{\text{excess energy content at time of dissolution}}{\text{energy lost by radiation during element lifetime}} \tag{2.55}$$

The excess energy is $\propto \nabla - \nabla_E$, whereas, if the fluid element had moved adiabatically, it would be $\propto \nabla - \nabla_{ad}$, so that the loss due to radiation is the difference of these two quantities, i.e.,

$$\gamma = \frac{\nabla - \nabla_E}{\nabla_E - \nabla_{ad}} \tag{2.56}$$

The radiation losses are different depending on whether the material is optically thick or optically thin.

1. $\underline{\tau < 1}$. $j_\nu = S_\nu \alpha_\nu$ = volume emission rate. Including emission into all solid angles and the element volume, we have

$$j_\nu = 4\pi\rho\kappa_\nu V \Delta B_\nu \tag{2.57}$$

The emission is for lifetime $\sim \ell_m/\bar{v}$ and the excess energy is $\rho C_p V \delta T$, so that, using $\Delta B = \frac{\partial B}{\partial T}\delta T = \frac{4\sigma T^3}{\pi}\frac{\delta T}{2}$ (we have assumed a grey atmosphere to remove the frequency dependence),

$$\gamma_{thin} = \frac{1}{8}\frac{C_p}{\sigma\kappa T^3}\left(\frac{gQ}{8H_p}\right)^{1/2}\frac{\ell_m}{H}(\nabla - \nabla_E)^{1/2} \tag{2.58}$$

We can cast this in terms of the optical depth, $\tau = \kappa\rho\ell_m$,

$$\gamma_{thin} = \frac{\rho C_p \bar{v}}{8\sigma T^3}\frac{1}{\tau} \tag{2.59}$$

2. $\underline{\tau \geq 1}$. In the optically thick case, we may use the diffusion approximation to set $-\partial T/\partial r \sim \delta T/\ell_m$ and get

$$\frac{\partial P_{rad}}{\partial \tau} = \frac{4\pi}{c}\frac{\partial K}{\partial \tau} = \frac{4\pi}{c}H = \frac{\pi F}{c} = \frac{\partial}{\partial \tau}\frac{1}{3}aT^4 \tag{2.60}$$

Thus

$$F_{tot} = \frac{c}{\pi}\frac{4}{3}aT^3\frac{\partial T}{\partial \tau} = -\frac{16}{3\pi}\frac{\sigma T^3}{\kappa\rho}\frac{\delta T}{\ell_m} \tag{2.61}$$

Thus,

$$\gamma = \frac{\rho C_p V \delta T}{\frac{16}{3}\frac{\sigma T^3}{\kappa\rho}\left(\frac{\delta T}{\ell_m}\right)A\left(\frac{\ell_m}{\bar{v}}\right)} = \frac{\rho C_p \bar{v}}{16\sigma T^3}3\kappa\rho\frac{V}{A} \tag{2.62}$$

where A is the area of the emitting surface and $V/A \sim \ell_m/3$ for a spherical bubble. In terms of optical depth this is

$$\gamma_{thick} = \frac{\rho C_p \bar{v}}{8\sigma T^3}\frac{\tau}{2} \tag{2.63}$$

We may combine the two limits into a single expression valid for all optical depths

$$\gamma = \frac{\rho C_p \bar{v}}{8\sigma T^3}\frac{1+\frac{1}{2}\tau^2}{\tau} \tag{2.64}$$

More generally,

$$\gamma = \frac{\rho C_p \bar{v}}{\sigma T^3}\frac{1}{d(\tau)} \tag{2.65}$$

where

$$d(\tau) = \frac{8\tau^2}{1+8\tau^2/c} \tag{2.66}$$

and c is 24 for ML1, 16 for ML2 (Böhm & Cassinelli (1971)) and ML3 (Bergeron, Wesemael & Fontaine (1992)).

Flux conservation requires

$$\pi F_{rad} + \pi F_{conv} = \sigma T_{eff}^4 \tag{2.67}$$

and, using $F_{rad}/F = \nabla/\nabla_{rad}$, we obtain a cubic equation (using ML1 and high optical depth)

$$x^3 + \frac{32U}{3}x^2 + 256U^2x - \frac{32UW}{3} = 0 \tag{2.68}$$

where

$$x = \sqrt{\nabla - \nabla_E} \tag{2.69}$$

$$W = \nabla_{rad} - \nabla_{ad} \tag{2.70}$$

$$U = \frac{\sigma T^3}{C_p \rho^2 \kappa \ell_m^2} \sqrt{\frac{8H_p}{gQ}}. \tag{2.71}$$

The properties of the solutions to a cubic equation are such that this has only one real solution if $D > 0$, where

$$D = \left(\frac{5888}{81}U^2\right)^3 + \left(\frac{4672}{729}U^3 + \frac{16}{3}UW\right)^2 \tag{2.72}$$

For real U and positive W (as our physical situation requires), this condition is satisfied, i.e. there is only one gradient given by

$$\nabla = \nabla_{ad} + 2Ux + x^2 \tag{2.73}$$

and x is written as

$$x = S + T - \frac{8}{27}U \tag{2.74}$$

where

$$R = \frac{4672}{729}U^3 + \frac{16}{3}UW \tag{2.75}$$

$$S = \left(R + \sqrt{D}\right)^{1/3} \tag{2.76}$$

$$T = \left(R - \sqrt{D}\right)^{1/3} \tag{2.77}$$

Note that we also require the derivatives of ∇ to put into the Henyey matrix. Thus

$$\partial\nabla = \partial\nabla_{ad} + 2x\partial U + 2(U + x)\partial x \tag{2.78}$$

Once we have a well-defined table of equation of state quantities and opacities, we can determine what regions of the phase space are convectively unstable by casting the Schwarzschild criterion ($\nabla_{rad} > \nabla_{ad}$) in the form

$$\frac{T^4 \nabla_{ad}}{\kappa P} < \frac{3}{64\pi G\sigma} \frac{L}{M} \tag{2.79}$$

The left-hand side is defined once we have an opacity table and an equation of state and the right hand side is determined by the ratio L/M. For the case of a white dwarf, both L and M are essentially unchanged throughout the atmosphere since they are determined primarily by the isothermal core. Hence, at any point in the evolution of a given star, we may determine what part of the parameter space is convective and so which parts of the opacity table are likely to be important.

Thus, in the case of a hydrogen atmosphere, in figure 2.5 we see that, at the low luminosities we are interested in, the top of the convective region lies in region A, which is where our assumption of an ideal gas for the opacity calculations is justified. This is not the case for the Helium atmosphere since the opacity is so low that the photosphere lies at densities high enough for pressure ionization to be important.

2.5 Emissivity

The primary source of energy for the cooling white dwarf is that stored in the thermal reservoir of ions in the core. The calculation of the emissivity due to the thermal leakage and the release of gravitational energy by contraction is outlined below. We must also remove from the energy generation expression that energy which is radiated in neutrinos and thus is not a contributor to the optical luminosity. Furthermore, we have to include the contribution due to any residual nuclear Hydrogen burning on the white dwarf surface.

The emissivity is expressed as

$$\epsilon = \epsilon_{\rm g} - \epsilon_{\nu} + \epsilon_{\rm nuc} \tag{2.80}$$

where

$$\epsilon_{\rm g} = -{\rm C_p}\frac{\partial {\rm T}}{\partial {\rm t}} + \frac{\rm Q}{\rho}\frac{\partial {\rm P}}{\partial {\rm t}} \tag{2.81}$$

Casting this in terms of our chosen variables, we get

$$\frac{\partial \ell}{\partial \xi} = {\rm f}'(\xi)\bar{\epsilon} \tag{2.82}$$

and

$$\bar{\epsilon} = \frac{{\rm P}_0}{\rho_0 \epsilon_0 \tau_0}\frac{\rm Q}{\nabla_{\rm ad}} e^{\pi-\phi}\left[\nabla_{\rm ad}\frac{\partial \pi}{\partial \tau} - \frac{\partial \theta}{\partial \tau}\right] - \bar{\epsilon}_{\nu} + \bar{\epsilon}_{\rm nuc} \tag{2.83}$$

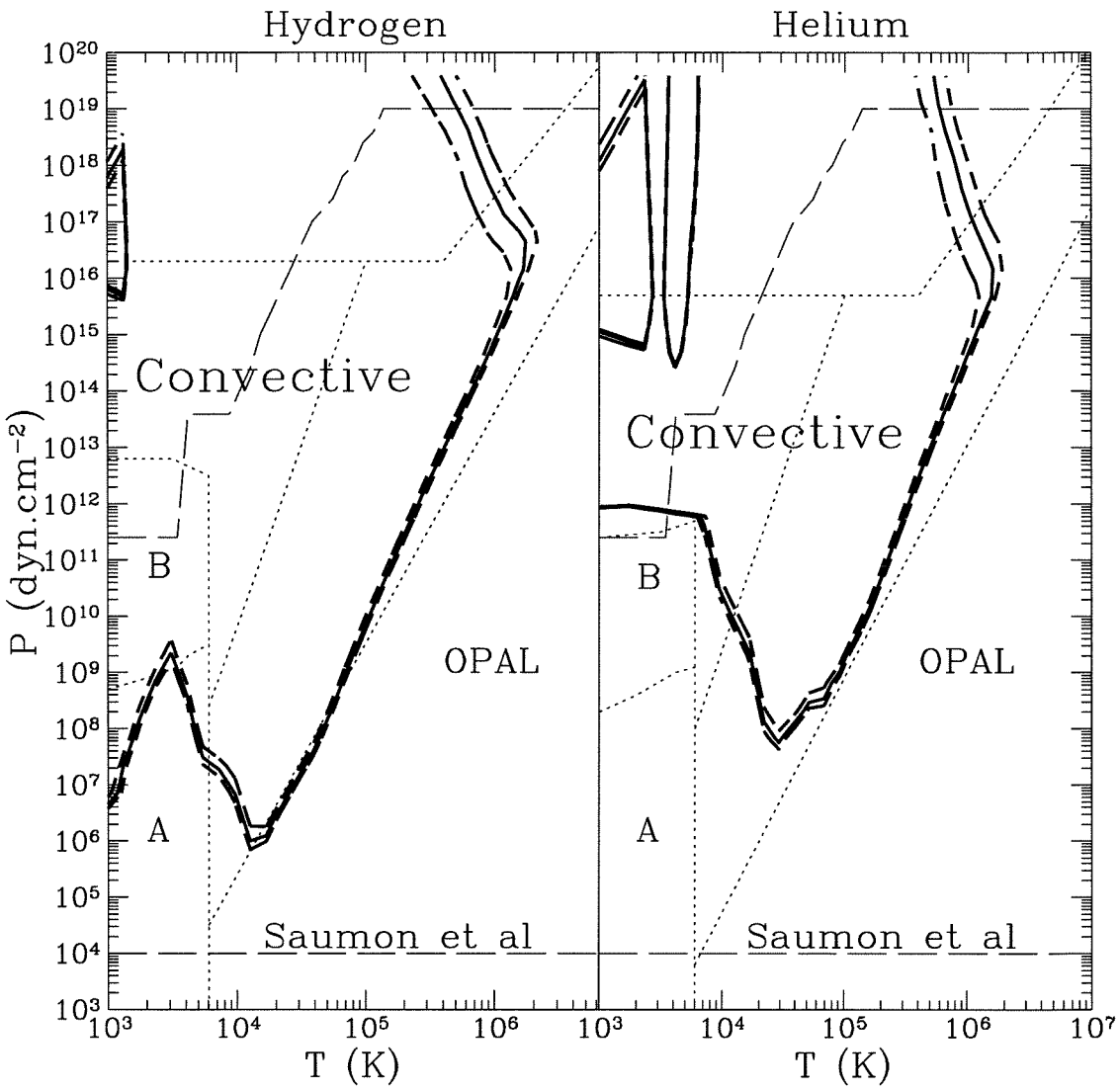

Figure 2.5: **The Convective Region:** The heavy solid and dashed lines indicate the boundaries of the convective region for stars with L = $10^{-4}L_{\odot}$ and M = 0.15, 0.25 and 0.4 $M_{\odot}$ respectively (the solid line is for the 0.25 case). The thin dashed lines indicate the boundaries of the region covered by the equation of state tables of Saumon et al. (1995). The dotted lines delineate the various different opacity calculations we used as in figure 2.1. In particular, regions A and B in each of the panels indicate the regions covered by our own opacity calculation. A is the region where our assumption of an ideal gas is justified while region B covers that region where non-ideal effects could be important up to the onset of pressure ionization. Thus we see that, in the case of Hydrogen atmospheres, the opacity calculations are trustworthy because the edge of the convective zone falls in regions where our assumptions are justified. For the case of a Helium photosphere, the edge of the convective zone is determined by the onset of pressure ionization, which means that opacity calculations without a careful treatment of pressure ionization cannot give accurate results.

We use the normalizations

$$\epsilon_0 = \frac{L_0}{M_0} \tag{2.84}$$

and

$$\tau_0 = \frac{P_0}{\epsilon_0 \rho_0} = 2.193 \times 10^7 \left(\frac{M_0}{M_\odot}\right)^2 \left(\frac{L_0}{L_\odot}\right)^{-1} \text{years} \tag{2.85}$$

leading to

$$\bar{\epsilon} = \frac{Q}{\nabla_{ad}} e^{\pi - \phi} \left[\nabla_{ad} \frac{\partial \pi}{\partial \tau} - \frac{\partial \theta}{\partial \tau}\right] - \bar{\epsilon}_\nu + \bar{\epsilon}_{nuc} \tag{2.86}$$

In differencing this, we need to use the information from the previous timestep. This is because we need to calculate the change in temperature and pressure at each individual point.

As the core cools, the significance of the Coulomb coupling between ions increases, and, when the coulomb coupling parameter Γ rises above 171, the ions form first a glass and then, when $\Gamma \geq 210$, an ionic crystal (Ichimaru (1983)). During this transition, a latent heat of kT per ion is released, which provides a second temporary heat source. For Helium cores, this turns out to be unimportant because the cores do not reach low enough temperatures in a Hubble time.

The calculation of the neutrino rates takes account of the emission of plasma, bremstrahlung, photo- and pair-production neutrinos. The bremstrahlung rates are taken from Itoh & Kohyama (1983), while the others come from Munakata et al. (1985). Figure 2.6 shows the combined emissivity from all these processes in ergs.s^{-1}.cm^{-3}. The emissivities shown do not include the neutrino emission from the nuclear reactions described in the section 2.7.

2.6 Gravitational Settling

The strong gravity leads to rapid separation of elements in the atmosphere of a white dwarf (Schatzmann (1958)). Many detailed calculations have been made of this process (Muchmore (1984), Dupuis et al. (1992), Pelletier et al. (1986)), but here we shall use the expressions of Alcock & Illarionov (1980), which are sufficient for illustrative purposes.

The diffusion equation governing the settling of a trace ionic species i of density n in a

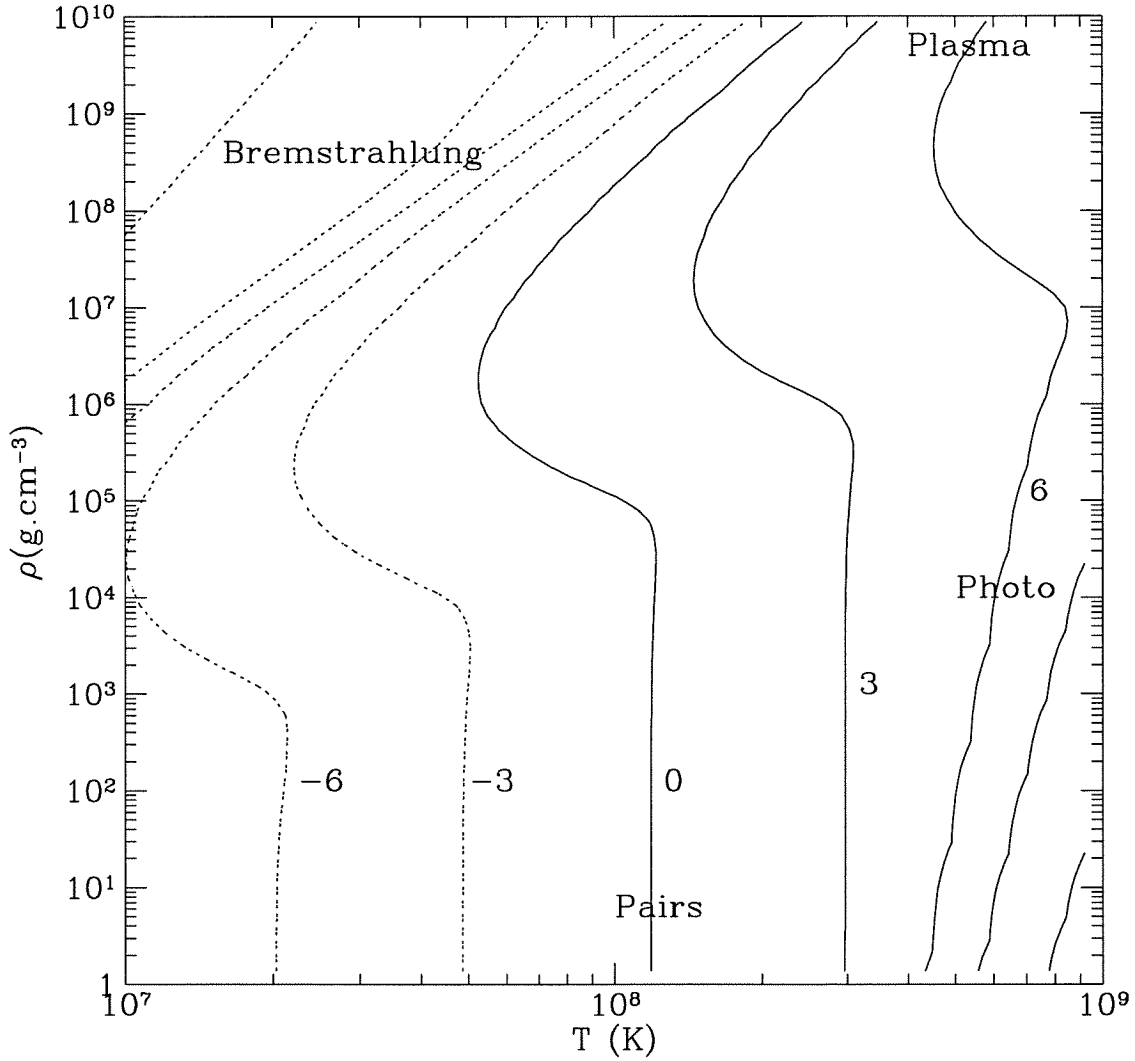

Figure 2.6: **The Neutrino Emissivity:** The contours are the logarithm of the cgs total neutrino emissivity ϵ_ν. At low densities the emission is dominated by pair production while the large bump at intermediate densities is due to plasma neutrino production, which then falls off towards high densities until bremstrahlung emission dominates.

background of species 1 (density n_1) is

$$\frac{\partial n}{\partial t} = \frac{\partial}{\partial z}\left(D\frac{\partial n}{\partial z} - wn\right) \tag{2.87}$$

where D is the diffusion coefficient and w is the settling velocity. Equilibrium is reached when

$$\frac{\partial n}{\partial z} = \frac{wn}{D} \tag{2.88}$$

which defines the local concentration scale height $\Delta z \sim D/w$. Combined with the settling velocity, this defines a local settling time

$$t_{set} = \frac{D}{w^2} \tag{2.89}$$

Thus, in regions where $t_s \ll$ cooling time of the star, the local concentration will be in equilibrium, which means the heavy and light elements will be separated in the white dwarf case. From Alcock & Illarionov (1980) the diffusion coefficient is

$$D = \frac{3\,(2k_bT)^{5/2}}{16n_1\,(\pi m_1)^{1/2}\,Z_1^2Z_i^2e^4\Lambda_i} \tag{2.90}$$

where

$$\Lambda_i = \ln\left(1 + \frac{(kT)^3 f(\eta)}{4\pi n_1 Z_1^3 Z_i^2 e^6}\right) \tag{2.91}$$

is the Coulomb logarithm and $f(\eta) \sim 1 + \eta^{1/2}e^{\eta-1}$. The settling velocity is given by

$$w \sim 2.5Z_i^2 D\frac{\partial \ln T}{\partial z}. \tag{2.92}$$

For a radiative atmosphere,

$$\frac{\partial \ln T}{\partial r} = \frac{3\kappa\rho L}{16\pi acT^4r^2} \tag{2.93}$$

and the final expression for the settling time becomes

$$t_{set} \sim 4.8 \times 10^5 \text{yrs}\,\Lambda_i T_7^{11/2}\rho_3^{-2}\kappa^{-2}r_9^4 L_\odot^{-2}. \tag{2.94}$$

In Figure 2.7 we show the local settling time for a 10^5 year old $0.3M_\odot$ white dwarf with a Hydrogen envelope of $5 \times 10^{-3}M_\odot$. We see that the cooling time increases inwards and so,

although settling occurs almost instantaneously in the outer layers of the star (producing the observed surface abundances), there is a depth below which the composition has not reached its equilibrium value. This is important for the results of the next section. For a more complete description of the time dependence of this transition depth, see Dupuis et al. (1992). Since our models only lose memory of their initial conditions after $\sim 10^7 - 10^8$ years, by which time much of the atmosphere has separated out, we shall assume complete stratification in our models (except where convection is present, in which case we assume complete mixing in the convective zone).

2.7 Nuclear Burning

Nuclear burning affects the white dwarf structure in two ways. Iben & Tutukov (1986) (see also Iben & MacDonald (1986)) have shown that, for stars with thick ($\sim 10^{-3}M_\odot$) Hydrogen envelopes, CNO shell flashes can result in the burning of a significant quantity of the surface Hydrogen to Helium, thus limiting the amount of Hydrogen that we can have on the surface of a white dwarf. The shell flash results from the fact that, if the Hydrogen envelope is thick enough, the settling time at the base of the envelope is long enough that the inwardly diffusing CNO distribution (due to the stars primordial composition, since there is little Helium burnt to Carbon in these stars) and outwardly diffusing Hydrogen distribution both have significant tails which overlap at a density and temperature such that the CNO cycle burning of Hydrogen is strong enough to lead to a shell flash (or self-induced nova in the terminology of Iben & MacDonald). Only a full evolutionary computation can demonstrate this mechanism properly, but we may get a qualitative understanding with a simple one-zone model of the white dwarf envelope. We consider the Hydrogen envelope as a single plane parallel zone, so that the values of various quantities at the base of the envelope are determined by the thickness via the stellar structure equations

$$P = \rho g \Delta r \tag{2.95}$$

$$L = 4\pi r^2 \rho \Delta r \left(\epsilon_{cno} - C_p \frac{\partial T}{\partial t}\right) \tag{2.96}$$

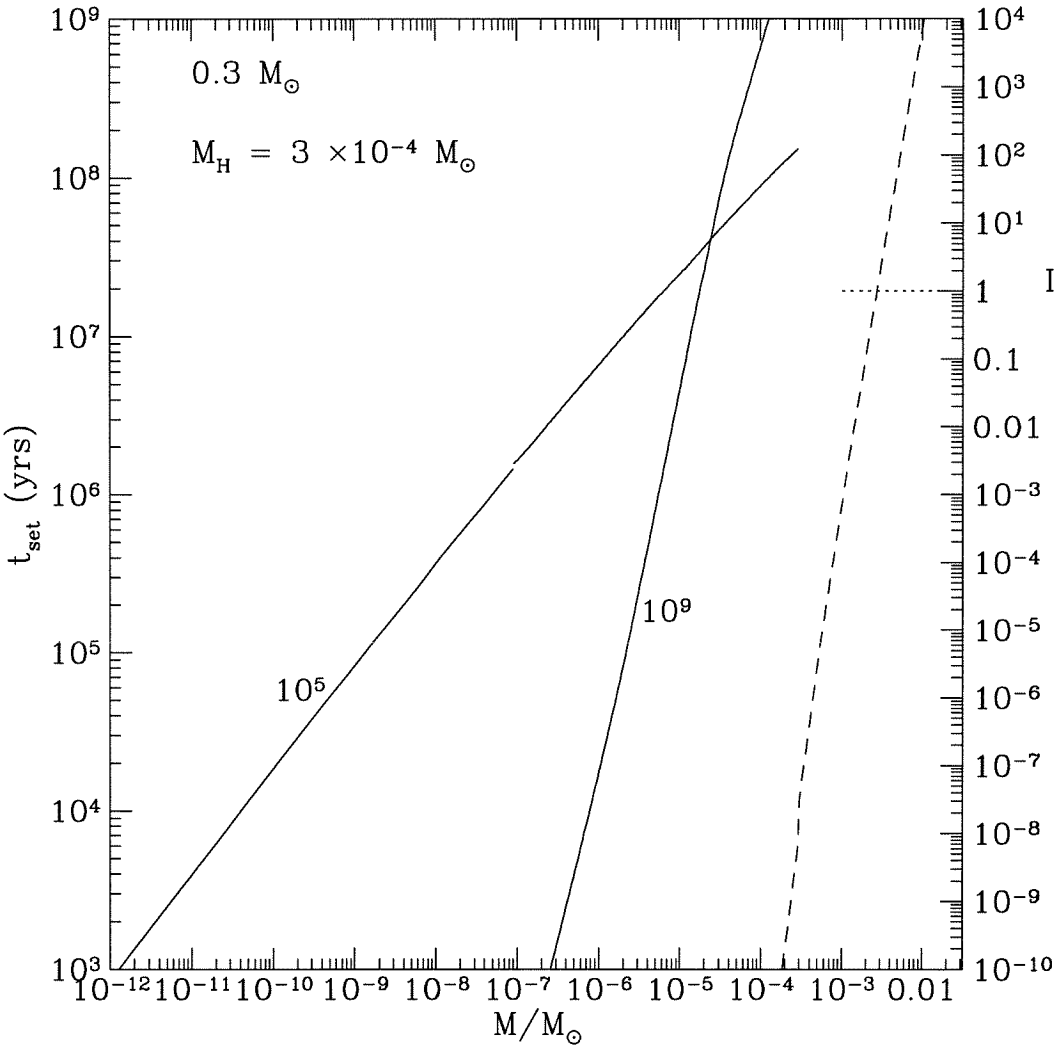

Figure 2.7: **Settling and Burning:** The solid line indicates the local settling times (left axis) for a 0.3 $M_\odot$ Helium core white dwarf with a thick Hydrogen envelope at ages of 10^5 and 10^9 years. The settling time is shown only for the Hydrogen part of the star. The dashed line is the value of the quantity I (right axis), which measures the stability of the star to CNO flashes (see section 2.7). The marginally stable value (I=1) is shown by a horizontal dotted line.

The radiative atmosphere yields a temperature gradient

$$-\frac{\partial T}{\partial r} \sim \frac{T}{\delta r} \sim \frac{3\kappa\rho L}{16\pi acT^3 r^2}. \tag{2.97}$$

Combining these, we obtain an evolution equation for the temperature at the base of the Hydrogen envelope,

$$C_p \frac{\partial T}{\partial t} = \epsilon_{cno} - \frac{4acT^4}{3\kappa}\left(\frac{g}{P}\right)^2 \tag{2.98}$$

This equation describes evolution on timescales much shorter than the cooling time. If the first term on the right-hand side exceeds the second term, the temperature will increase and the temperature dependence of ϵ_{cno} is such that it too will increase and a thermonuclear runaway will ensue. Hence our condition for a runaway in this simple model is

$$I = \frac{3\kappa\epsilon_{cno}}{4acT^4}\left(\frac{P}{g}\right)^2 > 1 \tag{2.99}$$

This can be made a little more accurate by replacing P/g by $M_H/4\pi r^2$ where r is the radius of the star at the base of the Hydrogen layer, rather than the outer radius of the star (which determines g). Numerically, our condition is thus

$$I \sim 5.72 \times 10^{-5} \frac{\kappa\rho_3}{T_7^{14/3}} \frac{Z}{10^{-2}} \frac{\left(M_H/10^{-3}M_\odot\right)^2}{r_9^4} e^{-70.697(T_7^{-1/3}-1)} > 1. \tag{2.100}$$

This quantity is shown in Figure 2.7. We see that, for this model, the shell flash should set in at a depth $\sim 4 \times 10^{-3} M_\odot$, although this is only a very rough estimate.

A second way in which nuclear burning may affect the evolution is through some residual contribution to the luminosity from the pp burning of Hydrogen (Webbink (1975)). The p-p burning reaction network consists of three branches, imaginatively named PPI, PPII and PPIII.

$$\left.\begin{array}{lcl} {}^1\mathrm{H} + {}^1\mathrm{H} & \rightarrow & {}^2\mathrm{D} + \mathrm{e}^+ + \nu \\ {}^2\mathrm{D} + {}^1\mathrm{H} & \rightarrow & {}^3\mathrm{He} + \gamma \\ {}^3\mathrm{He} + {}^3\mathrm{He} & \rightarrow & {}^4\mathrm{He} + 2{}^1\mathrm{H} \end{array}\right\} \text{PPI}$$

$$\left.\begin{array}{lcl} {}^1\mathrm{H} + {}^1\mathrm{H} & \rightarrow & {}^2\mathrm{D} + \mathrm{e}^+ + \nu \\ {}^2\mathrm{D} + {}^1\mathrm{H} & \rightarrow & {}^3\mathrm{He} + \gamma \\ {}^3\mathrm{He} + {}^4\mathrm{He} & \rightarrow & {}^7\mathrm{Be} + \gamma \\ {}^7\mathrm{Be} + \mathrm{e}^- & \rightarrow & \mathrm{Li}^7 + \nu \\ {}^7\mathrm{Li} + {}^1\mathrm{H} & \rightarrow & {}^4\mathrm{He} + {}^4\mathrm{He} \end{array}\right\} \text{PPII}$$

$$\left.\begin{array}{lcl} {}^1\mathrm{H} + {}^1\mathrm{H} & \rightarrow & {}^2\mathrm{D} + \mathrm{e}^+ + \nu \\ {}^2\mathrm{D} + {}^1\mathrm{H} & \rightarrow & {}^3\mathrm{He} + \gamma \\ {}^3\mathrm{He} + {}^4\mathrm{He} & \rightarrow & {}^7\mathrm{Be} + \gamma \\ {}^7\mathrm{Be} + {}^1\mathrm{H} & \rightarrow & {}^8\mathrm{B} + \gamma \\ {}^8\mathrm{B} & \rightarrow & {}^8\mathrm{Be} + \mathrm{e}^+ + \nu \\ {}^8\mathrm{Be} & \rightarrow & 2{}^4\mathrm{He} \end{array}\right\} \text{PPIII}$$

The primary reaction is the PPI chain, which is the only branch which occurs in a pure Hydrogen plasma. The PPII and PPIII chains only become important when the abundance of ^{4}He becomes significant.

A proper calculation of the nuclear burning requires the solution of the coupled equations describing the above reaction network. However, a couple of approximations can be made without loss of generality (Clayton (1968)). The first approximation is that the timescale for Deuterium to reach equilibrium abundance is of the order of seconds to hours, so that we may assume Deuterium is always in equilibrium. Similarly the equilibration timescales of Lithium and Beryllium are of the order of years in astrophysical situations. This means that we may solve the following set of three equations in Hydrogen, Helium-3 and Helium-4 to determine the nuclear energy generation.

$$\frac{\mathrm{dn_H}}{\mathrm{dt}} = -\frac{3}{2}\lambda_{\mathrm{pp}}\mathrm{n_H^2} + \lambda_{33}\mathrm{n_3^2} - \lambda_{34}\mathrm{n_3 n_4} \qquad (2.101)$$

$$\frac{dn_3}{dt} = \frac{1}{2}\lambda_{pp}n_H^2 - \lambda_{33}n_3^2 - \lambda_{34}n_3n_4 \quad (2.102)$$

$$\frac{dn_4}{dt} = \frac{1}{2}\lambda_{33}n_3^2 + \lambda_{34}n_3n_4 \quad (2.103)$$

The quantities λ_{pp}, λ_{33} and λ_{34} are the standard $< \sigma v >$ cross-section averages for the three reactions H-H, ^{3}He $-^3$ He and ^{3}He $-^4$ He (the cross-section information is taken from the review by Fowler, Caughlan & Zimmerman (1975)). The concentrations of Hydrogen and the two Helium isotopes are denoted by n_H, n_3 and n_4. There is no simple general solution for this system of equations. However, in the beginning, when the PPI chain is dominant and Helium can be treated as a trace element, we may consider the second two terms in (2.101) to be negligible, yielding a simple solution for the Hydrogen consumption,

$$\frac{n_H}{n_H(0)} = \frac{1}{1 + \frac{3}{2}\lambda_{pp}n_H(0)t} \quad (2.104)$$

A full solution of the above system of equations for the temperatures and densities at the base of the Hydrogen envelope ($T \sim 10^7$ K, $\rho \sim 10^3 g.cm^{-3}$) indicates that this remains a good approximation (within 20%) for $\frac{3}{2}\lambda_{pp}n_H(0)t < 1$ (see Figure 2.8). Furthermore, we see that this only becomes a poor approximation after $\sim 10^9$ years, by which time sedimentation will have resulted in the depletion of the Helium products (see Figure 2.7), effectively resetting the clock. Thus, to preserve the speed of our algorithm, we use the approximation (2.104) to calculate the consumption of Hydrogen by nuclear burning and its concomitant energy output.

2.8 Outer Boundary Conditions

The outer boundary conditions we require are the values of temperature and pressure at a given grid point as a function of radius and luminosity. It turns out that calculating a grid of values and interpolating between them is prohibitively expensive. This is because we want to keep our outer grid point at reasonably small optical depths (say $\tau < 10^3 - 10^4$) and thus the outer grid point changes significantly over the entire cooling curve for a given star (values used range from $\xi = 30$ to $\xi = 16$) due to the rapid drop in the atmospheric opacities when the temperatures in the outer envelope become small enough that the atmospheric material recombines. Hence we would want to sample a three dimensional space (ξ, R and

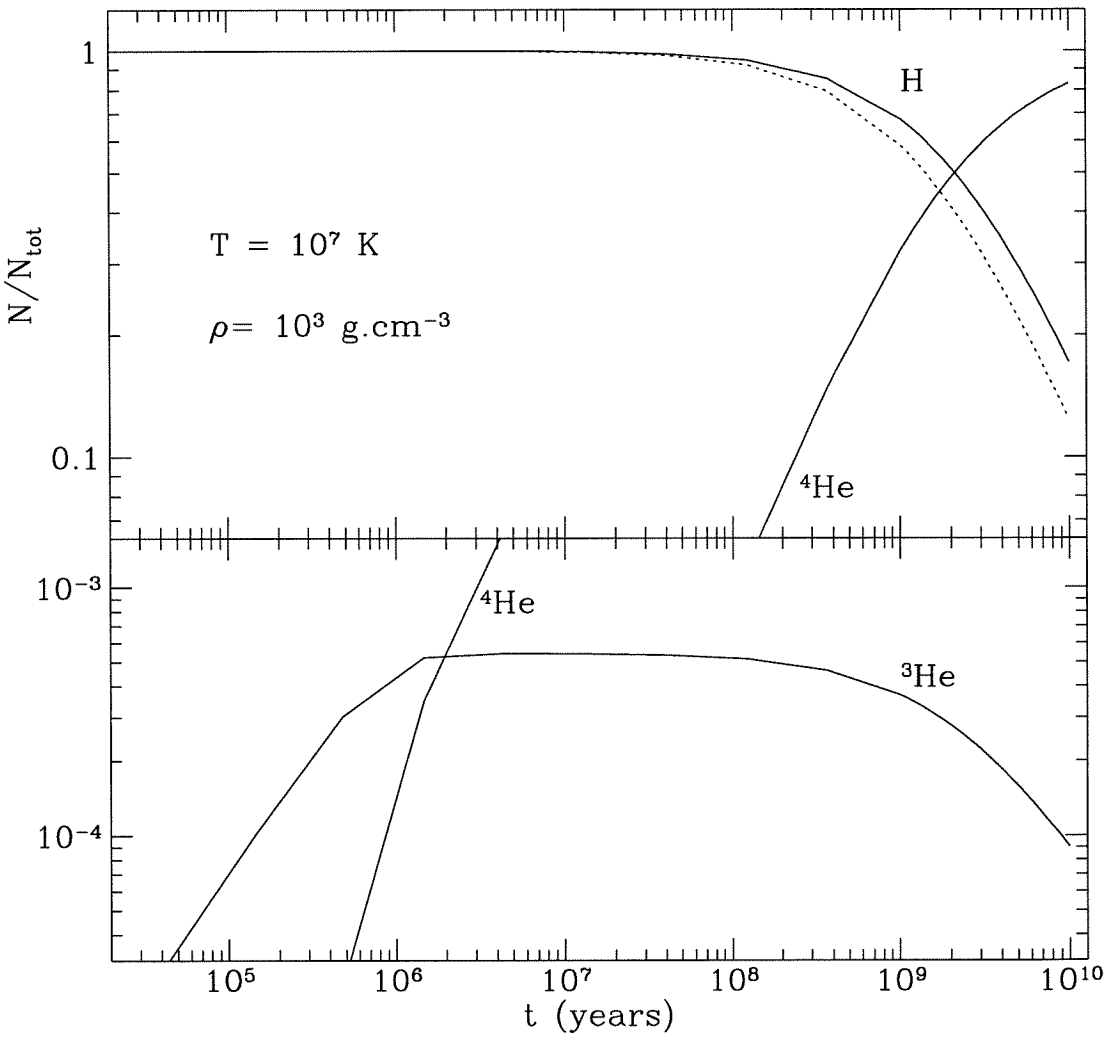

Figure 2.8: **PP Burning:** The dotted line is the approximation (2.104) for the Hydrogen consumption via pp-burning. The solid lines indicate the solution of the full reaction network for the various species.

L), which is too expensive.

Thus, we perform the calculation of the atmosphere as required. We have calculated a grey atmosphere $T/T_{eff}(\tau)$ relation, which we load into the program at the beginning. This solution was obtained by numerical solution of the grey atmosphere problem using variable Eddington factors. Figure 2.9 shows the comparison between our results and the values for the exact numerical solution of the Hopf function given in Mihalas (1970). Calculating T_{eff} from L and R immediately gives us the temperature at all points $\tau \leq 10$ (the upper bound of our relation). This assumes radiative transport. However, the atmosphere can become convectively unstable even at low optical depth (Böhm et al. (1977)) and so we also incorporate convection where needed using the formalism in section 2.4.

We also need the pressure. Assuming a plane parallel atmosphere, we can integrate the hydrostatic equilibrium equation

$$\frac{\partial P}{\partial \tau} = \frac{g}{\kappa} \tag{2.105}$$

since we know the temperature distribution and can calculate g from M and R. Note that, in a plane parallel atmosphere, $P = g\ m$, where m is the mass column density through the outer atmosphere. We must integrate inwards until we reach a critical m value which corresponds to our outer grid value ξ. This is given by the expression

$$m_{crit} = 1.592 \times 10^{10} g.cm^{-2} \frac{(1 - f(\xi))}{x^2} \frac{M_0}{M_\odot} \tag{2.106}$$

The pressure at the matching point can be calculated immediately because of the plane parallel approximation, and we get the expression (from integrating equation (2.15))

$$\pi_N = \ln \left[e^{\pi_{10}} - \frac{e^{-\xi_{10}}}{x_N^4} \left(1 - e^{\xi_{10} - \xi_N} + \frac{1}{2} e^{-\xi_{10}} \left(e^{2(\xi_{10} - \xi_N)} - 1 \right) \right) \right] \tag{2.107}$$

where the subscript 10 indicates the value at the point $\tau = 10$.

To get the temperature at the fitting point, we have to integrate the equation

$$\frac{\partial \theta}{\partial \pi} = \nabla \tag{2.108}$$

from $\tau = 10$ to m_{crit}, using the same ∇ calculation subroutine as in the main program.

The fitting of inner and outer boundary conditions is performed at a fixed mass point.

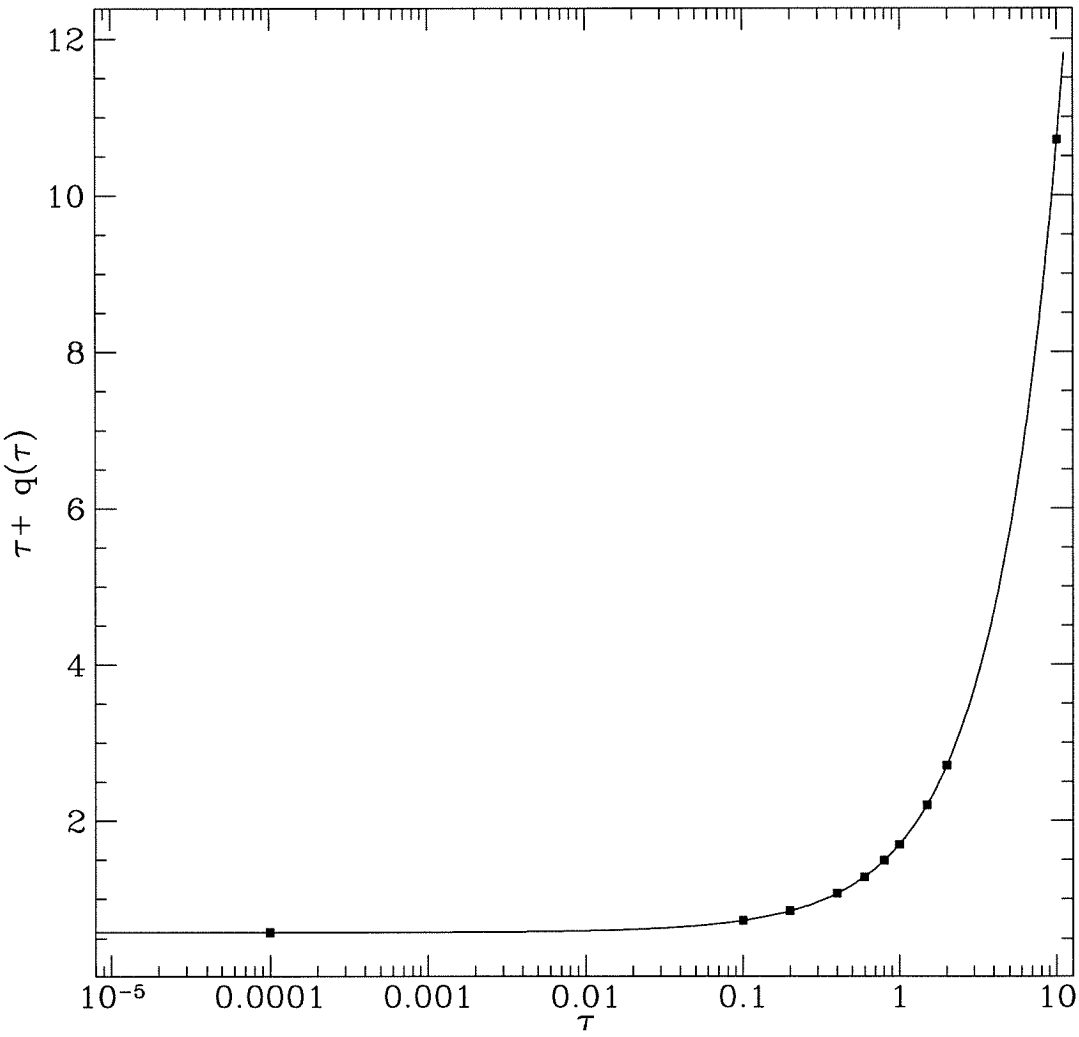

Figure 2.9: **Hopf Comparison:** The curve shows our numerical solution and the filled solid points are obtained by using the values from the table in Mihalas (1970). $q(\tau)$ is the Hopf function and τ is the grey atmosphere optical depth.

The above procedure produces a pair of functions F_1 and F_2 which represent P and T as functions of L and R (see equations (2.36) and (2.37)). These functions have no analytic solution, but are reasonably smooth functions of L and R, so that we can use the triangle method of Kippenhahn et al. (1967) to calculate them efficiently. The procedure involves tiling the L-R plane with triangles of sufficiently small size that the functions F_1 and F_2 can be accurately interpolated linearly between the three vertices of a given triangle. Thus, for sufficiently smooth functions, this represents an efficient way to calculate the functions using an algorithm to always bracket the boundary matching point (see Kippenhahn et al. (1967)).

2.9 Initial Solutions

To generate initial solutions, we start with simplified initial microphysics which admit a simple analytical solution. Then we gradually adjust each physical input and iterate until we have a consistent solution. As an illustration, consider a model obtained assuming the opacity $\kappa = \kappa_0 =$ constant. To incorporate the correct microphysics, we use an interpolation of the formula

$$\kappa = \epsilon\kappa_0 + (1 - \epsilon)\,\kappa_{\rm true} \tag{2.109}$$

and, beginning with $\epsilon = 1$, we iterate solutions until $\epsilon = 0$. The speed of this procedure is greatly enhanced by choosing values of κ_0 of the order of magnitude of the true opacity.

To determine the initial values of the central temperature appropriate to various kinds of star, we use results obtained from Eggleton's stellar evolution code (Eggleton (1971), Pols (1995)), which performs stellar evolution with mass loss. Various stars were evolved from different initial configurations to determine the central temperature as a function core mass when the giant detached from its Roche lobe and began to shrink towards the white dwarf sequence. We thank Glenn Soberman for performing these calculations for us. Subsequent tests with various initial conditions indicate that the effects of initial structure (other than core central temperature) are negligible for ages $> 10^7$ years. The effect of central temperature on age is discussed in section 3.4.1

REFERENCES

Alcock, C. & Illarionov, A., 1980, ApJ, **235**, 534.

Bergeron, P., Wesemael, F. & Fontaine, G., 1992, ApJ, **387**, 288.

Böhm-Vitense, E., 1958, ZAp, **46**, 108.

Böhm, K-H., Carson, T.R., Fontaine, G. & Van Horn, H.M., 1977, ApJ, **217**, 521.

Böhm, K-H & Cassinelli, J.P., 1971, A&A, **12**, 21.

Clayton, D.D., 1968, *Principles of Stellar Evolution and Nucleosynthesis*, McGraw-Hill

Dupuis, J., Fontaine, G., Pelletier, C. & Wesemael, F., 1992, ApJS, **82**, 505.

Eggleton, P.P., 1971, MNRAS, **151**, 351.

Fontaine, G., Graboske, H.C. & Van Horn, H.M., 1977, ApJS, **35**, 293.

Fontaine, G., Villeneuve, B. & Wilson, J., 1981, ApJ, **243**, 550.

Fowler, W.A., Caughlan, G.R. & Zimmerman.B.A., 1975, ARA&A**13**, 69.

Henyey, L.G., Wilets, L., Böhm, K.H., LeLevier, R. & Levee, R.D. , 1959, ApJ, **129**, 628.

Henyey, L.G., Forbes, J.E. & Gould, N.L., 1964, ApJ, bf 139, 306.

Hubbard, W.B. & Lampe, M., 1969, ApJS, **18**, 297.

Iben, I. & MacDonald, J. 1986, ApJ, **301**, 164.

Iben, I. & Tutukov, A.V., 1986, ApJ, **311**, 742.

Ichimaru, S., Iyetomi, H. & Mitake, S., 1983, ApJ, **265**, L83.

Itoh, N., Mitake, S., Iyetomi, H. & Ichimaru, S., 1983, ApJ, **273**, 774.

Itoh, N. & Kohyama, Y., 1983, ApJ, **275**, 858.

Kippenhahn, R., Weigert, A. & Hofmeister, E., 1967, in *Meth. in Comp. Phys.*, **7**, 129.

Kippenhahn, R. & Weigert, A., 1991, *Stellar Structure and Evolution*, Springer-Verlag

Lenzuni, P., Chernoff, D.F. & Salpeter, E.E., 1991, ApJS, **76**, 759.

Mihalas, D., 1970, *Stellar Atmospheres*, W.H.Freeman & Company

Mitake, S., Ichimaru, S. & Itoh, N., 1984, ApJ, **277**, 375.

Muchmore, D., 1984, ApJ, **278**, 769.

Munakata, H., Kohyama, Y. & Itoh, N., 1985, ApJ, **296**, 197.

Pelletier, C., Fontaine, G., Wesemael, F., Michaud, G. & Wegner, G., 1986, ApJ, **307**, 242.

Pols, O., Tout, C.A. & Eggleton, P.P., 1995, MNRAS, **274**, 964.

Press, W.H., Teukolsky, S.A., Vetterling, W.T. & Flannery, B.P., 1992, *Numerical Recipes*, Cambridge University Press

Rogers, F.J. & Iglesias, C.A., 1992, ApJS, **79**, 507.

Rogers, F.J., 1981, Phys.Rev.A, **23**, 1008.

Rogers, F.J. & de Witt, H.E., 1973, Phys.Rev.A**8**, 1061.

Saumon, D., Chabrier, G. & Van Horn, H.M., 1995, ApJS, **99**, 713.

Schatzman, E., 1958, *White Dwarfs*, Amsterdam: North-Holland

Webbink, R.F., 1975, MNRAS, **171**, 555.

Chapter 3 Stellar Forensics: I - Cooling Curves

We construct the first extensive grid of models of low mass white dwarfs with helium cores. Such stars are formed in binaries when the white dwarf progenitor overflows its Roche lobe before core helium ignition. We present detailed models of the structure and cooling of such stellar remnants.

3.1 Introduction

While there exists an extensive literature on the cooling of "normal" white dwarfs with Carbon/Oxygen cores (see D'Antona & Mazzitelli (1990) and references therein), the study of helium core white dwarfs has been largely neglected. In order for a single star to have evolved to form a white dwarf, the progenitor must have been massive enough to have left the main sequence and evolved to the white dwarf stage in the age of the galaxy. Such stars would ignite helium in their cores and will thus leave behind Carbon/Oxygen remnants. However, Kippenhahn et al. (1967) realised that stars in binaries could be disrupted during the course of their evolution before the core mass had grown large enough to ignite helium (i.e., $M_{core} < 0.49\,M_{\odot}$, Sweigart & Gross (1978), Mazzitelli (1989)), leaving behind a lighter remnant with a helium core composition.

Studies of binary pulsars (Phinney & Kulkarni (1994) and references therein) and close double degenerate systems (Marsh et al. (1995)) have discovered a number of such low mass degenerate dwarfs. In particular, the cooling of the companions in pulsar-white dwarf binaries offers an independent estimate of the age of the system, thus constraining the pulsar age as well. In this chapter we describe in detail the cooling of these stellar remnants. In Chapter 4 we shall describe the application of these cooling curves to the observational data.

In section 3.2 we briefly review the physical mechanisms which contribute to the white dwarf cooling process and discuss their relative importance. Section 3.3 describes our calculations of the low-temperature opacities necessary to obtain accurate cooling sequences. In section 3.4 we describe our numerical model and the tests of the code against other models

from the literature. Finally, in section 3.5 we present our cooling sequences and describe the details of the cooling models.

3.2 White Dwarf Cooling

The basic qualitative picture of white dwarf cooling is a well-known one, going back to Mestel (1952). The star is supported by the pressure of a degenerate electron gas while the heat content is dominated by the thermal reservoir of non-degenerate ions, which can form a gas or a crystalline solid, depending on the Coulomb coupling parameter $\Gamma = (Ze)^2/akT$, where a is the radius of the Wigner-Seitz sphere surrounding each ion. While the luminosity is dominated by the loss of thermal energy, young, hot white dwarfs may also have a contribution due to residual hydrogen burning at the base of the Hydrogen envelope.

The energy transport throughout most of the star is dominated by conduction due to the degenerate electrons, which maintains the degenerate core at an almost constant temperature throughout. The core is surrounded by a thin, non-degenerate envelope where the energy transport is by radiative diffusion and, at late times, by convection (Böhm et al. (1977)). This is the region of least efficient energy transport and thus it determines the rate at which the star cools. Hence, the chemical composition of these outer layers is important. The high gravities of white dwarfs lead to gravitational settling (Schatzmann (1958), Dupuis et al. (1992) and references therein) which results in chemical separation in the white dwarf envelope and hence the atmospheric opacity is dominated by the lightest species remaining on the surface, usually either hydrogen or helium.

Since the cooling is determined by the radiative transport, the accuracy of the cooling curves will be determined by the accuracy of the opacities we use. Over most of the cooling sequence we use the radiative opacities from the OPAL group (Rogers & Iglesias (1992)), which are good down to T = 6000K. For conductive opacities we use the results of Itoh et al. (1983) and Mitake et al. (1984) for the region where the ions are gas or liquid and the electrons degenerate (helium cores don't reach crystallization temperatures within a Hubble time). At temperatures and densities not covered by the Itoh results, we use the older conductivities of Hubbard and Lampe (1969). This still leaves the region T < 6000K unaccounted for. This is important because many of the objects we will discuss in Chapter 4 have $T_{eff} \sim 4000$K. To address this issue, we have calculated Z=0 opacities for an arbitrary

mix of hydrogen and helium using primarily the input physics of Lenzuni, Chernoff and Salpeter (1991), henceforth called LCS. In particular, we calculate the opacities from the collisionally induced absorption by molecular hydrogen. We describe this briefly below.

3.3 Low Temperature Z=0 Opacities

We calculate the opacity of a gas containing H, He, H_2, H^-,He^-,H^+,H_2^+,H_3^+,He^+ and electrons. We assume ideal gas and LTE. From the equation of state of Saumon et al. (1995), we determine that the assumption of an ideal gas is good for $\rho < 10^{-2}$g.cm^{-3}. The partition functions and cross-sections are taken largely from LCS. For the calculation of collisionally induced molecular opacities we used the fits of LCS for the H_2-H_2 roto-vibrational transitions (with corrections for typographical errors for which we thank Dr. Chernoff), after checking it with the original code (Borysow and Frommhold (1990)), kindly supplied to us by Dr. A. Borysow. The roto-translational contribution was recalculated using another code (Zhang & Borysow (1995)) again supplied by Dr. Borysow. We also recalculated the H_2-He opacity following LCS although most of our atmospheres end up with pure H or He compositions.

When we use the composition X=0.72 and Y=0.28, we find good agreement with LCS except at the high temperature, high density end T $\sim 6000 - 7000$ K and $\rho \sim 10^{-3}$g.cm^{-3}, where we have a 10-20% error. We attribute this to our LTE treatment of the H^- ion. LCS note that the equilibrium abundance of this ion is affected by the radiation field at almost any temperature because of its low dissociation energy. Since the OPAL opacities reach down to 6000 K and most atmospheres are convective in this region (see Figures 2.5 and 3.7), we opt for simplicity and use our LTE results.

For the case of a pure hydrogen atmosphere of moderate density $\rho > 10^{-5}$g.cm^{-3}, the opacity is dominated above $\sim$ 3000 K by the H^- ion and below by the collisionally induced opacity of H_2. As noted by Bergeron et al. (1995), the Rosseland opacity goes through a minimum near this temperature. For a pure helium atmosphere He^- and Rayleigh scattering provide most of what little opacity there is.

We extend our calculations up to densities $\rho \sim 1$ g.cm^{-3}. At higher densities, in lieu of an accurate calculation[1], we introduce abrupt pressure ionization and the opacity is determined

[1] The physics of partially ionised, partially degenerate plasmas is poorly known.

by electron conduction at higher densities. For the case of a hydrogen atmosphere, this is unimportant because the atmosphere is sufficiently opaque that convection will dominate by the time these densities are reached. However, for the case of a helium atmosphere,, this is the major source of uncertainty in our cooling times because the atmosphere is very optically thin and where we place the pressure ionization will determine the location of the photosphere.

Figures 3.1 and 3.2 show the contours of constant opacity in our density-temperature parameter space for each of the two compositions. They also show the regions where different opacity tables were used. In Figure 3.3, as an example, we show the opacity as a function of temperature at $\rho = 10^{-9}$g.cm^{-3} for a pure hydrogen atmosphere. There is excellent agreement between our calculation and the OPAL tables in the overlap region.

3.4 The Cooling Code

We have written a numerical cooling code using the Henyey method (Henyey et al. (1959,1964)) to solve the stellar structure equations. Our outer boundary conditions (obtained using a grey atmosphere calculation) are implemented using the Kippenhahn, Weigart & Hoffmeister (1967) method of triangles.

Apart from the opacity tables described above, we have used the hydrogen and helium equation of state of Saumon et al. (1995), supplemented by a Thomas-Fermi model where necessary (at high densities). For the Carbon/Oxygen sequences used in our comparisons (see 3.4.1), we also used the Carbon equation of state table of Fontaine et al. (1977). For completeness, we also include the effects of neutrino losses using the emissivities of Itoh & Kohyama (1983), Itoh et al (1984) and Munakata et al. (1985). To account for the residual nuclear burning, we incorporate the cross-sections of Fowler, Caughlan and Zimmerman (1975). We also use the mixing length theory of convection (we tested different parameterisations, ML1, ML2 and ML3 (see Bergeron et al. (1992) and references therein), and found no difference in their effect on the cooling).

3.4.1 Code Tests

The dearth of reliable helium white dwarf cooling sequences means that, in order to test our numerical method properly, we need to include Carbon cores so as to test our models

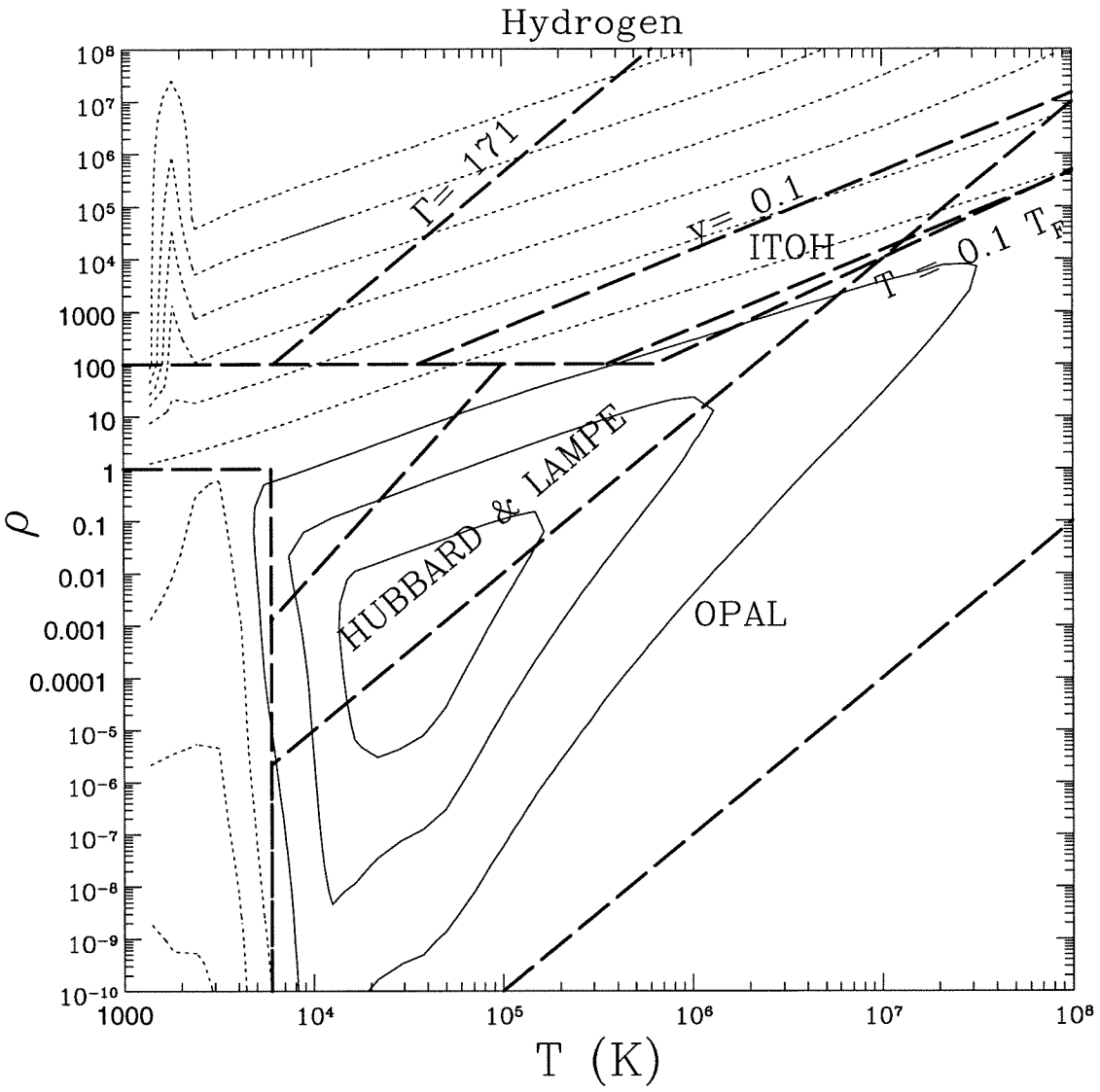

Figure 3.1: **The Hydrogen Phase Diagram:** The thin solid lines are contours of constant log κ, where κ is the Rosseland mean opacity in $cm^2.g^{-1}$. The contours have values 0, 2 and 4. The dotted lines are also contours of constant log κ but with values -2, -4, etc., down to -12. The heavy dashed lines delineate regions where different tables have been used to calculate the opacity. The Itoh opacities are valid for $T < 0.1\,T_F$ (where T_F is the Fermi temperature), y < 0.1 (y measures the importance of the wave nature of the ions) and $\Gamma < 171$. There is also a lower bound on the density $\rho > 100\,g.cm^{-3}$. Outside of this region we use the conductivities of Hubbard and Lampe. The radiative opacities in the region $T \sim 10^4 - 10^5$ K and $\rho \sim 10^{-4} - 1\,g.cm^{-3}$ were obtained by extrapolating the OPAL opacities to higher densities. This extrapolation is not important because the atmosphere is convective at these temperatures and densities. The box in the lower left-hand corner is the region covered by our opacity calculations. We can see the opacity minimum near 3000 K due to the change in the dominant opacity mechanism from H^- absorption to H_2 CIA. The strange behaviour in the upper left-hand corner is due to the extrapolation of the conductive opacities outside their range of validity. This is unimportant as no model we consider will approach this region.

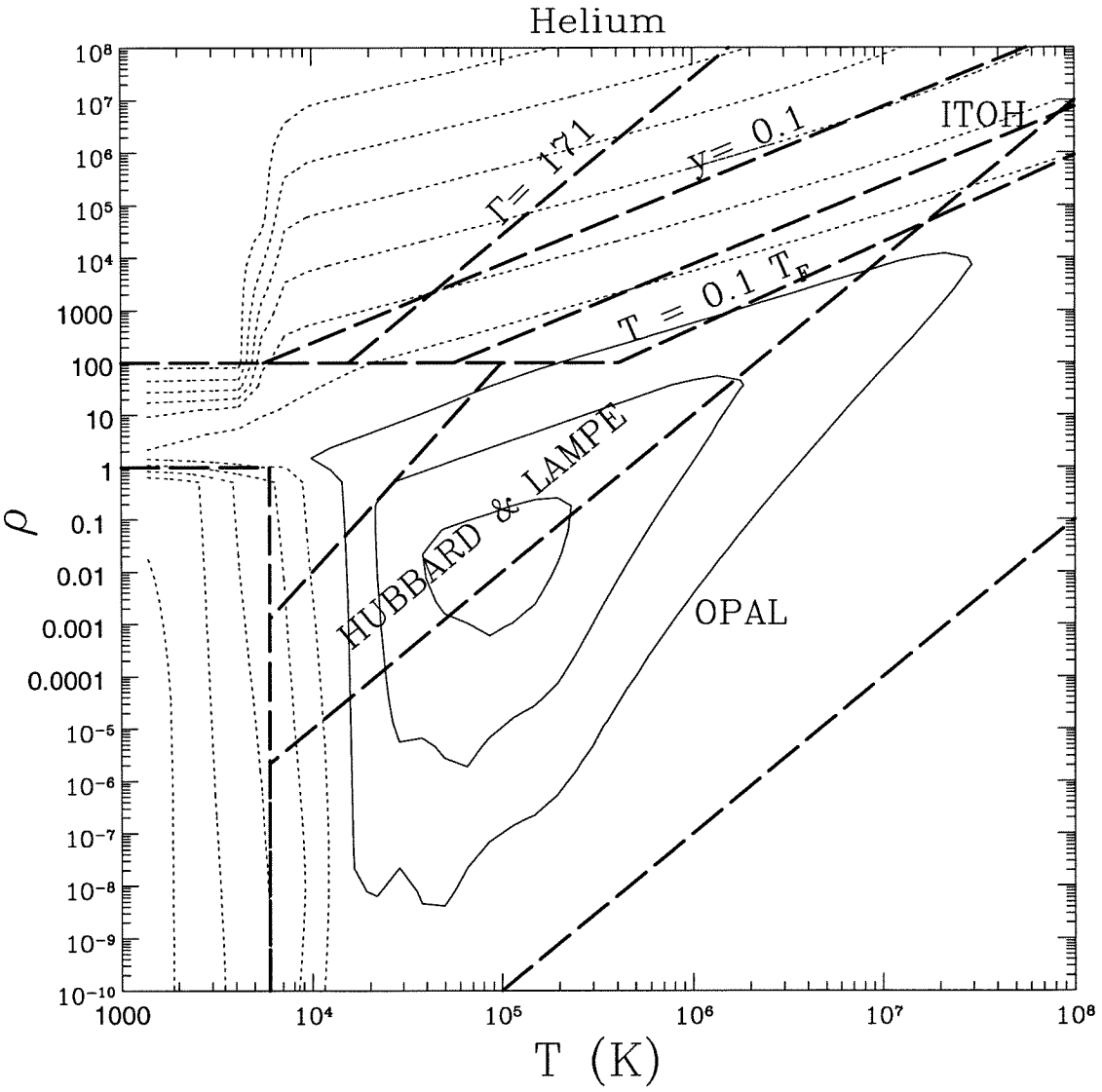

Figure 3.2: **The Helium Phase Diagram:.** We can immediately see that the helium opacities are much smaller at low temperatures and that the onset of pressure ionization at $\rho \sim 1 - 5 \mathrm{g.cm}^{-3}$ will have a major effect on the atmosphere.

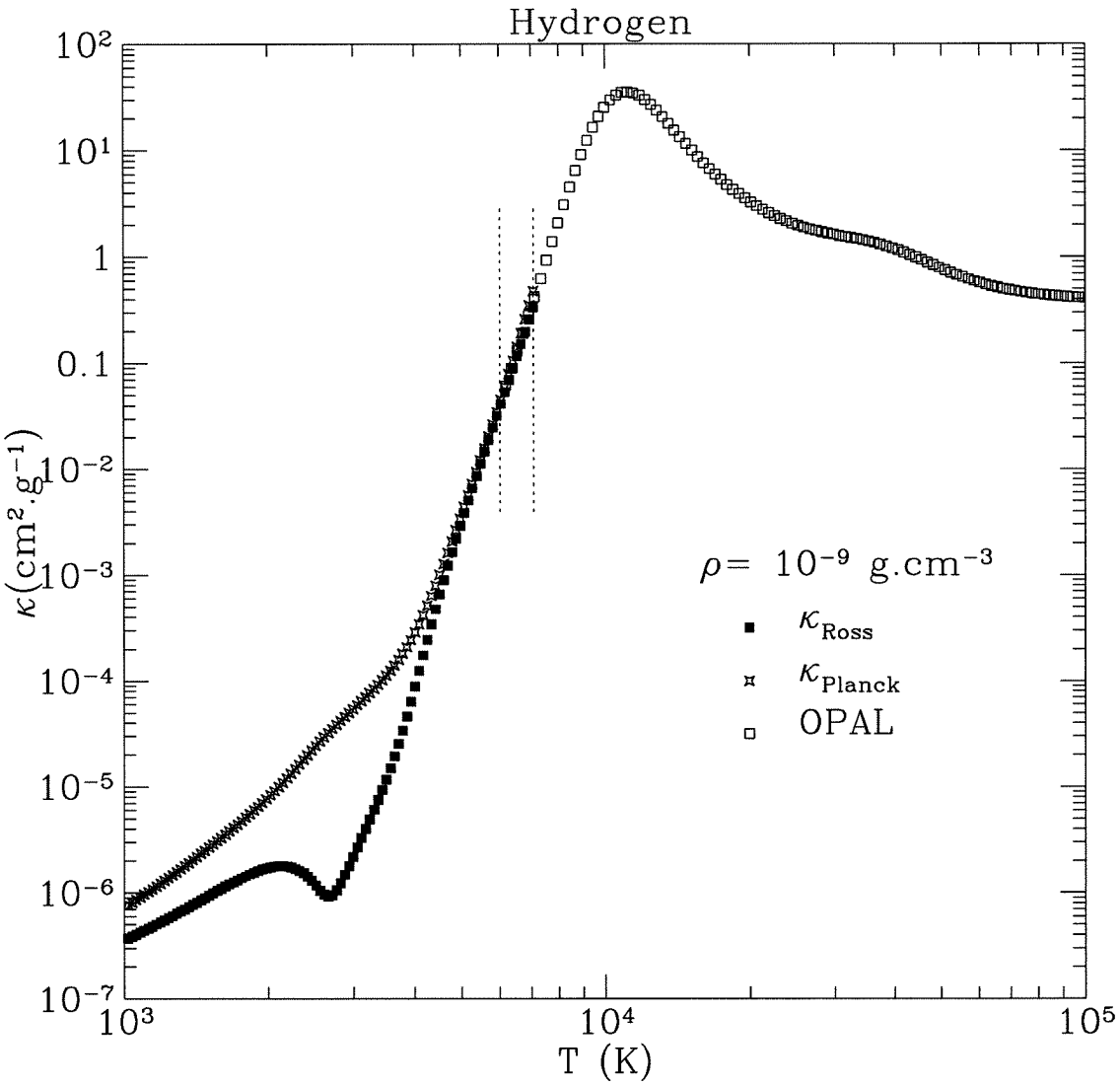

Figure 3.3: **Matching Opacities:** The solid points are Rosseland mean opacities calculated using our code. The open squares are the results of the OPAL calculation. The open stars are again our calculation but showing Planck mean opacities. The vertical dotted lines delineate the region 6000-7000 K which is where the two calculations overlap. Once again, the minimum in the opacity near 3000 K is due to the change in the dominant opacity contributor, from H_2 CIA at lower temperatures to H^- absorption at higher temperatures. We see that below 5000K there is a significant discrepancy between the Planck and Rosseland mean opacities.

against those in the accepted literature. We have made comparisons with three well known codes, adjusting our input physics to approximate the original input physics as closely as possible. The wide variation in input physics and parameters makes this a non-trivial proposition (see Winget and Van Horn (1987)). Nevertheless we obtain satisfactory fits that give us confidence in the accuracy of our numerical scheme and also incidentally reinforces the assertion of Winget and Van Horn that the wide variation in published white dwarf cooling models is a result of input physics and not numerical treatment. The comparison is shown in Figure 3.4. The three models are from D'Antona & Mazzitelli (1989), Koester & Schonberner (1986) and Wood (1992). Of particular interest is the comparison with the Wood cooling sequence because that is the most up-to-date, using Z=0 OPAL opacities. We don't expect agreement at late times because the calculations of the opacities for T < 6000K will vary, but the agreement for ages less than a few billion years is excellent.

The one useful test of our code for the case of a helium white dwarf is a comparison with the cooling sequence of Iben & Tutukov (1986), shown in Figure 3.5. Their model was for a $0.3\,M_\odot$ star which, after undergoing two hydrogen shell flashes, has a shell of $2.5 \times 10^{-4}\,M_\odot$ of pure hydrogen during the white dwarf phase. They caution that their opacities are uncertain at low luminosities, but it provides a useful comparison at least for $\log L/L_\odot > -3$. Their model also demonstrates another uncertainty for our higher luminosity models. Their white dwarf stage really only begins after the end of the second hydrogen shell flash which means that our t=0 corresponds to $t=10^8$ years in this case. The effect of this uncertainty in the starting point for the model is important for $\log L/L_\odot > -3$.

A second uncertainty in the initial conditions is the value of the core temperature at the beginning of the evolution. Tests of our code show that an uncertainty of 3×10^7 K corresponds to an age uncertainty $\sim 10^8$ years, although the exact numbers are model dependant. We solve this problem by using the results of evolutionary calculations (Soberman, pers. comm.) of the progenitors at a variety of binary separations around a neutron star, using the stellar evolution code of Eggleton (1973) (see also Pols et al. (1995)). This provides us with an estimate of the initial central temperature for a given remnant mass, which we use as a starting point for our calculations.

There are also uncertainties in the evolution associated with the uncertainties in the input physics. We investigated the effect of extrapolating the Itoh opacities to lower densities instead of using the old Hubbard and Lampe opacities for those regions. This was found to

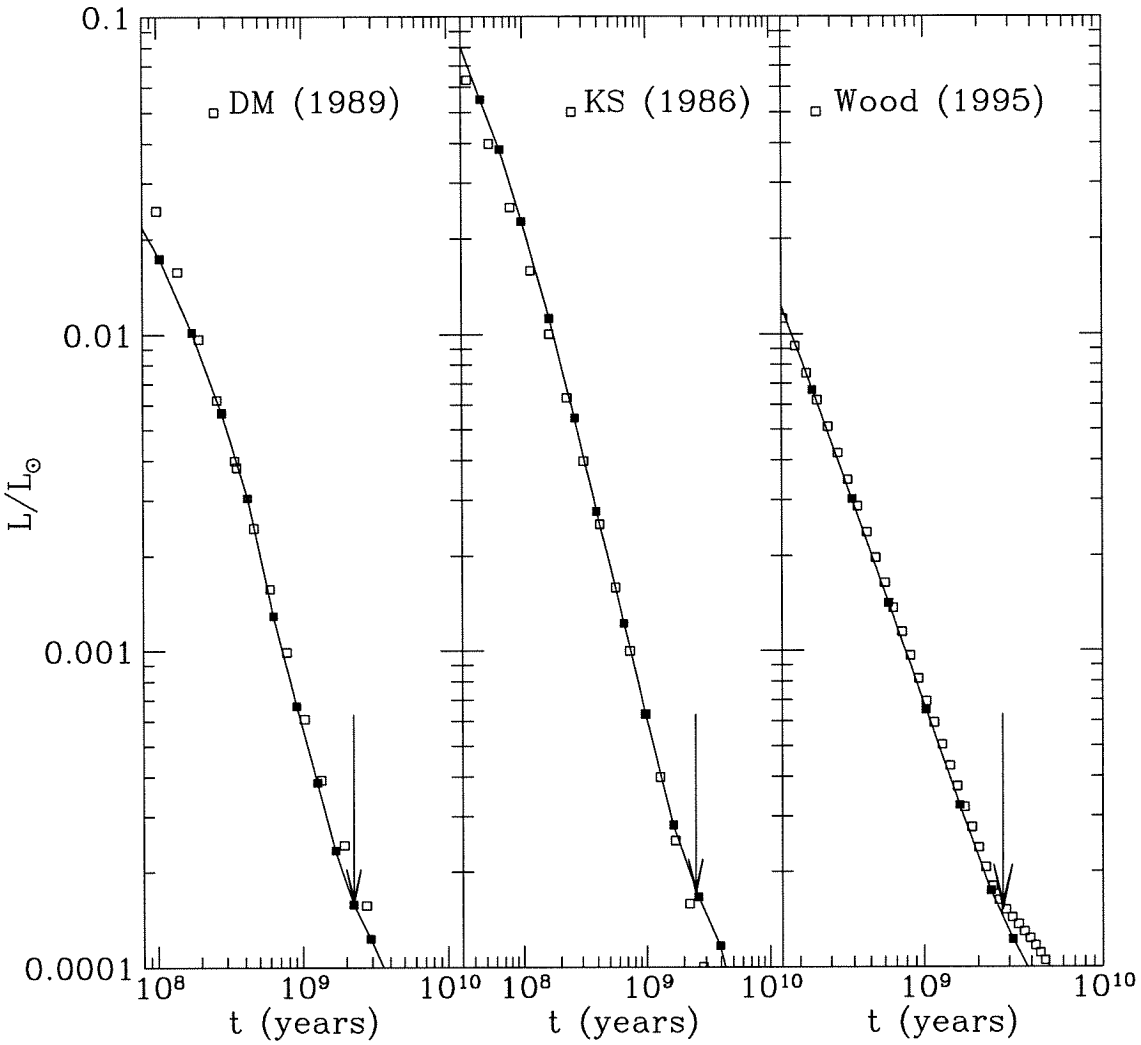

Figure 3.4: **Code Comparisons: C/O models:** The open squares denote the models we compare against. The filled squares are our own models. The arrows denote the point at which the core of the model begins to crystallize. The left panel describes a 0.564 $M_{\odot}$ Oxygen core surrounded by a helium envelope of $2.5 \times 10^{-3} M_{\odot}$ and a hydrogen envelope of $3 \times 10^{-4} M_{\odot}$. The metallicity is taken to be Z=0. The centre panel describes a 0.546 $M_{\odot}$ Carbon core with a helium envelope of $0.022 M_{\odot}$ and hydrogen envelope $10^{-4} M_{\odot}$. The metallicity is Z=0.02. The rightmost panel is a 0.6 $M_{\odot}$ star, with a Carbon core, mass fraction 10^{-2} of helium and 10^{-4} of hydrogen. The metallicity is Z=0. We had to adjust our conductive opacities to reproduce the above results. When prior authors used Hubbard & Lampe opacities in regions where we used Itoh opacities, we divided our opacities by a factor of 2 to compensate.

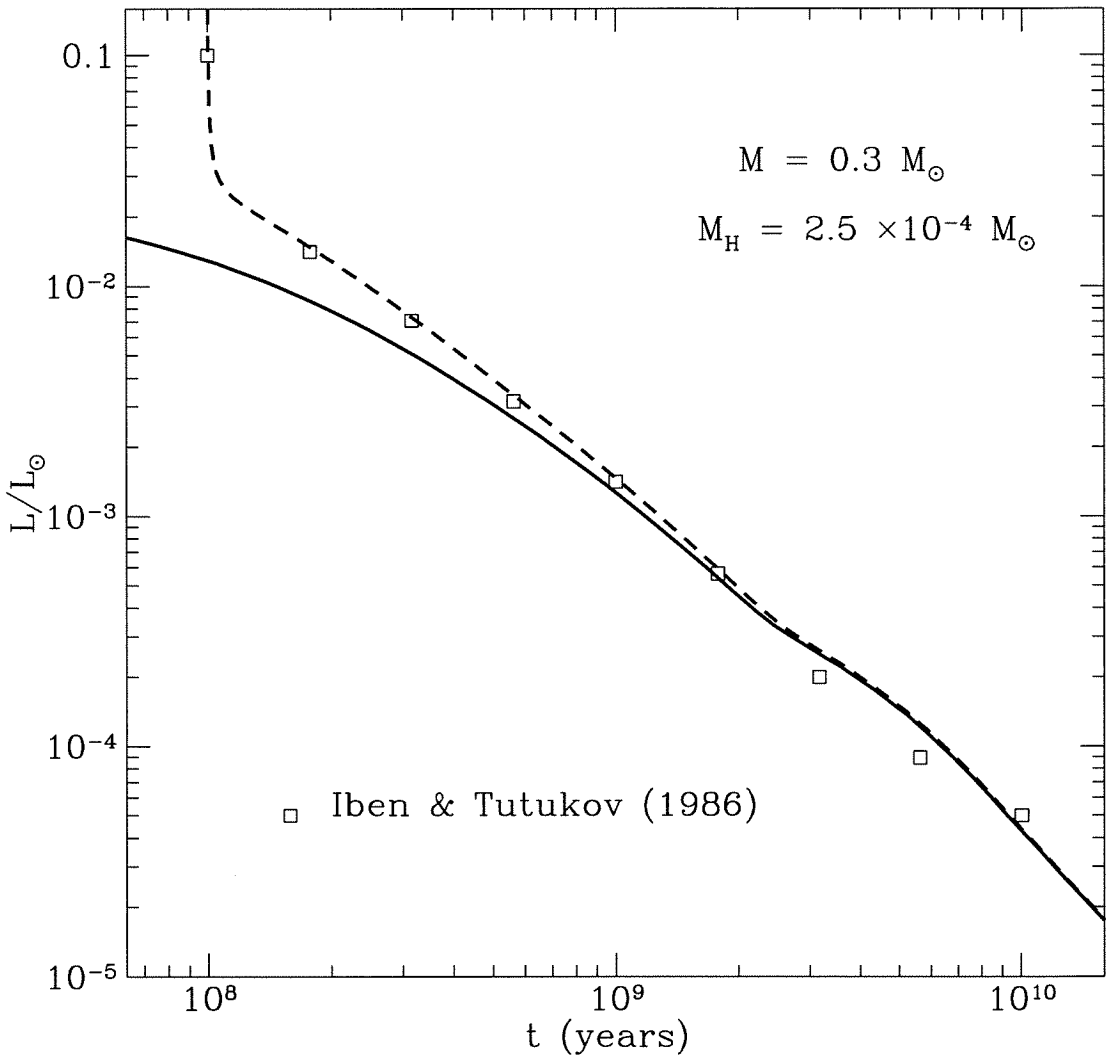

Figure 3.5: **Code Comparisons: He model:** The solid line shows our model with no corrections for different starting points. The dashed line corresponds to the same model, but with the age incremented by 10^8 years, to compensate for the time spent in prior evolutionary stages. The open squares are the results of Iben & Tutukov (1986). The agreement is excellent until t $\sim$ 2 Gyr, by which point Iben & Tutukov caution that their opacities are uncertain.

have little impact on the cooling sequences, because the conductivity is most important in the highest density regions, which is covered by the Itoh tables. A second uncertainty is the effect of extrapolating the OPAL opacities to higher densities in the region $T \sim 10^4 - 10^5$ K and $\rho \sim 10^{-3} - 1\,g.cm^{-3}$. This is not terribly important because the atmosphere is convective in this region, and so the extrapolation will affect only the point at which convection shuts off. By changing the slope of the extrapolation, we determine that $\Delta \log L/L_\odot \leq 0.2$ for ages > 3 Gyr. An exact estimate of this uncertainty is not possible without a proper model for the opacities in this region.

A major uncertainty of past calculations was for the low temperature ($T < 6000$ K) opacities. Our calculations in section 3.3 are designed to solve this problem, at least for the hydrogen atmospheres. The problem persists with the helium atmospheres, where the photospheric opacity is determined by the pressure ionization of helium, in a regime where accurate opacity calculations do not exist. For some models, we also have convective mixing of the elements. We assume that the convective zone is mixed to a uniform composition determined by the relative mass fractions of hydrogen and helium in the convective zone. When the convective zone retreats from the lower layers, we assume that the separation is instantaneous, i.e., at all times, the composition in the convective zone is determined by the depth of the convective base (i.e., the mass of helium in the convection zone relative to the hydrogen envelope mass). The admixture of helium into the Hydrogen atmosphere does not restrict the validity of our opacity calculations at low temperatures. Because of the extremely low neutral helium opacities, 5% of hydrogen by mass is still sufficient to provide enough opacity so that the photospheric pressure lies well below the pressure ionization value.

3.5 Results

In this section, we will describe in detail the cooling of a 0.3 $M_\odot$ helium core star with a thick ($3 \times 10^{-4} M_\odot$) hydrogen envelope. We start our models with an age of 10^8 years (the time taken for the Iben & Tutukov models to reach the end of the last shell flash). We find that, even for these hydrogen masses and at early ages, the residual nuclear burning contribution to the luminosity is never more than $\sim 1\%$ (see Figure 3.6). The neutrino luminosity is never more than $\sim 10\%$ of the photon luminosity. Thus, over the first few

$\times 10^6$ years the star completes the contraction to the white dwarf configuration that it began when the last shell flash ended (see, e.g., Iben & Tutukov (1986), Table 1). In these early stages, the helium core is only mildly degenerate (central degeneracies $\sim$ 30) with $\eta \sim 1$ at the hydrogen-helium boundary, although the core is already approaching an isothermal state (0.99 of the stellar mass has $T > 0.5\ T_c$). The hydrogen envelope is entirely radiative at this stage, so that this is the time at which the star most resembles the Mestel ideal.

When $T_{eff} \sim$ 15000K ($\sim 3 \times 10^8$ years), a small convection zone appears near the surface. This zone remains relatively thin until $T_{eff} \sim 10^4$K ($\sim 10^9$ years), when it starts to deepen as a consequence of the movement of the hydrogen ionization zone to greater depths (Figure 3.8). The recombination of hydrogen also leads to an increase in the photospheric density (since neutral hydrogen has a smaller opacity than ionized Hydrogen). This increase is only halted once molecular hydrogen begins to form ($T_{eff} \sim$ 5000K, $t \sim 4 \times 10^9$ years, see Figure 3.7). The deepening of the convective zone continues until the base reaches a depth where the conduction due to degenerate electrons is more efficient than convection. This occurs after 3×10^9 years. At its deepest extent, the convection zone contains $\sim 5 \times 10^{-5} M_\odot$. This is only a couple of scale heights above the hydrogen/helium interface, so we might expect some small amount ofatmospheric helium contamination (since the convection extends to $\tau \sim 0.3$) below $T_{eff} \sim$ 6000 K. However, the helium will be present only in trace amounts and will not affect the cooling. As the star cools, it will revert again to a pure DA character because of the formation of a radiative buffer zone near the surface below $T_{eff} \sim$ 3500 K. This occurs because there is a minimum in the atmospheric opacity as the primary opacity contribution changes from being Collisionally Induced Absorption (CIA) of H_2 to H^- opacity. If this minimum is low enough, convection will stop in the region of the minimum, but will continue to operate both above and below the minimum. This would allow the surface helium to diffuse out of the top convection zone, leaving the star once again in a pure DA state.

The sequence of Figures 3.6, 3.7 and 3.8 describe the evolution of this cooling sequence in some detail.

The features of the above sequence are common to most of the models we discuss here. The primary differences occur at the lower mass end of the models ($M \sim 0.15\ M_\odot$). The lower masses lead to lower central densities and lower degeneracy, so that the model radii are somewhat larger (hence with lower gravities) and convection extends deeper into the cooler

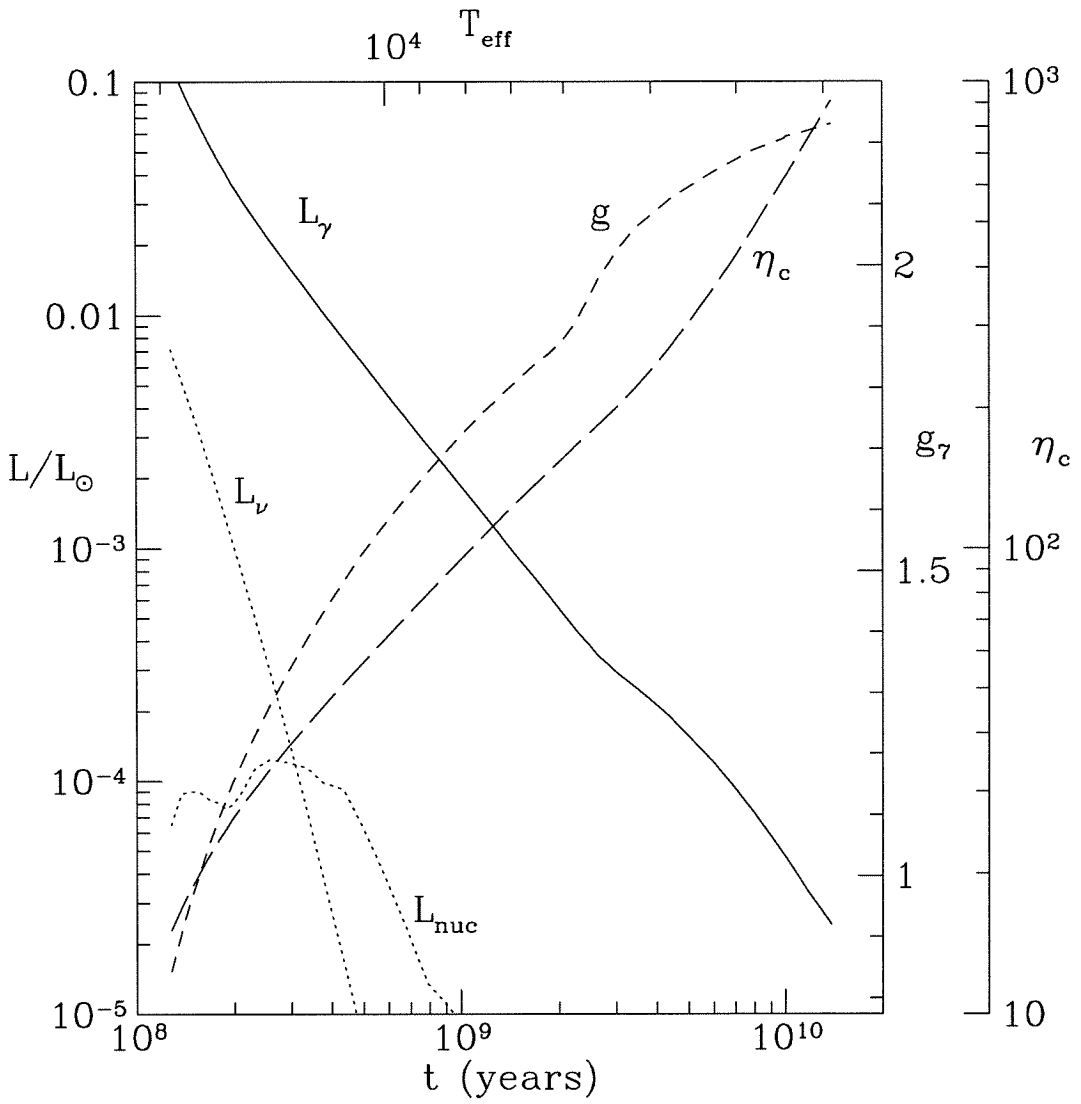

Figure 3.6: **Cooling of a 0.3 $M_\odot$ Model:** We show here the cooling of a 0.3 $M_\odot$ star with a hydrogen envelope of $3 \times 10^{-4} M_\odot$. The solid line is the electromagnetic bolometric luminosity, the dotted lines indicate the neutrino and nuclear luminosities respectively (the nuclear contribution is included in the bolometric luminosity) and the short and long dashed lines indicate the gravity (in units of $10^7 cm.s^{-2}$) and the central degeneracy (E_f/kT) respectively. The effective temperatures corresponding to the various ages for this model are shown on the top axis.

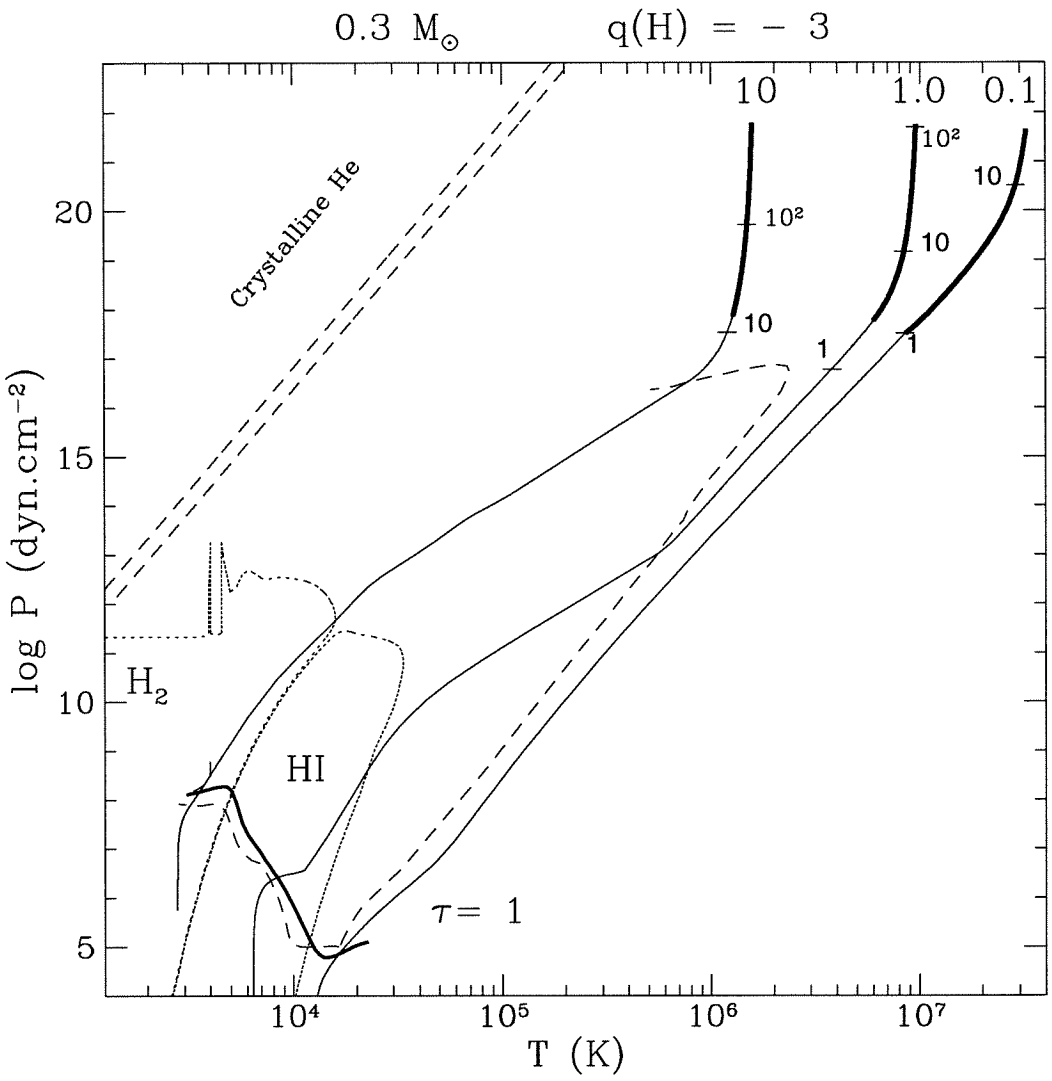

Figure 3.7: **Evolution in the Phase Diagram:** This T-P phase diagram shows three representative atmosphere profiles (labelled at the top by their age in Gyr) for the evolution of the same model shown in 3.6. The heavy solid lines indicate the helium parts of the star and the thin solid lines indicate the hydrogen part. The dotted lines delineate the regions of 50-50 division between HI-HII and H_2-HI respectively. The dashed line indicates the boundary of the convective region for this model (the other pair of dashed lines in the upper left-hand corner indicates crystallization boundary of helium). The thick solid line at the lower left indicates the location of the photosphere for this cooling sequence. The labelled dashes on each of the three curves indicate the points at which the degeneracy parameter $\eta = E_f/kT$ has that particular value.

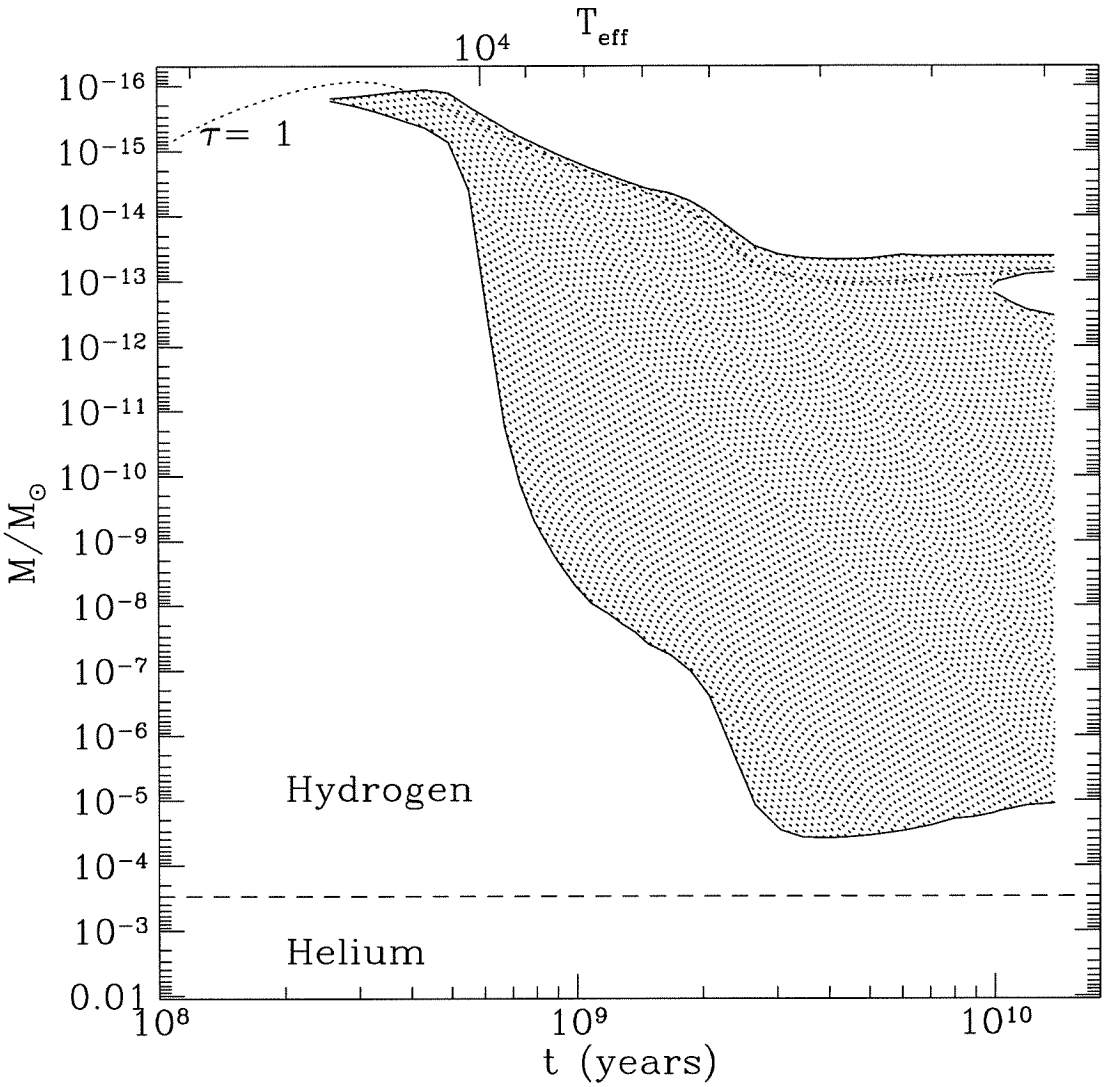

Figure 3.8: **0.3 $M_\odot$ Convective Zone:** Here we show the mass in the convective zone as a function of age (or effective temperature). The shaded region is the convective zone, while the dotted line indicates the location of the photosphere. The dashed line indicates the hydrogen-helium interface in this set of models. We note the appearance of a radiative buffer zone at late times associated with the transition from H^- opacity to H_2 opacity.

models (because conduction is less efficient). Thus, even for thick hydrogen envelopes, the 0.15 $M_\odot$ models do dredge up some helium, becoming mixed atmosphere stars for a short while until the base of the convective zone retreats again. Figure 3.9 shows a diagram similar to Figure 3.8 but for a 0.15 $M_\odot$ model. We see that the base of the convective zone penetrates to the helium layer, leading to an atmospheric Helium abundance of $\sim 15\%$ in this case. Hence, for about 1.5 Gyr, the star would exhibit the characteristics of a cool H/He star, although, with a temperature of 4000-5000 K, it would be difficult to identify it as such. For the thick hydrogen layer models, only the lowest mass models are affected by atmospheric helium contamination. In the sequence of models with thin ($\sim 10^{-6} M_\odot$) hydrogen masses, dredge-up occurs for all masses. In Figure 3.10 we show the effective temperature ranges in which this occurs for all model masses.

Figures 3.11 and 3.12 show the cooling sequences for six different models spanning the range of representative masses. We show curves for 0.15, 0.25 and 0.45 $M_\odot$, with two different hydrogen envelope masses, $3 \times 10^{-4} M_\odot$ (thick) and $10^{-6} M_\odot$ (thin). For completeness we also show the sequences for pure helium models in Figure 3.13, but the opacities for $T_{\rm eff} < 6000$ K are rather uncertain, and thus we do not expect the cooling curves to be accurate at temperatures below this value.

In order to make comparison with observations easier, we have also calculated the black-body absolute magnitudes for these sequences, using the flux calibrations of Bessell (1979). The most common bands used are V and I, which are shown in Figures 3.14 and 3.15.

For stars with hydrogen envelopes and effective temperatures > 7000 K, spectroscopic determinations of effective temperature and gravity can provide a direct measurement of the white dwarf mass, provided one has a relationship between radius and mass. We have calculated the mass-radius relations for both our thick and thin hydrogen layer models for the full range of helium white dwarf masses. This leads to a relationship between gravity $g = GM/R^2$ and effective temperature $T_{\rm eff}$ for a given mass, namely

$$g = f(T_{\rm eff})\,[a_2 - a_3 T_{\rm eff}] \tag{3.1}$$

with

$$f(T_{\rm eff}) = 1 + \frac{a_1 T_{\rm eff}}{1 + 9\exp\left(4 \times 10^{-3}\,(T_{\rm eff} - 5800{\rm K})\right)} \tag{3.2}$$

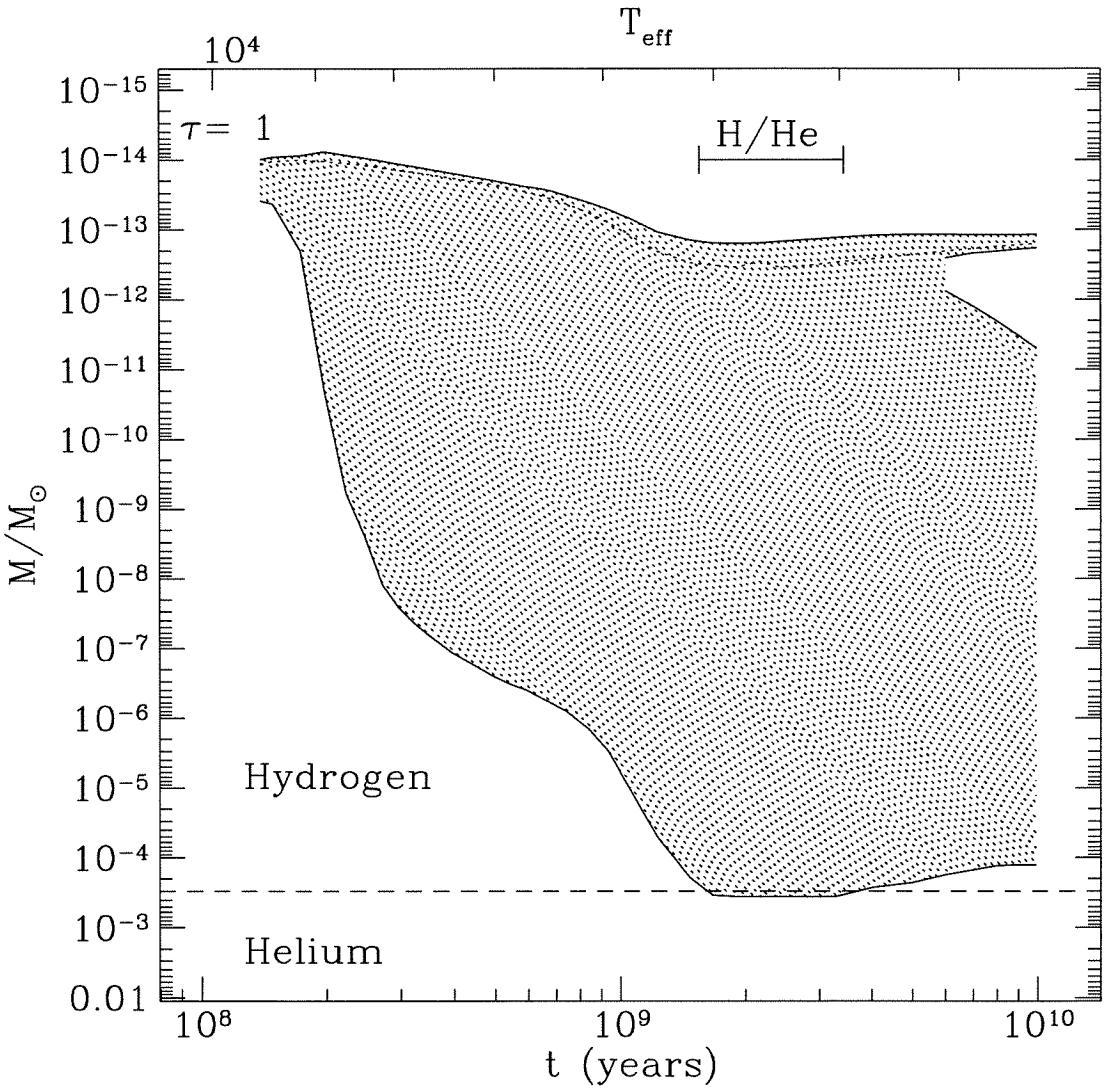

Figure 3.9: **0.15 $M_\odot$ Convective Zone:** Once again the shaded region is the convective zone, and the dotted line denotes the position of the photosphere. We note that, for $T_{eff} \sim 4000 - 5000$ K, the atmosphere will be contaminated with helium.

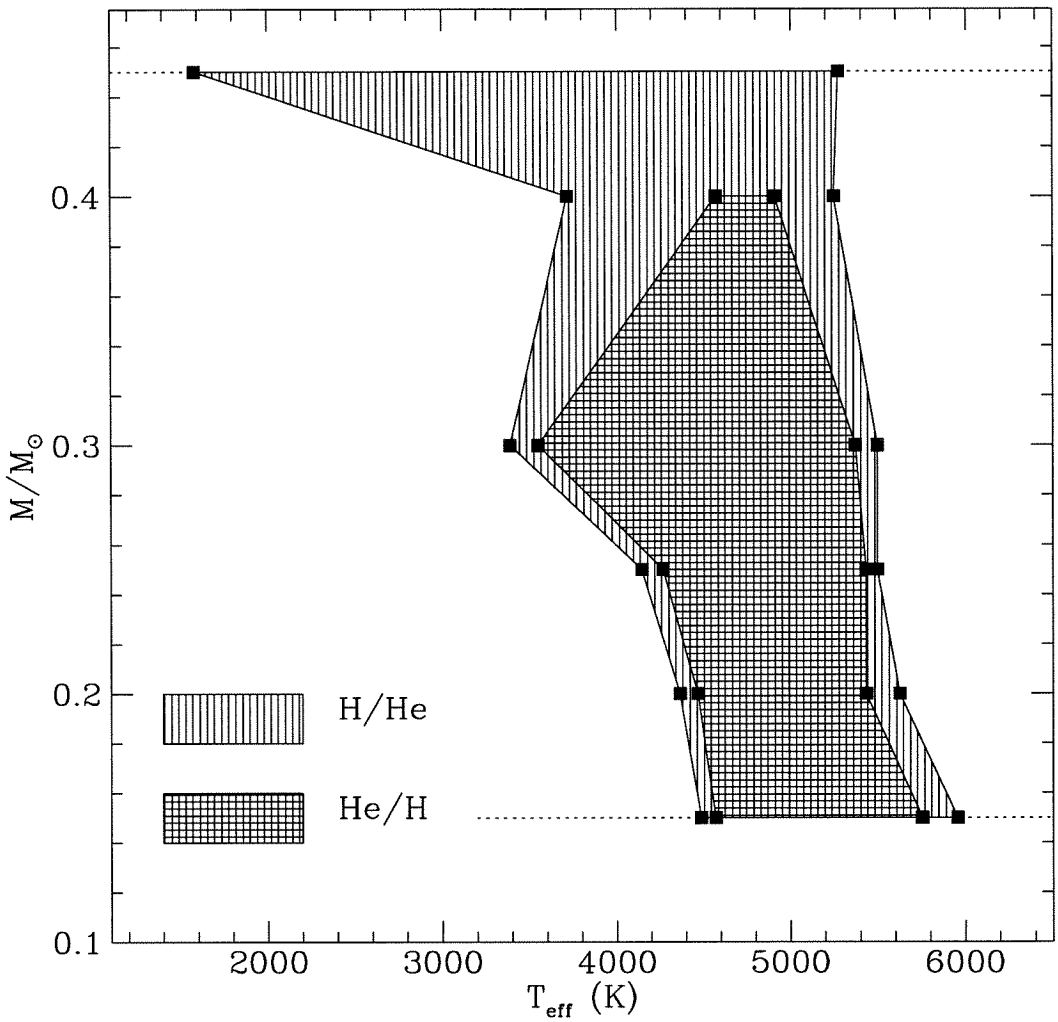

Figure 3.10: **Atmospheric Helium Contamination for Thin Hydrogen Envelopes:** The shaded regions indicate those models in which the convective zone extends into the helium layer and thus causes atmospheric Helium contamination. We consider two representative cases. The area marked as H/He is characterised by a mass fraction of helium, $X_{He} > 0.1$. The area marked as He/H is characterised by $X_{He} > 0.8$. This cutoff value may seem rather high, but we note that the dredge-up occurs for temperatures at which helium is neutral and thus makes little contribution to the opacity. The horizontal dotted lines indicate the mass limits of the models we calculated, so that the extent of the convective regions outside these bounds is unknown. These models are for a hydrogen envelope of mass $M_H = 10^{-6} M_\odot$.

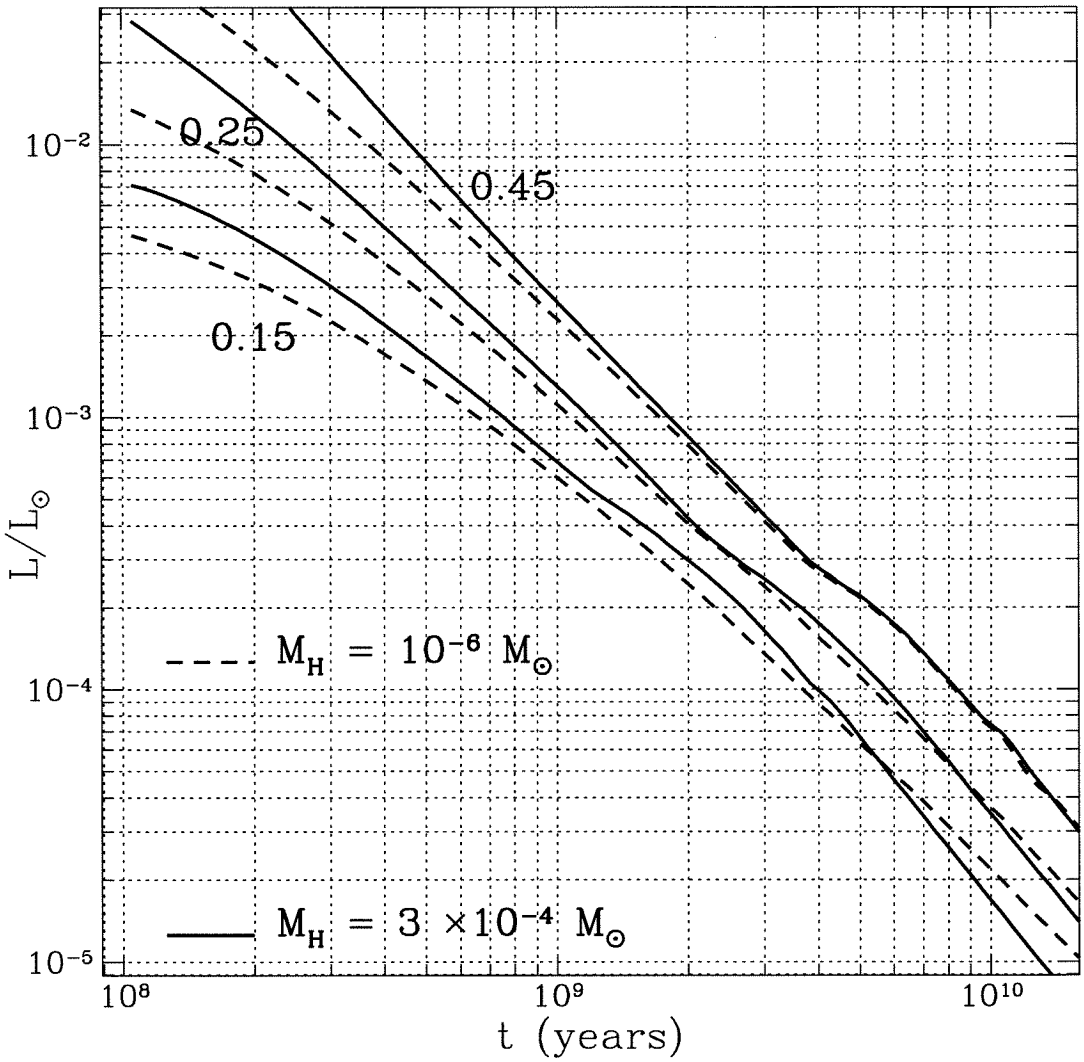

Figure 3.11: **Hydrogen Cooling Sequences 1: Luminosity Evolution:** The solid lines indicate model white dwarf cooling sequences with a hydrogen envelope of $3 \times 10^{-4} M_\odot$ for each of three representative total masses. The dashed lines are the equivalent sequences with a smaller hydrogen envelope of $10^{-6} M_\odot$. The difference in luminosities at earlier times is a result of the thicker hydrogen layer leading to a larger stellar radius (the effective temperatures are closer - see Figure 3.12.

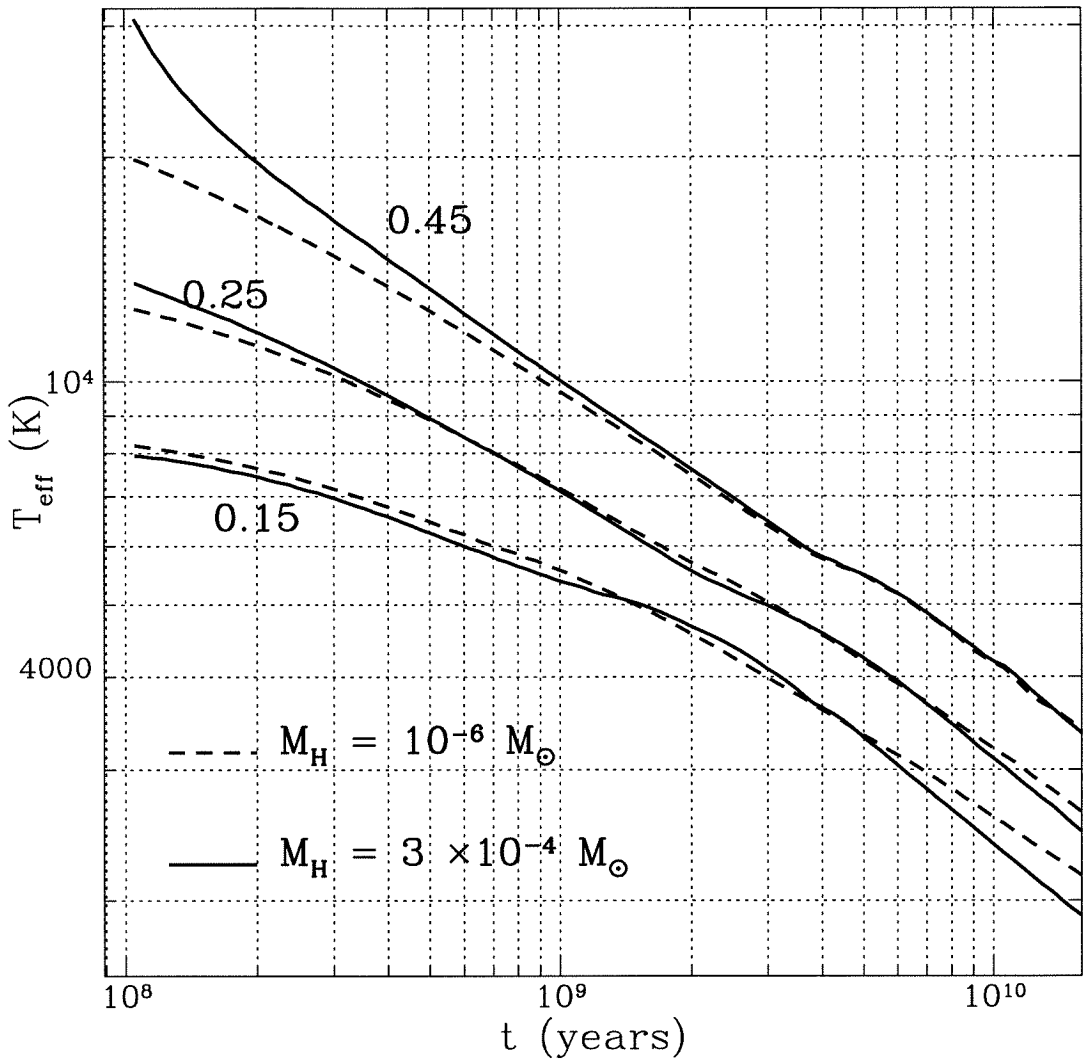

Figure 3.12: **Hydrogen Cooling Sequences 2: Temperature Evolution:** Here we show the effective temperature for the same sequences as in Figure 3.11. Note the large variation in temperature with envelope mass for the most massive models. This is the effect of the contribution of residual hydrogen burning at the base of the thicker hydrogen envelope.

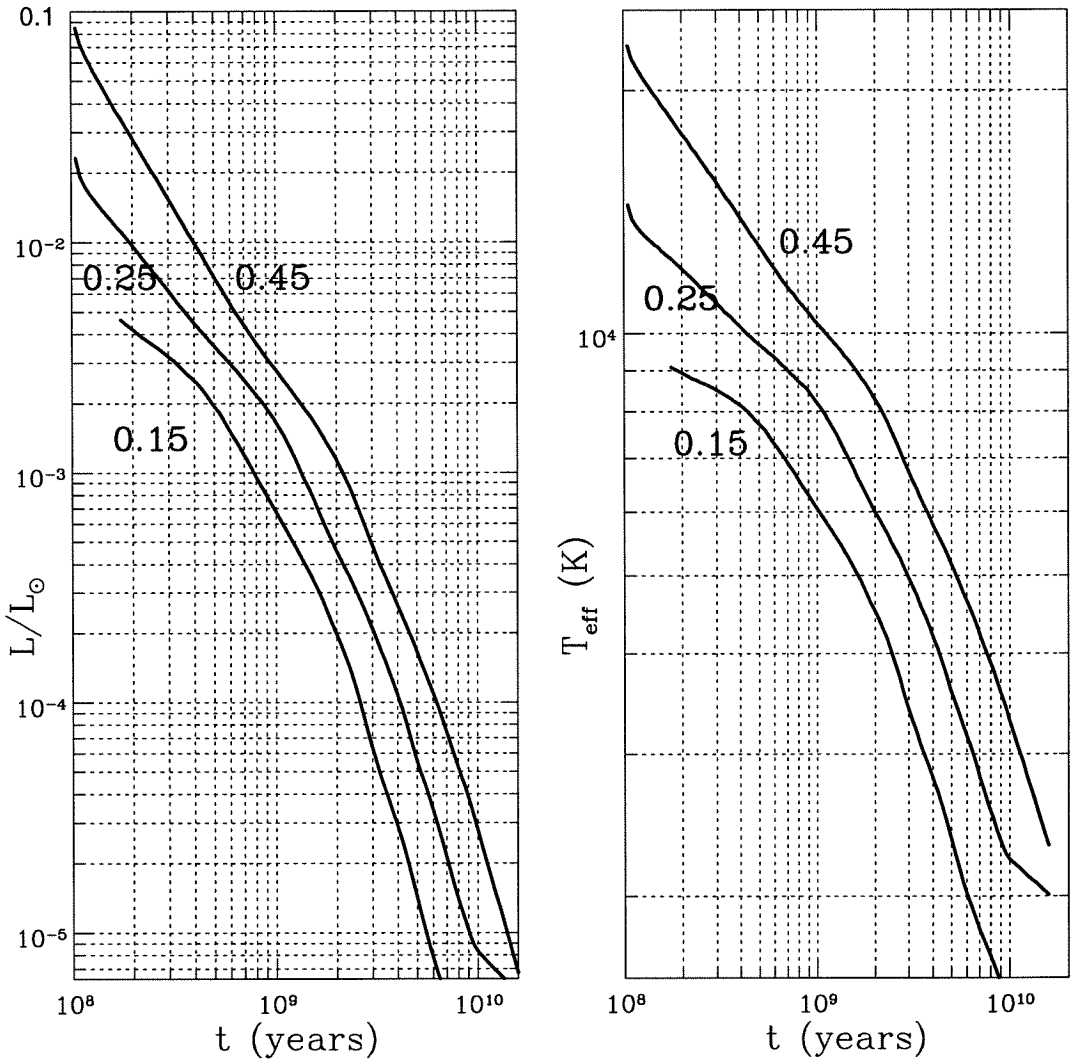

Figure 3.13: **Helium Cooling Sequences:** We show here pure helium models for the same masses as before. The evolution at effective temperatures below 6000 K is uncertain because of the inaccuracies of the photospheric opacities for neutral helium at these temperatures. We note that the faster cooling of these models means that crystallization sets in for the 0.25 $M_\odot$ sequence after 9 Gyr.

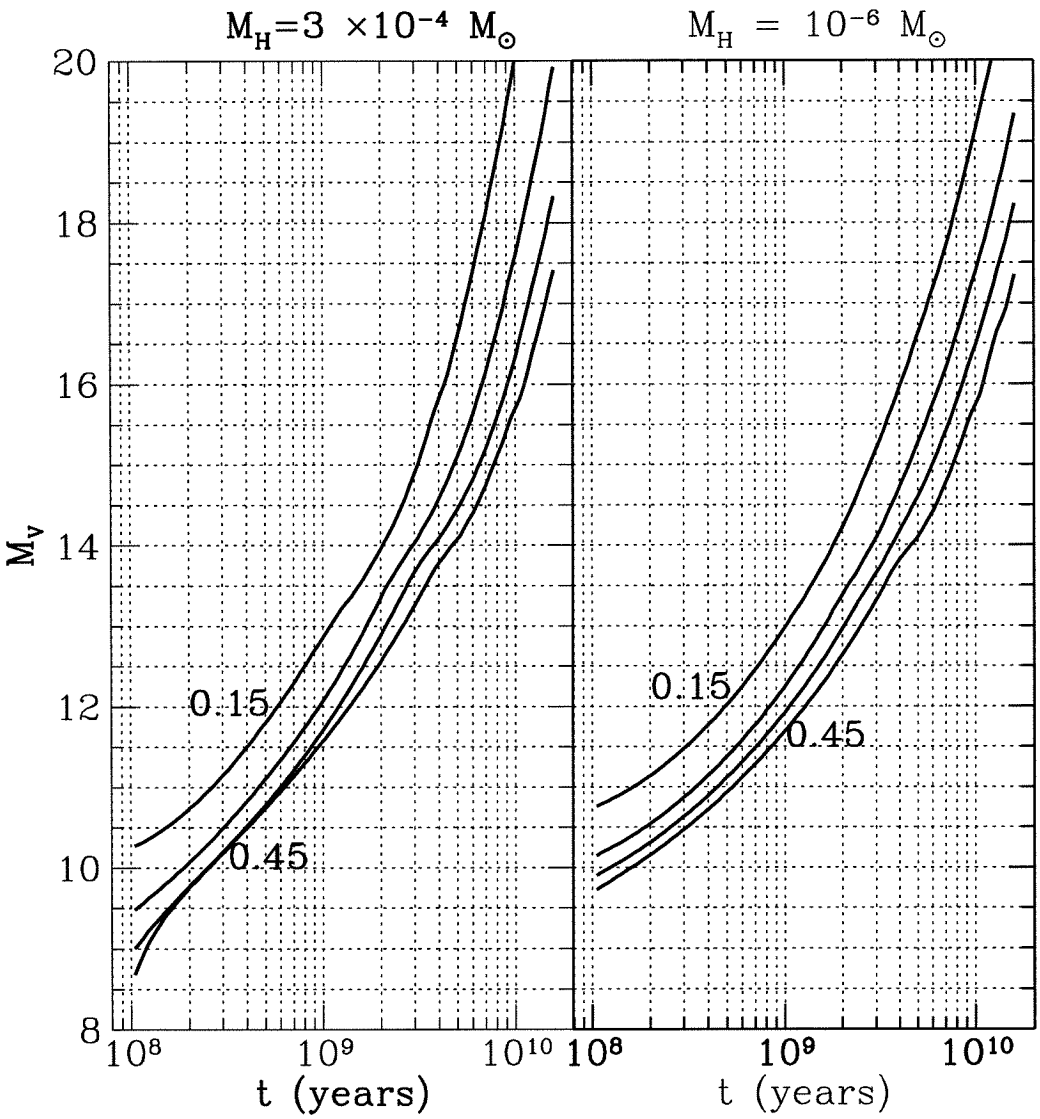

Figure 3.14: **V Band Cooling Sequences:** We show here the absolute V magnitude determined from our cooling sequences. The curves are for 0.15, 0.25, 0.35 and 0.45 $M_\odot$.

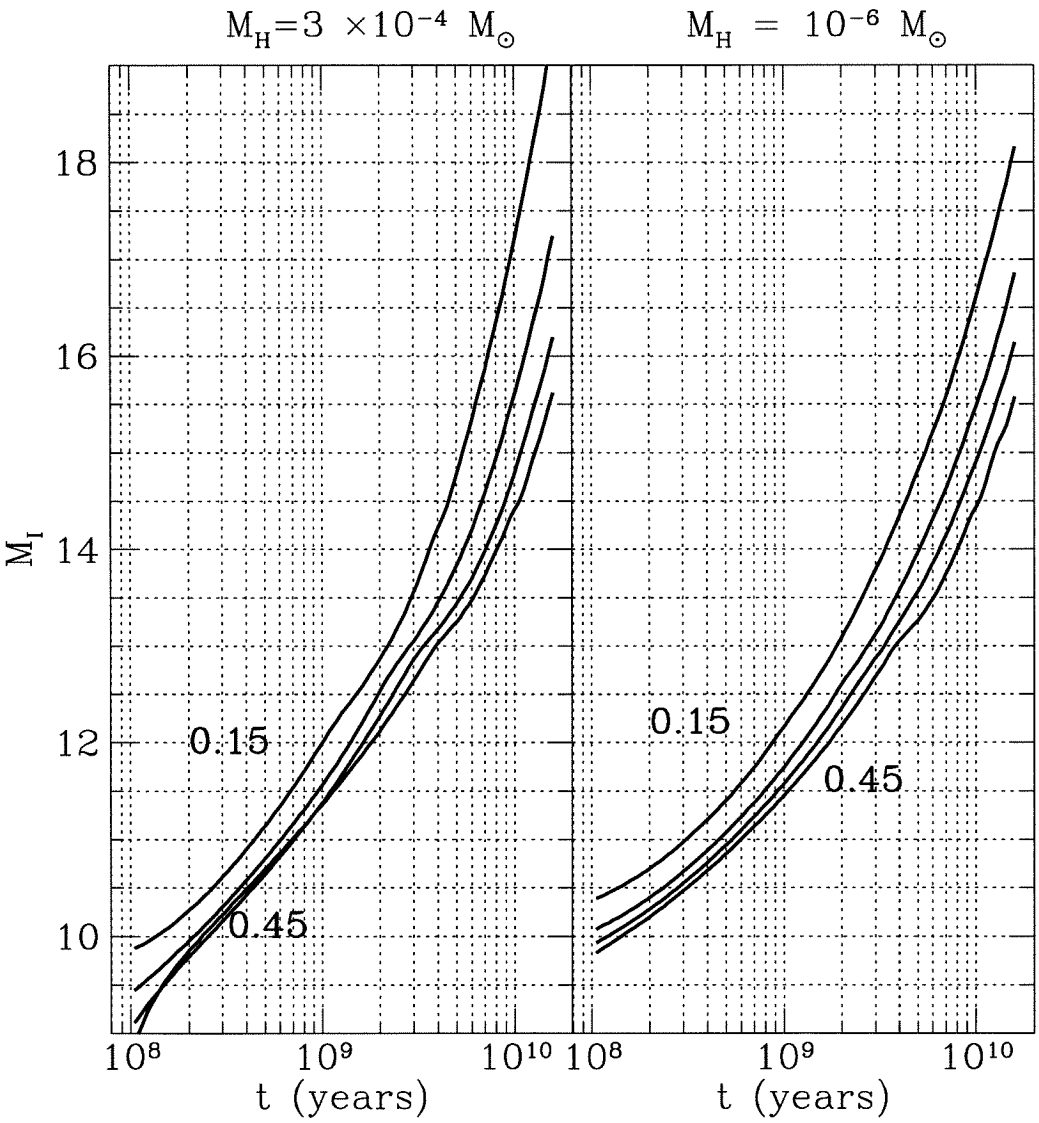

Figure 3.15: **I Band Cooling Sequences:** As for Figure 3.14, but for absolute I magnitude.

and

$$a_1 = 9.91 \times 10^{-7} \left(\frac{M}{M_\odot}\right)^{-2.33} \quad (3.3)$$

$$a_2 = 1.69 \times 10^{8} \left(\frac{M}{M_\odot}\right)^{1.68} \quad (3.4)$$

$$a_3 = 946 \left(\frac{M}{M_\odot}\right)^{0.17} \quad (3.5)$$

for the thick hydrogen envelope and

$$a_1 = 3.79 \times 10^{-7} \left(\frac{M}{M_\odot}\right)^{-2.18} \quad (3.6)$$

$$a_2 = 1.68 \times 10^{8} \left(\frac{M}{M_\odot}\right)^{1.55} \quad (3.7)$$

$$a_3 = 650 \quad (3.8)$$

for the thin hydrogen envelope and $M \leq 0.4 M_\odot$. Figure 3.16 compares the fits to the proper curves for the case of a thick envelope.

We may compare the $T_{eff} = 0$ limit of (3.1) with various well-known T=0 mass-radius relations. Converting the above into mass-radius relations and taking the T=0 limit we get

$$\frac{R}{R_\odot} = 0.013 \left(\frac{M}{M_\odot}\right)^{-0.32} \text{ (Thick H)} \quad (3.9)$$

$$\frac{R}{R_\odot} = 0.013 \left(\frac{M}{M_\odot}\right)^{-0.28} \text{ (Thin H)} \quad (3.10)$$

This is very close to the often used mass-radius relationship of Paczynski (1967) for low mass degenerate dwarfs $R/R_\odot = 0.013\,(M/M_\odot)^{-1/3}$. In Figure 3.17 we compare our T=0 curves with the Paczynski relation and that of Hamada and Salpeter (1961).

3.6 Conclusion

We have presented a set of cooling sequences for low mass helium white dwarfs of different masses and with different masses of surface hydrogen. We provide blackbody absolute magnitudes and surface gravity - effective temperature relations as an aid to the analysis of future observations. In Chapter 4 we shall apply these models to the optical observations of the companions to millisecond pulsars in order to derive cooling ages.

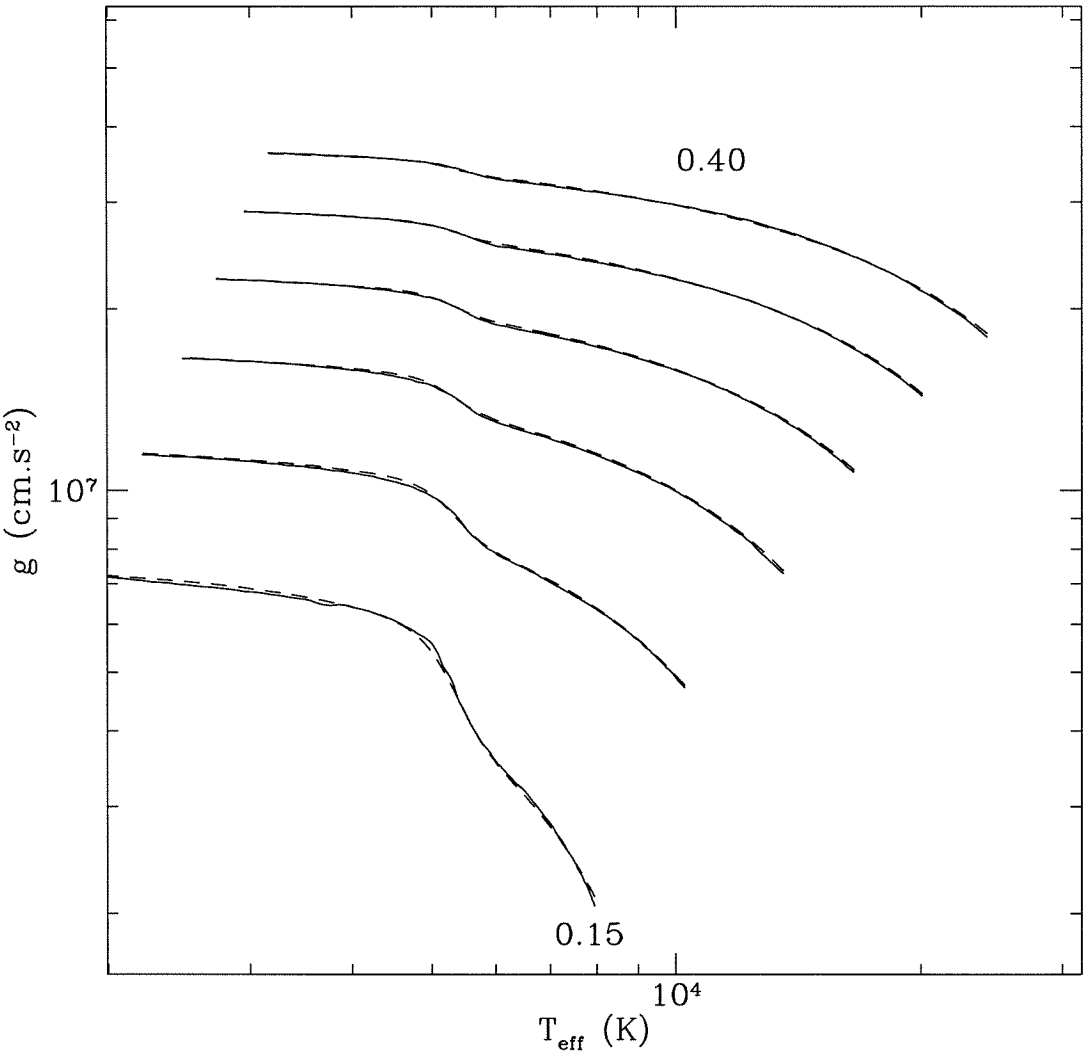

Figure 3.16: **The Gravity-Effective Temperature Relation:** The solid lines represent the true g-T_{eff} curves, and the dashed lines are the fits given by equations (3.1)-(3.5).

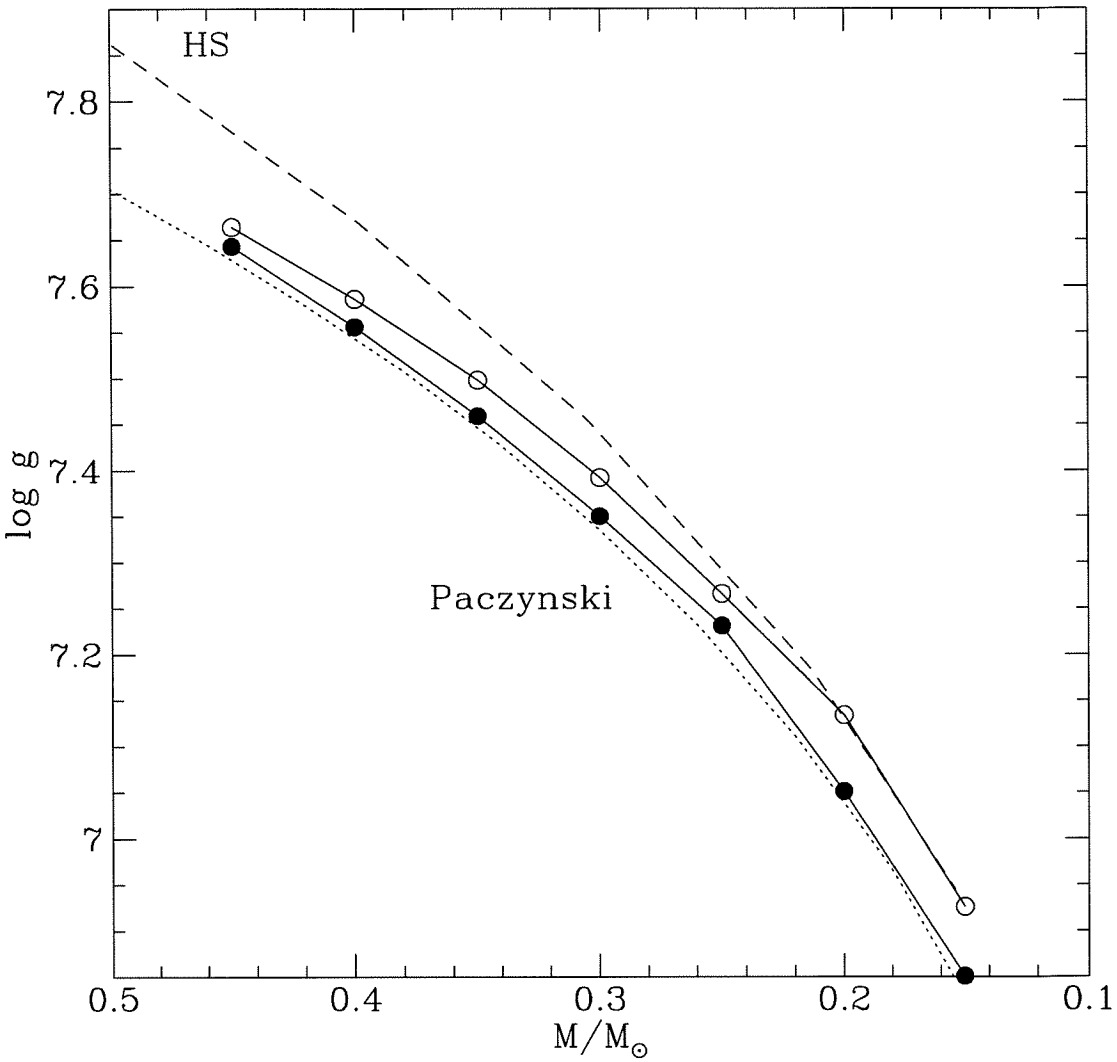

Figure 3.17: **The T=0 Mass-Radius Relation:** The dotted line is the gravity as determined from the Paczynski (1967) mass-radius relation. The dashed line was obtained using the Hamada and Salpeter (1961) pure helium mass-radius relation. The filled circles are for the thick H envelope models (3.9) and the open circles, for the thin H envelope models (3.10).

The authors would like to thank Marten van Kerkwijk and Yanqin Wu for lengthy discussions about white dwarf physics and Glenn Soberman for helping with the initial conditions for our models. The generosity of messrs D. Saumon, G. Fontaine, I. Mazzitelli, F. Rogers and C. Iglesias in providing their microphysical results is also appreciated.

REFERENCES

Bergeron, P., Saumon, D. & Wesemael, F. 1995 ApJ, **443**, 764.

Bergeron, P., Wesemael, F. & Fontaine, G., 1992, ApJ, **387**, 288.

Bessell, M.S., 1979, PASP, **91**, 589.

Böhm K.-H. et al., 1977 ApJ, **217**, 511.

Borysow, A. & Frommhold, L. 1990 ApJ, **348**, L41.

D'Antona, F. & Mazzitelli, I. 1989 ApJ, **347**, 934.

D'Antona, F. & Mazzitelli, I. 1990 ARA&A, **28**, 139.

Dupuis, J., Fontaine, G., Pelletier, C. & Wesemael, F., 1992, ApJS, **82**, 505.

Eggleton, P.P., 1971, MNRAS, **151**, 351.

Fontaine, , G. Graboske, H.C. & Van Horn H.M. 1977 ApJS, **35**, 293.

Fowler, W., Caughlan, G.R. & Zimmerman, B.A. 1975, ARA&A, **21**, 165.

Henyey, L.G., Wilets, L., Böhm, K.H., LeLevier, R. & Levee, R.D. , 1959, ApJ, **129**, 628.

Henyey, L.G., Forbes, J.E. & Gould, N.L. 1964 ApJ, 139, 306.

Hubbard, W.B. & Lampe, M. 1969, ApJS, **18**, 297.

Iben, I. & Tutukov, A.V., 1986, ApJ, **311**, 742.

Itoh, N. & Kohyama, Y. 1983 ApJ, **275**, 858.

Itoh, N., Matsumoto, N., Seki, M. & Kohyama, Y., 1984 ApJ, **279**, 413.

Itoh, N., Mitake, S., Iyetomi, H. & Ichimaru, S., 1983 ApJ, **273**, 774.

Kippenhahn, R., Kohl, K. & Weigert, A. 1967 ZAp, **66**, 58.

Kippenhahn, R., Weigert, A. & Hofmeister, E. 1967 Meth. in Comp. Phy., **7**, 129.

Koester, D. & Schonberner, D. 1986 A&A, **154**, 125.

Lenzuni, P., Chernoff, D.F. & Salpeter, E.E. 1991 ApJS, **76**, 759.

Marsh, T.R., Dhillon, V.S. & Duck, S.R., 1995, MNRAS, **275**, 828.

Mazzitelli, I., 1989, ApJ, **340**, 249.

Mestel, L., 1952 MNRAS, **112**, 583.

Mitake, S. Ichimaru, S. & Itoh, N. 1984 ApJ, **277**, 375.

Munakata, H., Kohyama, Y. & Itoh, N. 1985, ApJ, **296**, 197.

Paczynski, B., 1967, Acta Astron., **17**, 287.

Pols, O., Tout, C.A. & Eggleton, P.P., 1995, MNRAS, **274**, 964.

Rogers, F.J. & Iglesias, C.A. 1992 ApJS, **79**, 507.

Saumon, D., Chabrier, G. & Van Horn, H.M., 1995, ApJS, **99**, 713.

Schatzmann, E., 1958, White Dwarfs (Amsterdam: North-Holland)

Sweigart, A.V. & Gross, P.G., 1978, ApJS, **36**, 405.

Winget, D.E. & Van Horn, H.M. 1987 IAU Colloq. 95, ed A.G.Davis Philip et al., 363.

Wood, M.A., 1992, ApJ, **386**, 539.

Zhang, C. & Borysow, A. 1995 ApJ, **441**, 960.

Chapter 4 Stellar Forensics: II - The Coroner's Report

In this chapter, we apply the results of our low mass white dwarf cooling models in Chapter 3 to the companions of millisecond pulsars. We analyse the results of optical observations of these companions to determine cooling ages and initial spin periods for the millisecond pulsars and examine the implications of these results for binary evolution theories and for neutron star structure.

4.1 Introduction

The ages of millisecond pulsars are important for understanding both their nature and origin. Ages are usually estimated from the characteristic spin-down age $t_P = P/2\dot{P}$, but such estimates could be seriously in error if the current spin period is still close to the initial spin period at the beginning of the millisecond pulsar phase. If the average millisecond pulsar is significantly younger than its spin-down age, as suggested by Lorimer et al. (1995a), then it would affect current theories of magnetic field decay in such stars (Kulkarni (1986), Camilo et al.(1994)) as well as the birth-rate discrepancy between Low Mass Binary Pulsars and Low Mass X-Ray Binaries (Kulkarni & Narayan (1988),van den Heuvel (1995)).

Many millisecond pulsars are found in binaries, often with low mass degenerate companions. Accurate modelling of the cooling of the companions can allow one to estimate the age of the system (or rather the age of this particular incarnation). Since millisecond pulsars are thought to be spun-up as the result of accretion from the companion star, the pulsar will begin to spin down at the same time as the companion shrinks within its Roche lobe, ending mass loss and beginning the process of cooling to its final degenerate white dwarf configuration. Hence, the cooling age of the white dwarf should represent the millisecond pulsar age as well.

In Chapter 3, we calculated accurate cooling models for the low mass Helium white dwarfs thought to be the companions in these low mass binary pulsar systems. In this

paper we shall now apply the models to the optical observations of these systems to infer the cooling ages for these objects. Section 4.2 reviews the basic concepts used to infer the age of a pulsar from its spin parameters as well as simple models of magnetic field decay in such a pulsar. In section 4.3 we apply our cooling models to the observational data and in section 4.4 we discuss the implications.

4.2 Pulsar Spin Down

For a pulsar with period P and spin-down rate $\dot{P}$ related by $\dot{P} \propto P^{2-n}$, the age is given by

$$t = \frac{P}{(n-1)\dot{P}} \left(1 - \left(\frac{P_0}{P}\right)^{n-1}\right) \tag{4.1}$$

where n is the braking index and P_0 is the initial period. For magnetic dipole radiation n=3, leading to the familiar expression for the characteristic pulsar spin-down time $t_P = P/2\dot{P}$. For some young pulsars, measurements yield a range for n of 2.0 to 2.8 (Michel (1991) and references therein). However, n is not known for any millisecond pulsars. Because characteristic spin-down ages for millisecond pulsars are of the order of Gyr or higher, there is a very real danger that estimates of the pulsar age based on this quantity will be gross overestimates because of the second factor in equation (4.1).

The spin-down time is calculated from the spin-down rate $\dot{P}$, which can also be seriously affected by the proper motion of the pulsar (e.g., Camilo et al. (1994)). This is because of the Shklovskii effect (Shklovskii (1970)), which produces an additional contribution to the period derivative such that

$$\frac{\dot{P}}{P} = \left(\frac{\dot{P}}{P}\right)_i + \frac{V_\perp^2}{cD} \tag{4.2}$$

where $\left(\dot{P}/P\right)_i$ is the intrinsic contribution due to pulsar rotation, D is the distance to the pulsar, $V_\perp \propto D\mu$ is the transverse velocity and μ is the proper motion of the pulsar. Once μ is measured, we may remove this contribution to obtain the intrinsic spin-down time. Thus, with n=3, we obtain an expression for the ratio of the true age of the pulsar to its uncorrected characteristic age t_p

$$\frac{t}{t_p} = \left(1 - \left(\frac{P_0}{P}\right)^2\right) / \left(1 - \frac{2V_\perp^2 t_p}{cD}\right) \tag{4.3}$$

Apart from the initial period P_0, all the quantities on the right side are measurable in principle. An independent age estimate, such as that from the cooling of a white dwarf, can thus be used to estimate the initial period. If the companion is undetectable then only a lower limit to the age is possible, which in turn translates into an upper limit on P_0 (as long as $2V_\perp^2 t_p/cD < 1$, which is the case unless the intrinsic period derivative is negative, such as in the binary system 1620-26, where a second companion is believed to be responsible for the negative $\dot{P}$ (Backer et al. (1993), Thorsett et al. (1993)).

There is an additional complication, namely the possibility of magnetic field decay. For magnetic dipole radiation, the spin down rate is given by[1]

$$\dot{P} = \left(\frac{8\pi^2 R^6}{3Ic^3}\right)\frac{B^2}{P} \tag{4.4}$$

where B is the magnetic field strength on the surface of the neutron star. Thus, decay of B will alter the spin-down rate. The possibility of field decay was first advanced by Gunn & Ostriker (1969) but its occurrence is still not conclusively proven. Narayan & Ostriker (1991) have argued for an exponential field decay with a decay time of $\sim 10^7$ years. Bhattacharya et al. (1992), on the other hand, find no evidence for field decay. Furthermore, there may be a subdivision between 'normal' pulsars and 'recycled' pulsars (i.e., those spun up through accretion in binaries). Kulkarni (1986) and Camilo et al (1994) have argued that the fields on recycled pulsars do not decay, based on the ubiquitous nature of the field strength $\sim 10^{8-9}$G amongst this population of objects and on the presence of cool companions such as the ones we address here.

Thus, we shall also consider magnetic field decay of the form $B = B_0 \exp(-t/t_D)$, where t_D is the decay time. In this case, the equivalent of equation (4.3) is

$$\frac{t}{t_D} = \frac{1}{2}\ln\left[1 + \frac{2t_p}{t_D}\frac{\left(1-\left(\frac{P_0}{P}\right)^2\right)}{\left(1-\frac{2V_\perp^2 t_p}{cD}\right)}\right] \tag{4.5}$$

This introduces a second unknown parameter t_D into the equation. Nevertheless, we can obtain a lower limit to t_D by setting $P_0 = 0$, so that we may rearrange equation (4.5)

[1] Again, B is in fact B sin α, and so decay could be the result of field alignment.

in the form

$$t_D\,(\exp(2t/t_D) - 1) < \frac{2t_p}{\left(1 - \frac{2V_\perp^2\, t_p}{cD}\right)} \tag{4.6}$$

Once we have an estimate for t, the left-hand side is a monotonically decreasing function of t_D and the right-hand side consists of measurable quantities. Hence, we may constrain the exponential field decay time.

4.3 Results

Table 4.1 lists the known low mass binary pulsars with white dwarf companions. Most have Helium core companions (inferred from their mass) although three have companions whose masses indicate that they are Carbon/Oxygen white dwarfs. These measurements come from pulsar timing. In order to determine a cooling age, we need optical identifications of the companions. Those systems with detections or upper limits are shown in Table 4.2. It is these systems that we shall now discuss in turn. We note that, while the following analysis is quantitative, such an exercise is likely to contain small residual systematic uncertainties resulting from the use of a heterogeneous sample set from a number of independent groups using different instruments and analysis procedures. The cooling curves used in this procedure will be made public to enable improved estimates to be made with better understanding of individual measurement errors.

To determine the effective temperature from the observed colours, we have used both the original author's estimates as well as our own black body colour calculations. We use the bandpasses as described in Bessell (1990), with fluxes normalized to the spectrum of Vega taken from Hayes (1985). In the case of the more massive white dwarfs, we use the pure Hydrogen broad band colours of Bergeron et al. (1995).

In the following sections, we shall derive cooling ages for the various binary systems. We shall also convert these into constraints on the initial periods of the millisecond pulsars. In order to obtain conservative estimates, we consider dispersion measure distances to be accurate to within 30%, transverse velocities up to 100 km.s^{-1} for systems without a measured proper motion, and a braking index between n=2 and n=3.

Pulsar	P (ms)	P_b (d)	f(M) ($M_\odot$)	M_c ($M_\odot$)	log B (G)	t_p (Gyr)	Ref
J1022+1001	16.45	7.8	0.0829	0.72	8.9	5.9	1
B0655+64	195.67	1.0	0.0710	0.67	9.95(12)†	9.5(50)†	2
J2145-0750	16.05	6.8	0.0240	0.43	<8.8	>8.7	3
J2019+2425	3.93	76.5	0.0107	0.32	7.9(2)†	43.3(265)†	4
J1713+0747	4.57	67.8	0.0079	0.28	8.3†	9.0†	5
J1455-3330	7.99	76.2	0.0063	0.26	< 8.6	> 5.3	6
J1640+2224	3.16	175.5	0.0059	0.25	<8.0	>17.3	7
B1855+09	5.36	12.3	0.0057	0.25	8.5†	4.9†	8
B0820+02	864.87	1232.5	0.0030	0.20	11.5†	0.13†	9
J2033+17	5.95	56.2	0.0028	0.19	...	...	10
B1953+29	6.13	117.3	0.0024	0.18	8.6	3.3	11
J2317+1439	3.45	2.5	0.0022	0.18	7.9†	36.3(69)†	12
J0218+4232	2.32	2.0	0.0020	0.17	8.6	0.5	13
J1045-4509	7.47	4.1	0.0018	0.16	8.6	6.2	3
J1803-2712	334.42	406.8	0.0013	0.15	10.9	0.3	10
J0034-0534	1.88	1.6	0.0012	0.14	<8.1	>4.4	3
J0437-4715	5.76	5.7	0.0012	0.14	8.5(1)†	5.4(25)†	14
J0751+1807	3.48	0.3	0.0012	0.14	8.2	6.9	15
J2229+2643	2.98	93.0	0.0011	0.13			17
J0613-0200	3.06	1.2	0.0010	0.13	8.3	4.4	6
J1643-1221	4.6	147	0.0008	0.12	8.6	2.2	6
J1012+5307	5.26	0.6	5.8×10^{-4}	0.11	<8.5	>5.7	16

Table 4.1: The pulsar binary systems with suspected and confirmed white dwarf companions, sorted in order of decreasing mass function. The characteristic ages are uncorrected for proper motions. The daggers mark those pulsars for which the magnetic field and spin-down ages have been corrected for the Shklovski effect using measured proper motions. The references are as follows:1 - Camilo (1996), 2-Jones & Lyne (1988), 3-Bailes et al. (1994),4-Nice et al. (1993), 5- Foster et al. (1993), 6-Lorimer et al. (1995b), 7- Foster et al. (1995), 8-Kaspi et al. (1994), 9- Taylor & Dewey (1988), 10 - Taylor, Manchester & Lyne (1993), 11-Rawley et al. (1988), 12-Camilo et al. (1993), 13 - Navarro et al. (1995), 14 -Johnston et al. (1992), 15- Lundgren et al. (1995), 16-Nicastro et al. (1995), 17-Camilo, Nice & Taylor (1996)

Name	D (kpc)	T_{eff} (K)	m_B	m_V	m_R	m_I	Reference
J0034-0534	0.98	< 3600	...	> 26.8	> 25.0	24.8(3)	1,2
J1713+0747	1.1	3450(350)	> 27.1	26.0(2)	...	24.1(1)	1
J0437-4715	0.14	3950(550)	22.1(2)	20.8(3)	19.6(4)	19.5(2)	3,4,5
J1640+2224	1.18	4200(600)	...	26.0(3)	24.5(3)	24.6(2)	1,6
J1012+5307	0.52	8550(25)	19.78(4)	19.58(2)	19.49(4)	19.32(4)	7, 8
B0820+02	1.4	15250(1250)	...	22.8(1)	...	...	9,10
B1855+09	0.9	...	...	> 25.4	> 24.6	> 23.4	11,12
J0751+1807	2.0	...	...	>23.5	...	...	8
J2229+2643	1.4	...	...	>25.0	...	...	8
J2019+2425	0.9	5400(1300)	...	26.4(4)	...	25.0(3)	6
J2145-0750	0.5	6500(500)	23.89(11)	23.7(1)	...	22.97(7)	1
J1022+1001	0.6	8100(300)	...	23.10(4)	...	22.665(7)	1
B0655+64	0.48	7500(1500)	...	22.2	22.1	...	13

Table 4.2: The parameters of optically identified pulsar companions. All quoted distances are subject to a 30 % uncertainty from the dispersion measure. The figures in brackets are the uncertainties in the last quoted digit. The upper group are expected to be Helium core stars and the lower group are thought to be C/O white dwarfs. The reference numbers are as follows: 1- Lundgren et al. (1996b), 2-Bell et al. (1995), 3-Danziger et al. (1991), 4-Bell et al. (1991), 5-Bailyn (1991), 6-Lundgren at al (1996a), 7-van Kerkwijk et al (1996), 8-Lorimer et al. (1995a), 9-van Kerkwijk & Kulkarni (1995), 10-Koester et al. (1992), 11-Kulkarni et al. (1991), 12-Callanan (1989), 13-Kulkarni (1986).

4.3.1 PSR J0437-4715

We shall start with the best determined case. The PSR J0437-4715 system contains the closest known millisecond pulsar, at a nominal dispersion measure distance of 0.14 kpc, with a 30% error (Taylor & Cordes (1993)). The proximity of this pulsar means that the distance will get better as VLBI and timing parallaxes are measured. Until then the dispersion measure distance is all we have. Optical observations of the companion have been carried out by Bell et al. (1993), Bailyn (1993) and Danziger et al. (1993). Between them these three groups measured B,V,R and I magnitudes, but the only band in which the results agree is the I band. We shall adopt an apparent magnitude of I = 19.5 ± 0.2 as the synthesis of these observations. Based on the colours obtained by these various groups, we adopt the temperature range 3950 K ± 550 K for the companion.

This pulsar has a large proper motion (μ = 135 mas.yr^{-1}) (Bell et al. (1995)), which gives it a transverse velocity of 96 km.s^{-1} at 150 pc. This affects the spin-down rate, leading to a kinematically corrected spin-down age of 2.9 - 8.4 Gyr, depending on the distance to the pulsar. Given the above distances we can find the absolute magnitude required, namely M_I= 13.85 ± 0.65. Our models must satisfy both the temperature and magnitude requirements. We see that we can find consistent solutions for all masses 0.15-0.45 $M_\odot$ models as shown in Figure 4.1. These models are for a Hydrogen envelope of $3 \times 10^{-4} M_\odot$ (thick Hydrogen envelope in the terminology of paper I). Similar analysis with thin Hydrogen envelope models ($10^{-6} M_\odot$) yields similar answers, with cooling ages $\sim$ 0.3 Gyr smaller on average. Better distance determinations should allow us to constrain the mass range. The cooling age is thus constrained to lie in the range 2.2-10.7 Gyr, depending on the companion's total mass and Hydrogen envelope mass.

Further timing measurements by Anderson et al. (1996, in preparation) have detected a rate of change in the orbital timing delay x = a sin i, which they interpret as a change in the inclination angle. Assuming that this is the result of the known proper motion, this implies a lower limit to the inclination angle (i < 30°) and a new lower limit to the mass of the companion, M > 0.3 $M_\odot$. This is consistent with our cooling models.

If we assume we know the braking index of the pulsar (the default assumption is n=3, the value for magnetic dipole radiation), then we may compare the lowest allowed cooling age with the timing age to get an upper limit on the initial spin period. For pulsar J0437-4715,

the proximity and large proper motion mean that the Shklovskii correction is very important for this comparison. For each possible value of the distance, this distance-dependant term yields a value for the timing age. Similarly, each different distance leads to a different inferred absolute magnitude. Thus, t_P may be plotted as a function of M_I in Figure 4.1. If we are conservative and adopt the dispersion measure distance limits, allow all masses and take n=3, we obtain an upper limit on the initial period of $P_0 < 0.828$ P or $P_0 <$ 4.9 ms. However, the mass limit $M > 0.3M_\odot$ is just barely consistent with an n=3 t_P (within the error resulting from the uncertainty in the apparent magnitude). Future distance determinations may allow us to constrain the braking index of J0437-4715. We also note that $M > 0.3M_\odot$ requires that the distance be less 161 pc for the cooling models to be consistent with the I magnitude used here.

For completeness we have also compared the observations with the Carbon/Oxygen models of Wood (1992). For J0437-4715, we find that consistent solutions may be obtained for C/O models with a mass fraction $\sim 10^{-4}$ of surface Hydrogen and M = 0.5 - 0.55 $M_\odot$. The cooling ages allowed by this are 5.6-5.9 Gyr, although again it requires a braking index ~ 2.

4.3.2 PSR J1713+0747

Lundgren et al. (1996b) have measured V=26.0 $\pm$ 0.2 and I=24.1 $\pm$ 0.1 for this companion. This yields a conservative temperature estimate of 3450 $\pm$ 350 K. Given the pulsar distance of 1.1 kpc, we use this temperature and the absolute I magnitude $M_I = 13.9 \pm 0.5$, where the error is dominated by the distance uncertainty. The spin-down age for this pulsar is 9.0(2) Gyr, including the correction for proper motion.

We can find acceptable solutions for all masses from 0.15-0.31 $M_\odot$ with a thick H envelope and for all masses below 0.27 $M_\odot$ for a thin H envelope. However, the mass function for this system restricts the companion mass to be $\geq 0.28M_\odot$, so that many of these solutions are excluded. If we keep only those models with masses greater than 0.28, then the cooling age must lie in the range 6.3-8.0 Gyr. Figure 4.2 shows the range of acceptable solutions. If we assume an n=3 braking index, we may constrain the initial period to lie in the range $1.4 < P_0 < 2.6$ ms. To be conservative we also consider the effects of n=2. This leads to a more conservative upper limit of 3.0 ms, so that we have $2.5 < P_0 < 3.0$ ms for n=2. The upper mass limit of 0.31 $M_\odot$ on the companion implies a neutron star mass less than 1.63

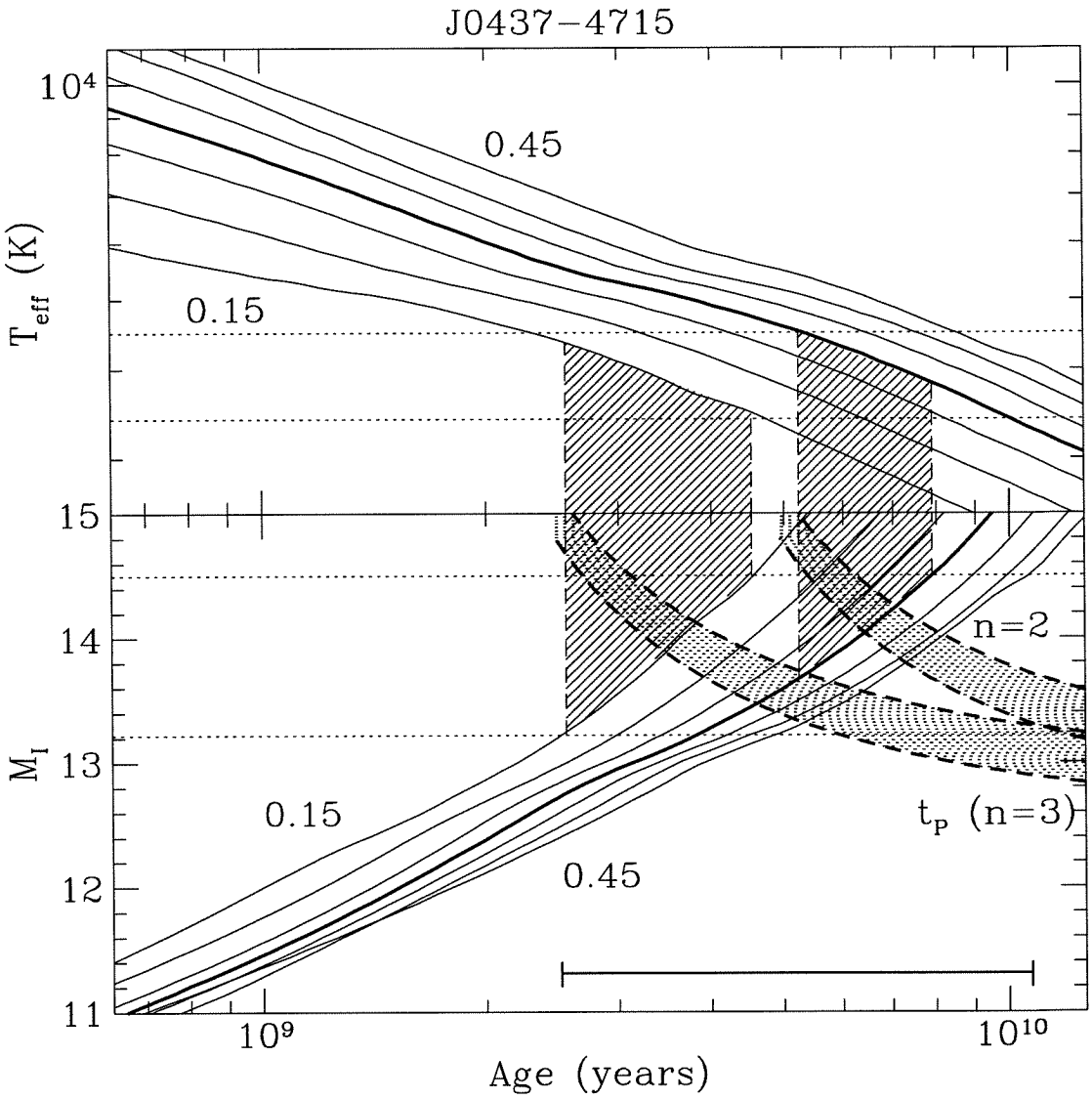

Figure 4.1: **J0437-4715:** We show the effective temperature and absolute I magnitude as a function of age for cooling sequences of mass 0.15 to 0.45 $M_\odot$, in steps of 0.05 $M_\odot$. The heavy solid line is the 0.30 $M_\odot$ model. The horizontal dotted lines in the upper panel indicate the allowed range of T_{eff}. In the lower panel, the dotted lines indicate the allowed range in absolute magnitude from the observations. In order for a solution to be consistent, it must satisfy both observational criteria. The vertical shaded regions indicate two consistent solutions. Given the apparent I magnitude, each absolute magnitude corresponds to a different distance, and hence a different spin-down age (once corrected for the Shklovskii term). This is shown by the heavy dashed lines and the lightly shaded regions, corresponding to spin-down indices of n = 2 and 3. The width of these regions are due to the 0.2 magnitude uncertainty in m_I. The models shown here are for the Thick Hydrogen layer models (as defined in Chapter 3).

$M_\odot$.

We can find no consistent C/O solutions for this object.

4.3.3 PSR J1640+2224

Lundgren et al. (1996b) have also detected the companion in this system, with V=26.0 $\pm$ 0.3 and I=24.6 $\pm$ 0.2, yielding $T_{eff} = 4200 \pm 600$ K. The spin-down age for this system is at least 17 Gyr and the distance 1.2 kpc, so that (including distance errors) we have an absolute I magnitude I = 14.2 $\pm$ 0.5. Once again, the mass function of this system requires the companion to be more massive than 0.252.

Figure 4.3 shows that we obtain consistent solutions for all masses 0.25-0.45 $M_\odot$. The range of cooling ages obtained is 4.0-11.8 Gyr, including both thick and thin Hydrogen envelopes. The extremely low $\dot{P}$ of this pulsar means the t_P is both large and sensitive to $V_\perp$. A transverse velocity of 100 km.s^{-1} at the dispersion measure distance of 1.2 kpc leads to a corrected spin-down age of 1058 Gyr! Thus, we can only obtain a lower limit on the initial period by taking the smallest spin-down age and largest cooling age, yielding $P_0 > 1.8$ ms.

We also find consistent C/O solutions for 0.5-0.8 $M_\odot$ and cooling ages 4.6-8.2 Gyr.

4.3.4 PSR J1012+5307

Even without the benefit of a detailed model, the companion of this system is obviously much brighter than it should be if the system were truly as old as the pulsar spin-down age of 5.7 Gyrs (Lorimer et al. (1995a))[2]. The system is also closer than average at a distance of 0.52 kpc, thus making it an ideal candidate for more detailed study. van Kerkwijk, Bergeron and Kulkarni (1996) have determined the effective temperature and gravity using the spectroscopic analysis of Bergeron et al. (1991). The star has log g = 6.75 $\pm$ 0.07 and $T_{eff} = 8550 \pm 25$ K. Furthermore, we can use the photometry of Lorimer et al. (1995a) to infer an absolute magnitude. Combining these three data in Figure 4.4 we find that we can obtain consistent solutions for both thick and thin Hydrogen atmospheres.

Using our mass-radius relations from Chapter 3, we can determine that the mass limits on the companion are 0.195-0.215 $M_\odot$ for a thick Hydrogen envelope and 0.165-0.183 $M_\odot$

[2]The spin-down age could be even larger if the pulsar has a significant transverse velocity. $V_\perp$ = 100 km.s^{-1} would increase t_p to 20.6 Gyr!

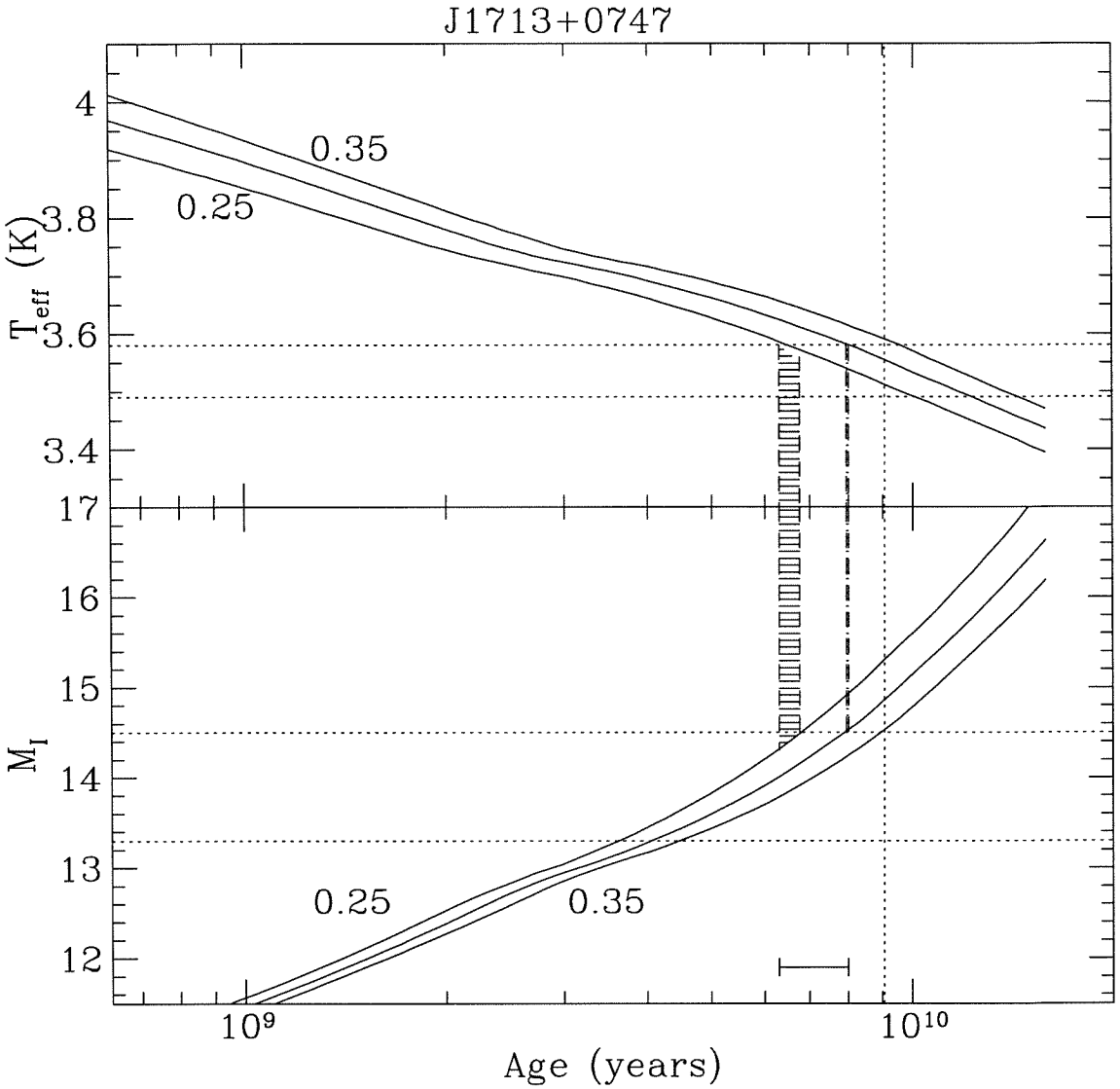

Figure 4.2: **J1713+0747:** We show the effective temperature and absolute I magnitude as a function of age for cooling sequences of mass 0.25, 0.30 and 0.35 $M_\odot$ respectively. The horizontal dotted lines in the upper panel indicate the allowed range of T_{eff}. In the lower panel, the dotted lines indicate the allowed range in absolute magnitude from the observations. In order for a solution to be consistent, it must satisfy both observational criteria. The shaded regions indicate for which ages and which masses we can find a consistent solution. The vertical dotted line indicates the spin-down age for this pulsar (for n=3). The models shown here are for the Thick Hydrogen layer models (as defined in Chapter 3).

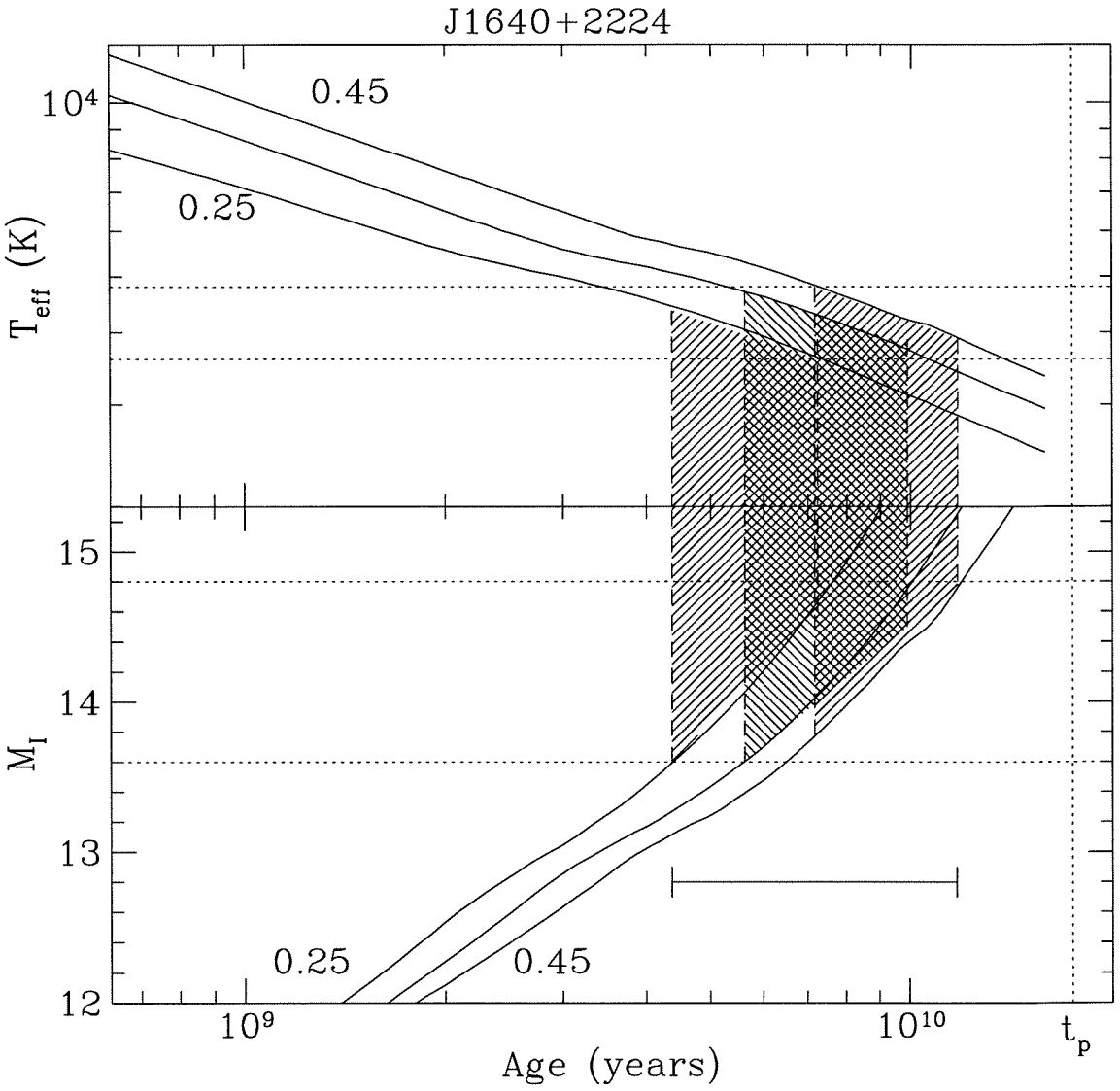

Figure 4.3: **J1640+2224:** In this case, we see that we get consistent solutions for all three sequences, 0.25, 0.35 and 0.45 $M_\odot$.

for a thin Hydrogen envelope. The corresponding cooling ages are thus 0.18-0.4 Gyr and $\leq$ 0.23 Gyr respectively. Thus, our combined result for the PSR J1012+5307 companion is that M $\sim 0.165 - 0.215 M_{\odot}$ and the age is 0.3 - 0.7 Gyr.

van Kerkwijk et al. (1996) have also measured the radial velocity of the companion, making this a double lined spectroscopic binary. This allows us to calculate the mass ratio of the two components. Thus, using the companion mass range derived above, we can constrain the neutron star mass to be $M_{NS} = 2.05 - 2.93\, M_{\odot}$, as is shown in Figure 4.5.

Alberts et al. (1996) have determined that a 0.185 $M_{\odot}$ white dwarf burning $\sim 2 \times 10^{-3} M_{\odot}$ of Hydrogen can have the correct gravity and effective temperature at a cooling age commensurate with the pulsar's timing age (although, as noted above, the timing age could increase further). Their solar metallicity model does not undergo shell flashes and constitutes this decade's installment in the conflict between the calculations of Webbink (1975) and Iben and Tutukov (1986)! An examination of Figure 1 and Table 1 of Iben and Tutukov (1986) (henceforth IT) suggests that the $>$ 50 yr timesteps used by Alberts et al. may still not be enough to resolve the shell flash behaviour reported in IT. The shell flash results in the burning of much of the surface Hydrogen, which leads to the difference in surface Hydrogen masses that is the source of the different cooling ages.

Since this mass limit has profound implications for some nuclear equations of state, we need to test the uncertainties of the white dwarf mass-radius relation to provide a solid foundation for our conclusions. In order for a 1.4 $M_{\odot}$ neutron star to be consistent with all the observational evidence, we need to obtain a consistent cooling solution for a 0.11 $M_{\odot}$ white dwarf (see Figure 4.5). The standard 'thick' and 'thin' Hydrogen envelope white dwarf models have effective temperatures that are too low by the time the gravity is in the observed range. To increase the gravity at the desired effective temperature, we may reduce the Hydrogen layer mass still further. However, in this case the convection zone dredges up Helium, reducing the Hydrogen mass fraction in the photosphere. Bergeron et al. (1991) have demonstrated that the presence of undetected neutral Helium in the photosphere can change the gravity inferred from the Balmer line shapes. Furthermore, Reid (1996) has shown that the masses inferred from the line shapes can differ substantially from those inferred from gravitational redshifts for cooler atmospheres ($T_{eff} < 12000$ K). Thus we have to apply a correction to the gravity if our atmosphere contains Helium. If we extrapolate the results of Bergeron et al. to lower gravities, we can obtain satisfactory

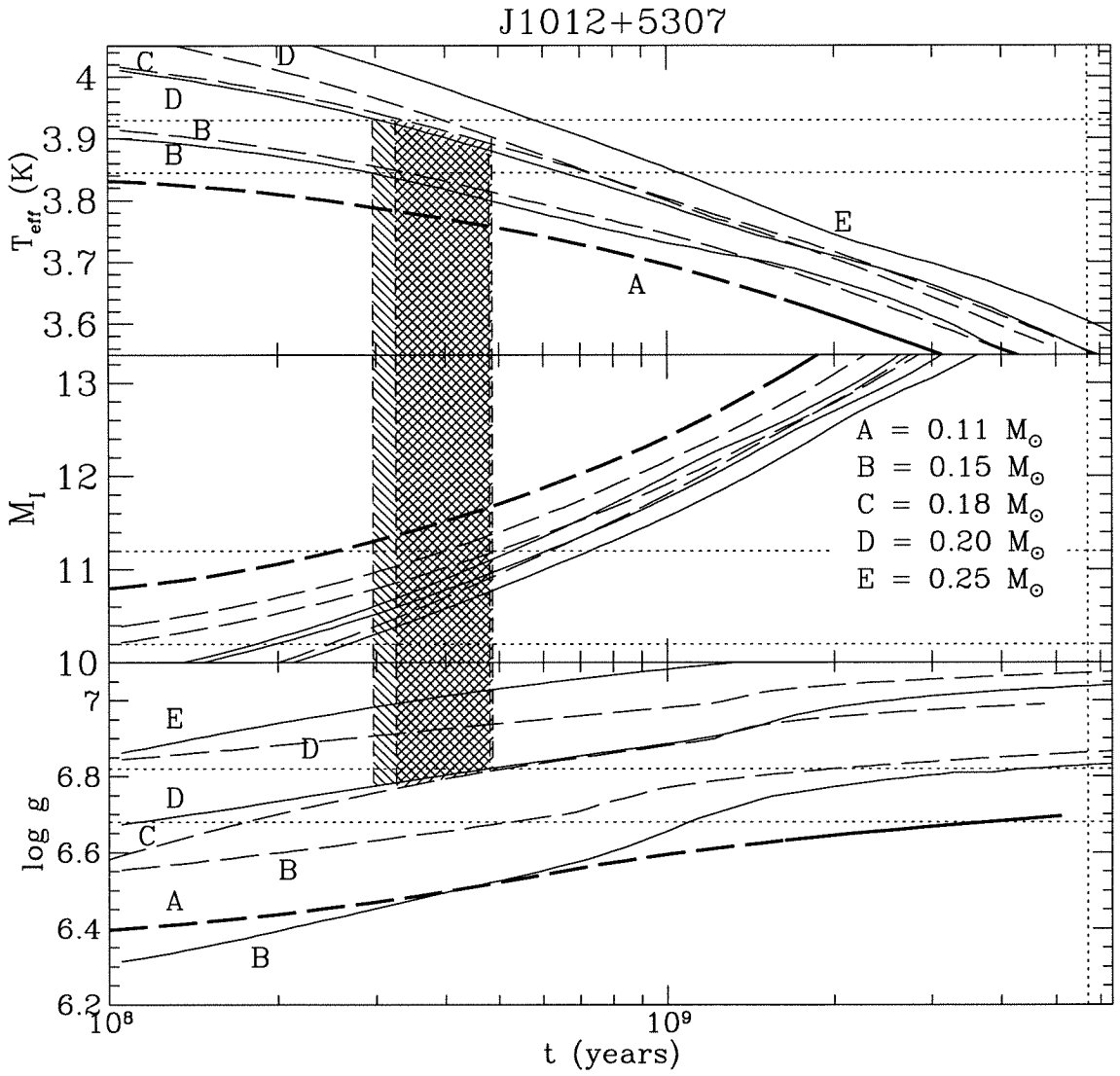

Figure 4.4: **J1012+5307:** Here we use the effective temperature, luminosity and gravity to constrain the age and mass of the white dwarf companion. The solid lines are models with a thick Hydrogen atmosphere and masses 0.15, 0.20 and 0.25 $M_\odot$ respectively. The long dashed curves are for models with a thin Hydrogen envelope and masses 0.15, 0.18 and 0.20 $M_\odot$. We show consistent solutions for the 0.20 thick H model and 0.18 thin H model, both yielding ages significantly younger than the spin down age, shown by the vertical dotted line at the far right. The heavy dashed line indicates the 0.11 $M_\odot$ model. We see that the effective temperature is too low by the time the (uncorrected for Helium) gravity is in the correct range.

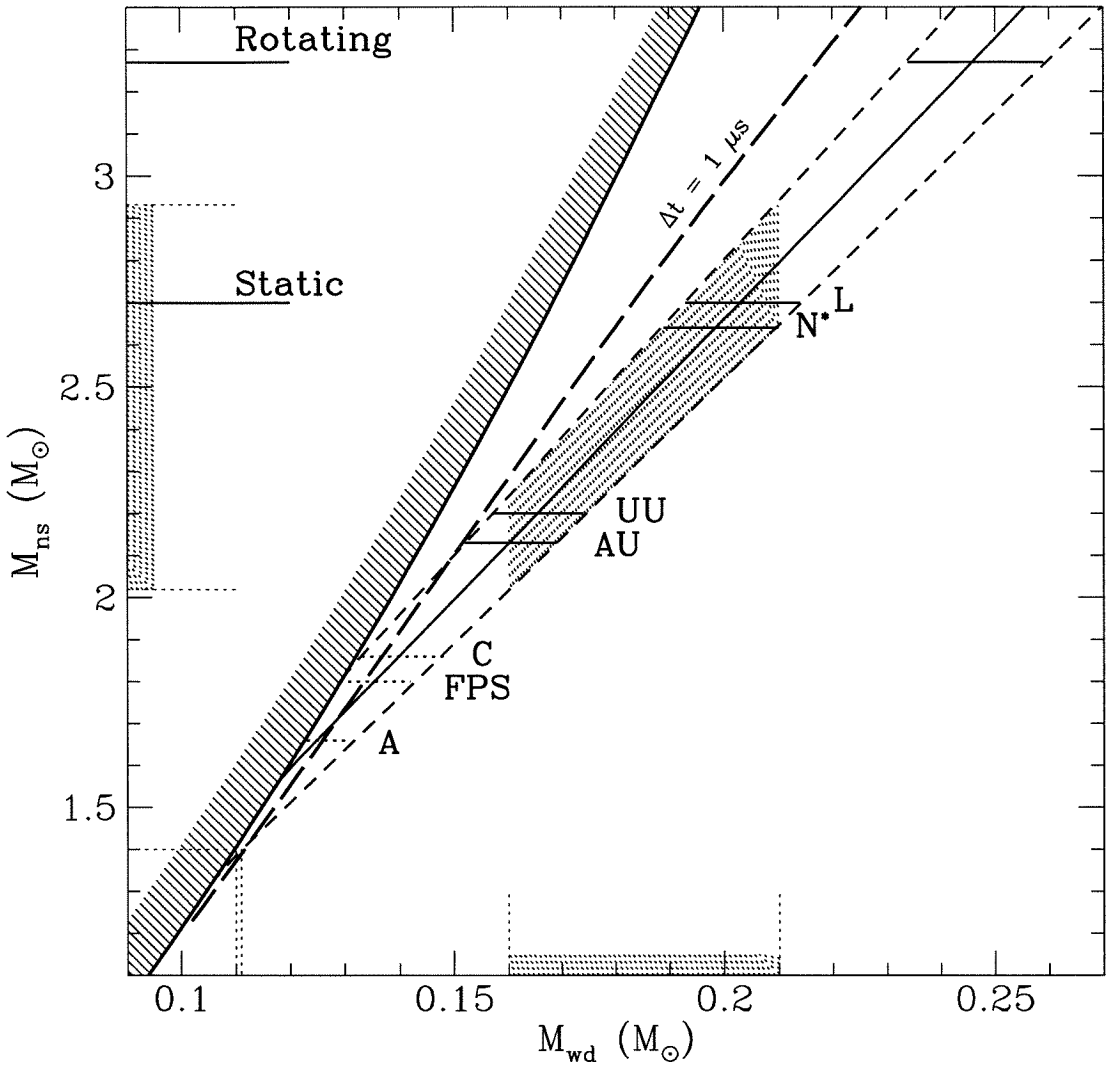

Figure 4.5: **Equation of State Constraints from J1012+5307:** The heavy solid line represents the limit from the mass function f(M) measured from the pulsar timing. The diagonal dashed lines enclose the limit based on the mass ratio determined from the companion radial velocity. The shaded parts indicate the values allowed by the combination of the spectroscopic gravity and mass radius relation. The labels Rotating and Static denote the maximum neutron star masses allowed for maximally rotating stars and maximum static mass stars respectively. The labelled horizontal lines represent the maximum static masses for the different equations of state, labelled as in Cook et al.(1995). We see that the C, FPS and A equations of state are ruled out (as well as the B,D,E,F,G,M and UT equations of state which are not shown). For a standard 1.4 $M_\odot$ neutron star to be consistent with the observations, the companion would have to have a mass of 0.11 $M_\odot$, which is consistent with our models only for absurdly young ages. The thick long-dashed line indicates the combination of masses which will yield a relativistic time delay signal of amplitude 1 μs in the timing residuals.

fits to the observations for a 0.11 $M_\odot$ white dwarf with a very thin Hydrogen envelope ($\sim 10^{-6} - 10^{-7} M_\odot$) and with appropriate corrections for Helium content, but only for improbably young white dwarfs (for ages $\sim 10^5 - 10^6$ years). Furthermore, at such young ages our models are still strongly influenced by initial conditions. Hence we cannot claim an unambiguous solution. Only a detailed evolutionary calculation of such a system can truly determine whether such a young star can fit the observations. Nevertheless, we can assert that such a solution would require an implausibly young age for the system. A possible way to verify this solution, independent of white dwarf physics, is to measure the relativistic time delay from the pulsar timing. Figure 4.5 shows that a 1.4 $M_\odot$ neutron star solution would have to be very close to edge-on. With orbital eccentricity $< 2 \times 10^{-5}$, we may approximate the expression for the amplitude of the time delay signal as (using equation (2.20) from Blandford & Teukolsky (1976)),

$$\Delta t = 4.94 \mu s \left(\frac{M_{wd}}{M_\odot}\right) \log\left[\frac{1}{1 - \sin i}\right]. \tag{4.7}$$

Figure 4.5 shows the relation between M_{wd} and M_{ns} for a timing residual of $1\mu s$. We see that if this measurement is possible, it would clearly differentiate between a massive neutron star and a canonical 1.4 $M_\odot$ neutron star.

There are two possible systematic uncertainties in the equation of state that may also conceivably change the solution. The first is the treatment of the Hydrogen/Helium plasma in the region $\rho \sim 0.1 - 1\,g.cm^{-3}$ and $T \sim 10^4 - 10^5$ K. In this part of the phase diagram, the plasma is partially degenerate and partially ionized. No published equation of state provides a detailed microphysical description of the plasma in this region. Rather, various procedures are used to interpolate between the high and low density regions where the microphysics is better understood. Saumon et al. (1995) estimate (based on intercomparisons of the different available treatments) that the pressure-density relation could be uncertain to within a factor of 2 in this region. Thus, we have artificially varied the density in this region by a factor of 2 in our input equation of state to test the impact of such uncertainties on the models. For a 0.11 $M_\odot$ white dwarf, such changes do not affect the cooling in any way. The only observable effect in our models is a slight difference in the surface abundance of Helium when the first dredge-up occurs, due to the slightly different rate of descent of the bottom of the convection zone. The affected region is shown in figure 4.6. We see that

the reason this uncertain region is not crucial to the cooling is that the model atmosphere enters this part of the phase diagram only when the base of the convection zone already lies at higher densities, thus it has a minimal effect on the structure of the convection zone, which is really the only way the equation of state can have an effect in the outer layers. Our deep convection region maintains a constant entropy to an accuracy of 1 %, even through the uncertain region.

A second possible influence on the mass-radius relation is changes in the high density equation of state, changing the central structure of the star and thus the radius. Our equation of state calculation uses the Saumon et al. (1995) results supplemented by a Thomas-Fermi model at densities above the limits of the aforementioned table. Salpeter (1961) discusses the various order corrections to the degenerate equation of state at length. The next order effect beyond the Thomas-Fermi (non-uniform electron distribution) correction is the exchange energy correction. However, at central densities of $10^5\,\mathrm{g.cm^{-3}}$ this is a 2% change in the internal energy and a similar variation in the pressure. Thus it is unlikely that this could cause any significant variation. Further corrections could arise when the central ions form a crystal lattice, but this will not occur in a Hubble time for Helium cores.

Hence, we claim the observations of the white dwarf companion to PSR J1012+5307 constrain the neutron star mass to be in the range 2.05 - 2.93 $M_\odot$. The age of the current binary incarnation is also constrained to be less than 0.7 Gyr. Allowing for a braking index of n=2-3, this results in the constraint $P_0 > 4.9$ ms. Given the above uncertainties about the gravity measurement, it is useful to calculate the constraints without using the gravity. If we use only the magnitude and temperature, then the white dwarf mass is constrained to lie in the range 0.12 - 0.32 $M_\odot$, and the age is < 0.8 Gyr. Thus, this pulsar is still much younger than the pulsar spin-down age.

4.3.5 PSR B0820+02

The pulsar in this system has the longest spin-period (864.8 ms), largest magnetic field ($10^{11.5}$G) and shortest spin-down time (0.13 Gyr)[3] of all the low mass binary pulsars. The companion has been studied optically by Kulkarni (1986) and Koester et al. (1992). We shall use the Koester et al. apparent magnitude V=22.76 $\pm$ 0.05. van Kerkwijk &

[3]Recall that these are not independent quantities!

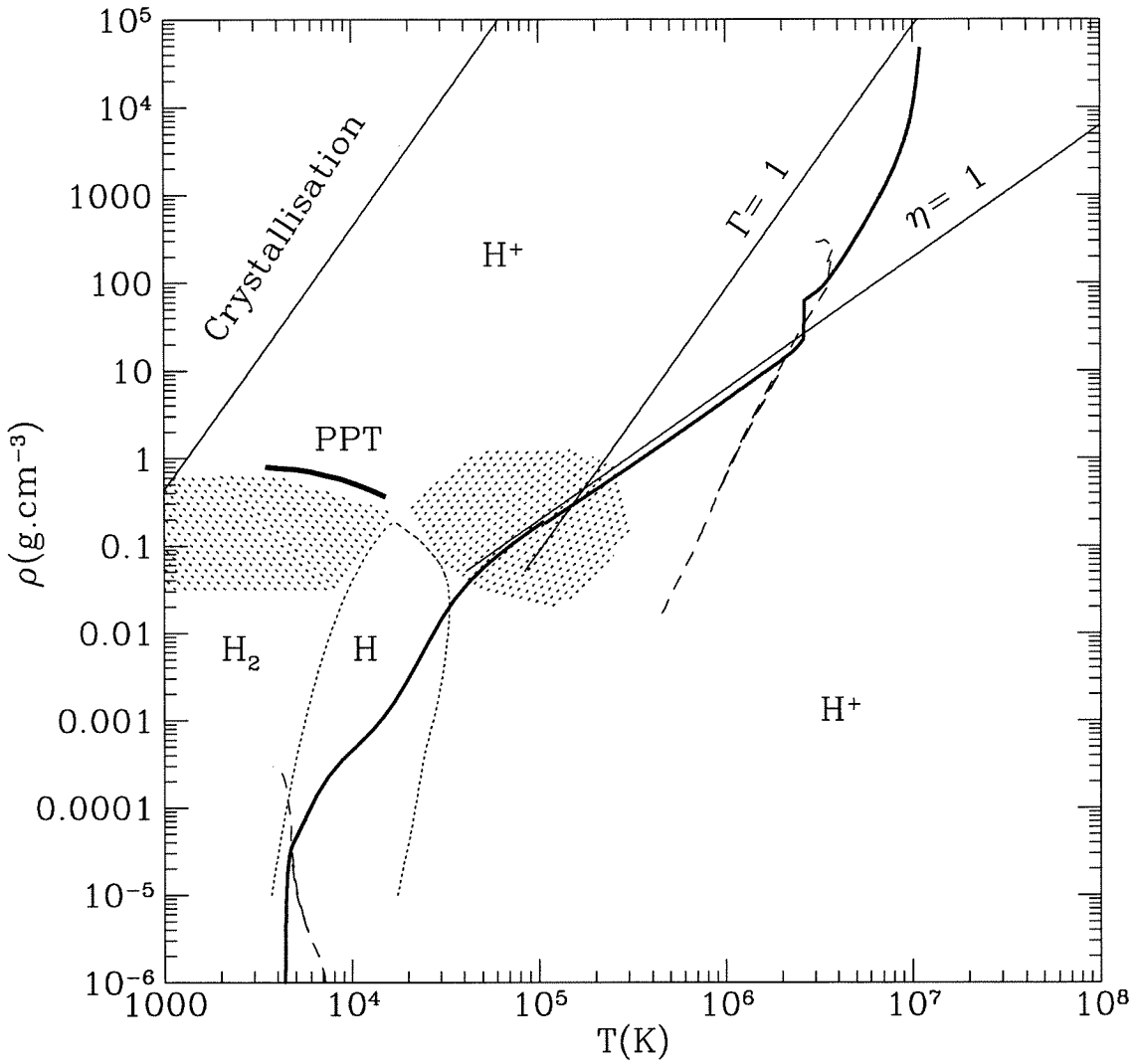

Figure 4.6: **Uncertainties in the Equation of State:** The Hydrogen phase diagram shown here indicates the two shaded regions where the equation of state calculations are most uncertain. The leftmost region is the region where three-body interactions (not included in the opacity calculations) will affect the dissociation equilibrium of molecular Hydrogen. The rightmost shaded region is where the plasma is partially ionized and partially degenerate and feeling the effects of both pressure and temperature ionization. The quantities Γ and η are the Coulomb coupling and degeneracy parameters respectively and PPT indicates the Plasma Phase Transition of Saumon et al. (1995) (and references therein). The dashed lines indicate the upper and lower boundaries of the convection region for a 0.11 $M_\odot$ white dwarf with $10^{-4} M_\odot$ of Hydrogen on the surface. The heavy solid line is the stellar model for such a star and an age of 5×10^8 years.

Kulkarni (1995) have also identified Hydrogen balmer lines in the companion spectrum, yielding an effective temperature consistent with the photometric temperature estimate of 15250 ± 1250 K by Koester et al.. The signal to noise ratio is not yet good enough to determine a spectroscopic gravity.

The dispersion measure distance to this pulsar is 1.4 ± 0.4 kpc. This yields an absolute V magnitude $M_V = 12.0 \pm 0.5$. This leads to a problem when we try to find consistent temperature-luminosity solutions for this pulsar. As shown in Figure 4.7, the effective temperature constraints imply much higher luminosities than observed for all models, both Helium core and Carbon-core. A solution to this problem would be for the true distance to be larger than the dispersion measure distance. If we use the additional constraint that we expect the spin-down age to be an upper limit to the true age, then we can place some constraints on the acceptable models using only the temperature constraints and infer what the true distance would have to be for a consistent solution.

If we assume a Helium core white dwarf (allowing for n=3 and n=2), then the mass is limited to the range 0.27-0.42 $M_\odot$, and the true distance has to be $\sim$ 3.5 - 4.5 kpc! If we assume a Carbon core white dwarf, the mass range is 0.4-0.8 $M_\odot$, with a true distance of $\sim$ 2 - 2.8 kpc. This is probably the more palatable of the two options, which would make this the fourth binary pulsar to contain a 'normal' white dwarf, and the first of those to have not undergone significant inspiral during its evolution. We note that Koester et al. (1992) also infer a distance range of 1.7-3 kpc based on a similar analysis (although their final published solution is 1.7-1.9 kpc, based on the supposed allowed error in the dispersion measure). The determination of a spectroscopic gravity for this star should answer the question conclusively, as the Helium dwarfs should have log g $\sim$ 7.05 and the Carbon dwarfs should have log g $\sim$ 7.8.

4.3.6 PSR J0034-0534

The spin-down age is 4.5 ± 0.4 Gyr and the distance is 1.0 ± 0.3 kpc. The proper motion of this pulsar is not known. However, if the pulsar had a transverse velocity of 100 km.s^{-1}, the spin-down age would be 6.5 Gyr, so we adopt this as a conservative upper limit to the spin-down age. Lundgren et al. (1996b) have detected this companion at $I = 24.8 \pm 0.3$ and set a limit of $V > 26.8$, which implies that the temperature < 3600 K. This is sufficient to constrain the ages of cooling models of various masses (see Figure 4.8) to lie within the

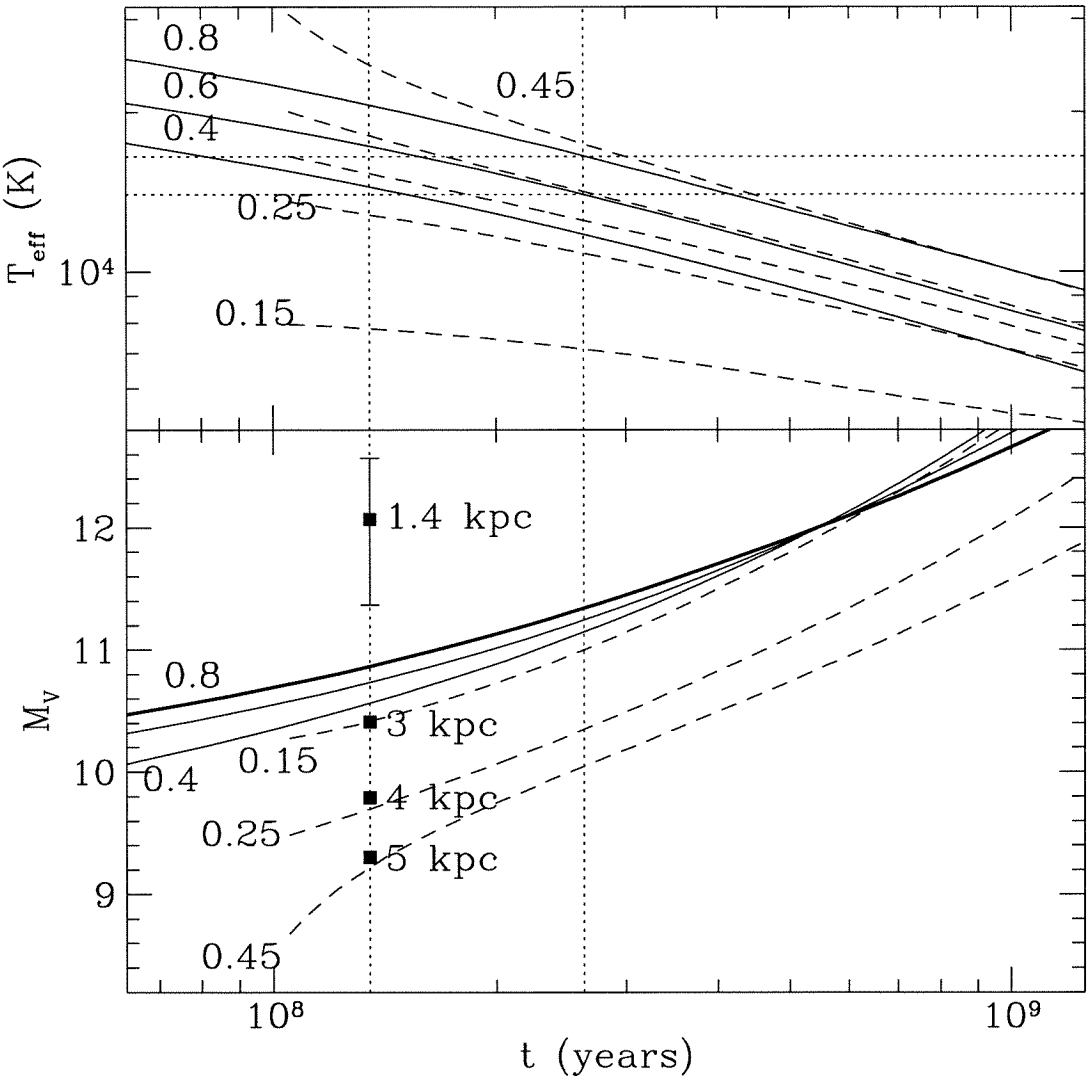

Figure 4.7: **B0820+02:** The dashed curves are the models for Helium white dwarfs, while the solid curves are for carbon core white dwarfs. The vertical dotted lines indicates the spin-down age of the pulsar for n=3 (lower value) and n=2. In the bottom panel we show the absolute magnitude for the dispersion measure distance as well as for several other assumed distances, to demonstrate the effect such distance errors have on the comparison.

range 4.1 - 15 Gyr. However, if we require that the cooling age be less than the spin-down age (using our upper limit of 6.5 Gyr), then the mass range is 0.15 - 0.21 $M_\odot$ (assuming n=3). If we allow n=2, then the mass is 0.15 - 0.35 $M_\odot$. Thus we get a range of cooling ages of 4.1 - 13 Gyr. This leads to a conservative upper limit on the initial period of $P_0 < 1.3$ ms (using n=2 and assuming a 100 km.s^{-1} transverse velocity). A measurement of the proper motion for this pulsar would provide a useful constraint on the initial period, although it will not prove to be a useful constraint on the nuclear equation of state unless the braking index can be measured (see Figure 4.9). For n=3 and $V_T = 0$, the upper limit on P_0 is 0.6 ms, which is sufficient to rule out many of the harder equations of state. However, even the hardest equation of state would survive if n=2.

4.3.7 PSR J2145-0750

For the Carbon/Oxygen-core white dwarfs, we use Wood's models (Wood (1991)), which have a more complete description of crystallization, to perform the same sort of analysis as above. For PSR J2145-0750, the spin-down age is 8.7 Gyr and the dispersion measure distance is 0.5 kpc. The minimum mass is 0.43 $M_\odot$. Optical observations by Lundgren et al. (1996b) give V = 23.7(1) and I = 23.0(1). The V-I broad band colours of Bergeron et al. (1995) yield a temperature estimate of 6500 $\pm$ 500 K.

The determination of ages and masses for the Carbon sequences requires a little care, because the cores of $M > 1\,M_\odot$ white dwarfs can begin to crystallize after $\sim$ 1 Gyr. This means that the absolute magnitude curves for different masses can cross, making the determination of consistent solutions slightly more complicated. We show the V band magnitudes for this case because the theoretical M_V curves are more dispersed than the M_I curves. Figure 4.10 shows the analysis using the Wood curves for both Carbon and Oxygen cores, Helium mass fraction = 10^{-2} and a Hydrogen mass fraction of 10^{-4}. For models with pure Helium envelopes, the age limits are similar. We find consistent models for masses $M > 1.0$ $M_\odot$ (in both C and O cases, the cores have begun to crystallize), and a range of cooling ages 3.2 - 5.2 Gyr. We note that the upper limit is uncertain to within $\sim$ 1 Gyr because the Wood models did not extend far enough and a modest extrapolation was required.

A transverse velocity of 100 km.s^{-1} would change the sign of $\dot{P}$ for this pulsar, so the spin-down age of 8.7 Gyr is only a lower limit. Using the largest cooling age, we can thus get a lower limit on the initial period $P_0 > 10.2$ ms (assuming an n=2 braking index).

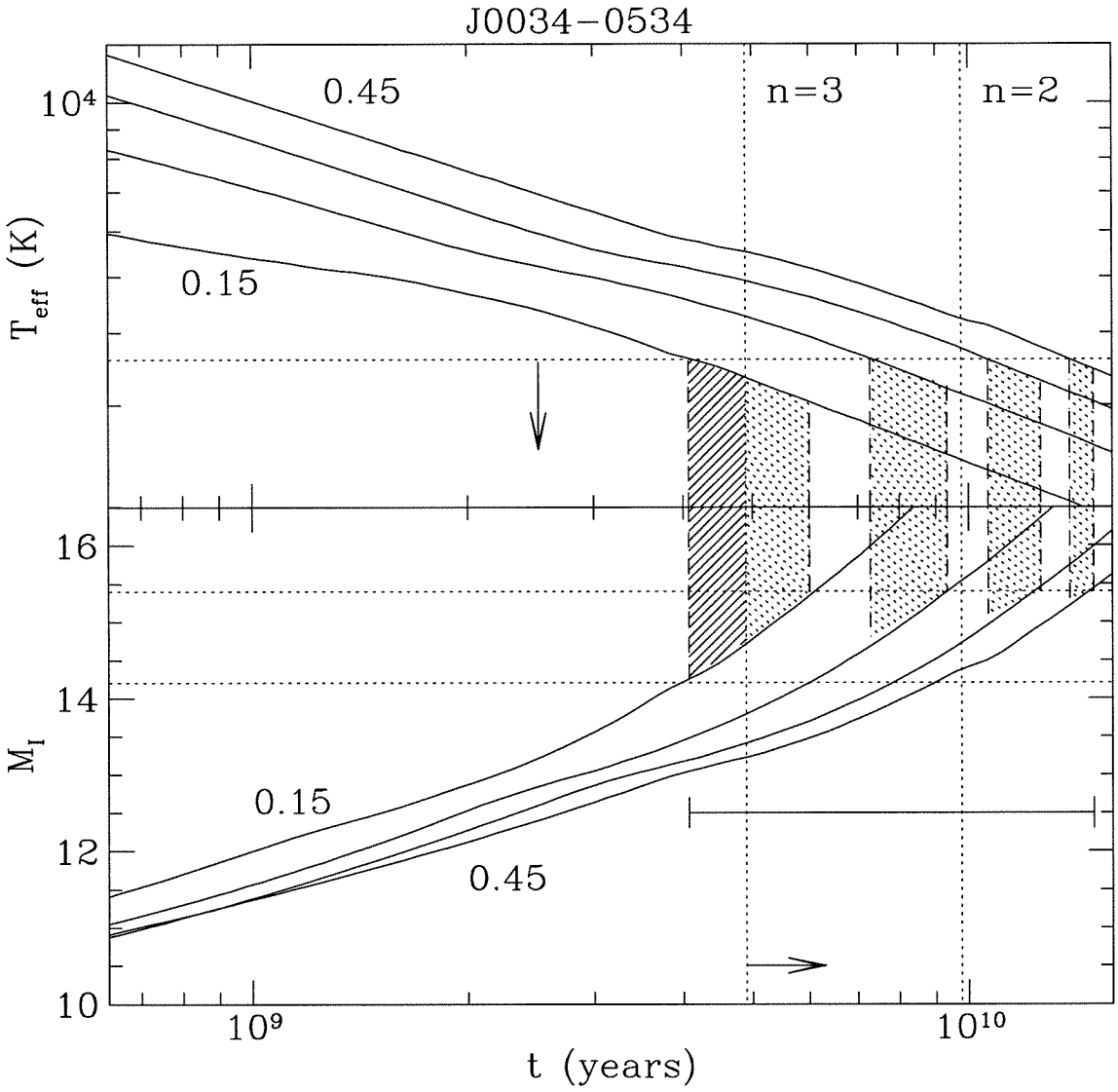

Figure 4.8: **J0034-0534:** The solid line shading indicates consistent cooling solutions that lie at ages less than the spin-down age. The dotted lines indicate cooling solutions that lie above the current spin-down age but could be made consistent if the pulsar has a substantial transverse velocity. The size of the horizontal arrow indicates the change in t_P that would result from a transverse velocity of 100 km.s^{-1}.

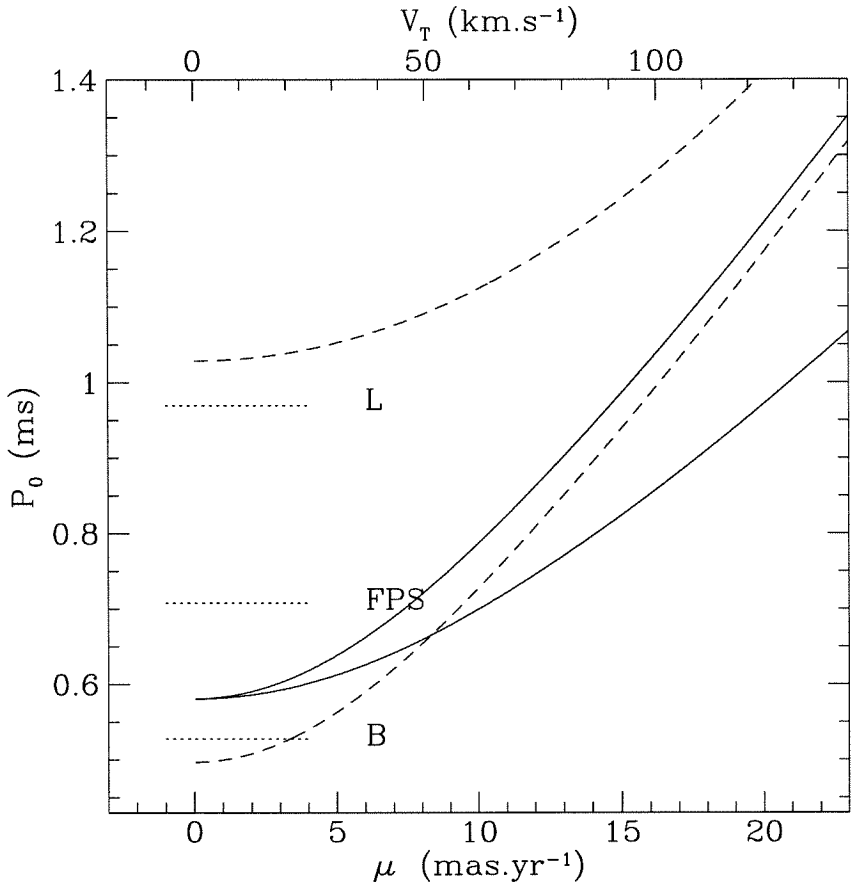

Figure 4.9: **Equation of State Constraints from the Proper motion:** The solid lines indicate P_0 for PSR J0034-0534 for the indicated proper motion and an assumed distance of 0.7 (lower curve) and 1.3 (upper curve) kpc respectively. These curves were obtained using the smallest uncorrected $\dot{P}$ allowed within the measured precision (making the upper solid curve the most conservative estimate) and n=3. The lower dashed line indicates the same data as the upper solid curve but using the best fit $\dot{P}$. The upper dashed line again uses the same data as the upper solid line except that n=2. The three horizontal dotted lines indicate the minimum periods for three representative equations of state, those of Pandharipande (1971) (B - soft), Lorenz, Ravenhall & Pethick (1993) (FPS - medium) and Pandharipande & Smith (1975) (L - hard). The minimum periods shown are those obtained by spinning up a maximum mass static model. Smaller rotation periods can be obtained for masses which don't have a stable static limit; see Cook et al. (1995).

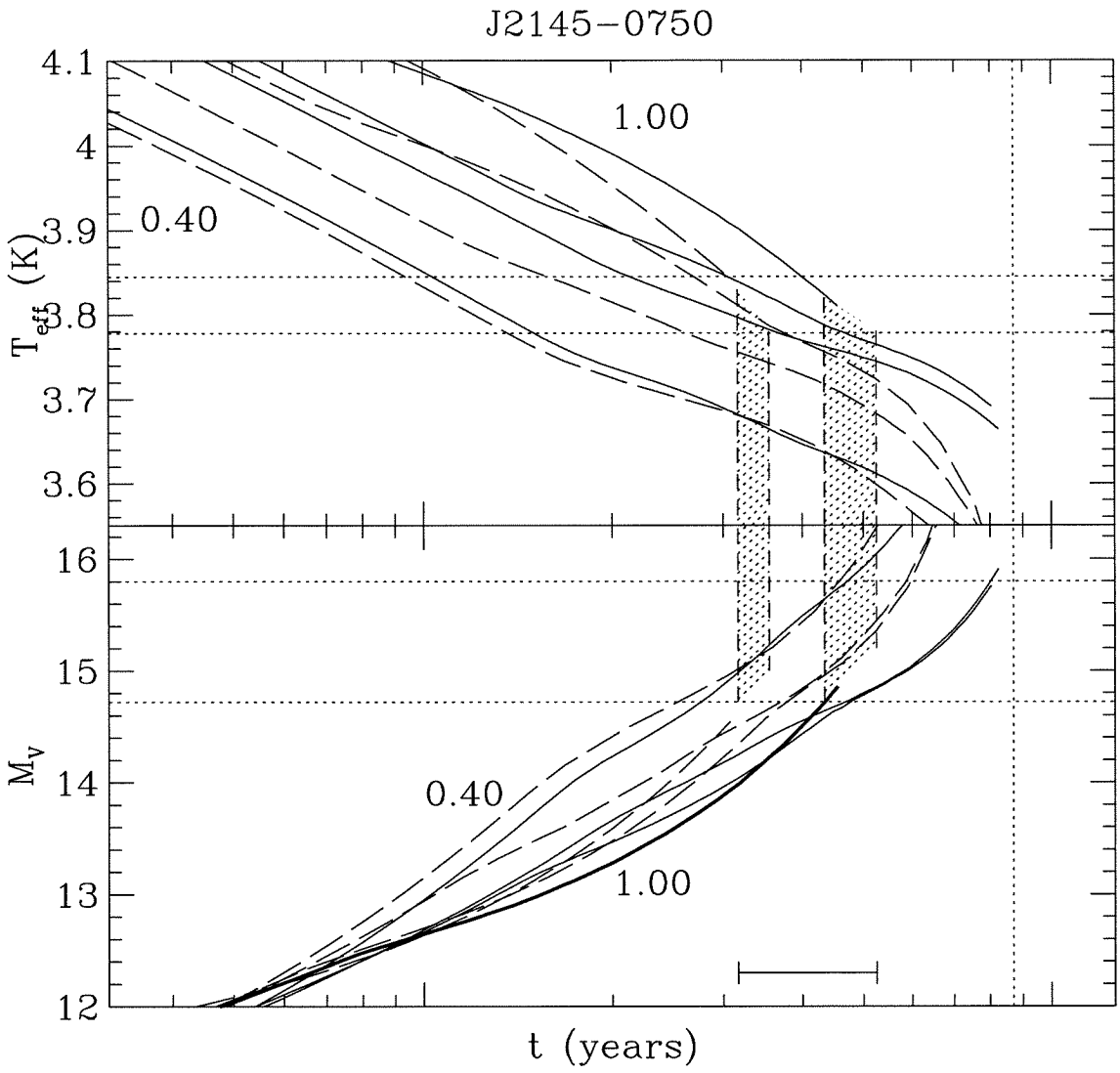

Figure 4.10: **J2145-0750:** The solid lines indicate Carbon core sequences of mass 0.4, 0.7, 0.8 and 1.0 $M_\odot$ respectively. The long dashed lines represent Oxygen core sequences of mass 0.4, 0.6, 0.8 and 1.0 respectively. The most massive models begin to crystallize after 0.8 Gyr, and the least massive after 3.6 Gyr. The shaded regions shows the consistent solution for the 1.0 $M_\odot$ C and O models. The other solutions are omitted because the crossing of the model curves means they lie largely on top of one another.

4.3.8 PSR J1022+10

This pulsar has a spin period of 16.45 ms and spin down age 5.9 Gyr (although this would be 18.3 Gyr with a 100 km.s^{-1} transverse velocity). It lies at a distance of 0.6 kpc and has been observed by Lundgren et al. (1996b), yielding V = 23.09 $\pm$ 0.04 and I = 22.665 $\pm$ 0.007. The mass function for this pulsar requires a companion of mass M > 0.72M$_\odot$, putting this firmly in the Carbon/Oxygen mass range. Our temperature estimate for this star is 8100 $\pm$ 300 K. Figure 4.11 shows our comparison of the observations with the Wood models, yielding an age range of 2.3 - 3.3 Gyr and a mass range M > 0.9M$_\odot$. Thus we obtain 10.9 < P$_0$ < 15.4 ms.

4.3.9 PSR B0655+64

This was one of the first pulsars with an optically identified companion. Upper limits on the proper motion mean that we can constrain the spin-down age to the range 4.5-13.6 Gyrs. The distance is 0.48 kpc. The mass function constrains the companion to have M $\geq$ 0.67 M$_\odot$. van Kerkwijk & Kulkarni (1995) have identified the white dwarf companion as a DQ star, i.e., it shows traces of molecular Carbon in the optical spectrum. This makes accurate temperature determination difficult but does constrain the temperature to be in the range 5500-8000 K, when the convection zone is deep enough to dredge up trace amounts of Carbon from the core and deposit them in the atmosphere. Kulkarni (1986) has measured V = 22.2 for this star. Since molecular Carbon is seen, the Helium and Hydrogen envelopes must be quite thin. We use the pure Helium envelope/Carbon core models ($q_{He} = 10^{-4}$) of Wood (1991) to calculate the cooling ages in Figure 4.12. We find solutions for all models M $\geq$ 0.7 M$_\odot$. The range of cooling ages is 2.6 - 4.8 Gyr. The largest possible timing age, the smallest possible cooling age and n=2 yield a limit on P$_0$ > 177ms.

4.3.10 PSR 2019+2425

This pulsar has one of the largest spin-down ages (corrected for proper motion) of any pulsar, ranging from 17 to 70 Gyr, depending on the rather uncertain distance. It lies close to the galactic plane, which means that extinction is an important problem. Lundgren et al. (1996) have detected the pulsar companion at V=26.4(4) and I=25.0(3). To estimate the extinction to the companion, we can find the extinction in the general direction of

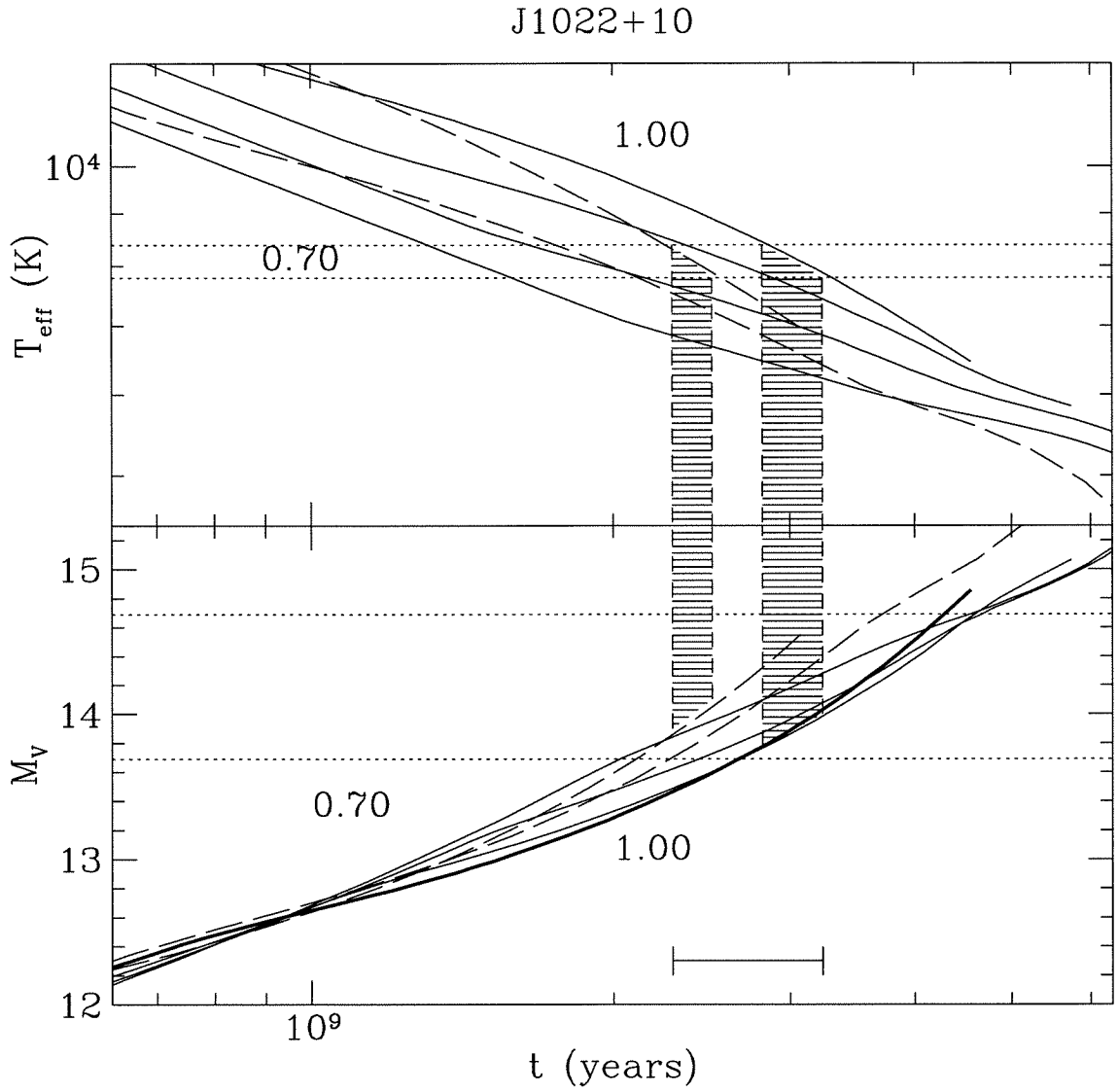

Figure 4.11: **J1022+1001:** The solid lines indicate Carbon core sequences of mass 0.7, 0.8, 0.9 and 1.0 $M_\odot$ respectively. The long dashed lines represent Oxygen core sequences of mass 0.8 and 1.0 respectively. We are able to find consistent age ranges for models greater than 0.9 $M_\odot$, spanning the range of ages from 2.3 - 3.3 Gyr.

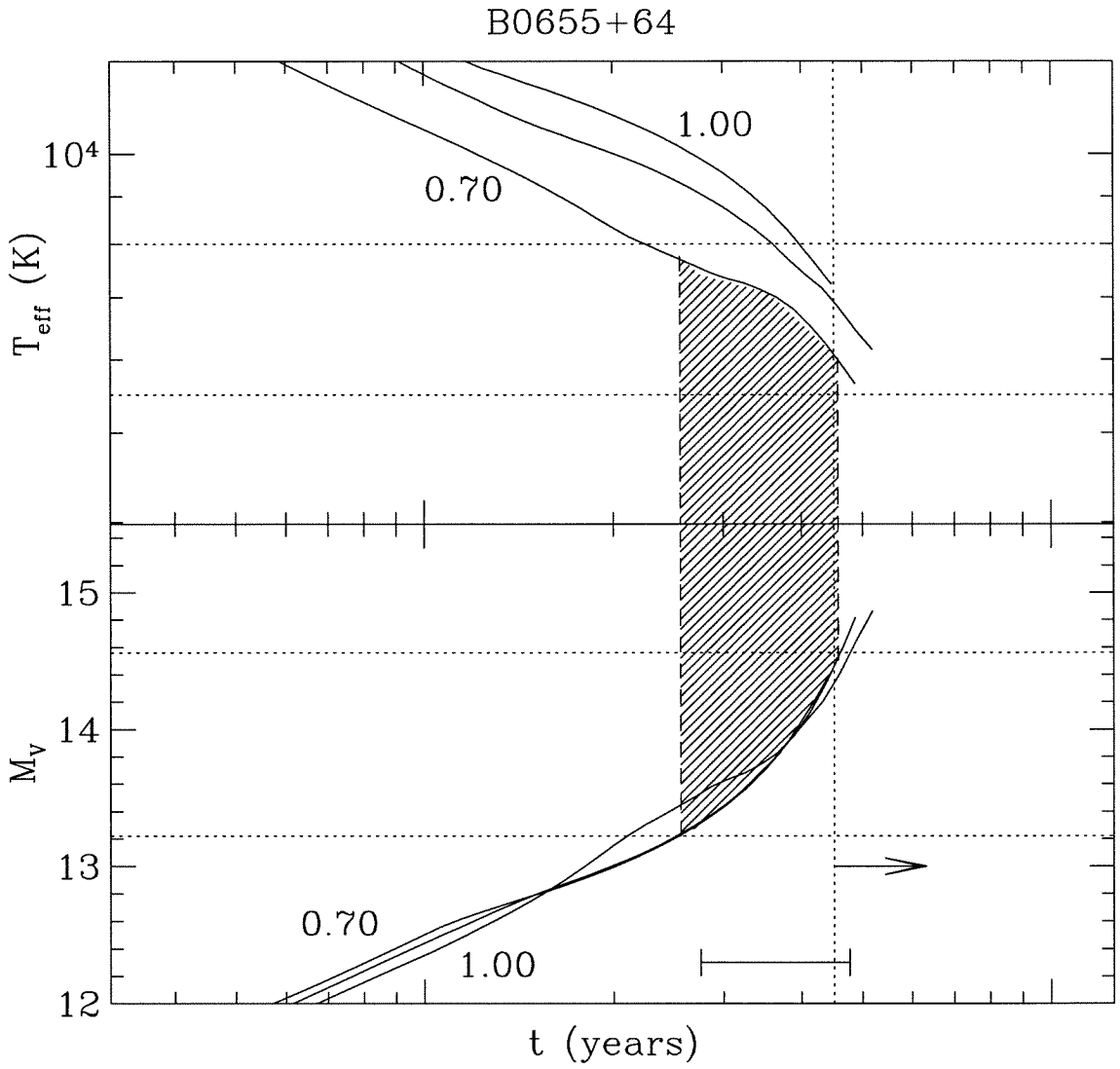

Figure 4.12: **B0655+64:** We show here the curves for 0.7-1.0 $M_\odot$ and a Helium envelope mass fraction = 10^{-4}. These models have no Hydrogen envelope. The shaded region shows the solution for 0.7 $M_\odot$.

J2019+2425 from Neckel & Klare (1980). For distances less than 1 kpc, A_V rises linearly to 0.4 magnitudes, but then rises steeply to $\sim$ 3 magnitudes at a distance of 1.5 kpc (i.e. 1.5 magnitudes for A_I). Using this extinction law and the 30% distance uncertainty, we find that V-I=1.0(4), which implies $T_{eff} \sim 4100 - 6700$ K. Similarly, we estimate the absolute I magnitude as $M_I = 14.9(10)$. A further constraint is that the mass function requires that the companion mass > 0.32 $M_\odot$.

Using these limits we find consistent solutions for all masses above the minimum allowed by the mass function. Figure 4.13 shows the solution for the 0.35 $M_\odot$ case. The approach taken here is slightly different because the allowed ranges of T_{eff} and M_I are not uncorrelated (as they are if observational error is the prime source of uncertainty). The large extinction correction implies that the allowed V-I and M_I ranges are a function of distance, as shown in 4.13. Using this approach we find a range of cooling ages from 7.6-13.9 Gyr. Although Woods models again do not extend to low enough temperatures in most cases, modest extrapolation indicates that consistent solutions may also be found with C/O models for all masses (a sample 0.6 $M_\odot$ model is shown in Figure 4.13). These models allow cooling ages < 1 Gyr, so that our most reasonable constraint on the age of the white dwarf is only an upper limit, $t_{cool} < 13.9$ Gyr.

Using these values and the range 16.7-69.8 Gyr for the spin-down age, we may derive a lower limit to the initial period of 1.6 ms for n=3 (or 2.3 ms for n=2). Despite the uncertainty in the cooling age resulting from the extinction correction, we find that this result is quite robust, primarily because the measured proper motion constrains the timing age to be significantly greater than the age of the galaxy.

4.3.11 PSRs B1855+09, J0751+1807 & J2229+2643

For those systems where we have only upper limits on the companion magnitudes, it is sometimes still possible to place some constraints on the ages and masses of the stars involved.

For PSR 1855+09, the almost 90° inclination of this orbit has allowed Kaspi et al. (1994) to determine the masses of both components as well as the parallax and distance. The companion mass is $0.258^{+0.028}_{-0.016} M_\odot$ and the distance is $0.9^{+0.4}_{-0.2}$ kpc. The spin-down age, corrected for kinematic effects, is $4.86^{+0.06}_{-0.03} \times 10^9$ kpc. We can thus restrict our model comparisons to the 0.25 $M_\odot$ model in this case. Kulkarni (1991) obtained limits of R$>$ 24.6

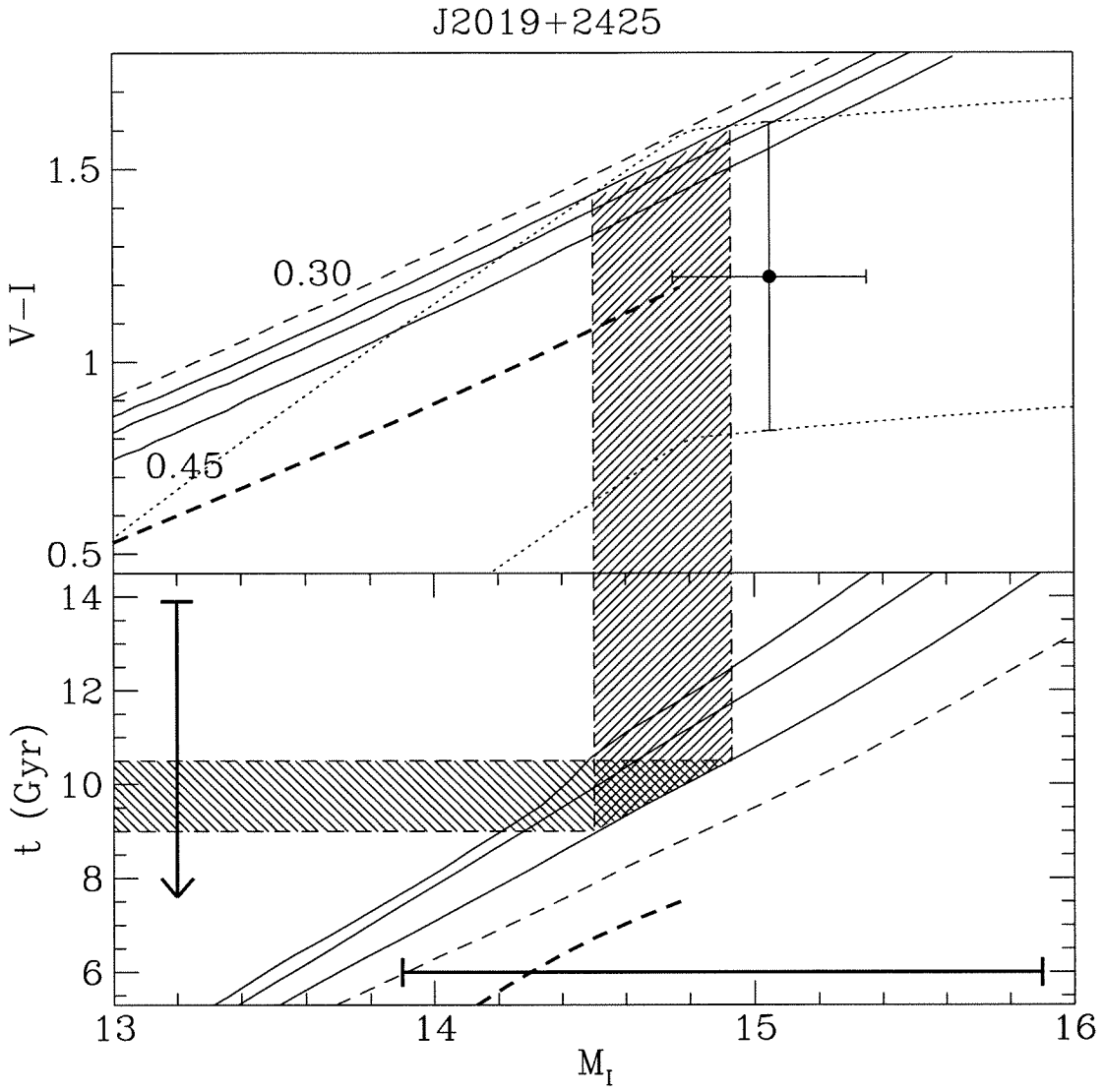

Figure 4.13: **J2019+2425:** The solid lines are the models for 0.35, 0.40 and 0.45 $M_\odot$. The thin dashed line is for a 0.30 $M_\odot$ He core model and the heavy dashed line is for a 0.60 $M_\odot$ Carbon core model. The dotted line in the upper panel indicates the allowed range of V-I for each M_I (and hence each distance). The shaded region demonstrates the consistent solution for the 0.35 $M_\odot$ model. The filled circle (with error bars) is the allowed range at the nominal dispersion measure distance. In the bottom panel the vertical and horizontal bars indicate the allowed range of cooling ages (for all models) and the expected range in M_I consistent with the dispersion measure uncertainty.

and I > 23.4, while Callanan et al (1989) obtained V> 25.4. Callanan et al. estimated the extinction to the system to be $A_V = 1.5 - 2.0$ mags/kpc. Using the extinction law of Savage and Mathis (1979), this becomes A_R=1.1-1.5 and A_I=0.7-1.0 mags/kpc. Figure 4.14 shows the comparison of the model curves with each constraint. We use two constraints, using the largest extinctions and furthest distance estimate; and the smallest extinctions and closest distance estimates, to examine the range of possible solutions. We see that the 0.25 $M_\odot$ sequence is perfectly consistent with the bounds on the absolute magnitude for all ages between the spin-down age of 4.9 Gyr to a minimum age of 0.98 Gyr. This yields a constraint $P_0 > 4.8$ ms.

Also shown in Figure 4.14 are the detection limits for the companions to J0751+1807 and J2229+2643, with spin-down ages of 6.9 and 24.9 Gyrs respectively. The only meaningful limits that can be placed on these systems is that the cooling times are longer than 0.4 and 1.7 Gyrs respectively.

The various constraints on the cooling ages are collected together in Figure 4.15

4.4 Discussion

4.4.1 Binary Evolution

The formation of low mass binary pulsars (LMBPs) has been discussed by many authors (for reviews see Phinney and Kulkarni (1994), Verbunt (1993) and references therein). If we consider a binary containing a pulsar and a stellar companion, the binary will undergo mass transfer if the non-degenerate companion begins to expand as a result of nuclear evolution or if the orbit decreases due to magnetic braking or gravitational wave radiation. This mass transfer results in the spin-up of the neutron star to form a millisecond pulsar. The mass loss also means that the companion never evolves far enough to grow a core of mass large enough to ignite Helium. Rather, the envelope is lost during the course of the evolution and the remnant of the secondary settles down to a degenerate configuration, a low mass Helium core white dwarf. The fact that giants have a well-defined relationship between core mass and giant radius, allied with the fact that the star must fill its Roche lobe to lose matter to the companion (assuming corotation), means that there exists a relationship between orbital period and secondary mass in the LMBPs (Refsdal and Weigart (1971), Joss, Rappaport and Lewis (1983), Rappaport et al. (1993)). However, this holds only

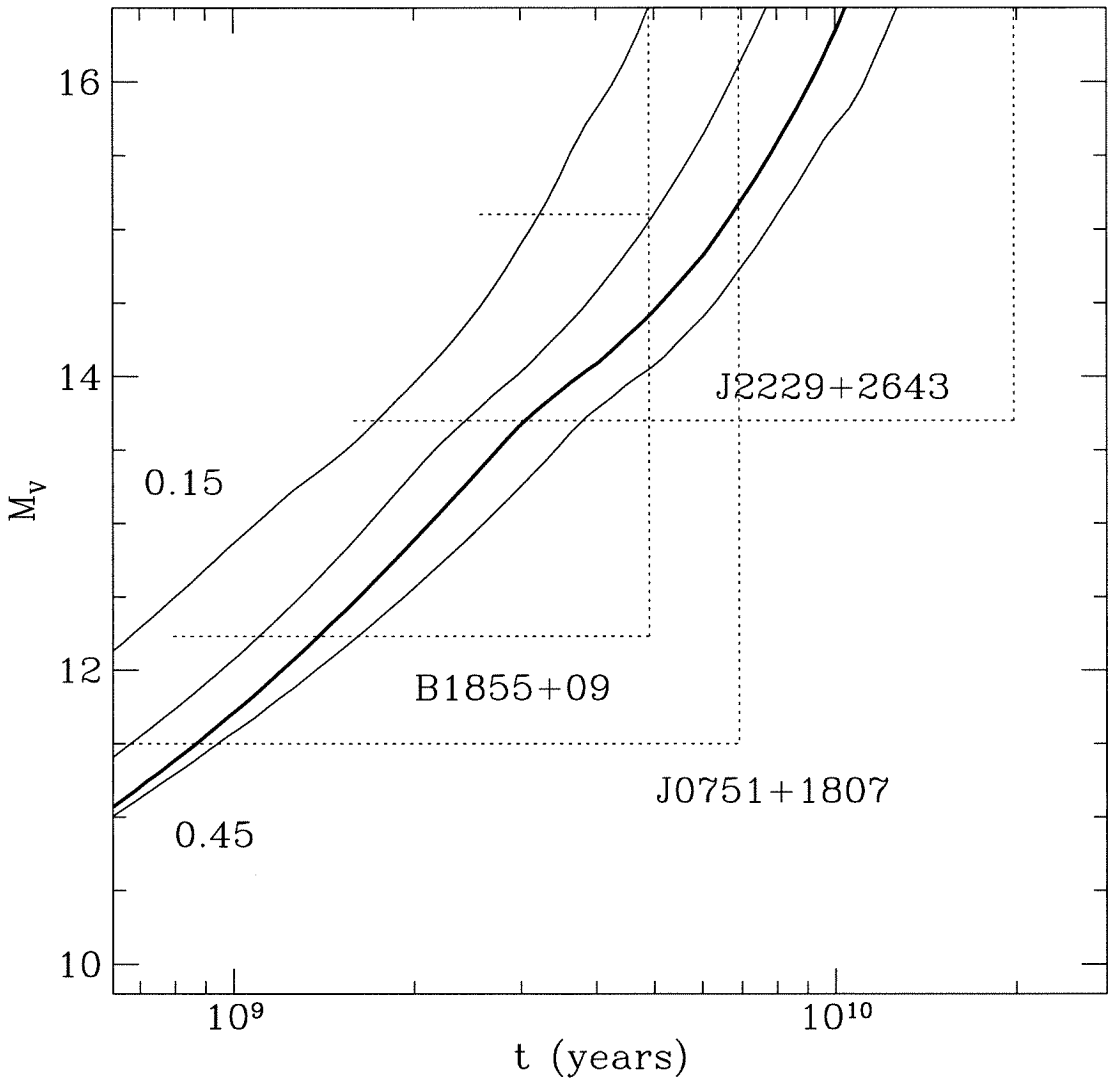

Figure 4.14: **Limits for Other Pulsar Companions:** We compare the absolute V magnitudes of our models with the limits determined for three binary pulsar systems. The vertical dotted lines indicate the (n=3) spin-down ages for each binary system and the horizontal dotted lines are the magnitude limits determined from the observations. The models are for 0.15, 0.25, 0.35 and 0.45 $M_\odot$ respectively. The heavy solid line indicates the 0.25 $M_\odot$ model (for comparison with the B1855+09 limits).

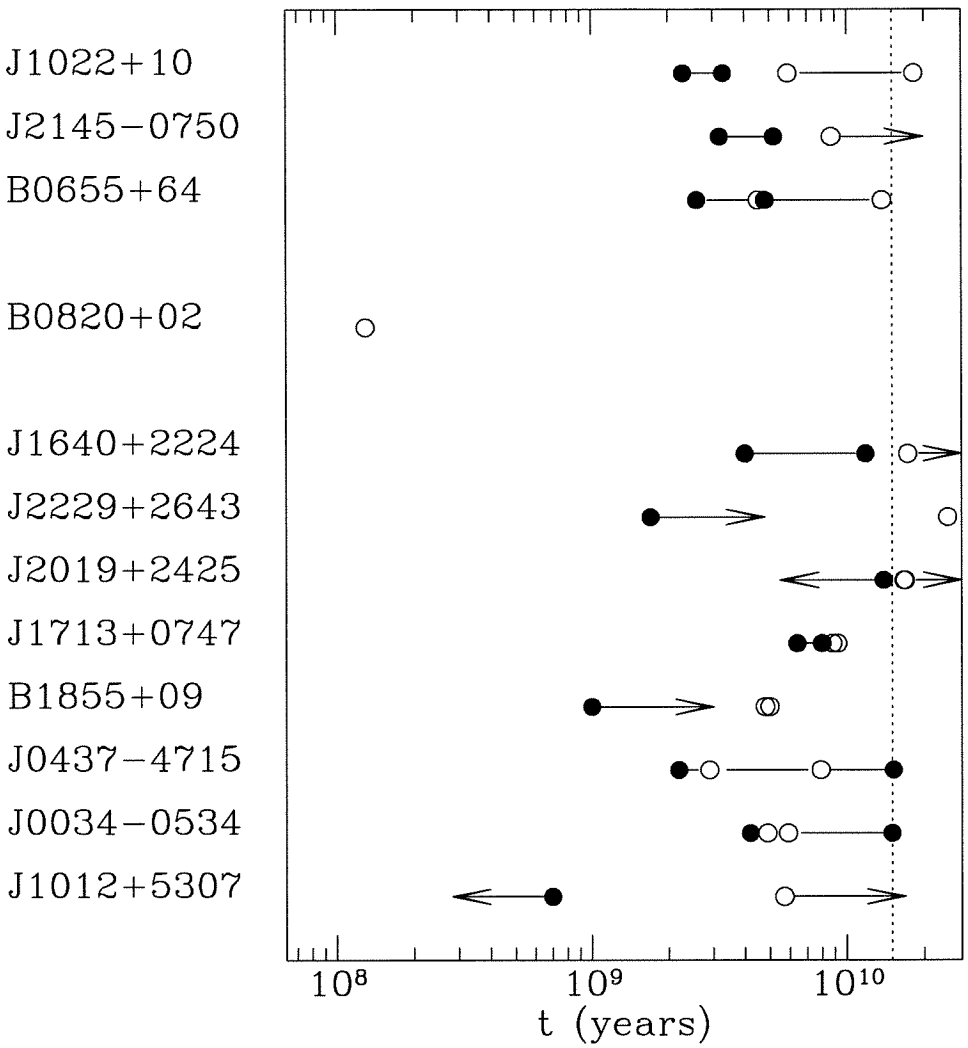

Figure 4.15: **Cooling Ages for Millisecond Pulsar Companions:** Here we show the constraints on the cooling age for the various binaries discussed in this paper. The open circles indicate timing ages (for a braking index n=3), and the filled circles indicate cooling ages. The uncertainties in the timing ages are because of the Shklovskii term. The systems are separated into C/O and He white dwarfs (B0820+02 is placed in limbo due to the uncertainty in its mass) and ordered in increasing orbital period. No cooling ages are shown for B0820+02 because of the uncertainties discussed in the text.

as long as the secondary star is sufficiently evolved to have a convective envelope when it overflows its Roche lobe. This is because mass loss from the secondary results in expansion of the orbit, shutting off mass loss unless the donor star increases as well (which requires a convective envelope, rather than a radiative one). Thus, this scenario describes systems with orbital periods $\sim 10 - 10^3$ days.

For shorter period systems, the donor star overflows its Roche lobe either on the main sequence or during the transition from the main sequence to the giant branch. The envelope is still primarily radiative in this case, and the star will shrink in response to mass loss. The result is that one needs angular momentum loss mechanisms such as gravitational radiation and magnetic braking to maintain mass transfer in these systems. The competition between these loss mechanisms and the mass-transfer induced evolution of the system leads to a very steep relationship between final orbital period and initial orbital period/final core mass (Pylyser and Savonije (1988), Coté and Pylyser (1989)).

In Figure 4.16 we compare our mass determinations for these companions with the results of Rappaport et al. (1993) and Pylyser & Savonije (1988) (omitting models in the latter sample where the accretor was far from 1 $M_\odot$). We find excellent agreement with the models. We are able to identify each system we discuss as definitely belonging to either one class or the other.

4.4.2 Neutron Star Spin-up

Under the assumption that the magnetic field does not decay, the cooling age of the white dwarf allows us to estimate the initial spin period of the millisecond pulsar, by inverting formula (4.1). These estimates are shown in table 4.3.

The simplest theories regarding spin-up of recycled pulsars to millisecond periods (Smarr & Blandford (1976), Ghosh (1995) and references therein) predicts that the initial period should be equal to the equilibrium spin-period of the neutron star of magnetic field B accreting at a rate $\dot{M}$. This predicts an initial spin period

$$P_0 = 1.89\,\mathrm{ms}\,B_9^{6/7}\left(\frac{\dot{M}}{\dot{M}_{\mathrm{Edd}}}\right)^{-3/7}, \tag{4.8}$$

where $\dot{M}$ is the accretion rate. Thus, a comparison between the inferred initial spin period and magnetic field can determine the accretion rate onto the neutron star during spin-up.

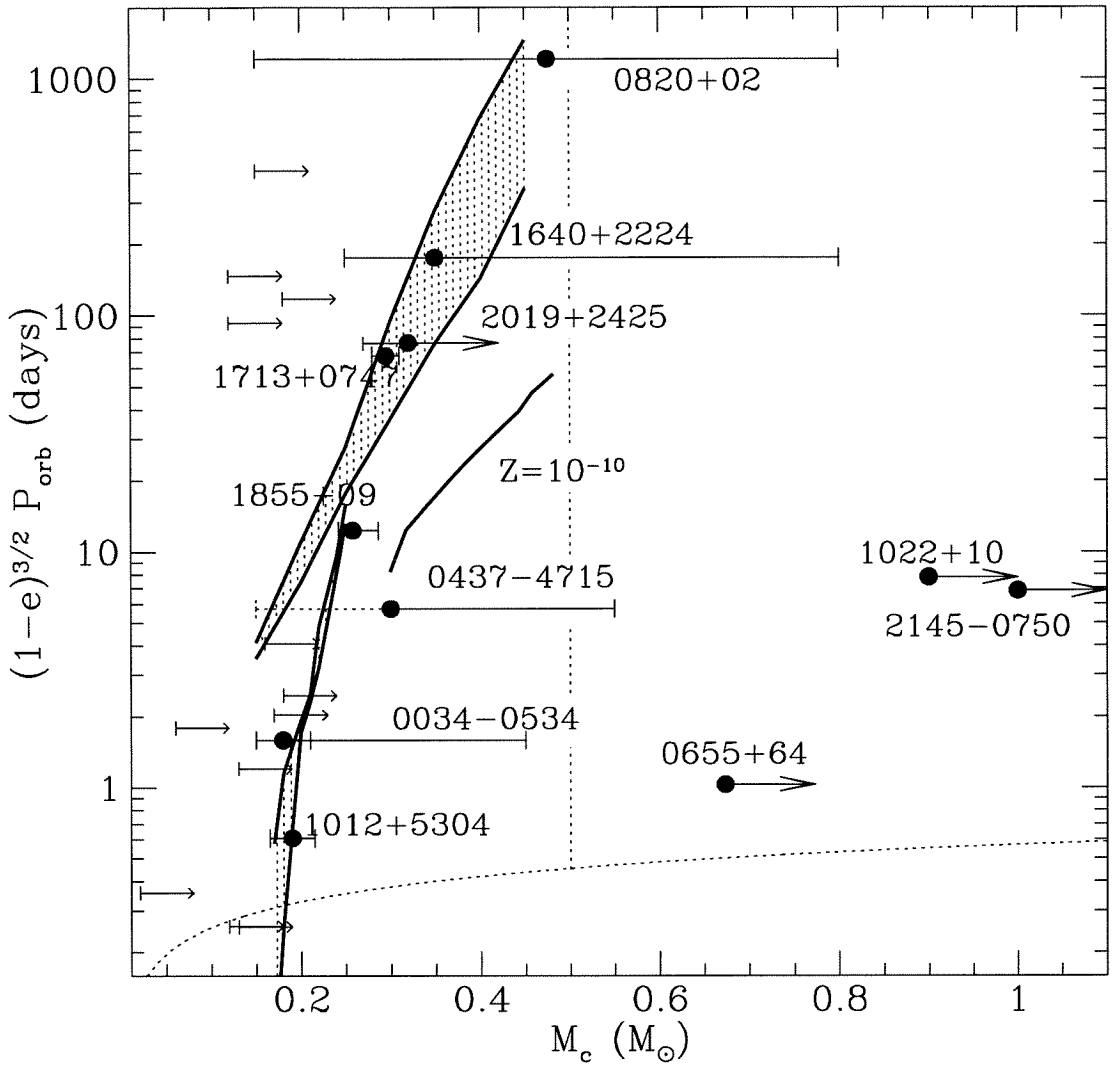

Figure 4.16: **The Orbital Period-Mass Relation:** The upper shaded region is the parameter space spanned by the models of Rappaport et al. (1993) while the lower shaded region is that spanned by the models of Pylyser & Savonije (1988). Also shown are the mass constraints for various systems determined in this paper as well as those of Kaspi et al. (1993) for B1855+09 and the mass function limits for those systems without further constraints. The dotted line at the bottom of the diagram indicates the boundary below which the companion will spiral into a 1.4 $M_\odot$ neutron star in a Hubble time due to gravitational radiation. The vertical dotted line indicates the dividing line between Carbon cores ($> 0.5M_\odot$) and Helium cores ($< 0.5M_\odot$). The error bars for B0820+02, J1640+2224 and J0437-4715 are from two overlapping mass estimates, one for a Helium core white dwarf and one for a Carbon core. J0034-0534 has two upper mass limits, for n=3 (0.21 $M_\odot$) and n=2 (0.35 $M_\odot$). The dotted error bar for J0437-4715 denotes those masses below the mass limit derived by Anderson et al. (1995). If the secondary progenitor in this system were a 1 $M_\odot$ star of very low metallicity, the $P_{orb} - M_c$ relationship would be given by the curve labelled $Z = 10^{-10}$, which lies closer to the new mass limit.

Name	P (ms)	t_p (Gyr)	t_{cool} (Gyr)	P_0^3 (ms)	P_0^2 (ms)
J0034-0534	1.88	5.4(5)	9.6(54)	< 1.1	< 1.3
J1713+0747	4.57	9.0(2)	7.2(8)	2.0(6)	2.7(3)
J0437-4715	5.76	5.4(25)	8.7(65)	$< 5.3/0.9$	$< 5.4/3.0$
J1640+2224	3.16	>17.3	7.9(39)	> 1.8	> 2.1
J1012+5307	5.26	>5.7	< 0.7	> 4.9	> 4.9
B1855+09	5.36	4.9(1)	> 1.0	< 4.8	< 4.9
J2229+2643	2.98	24.9	> 1.7	< 2.9	< 2.9
J2019+2425	3.94	37.4(265)	< 13.9	> 1.6	> 2.3
J2145-0250	16.05	> 8.7	4.2(10)	> 10.2	> 11.3
J1022+1001	16.45	12.1(62)	2.8(5)	13.2(22)	13.6(18)
B0655+64	195.7	9.1(46)	3.7(11)	< 176	< 177

Table 4.3: Initial spin periods estimated on the basis of the cooling ages to various pulsars. We include estimates based on both n=2 and n=3 (superscript indicates the value of n). For J0437-4715, we include two numbers. The first is derived allowing all cooling models, while the second is restricted to cooling models with masses $> 0.3\,M_\odot$.

However, this inversion is complicated somewhat by the uncertainty in the macroscopic dimensions of the neutron star. Figure 4.17 shows the spin period-magnetic field diagram for the millisecond pulsars. We see that canonical values of M and R lead us to infer accretion rates $\sim 10^{-2} - 0.1\,\dot{M}_{Edd}$. However, a $1.4\,M_\odot$ star with a hard equation of state could yield an Eddington rate spin-up line much closer to the inferred initial periods. Although we cannot accurately determine the accretion rate for most of these systems, we can confidently assert that PSR J1012+5304 had an accretion rate significantly sub-Eddington ($< 0.1\,\dot{M}_{Edd}$), no matter what the equation of state. Of the other systems, pulsars J0034-0534, J1713+0747 and B1855+09 are all consistent with Eddington accretion rates, while pulsars J1640+2224, J0437-4715 and J2145-0750 must have had sub-Eddington accretion rates (a similar conclusion was reached by Lundgren et al. (1996)), regardless of the equation of state. This is consistent with the findings that low mass X-ray binaries have a range of sub-Eddington accretion rates (Bradt & McClintock (1983)).

4.4.3 Magnetic Field Decay

Although many authors have noted that millisecond pulsars must have very long magnetic field decay times (Kulkarni (1986), Camilo et al. (1994)), the determination of a cooling age allows us to make a quantitative estimate of t_D in the context of the paradigm outlined

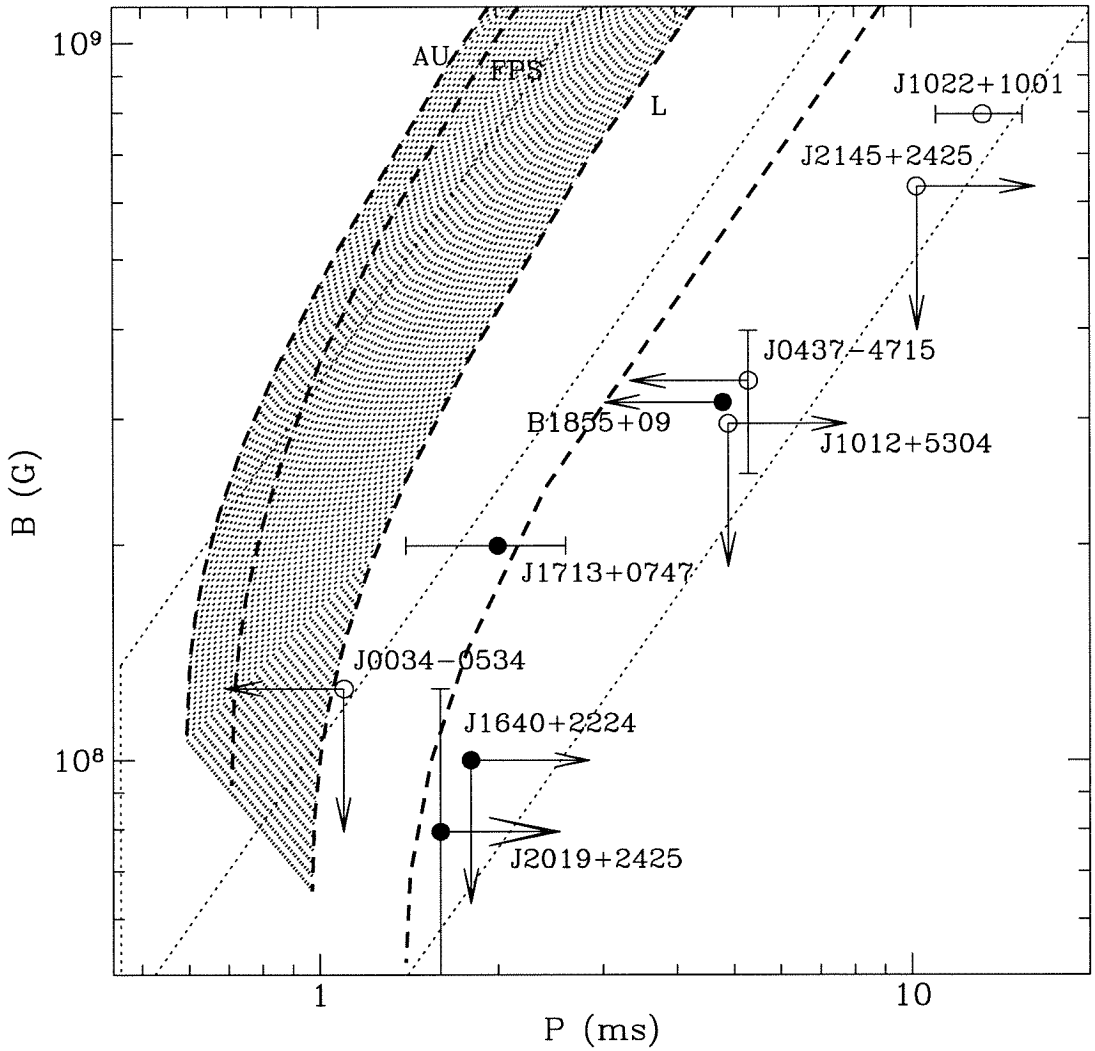

Figure 4.17: **Initial spin periods for millisecond pulsars:** We show here the inferred limits on the initial spin periods for the neutron stars discussed in the text. The three parallel dotted lines indicate the spin-up lines (4.8) for $\dot{M}/\dot{M}_{Edd} = 1$, 0.1 and 0.01 respectively, and canonical neutron star values of $M = 1.4\ M_\odot$ and $R = 10$ km. The heavy dashed lines indicate the Eddington rate spin up lines for different equations of state taken from Cook et al. (1995), and spanning the range from hard (L) to soft (AU). The three curves contained in the shaded region represent the case for maximal spin-up for each equation of state (i.e., they result from the spin-up of a maximum static mass model). Also shown is the spin-up line for a $1.4\ M_\odot$ star with a hard equation of state. Many of the pulsar magnetic fields are uncertain because of the Shklovski effecti on $\dot{P}$. The derivation of the limits on P_0 are discussed in the text.

in 4.2. To get the upper limits on t_D, we must use the lower limits on both the distance and the cooling age. We find that J0034-0534 and J1713+0747 both have lower limits on $t_D \sim 10$ Gyr which strongly supports the view that millisecond pulsar fields do not decay at all.

4.4.4 Nuclear Equation of State

In addition to constraining evolution scenarios, we note that the mass estimate of the pulsar J1012+5307 obtained in 4.3.4 rules out all equations of state with maximum masses < 2.05 $M_\odot$. The four hardest of the fourteen equations of state in Cook et al. (1995) pass this test. These fur have minimum periods spanning the range 0.593 - 0.97 ms.

If one assumes n=3, the initial spin period of J0034-0534 can also provide a useful constraint on the harder equations of state (Figure 4.9), but this conclusion is not robust, because a braking index n=2 will yield an upper limit that lies above all minimum spin periods.

In conclusion, we have shown that using the white dwarf cooling ages as an independent chronometer for binary pulsars can teach us a lot about both neutron star structure and binary evolution. In particular, the determination of initial spin periods provides us with new information about the final stages of pulsar spin-up and evolution. Further observations of low mass binary pulsars, both in radio and optical, will lead to even better constraints in the future.

The authors would like to thank Marten van Kerwijk for use of results prior to publication and extensive discussion of white dwarf observational uncertainties and Glenn Soberman for discussions about mass transfer in binaries.

REFERENCES

Alberts, F., Savonije, G.J., Pols, O.R. & van den Heuvel, E.P.J., 1996, preprint

Anderson, S.B. et al., in prep, 1996.

Arponen, J., 1972, Nucl. Phys., **A191**, 257.

Backer, D.C., Foster, R.S. & Sallmen, S., 1993, *Nature*, **365**, 817.

Bailes, M., et al., 1994, ApJ, **425**, L41.

Bailyn, C., 1993, ApJ, **411**, L83.

Bell, J.F., Bailes, M. & Bessell, M.S., 1993, *Nature*, **364**, 603.

Bell, J.F., Bailes, M., Manchester, R.N., Weisberg, J.M. & Lyne, A.G., 1995, ApJ, **440**, L81.

Bergeron, P., Saumon, D. & Wesemael, F., 1995, ApJ, **443**, 764.

Bergeron, P., Wesemael, F. & Fontaine, G., 1991, ApJ, **367**, 253.

Bessell, M.S., 1990, PASP, **102**, 1181.

Bhattacharya, D., Wijers, R.A.M.J., Hartman, J.W. & Verbunt, F., 1992, A&A, **254**, 198.

Blandford, R.D. & Teukolsky, S.A., 1976, ApJ, **205**, 580.

Bradt, H.V.D. & McClintock, J.E., 1983, ARA&A, **21**, 13.

Callanan, P. et al., 1989, MNRAS, **238**, pP25.

Camilo, F., 1996, *Pulsars: Problems and Progress*, IAU Colloq. 160.

Camilo, F., Nice, D.J. & Taylor, J.H. , 1993, ApJ, **412**, L37.

Camilo, F., Nice, D.J. & Taylor, J.H., 1996, ApJ, **461**, 812.

Camilo, F., Thorsett, S.E. & Kulkarni, S.R., 1994, ApJ, **421**, L15.

Cassisi, S. & Castellani, V., 1993, ApJS, **88**, 509.

Cook, G.B., Shapiro, S.L. & Teukolsky, S.A., 1994, ApJ, **424**, 823.

Cote′, J. & Pylyser, E.H.P., 1989, A&A, **218**, 131.

Danziger, I.J., Baade, D. & Della Valle, M., 1993, A&A, **276**, 382.

Foster, R.S., Cadwell, B.J., Wolszczan, A. & Anderson, S.B., 1995, ApJ, **454**, 826.

Foster, R.S., Wolszczan, A. & Camilo, F., 1993, ApJ, **410**, L91.

Ghosh, P., 1995, J.Astroph., **16**, 289.

Gunn, J.E. & Ostriker, J.P. 1970, ApJ, **160**, 979.

Hamada, T. & Salpeter, E.E., 1961, ApJ, **134**, 683.

Hayes, D.S., in IAU Symp. 111, *Calibration of Fundamental Stellar Quantities*, ed. D.S.Hayes, L.E.Pasinetti & A.G.Davis Philip (Dordrecht: Reidel), 225.

Johnston, S. et al., 1992, ApJ, **387**, L37.

Jones, A.W. & Lyne, A.G., 1988 MNRAS, **232**, 473.

Joss, P.C., Rappaport, S. & Lewis, W., 1987, ApJ, **319**, 180.

Kaspi, V.M., Taylor, J.H. & Ryba, M.F. 1994 ApJ, **428** 713.

Koester, D., Chanmugam, G. & Reimers, D., 1992, **395**, L107.

Kulkarni, S.R., 1986, ApJ, **306**, L85.

Kulkarni, S.R., Djorgovski, S. & Klemola, A.R., 1991, ApJ, **367** , 221.

Kulkarni, S.R. & Narayan, R., 1988, **335**, 755.

Lorenz, C.P., Ravenhall, D.G. & Pethick, C.J., 1993, Phys.Rev.Lett, **70**, 379.

Lorimer, D.R., Lyne, A.G., Festin, L. & Nicastro, L., 1995a, *Nature*, **376**, 393.

Lorimer, D.R., et al., 1995b, ApJ, **439**, 933.

Lundgren, S.C., Cordes, J.M., Foster, R.S., Wolszczan, A. & Camilo, F., 1996a, **458**, L33.

Lundgren, S.C., Foster, R.S. & Camilo, F., 1996b, Preprint for IAU Colloq. 160, *Pulsars: Problems & Progress*

Lundgren, S.C., Zepka, A.F. & Cordes, J.M., 1995, ApJ, **453**, 419.

Michel, F.C., 1991, *Theory of Neutron Star Magnetospheres*, Chicago: Chicago University Press

Narayan, R. & Ostriker, J.P., 1990, ApJ, **352**, 222.

Navarro, J., De Bruyn, A.G., Frail, D.A., Kulkarni, S.R. & Lyne, A.G., 1995, ApJ, **455**, L55.

Neckel, T. & Klare, G. , 1980, A&AS, **42**, 251.

Nicastro, L., Lyne, A.G., Lorimer, , D.R., Harrison, P.A., Bailes, M. & Skidmore, B.D., 1995, MNRAS, **273**, L68.

Nice, D.J., Taylor, J.H. & Fruchter, A.S. , 1993, ApJ, **402**, L49.

Pandharipande, V.R., 1971, Nuc. Phys. A, **178**, 123.

Pandharipande, V.R. & Smith, R.A., 1975, Phys. Lett. B, **59**, 15.

Phinney, E.S. & Kulkarni, S.R., 1994, ARA&A, **32**, 591.

Pylyser, E.H.P. & Savonije, G.J., 1988, å, **191**, 57.

Rappaport, S., Podsiadlowski, P., Joss, P.C., Di Stefano, R. & Han, Z., 1995, ApJ, **273**, 731.

Rawley, L.A., Taylor, J.H. & Davis, M.M., 1988, ApJ, **326**, 947.

Refsdal, S. & Weigart, A., 1971, å, **13**, 367.

Reid, I.N., 1996, preprint

Salpeter, E.E., 1961, ApJ, **134**, 669.

Savage, B.D. & Mathis, J.S., 1979, ARA&A, **17**, 73.

Saumon, D., Chabrier, G. & van Horn, H.M., 1995, ApJS, **99**, 713.

Shklovskii, I., 1970 Soviet Ast., **13**, 562.

Smarr, L.L. & Blandford, R.D., 1976, ApJ, **207**, 574.

Taylor, J.H. & J.M.Cordes, 1993, ApJ, **411**, 674.

Taylor, J.H. & Dewey, R.J. 1988, ApJ, **332**, 770.

Taylor, J.H., Manchester, R.N. & Lyne, A.G., 1993, Ap&SS, **88**, 529.

Thorsett, S.E., Arzoumanian, Z., McKinnon, M.M. & Taylor, J.H., 1993, ApJ, **405**, L29.

Thorsett, S.E., Arzoumanian, Z. & Taylor, J.H., 1993, ApJ, **412**, L33.

van den Heuvel, E.P.J., 1995, J., Ap. Astr., **16**, 255.

van Kerkwijk, M.H., Bergeron, P. & Kulkarni, S.R. 1996, ApJ, submitted

van Kerkwijk, M.H. & Kulkarni, S.R., 1995, ApJ, **454**, L141.

Verbunt, F., 1993, ARA&A, **31**, 93.

Webbink, R.F., 1975, MNRAS, **171**, 555.

Wolszczan, A., 1991, *Nature*, **350**, 688.

Chapter 5 Pulsar Winds and Their Effect on Close Binary Companions

We discuss the effect that the relativistic wind from a pulsar may have on its white dwarf companion. In particular we consider the spallation of the white dwarf atmospheric Helium to produce Hydrogen. This has a significant effect on the white dwarf cooling age and may have the observational consequence that Deuterium could be observable in the hotter companions.

5.1 Introduction

More than 25 years after the discovery of the first pulsar, still relatively little is known about the energy loss mechanisms by which such objects spin down. The defining characteristic, radio emission, is a negligible contributor to the energy budget, although some young pulsars may lose a significant fraction ($\sim 10\%$) of their energy via gamma rays (Fierro (1996)). Detailed studies of the Crab Nebula imply that the nebular emission is driven by a relativistic, particle dominated, magnetohydrodynamic wind emanating from the pulsar (Kennel and Coroniti (1984), Gallant and Arons (1994) and references therein). Early work favoured a pair-dominated kinetic luminosity, although Gallant and Arons (1994) (hereafter GA) find that most of the kinetic energy is carried by an ionic component. The presence of such a wind can also be inferred from the presence of bow-shocks around pulsars moving with respect to the surrounding medium (Hester and Kulkarni (1988), Kulkarni and Hester (1988)).

The significance of pulsar winds for the energy balance of very close binary companions has been recognised by a number of previous authors (Ruderman, Shaham and Tavani (1989), Kluzniak et al. (1988), Phinney et al. (1988), Arons and Tavani (1993)). Furthermore, Eichler and Nath (1996) have noted that the spallation of heavy materials in more widely separated companions may serve as a diagnostic of the pulsar wind content. In this paper we examine the importance of the pulsar wind for the atmospheric composition of

the low mass Helium core white dwarfs that constitute the majority of millisecond pulsar companions. This is of particular importance for the dwarf white cooling age, which can be used as an independent estimate of the millisecond pulsar age (Chapter 4).

In section 5.2 we review the basic nature of the relativistic pulsar wind and its interaction with a close stellar companion. In section 5.3 we discuss the mechanism of spallation in a white dwarf atmosphere for various possible wind compositions. Finally, in section 5.4, we discuss the implications of this for the cooling of pulsar companions.

5.2 The Pulsar Wind

The spin-down rate of a pulsar is given by (e.g., Shapiro and Teukolsky (1983)),

$$\dot{E} = I\Omega\dot{\Omega} = 5.6 \times 10^{33} \mathrm{ergs.s^{-1}}\, I_{45} \left(\frac{B}{B_0}\right)^2 P_5^{-4} \tag{5.1}$$

where I_{45} is the pulsar moment of inertia in units of 10^{45} g.cm^2, $B_0 = 3 \times 10^8$ G, B is the pulsar surface magnetic field and P_5 is the period in units of 5 ms. A companion, with stellar radius R and orbiting at distance R_{bin} from the pulsar, will intercept a fraction $\sim \frac{1}{f}\left(\frac{R}{2R_{bin}}\right)^2$ of this luminosity, where f is the beaming fraction of the pulsar wind (assuming the companion falls within the wind beam[1]). Thus, the wind luminosity impinging on the companion is

$$L_{wind} = 3 \times 10^{-6} L_\odot \frac{I_{45}}{f} \left(\frac{B}{B_0}\right)^2 P_5^{-4} R_9^2 \left(\frac{P_{orb}}{1day}\right)^{-4/3} \tag{5.2}$$

Models of the Crab nebula (GA) indicate that the ratio of magnetic to kinetic energy in the pulsar wind is ~ 0.003, so that $L_{kin} \sim L_{wind}$. We adopt as our default model the model of GA, in which the kinetic energy is carried primarily by relativistic ions. GA find the Lorentz factor of the ions to be $\sim 10^6$. To adapt this model to millisecond pulsars, we shall assume that the Lorentz factors scale as a constant fraction η of the energy drop across the pulsar polar cap ($\eta \sim 0.04$ for the Crab). Thus, we obtain the ion Lorentz factor

$$\gamma_i \sim 3.6 \times 10^3 \frac{Z}{A} \left(\frac{B}{B_0}\right) P_5^{-2} \tag{5.3}$$

where Z,A are the atomic and mass numbers of the constituent nuclei. The results of Rosen

[1] Models of the Crab Nebula suggest that much of the wind emission may be equatorial.

and Cameron (1972) indicate that the most likely constituents are iron nuclei, although anything $Z \geq 2$ is possible.

The interaction of the pulsar wind with the companion is governed by a bow shock surrounding the companion. The upstream magnetic field in the wind at the bow shock is $\sim 2.14\,\mathrm{G}\left(\frac{\mathrm{B}}{\mathrm{B}_0}\right)\mathrm{P}_5^{-2}\left(\frac{\mathrm{P}_{\mathrm{orb}}}{1\,\mathrm{day}}\right)^{-2/3}$, yielding an ion Larmor radius of $\mathrm{r_L} \sim 5.3\times10^9\mathrm{cm}\left(\frac{\mathrm{P}_{\mathrm{orb}}}{1\,\mathrm{day}}\right)^{2/3}$. This is larger than white dwarf dimensions, and so the companion will be irradiated by ions from all directions (i.e., we should not expect to see any 'day/night' variations in the effect on the companion). Furthermore, although the ions would lose $\sim$ 20% of their energy to the downstream pairs by excitation of magnetosonic waves (Hoshino et al. (1992)) behind an isolated shock, the presence of the companion is likely to reduce this efficiency by intercepting the ions before they have had a chance to complete a gyration.

Other external sources of Hydrogen, such as cometary impacts (Tremaine and Żytkow (1986)) or interstellar accretion (Alcock and Illarionov (1980b)) are precluded by the presence of the pulsar. The ram pressure of the pulsar wind will clear out a cavity of radius

$$\mathrm{R_{cav}} \sim 1.8 \times 10^16\,\mathrm{cm}\left(\frac{\mathrm{I_{45}}}{\mathrm{n_1}}\right)^{1/2}\frac{\mathrm{B_8}}{\mathrm{P_5^2 V_{10}}} \tag{5.4}$$

where $\mathrm{n_1}$ and $\mathrm{V_{10}}$ are the density of the ISM (in $\mathrm{cm^{-3}}$) and the binary system velocity (in units of 10 $\mathrm{km.s^{-1}}$) respectively. This corresponds to an orbital period of 3×10^4 years, so that all the binaries we are interested in will orbit within this cavity. Furthermore, the kick velocities ($\sim 10 - 100\,\mathrm{km.s^{-1}}$) acquired in the supernova that formed the pulsar will be enough to free the binary from any pre-existing Oort cloud (inner Oort cloud comets have $\mathrm{V}\sim 1\,\mathrm{km.s^{-1}}$).

5.3 Companion Spallation

We shall consider in turn the behaviour of high energy electrons, photons and ions entering the companion atmosphere.

5.3.1 Electromagnetic Cascade

We consider electrons, positrons and photons together, because all three kinds of primary particle will initiate an electromagnetic cascade of electrons, positrons and photons, with

approximately equal amounts of energy residing in leptons and photons. At energies above 1 GeV, electrons lose energy primarily through bremstrahlung and photons primarily through pair production. At lower energies, ionization and compton losses prevail respectively. Spallation of atmospheric nuclei by the electromagnetic cascade is performed by photons in the energy range 20-150 MeV (Puget, Stecker and Bredekamp (1976)). Above 150 MeV, the photohadron cross-section is dominated by pion production, and below 20 MeV the energy is below the spallation threshold.

Approximately half the primary energy will, at some point in the cascade, pass through the energy range 150-20 MeV in the form of photons. The fraction of this energy that goes into spallation will be determined by the comparison of the spallation cross-section to the other photon energy loss mechanisms, pair creation and Compton losses. From Rossi (1952),

$$\sigma_{\rm comp} \sim \frac{8.5{\rm mb}}{E_{30}} \left(\frac{Z_a}{2}\right) \left[\ln\left(117.1E_{30}\right) + \frac{1}{2}\left[1 - \left(\frac{8.541\times10^{-3}}{E_{30}}\right)^2\right]\right] \tag{5.5}$$

$$\sigma_{\rm pair} \sim 37.2{\rm mb} \left(\frac{Z_a}{2}\right)^2 \left[\frac{7}{9}\ln 117.1E_{30} - \frac{109}{54}\right] \tag{5.6}$$

where E_{30} is the energy in 30 MeV and Z_a is the atmospheric atomic number (the pair cross-section is for the complete screening limit ($E < 55$ MeV)). These are to be compared with the mean spallation cross-sections from Puget et al. (1976),

$$\sigma_{\rm spall} \sim 1.7{\rm mb\ at\ 150\,MeV} \tag{5.7}$$

and

$$\sigma_{\rm spall} \sim 2.3{\rm mb\ at\ 30\,MeV} \tag{5.8}$$

At 150 MeV (and using the no screening formula for pair production), we get that $\sigma_{\rm comp} = 11.7\,{\rm mb}$, $\sigma_{\rm pair} = 144\,{\rm mb}$, $\sigma_{\rm spall} = 1.7\,{\rm mb}$, yielding a spallation fraction of ~ 0.01, i.e., 1% of the photons with this energy will spall a nucleus. Similarly, at 30 MeV, $\sigma_{\rm comp} = 45\,{\rm mb}$, $\sigma_{\rm pair} = 16\,{\rm mb}$, $\sigma_{\rm spall} = 2.3\,{\rm mb}$, which implies a spallation fraction ~ 0.04.

Thus, we find $\sim$ 3% of photons in this energy range will spall nuclei. This implies that, for a primary photon/electron of energy E_0, approximately $\sim \frac{1}{2} \times 0.03 \frac{E_0}{50{\rm MeV}}$ nuclei are spalled. If we consider the companion to be a pure Helium star, then the spallation of atmospheric Helium will result in the production of 1 Hydrogen per spallation. Thus, our

kinetic luminosity may be converted into a mass accumulation rate of Hydrogen due to the spallation of atmospheric Helium. Assuming that a fraction ζ of the pulsar wind energy enters the atmosphere as high energy electrons and photons, we obtain

$$\dot{M}_H \sim 4 \times 10^{-20} M_\odot.yr^{-1} \frac{\zeta}{f} I_{45} \left(\frac{B}{B_0}\right)^2 P_5^{-4} R_9^2 \left(\frac{P_{orb}}{1day}\right)^{-4/3} \quad (5.9)$$

5.3.2 The Ionic Component

In this section we consider the spallation of atmospheric ^{4}He by the ionic component of the pulsar wind. Once again our concern is the production rate of Hydrogen. An ion of mass number A and energy E_0 is considered to interact as A independent nuclei of energy E_0/A. This is valid because the total mass-changing cross section scales as $\sigma_{in} \sim 97A^{0.64}$ mb for a Helium target (Webber et al. (1990) - for a beam energy of 1.5 GeV/nucleon - it is of this order for higher energies). Thus, the mean free path of an iron nucleus is 0.08 that of a proton and, if we assume a heavy nucleus fragments into two equal mass products with each collision, an iron nucleus will break into particles of $A \sim 3 - 4$ in one proton mean free path. Tsao et al. (1995) have shown that the approximation that product nuclei share the same energy/nucleon of their parent nuclei is good to within 5% (Note that this applies to product nucleons resulting from the primary particle - it does not necessarily describe the energy distribution of the products spalled from the target). Thus, we shall consider in detail the case of high energy protons spalling in a Helium atmosphere.

The spallation of ^{4}He has been considered in detail by Meyer (1972). The four most likely reaction channels are listed in table 5.1. We consider the ^{3}He and ^{3}H reaction channels together, because ^{3}H is unstable and will decay to ^{3}He. Furthermore, we will assume the mirror reactions (n + ^{4}He) have the same cross-sections, an assumption valid for $E \geq 40$ MeV, because then Coulomb energies are negligible with respect to the kinetic energies available in the centre of mass frame after the destruction of the Helium nucleus.

At high energies, the spallation reaction is described by the participant-spectator model (see, e.g., Lynch (1987)), in which the primary nucleon interacts strongly with one or two of the nucleons in the target nucleus, with a resultant large transfer of energy and ejection of the nucleons from the parent nucleus. The rest of the target nucleons are spectators in this interaction, resulting in a remnant 'wounded nucleus', possibly in an excited state. This may subsequently decay, with the resultant emission of further product nucleons, but at

Symbol	Reaction	$E_{threshold}$ (MeV)	σ(1 GeV) (mb)
^{3}H	p + ^{4}He $\rightarrow$ ^{3}H + 2p (+ π)	24.9	40
^{3}He	p + ^{4}He $\rightarrow$ ^{3}He + n + p (+ π)	25.8	35
dd	p + ^{4}He $\rightarrow$ D + D + p (+ π)	29.8	12
d	p + ^{4}He $\rightarrow$ D + n + 2p (+ π)	32.7	25

Table 5.1: The dominant proton-Helium spallation reaction channels.

energies of order of the nuclear binding energy. Thus, to determine the secondary energy spectrum, we consider that each spallation reaction produces one spalled nucleon in addition to the primary nucleon, the rest of the material remaining in the spectator nucleus. Energy and momentum conservation in the centre of mass frame yields a secondary particle energy distribution

$$P(\gamma) = \frac{1}{\pi} \frac{1}{\left[(\gamma'\gamma_b\beta'\beta_b)^2 - (\gamma - \gamma'\gamma_b)^2\right]^{1/2}} \tag{5.10}$$

where γ is the lab frame Lorentz factor of the secondary particle, γ' is the C.o.M. frame Lorentz factor of the the secondary particle (a unique function of the incident primary energy) and γ_b is the Lorentz boost factor between the Lab and C.o.M. frames. The average secondary Lorentz factor is $\gamma_{ave} = \gamma'\gamma_b$ and the maximum/minimum is $\gamma_{max/min} = \gamma_{ave}(1 \pm \beta'\beta_b)$. Expressions for these quantities is given in Appendix C. High energy hadronic interactions also result in significant losses to pion production. Mannheim and Schlickeiser (1994) provide expressions for the multiplicity[2]

$$\xi_\pi \sim 3\left[\frac{E}{GeV} - 1.22\right]^{1/4} \tag{5.11}$$

and average energy

$$< E_\pi > \sim \frac{1}{6}\left[\frac{E}{GeV} - 0.94\right]^{3/4} \tag{5.12}$$

of the pions produced in a hadronic interaction (E is the lab frame energy of the incident nucleon). Thus, we calculate the results of a spallation reaction as follows. At each interaction, the energy lost to pions is removed from the nucleonic shower. The interaction channel is chosen from amongst those in table 5.1 according to the relative cross-section and the energies of the secondary particles is chosen from the distribution (5.10). We note that, in

[2]We have added the contribution from neutral pions.

the case of a reaction via channel dd, one of the emergent secondaries is a deuteron. We describe this as two emergent nucleons each with half the energy of the emergent deuteron. The results of these calculations can be described as a function f(E',E)dE, the probability that a primary particle of energy E' will give rise to a secondary of energy between E and E+dE. This function is shown in figure 5.1.

Using this function, we calculate the propagation of a proton-induced nucleonic shower in a Helium atmosphere, using our simple formalism above in the continuous loss approximation. The number of shower nucleons of energy in the range E,E+dE at depth y in the atmosphere is N(E,y) dE. The evolution with depth is described by the equation

$$\frac{\partial \mathrm{N(E,y)}}{\partial \mathrm{y}} = -\frac{\mathrm{N(E,y)}}{\lambda(\mathrm{E})} + \int_{\mathrm{E}}^{\mathrm{E_0}} \frac{\mathrm{N(E',y)}}{\lambda(\mathrm{E'})} \mathrm{f(E,E')dE'} \tag{5.13}$$

where λ is the mean free path of nucleons of energy E in the atmosphere. The result of this calculation is a function W(y), describing the number of wounded nuclei left by the passage of the shower particles as a function of depth. The shower particles themselves also make a significant contribution to the global Hydrogen production. Once they reach energies $\leq$ 50 MeV, they no longer spall other nuclei and simply constitute another source of Hydrogen. The relative contributions of wounded and shower particles to the white dwarf cooling will be discussed in section 5.4.

The energy losses to the pionic cascade can also make a contribution to the spallation yield. Pions eventually decay into photons and electrons (with some neutrino losses along the way), and thus will provide photons to spall nuclei as discussed in section 5.3.1. We may estimate the contribution as follows. Of the energy lost to pions, 1/3 is lost to neutral pions and 2/3 to charged pions (Mannheim and Schlickeiser (1994)). The neutral pions have a short decay time and will decay to two gamma rays, contributing all of their energy to the electromagnetic cascade. Charged pions have a longer decay time, and have a significant chance of interacting with a nucleus before decaying (especially at high energies, where relativistic time dilation increases their lab frame decay time). However, the dominant result of pion-nucleus interactions is further pion production, so that we consider all energy in charged pions to eventually decay to muons and neutrinos (with an average of $\sim$ 20% of the energy carried off by the ν). The muons will also decay to electrons, with a further loss of energy to neutrinos ($\sim$ 1/2 in this case) and thus 40% of the energy in the charged pions

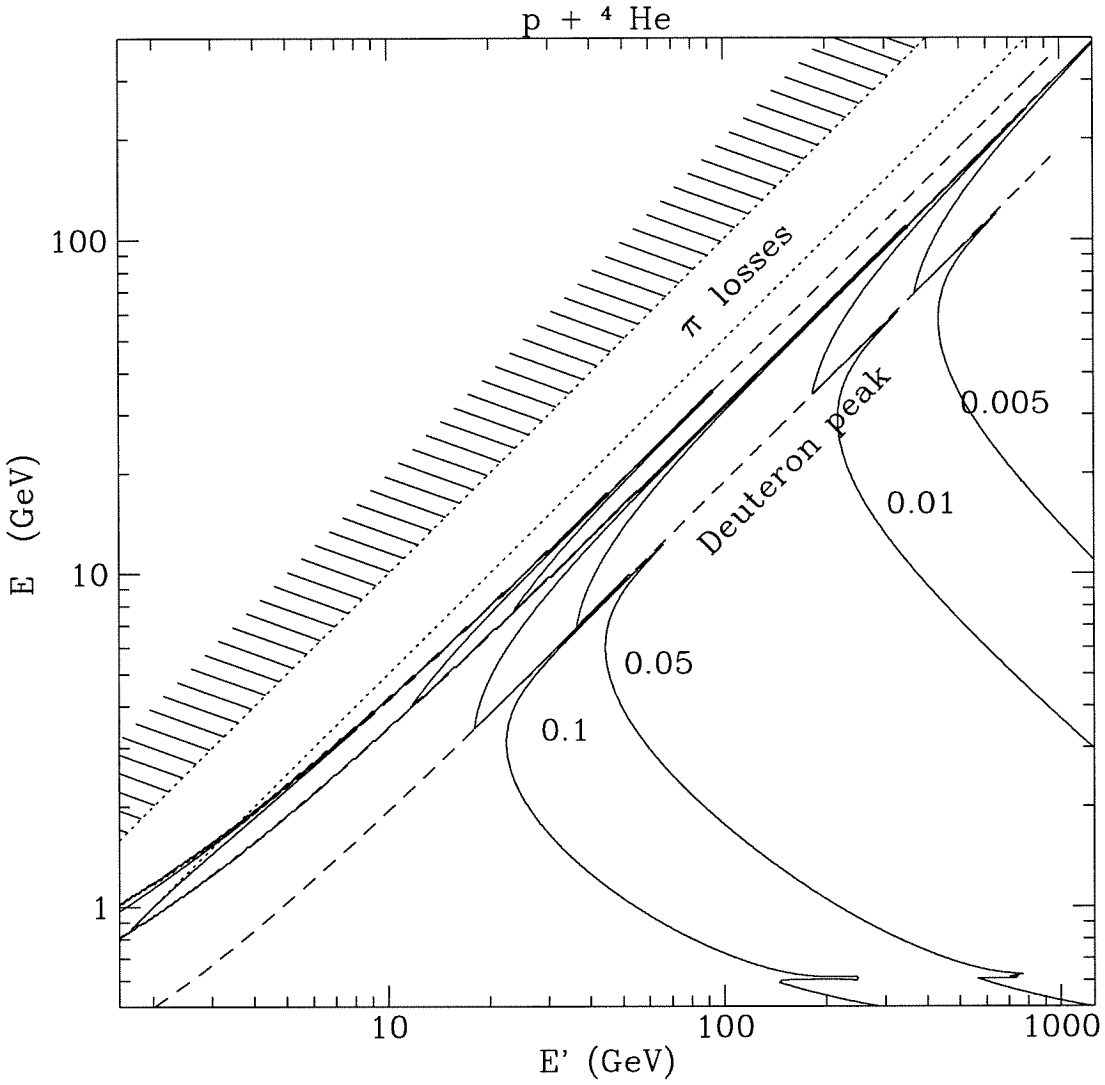

Figure 5.1: **Secondary Energy Distribution:** The solid lines are contours of constant f(E′,E). The dotted lines indicate E=E′ and E=E′/2, which is the region labelled pion losses, since the energy lost to pions is $\sim 1/2$ the primary energy for energies much greater than 1 GeV. f(E′,E) has three sharp peaks shown by the dashed lines. These are due to the fact that P(γ) peaks near the maximum and minimum allowed energies. The largest peak is for the two emission channels in which the products are all of 1 nucleon mass. The other two peaks result from reactions in which one of the products is a deuteron (the peak corresponding to the deuteron emission is labelled as such) and the other is a single nucleon.

is transferred to the electromagnetic cascade. So 60% of the energy lost by the nucleons will reside in an electromagnetic cascade as discussed in section 5.3.1, implying that the the resulting electromagnetic cascade will spall ~ 0.2 nuclei for every GeV of primary nucleon energy.

Figure 5.2 shows the evolution of a shower begun by a 1 TeV proton. The peak of the Hydrogen deposition is at ~ 350 g.cm^{-2} for this case. We define the efficiency of Hydrogen production by the quantity

$$\epsilon = \frac{\int_0^{y_{stop}} W_D(y) + W_H(y) + N_{slow}(y)dy}{E_0/50MeV} \sim 0.67 \left(\frac{E_0}{10GeV}\right)^{-0.22} \tag{5.14}$$

as determined from our shower calculation. (The functions W and N_{slow} are shown in Figure 5.3). The reason that this efficiency is not constant with energy is the fact that the efficiency of converting pionic energy to spalled Hydrogen is much lower than the conversion of nucleonic energy to spalled Hydrogen. Thus, higher energy primaries result in greater losses to the pion production and a corresponding decrease in the Hydrogen yield. The calculated efficiencies are shown in Figure 5.2. We should also note that the Hydrogen material deposited has D/H ~ 0.24 by number. Thus, using equations (5.2) and (5.3), we find a global Hydrogen accumulation rate of

$$\dot{M}_H \sim 9 \times 10^{-19} M_\odot.yr^{-1} \left(\frac{Z/A}{1/2}\right)^{-0.22} \left(\frac{B}{B_0}\right)^{1.78} P_5^{-3.56} R_9^2 P_{days}^{-4/3} \tag{5.15}$$

5.4 The Effect on White Dwarf Cooling

The spallation of atmospheric material in a pure Helium white dwarf star can have dramatic consequences for the cooling of such a star. This is because the efficiency of electron conduction in the degenerate core means that the cooling rate of the star is determined primarily by the efficiency of the radiative diffusion of energy through the thin, non-degenerate surface layers of the star. This efficiency is determined by the atmospheric opacity, and so the presence of a small amount of Hydrogen on the surface of the star can have a dramatic effect on the cooling by virtue of the greater opacity of Hydrogen at the temperatures of observational interest ($T_{eff} \sim 4000 - 15000$ K).

The deposition of Hydrogen as described in section 5.3 takes place in a region on the

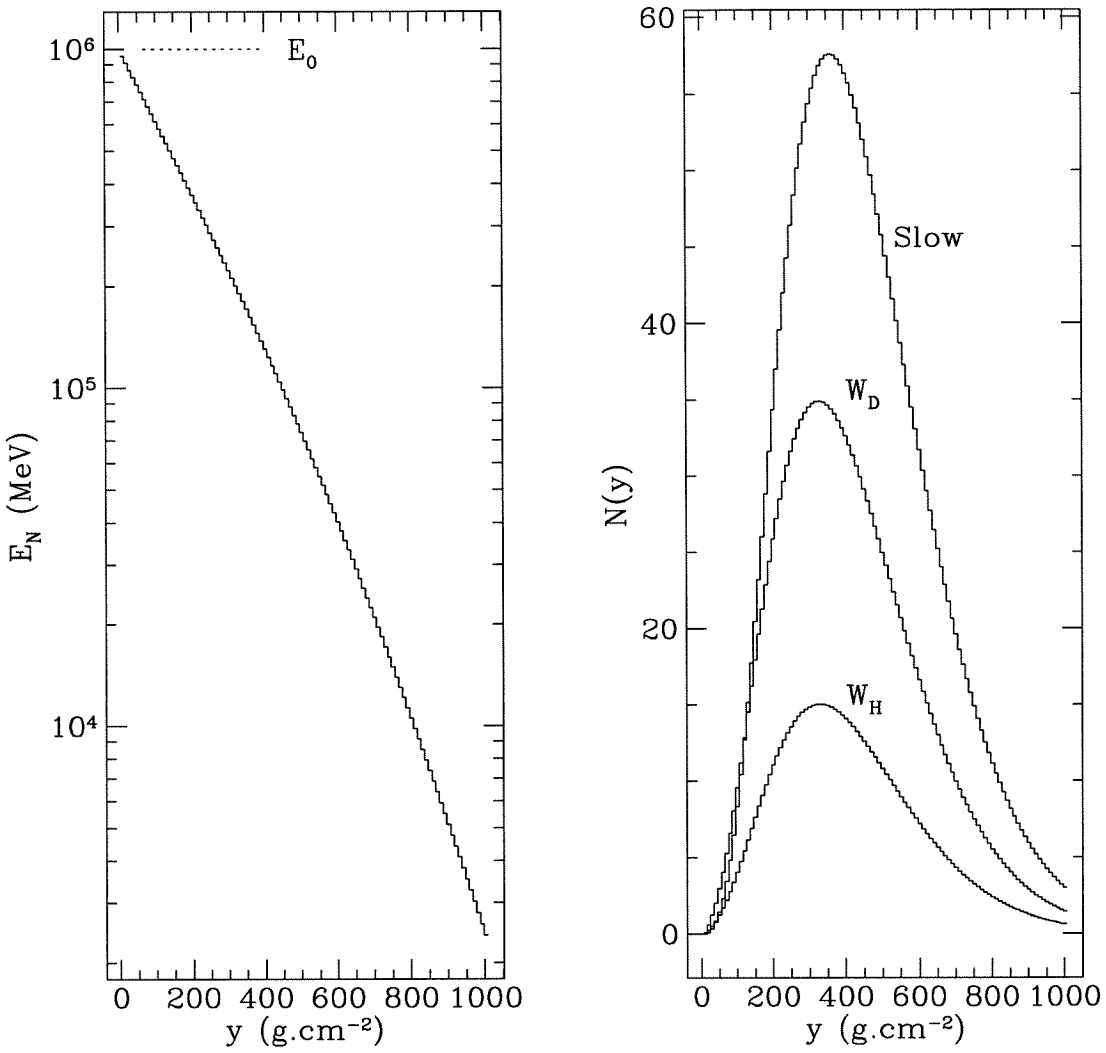

Figure 5.2: **Shower Developement:** The left panel shows the energy in the shower as a function of atmospheric column depth. This is defined as particles of energy $E \geq 50$ MeV. The right panel shows the deposition of various kinds of Hydrogen particles as a function of depth. W_H indicates 'wounded Hydrogen' and W_D indicates 'wounded Deuterium'. The curve labelled slow is shower particles with $E \leq 50$ MeV.

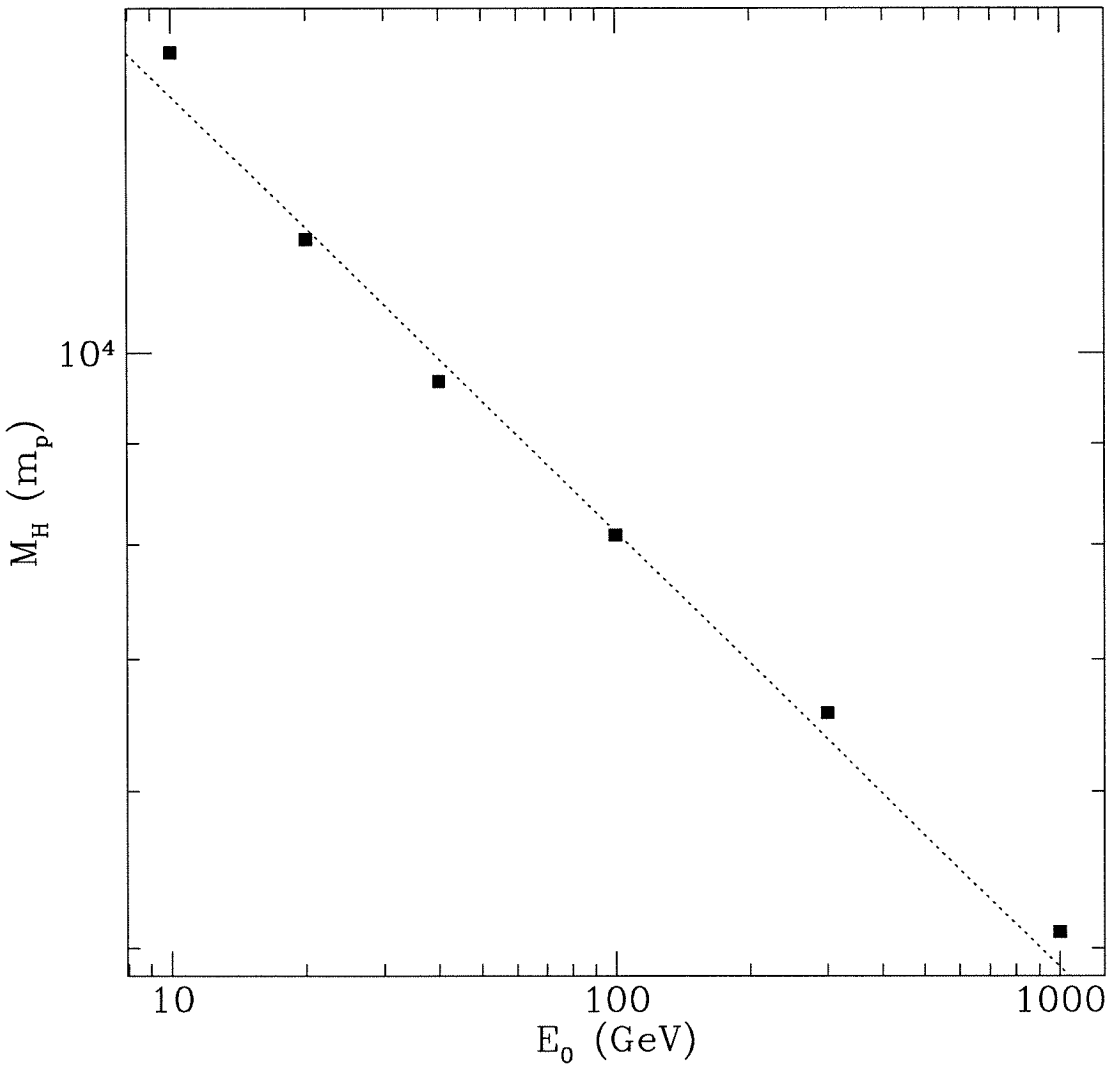

Figure 5.3: **Hydrogen Production Efficiency:** The dotted line is our approximation (5.14) to the calculated efficiencies, determined from our shower calculation.

surface of the white dwarf $\sim y_{stop}$ deep, where $y_{stop} \sim 800\,g.cm^{-2}$, corresponding to a surface mass $\sim 4\pi R^2 y_{stop} \sim 5 \times 10^{-12} R_9^2\, M_\odot$. The spalled Hydrogen will rise to the surface under the action of gravitational separation (Schatzmann (1958)) and will form a surface layer of pure Hydrogen on the surface. This occurs as long as the surface is radiative. The formation of a convection zone will mean that only the material above the convection zone will separate, the rest remaining fully mixed. Thus, the accumulation rate (5.15) will apply only as long as there is no surface convection zone.

For a Helium atmosphere, convection starts at $T_{eff} \sim 25000$ K, so that the star has $\sim 10^6$ years after it starts to shrink from its giant configuration till it forms a surface convection zone. In this period of time, the material will form an amount of Hydrogen

$$M_H \sim 10^{-12} M_\odot \left(\frac{t}{10^6 yrs}\right) \left(\frac{Z/A}{1/2}\right)^{-0.22} \left(\frac{B}{B_0}\right)^{1.78} P_5^{-3.56} R_9^2 P_{days}^{-4/3} \tag{5.16}$$

if the wind is ionic, and an amount

$$M_H \sim 4 \times 10^{-14} M_\odot \left(\frac{t}{10^6 yrs}\right) \frac{\zeta}{f} \left(\frac{B}{B_0}\right)^2 P_5^{-4} R_9^2 P_{days}^{-4/3} \tag{5.17}$$

if the wind is photons and pairs. Using the settling velocity expression of Alcock and Illarionov (1980a), the characteristic[3] settling time $t_{set} \sim z_{stop}/v_{set}(z_{stop})$ is

$$t_{set} \sim 0.025 years \frac{\Lambda_2}{\kappa_{10}} \frac{M/0.3M_\odot}{L/L_\odot} \tag{5.18}$$

where $\kappa_{10} = \frac{\kappa}{10\,cm^2.g^{-1}}$ is the opacity and $\Lambda = \ln\left(1 + 7.14\frac{T_5^4}{y_s g_7}\right)$ is the Coulomb logarithm in terms of the temperature T (in units of 10^5 K), column depth y (in units of $800\,g.cm^{-3}$) and gravity g (in units of $10^7 m.s^{-2}$). For all reasonable values of the parameters, this is much less than the cooling time to formation of a convection zone, and so we may consider the spalled hydrogen to reside on the surface in a layer of mass given by (5.16). We note that this mass is of order of 20% of the entire stopping column mass, which represents a rough upper limit to the amount of Hydrogen that will accumulate. This is because p-p collisions result in losses to pion and electromagnetic cascades and thus the wind that impinges on the white dwarf after the formation of this layer will lose most of its energy to the induced

[3]Note that this is different from the local settling time defined in section 2.6. Our expression here is the time for sedimentation on length scales comparable to the stopping depth of the shower particles.

electromagnetic cascade, resulting in an accumulation rate $\sim 60\%$ of (5.9).

A star modified in this manner will appear initially as a normal DA white dwarf, since the photospheric mass $M_{phot} \sim 4\pi R^2/\kappa \sim 6 \times 10^{-17} M_\odot R_9^2 \kappa_{100}^{-1}$. Figure 5.4 shows the Hydrogen masses for various pulsar companions obtained using equation (5.16). The shaded region indicates the range of photospheric masses expected from our white dwarf models (Chapter 3). We see that all but the most widely separated binaries should have begun their cooling sequence with at least a few optical depths of Hydrogen on their surfaces, even if they lost all of their original Hydrogen envelope in the mass transfer process. Thus, we expect nearly all of these stars to cool with a rate regulated by the Hydrogen opacity at the surface.

As these stars cool, a surface convection zone develops. Depending on the amount of Hydrogen on the surface, this could lead to the dredge up of heavier species into the photosphere. In the case of Helium stars, this leads to the appearance of DAB or DBA stars, depending on the relative abundances of Hydrogen and Helium. For Carbon core stars, this could result in the appearance of DQ stars, such as has been observed in the binary system PSR B0655+64 (van Kerkwijk and Kulkarni (1995)). Nevertheless, we expect all such stars in millisecond pulsar binaries to contain traces of Hydrogen in the atmosphere. The spallation of the molecular Carbon in the PSR 0655+64 companion is unlikely to be observable since the spalled material will be mixed with the entire convection zone, diluting the products beyond observable limits. For PSR 0655+64, a Helium layer of $10^{-4} M_\odot$ and a convective zone Carbon abundance of 10^{-2}, we estimate a destruction rate of Carbon $\sim 5 \times 10^{-24} M_\odot.yr^{-1}$, so that the ratio of products to Carbon $\sim 5 \times 10^{-9}$ after 10^9 years.

5.5 Discussion

The primary intention of this paper is to justify the use of Hydrogen atmospheres in studying the cooling of the white dwarf companions to millisecond pulsars. These cooling rates are used to constrain the ages of the companions and therefore also the millisecond pulsars (Chapter 4). One of the uncertainties in the age determination is the composition of the white dwarf atmosphere. We have demonstrated that it is unlikely that any but the most widely separated companions will have a pure Helium envelope and a correspondingly larger uncertainty in the timing age, regardless of whether the pulsar wind is dominated by ions

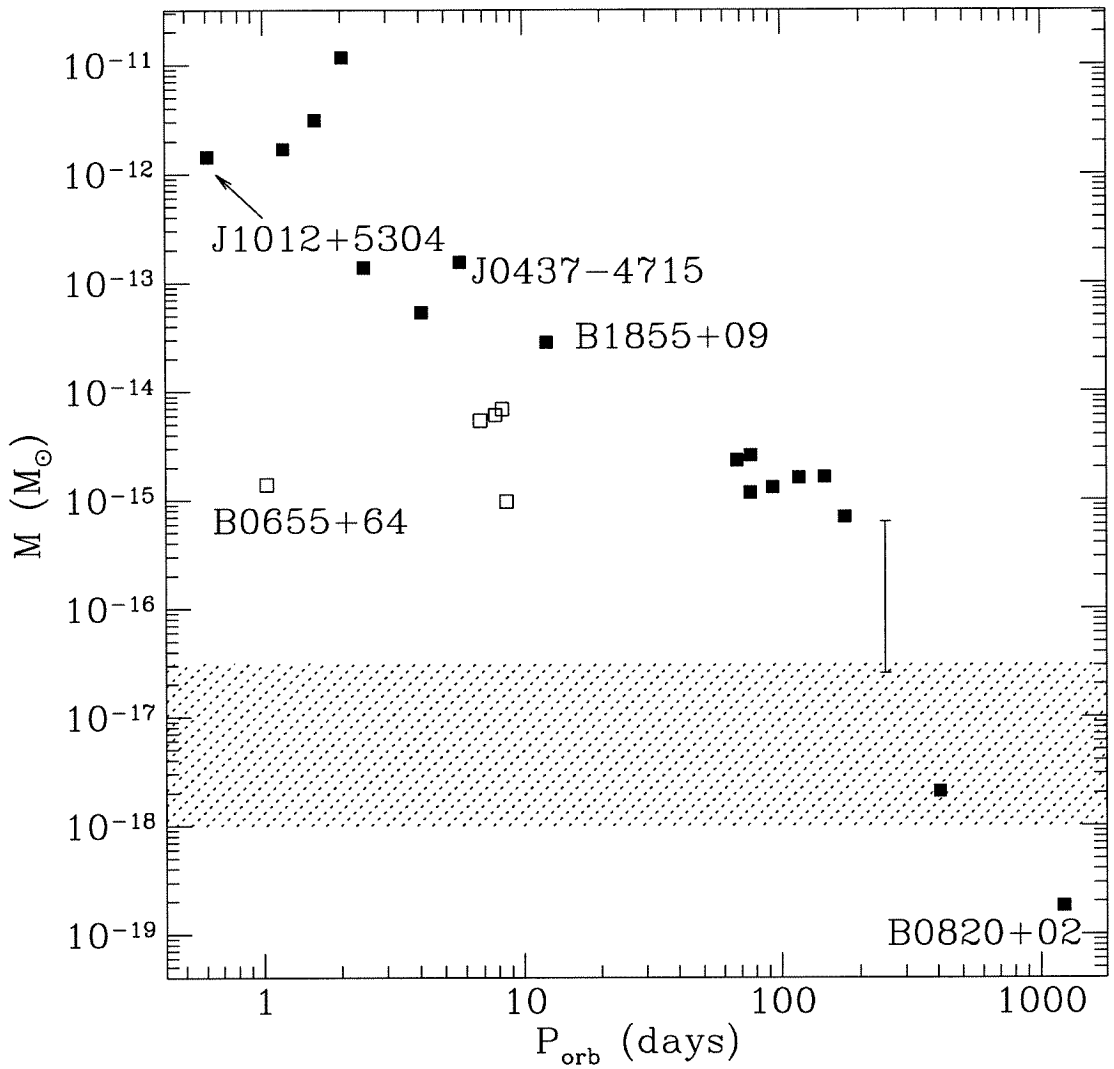

Figure 5.4: **Spalled Hydrogen Masses for known White Dwarfs:** The filled squares are pulsar binaries in which the companion is thought to be a Helium core white dwarf. The open squares are systems in which the companion is thought to be a Carbon core white dwarf. The shaded region indicates the range of photospheric masses obtained from various white dwarf cooling models. These masses assume a pulsar wind dominated by ions. The vertical bar indicates the reduction in the Hydrogen mass if one assumes that the wind is dominated by pairs and photons.

or by electron-positron pairs or by high energy photons. This allows us to constrain the white dwarf/pulsar ages using only our Hydrogen surface models.

The identification of observational signatures of spallation would allow us to study the composition of the pulsar wind, in particular its ionic content. One notable consequence of the above model for an ionic wind is the Deuterium-rich nature of the manufactured Hydrogen. Rapid gravitational settling will lead to the presence of a Deuterium layer between the Hydrogen and Helium layers, shielded by the Hydrogen layer from the debilitating effects of the pulsar wind. Although Figure 5.4 indicates that the bulk of this layer lies at optical depths ≥ 10 for most of the observed companions, the equilibrium scale height is $\sim 40\%$ of the thermal scale height, which is comparable to the optical depth for modest optical depths. Thus it is possible that the tail of the Deuterium layer could be observable. We should note, however, that this will only result if the Hydrogen on the surface of the star is the result of spallation. A pulsar wind acting on a primordial Hydrogen envelope will not produce Deuterium in any observable amounts, because there is no surface Helium to spall.

Figure 5.4 also implies that the companion to PSR 0655+64, identified as a DQ star, should nevertheless possess some Hydrogen on the surface, although it may be hard to detect because of the low effective temperature[4]. Indeed, the determination of accurate photospheric Hydrogen/Helium ratios in white dwarfs has long been a subject of much uncertainty (see Liebert (1991), Bergeron et al. (1990)). Until this problem has been solved, it is unlikely that one will be able to accurately determine the Hydrogen layer mass on the surface of a white dwarf.

REFERENCES

Alcock, C. & Illarionov, A., 1980a, ApJ, **235**, 534.

Alcock, C. & Illarionov, A., 1980b, ApJ, **235**, 541.

Arons, J. & Tavani, M., 1993, ApJ, **403**, 249.

Bergeron, P., Wesemael, F., Fontaine, G. & Liebert, J., 1990, ApJ, **351**, L21.

Eichler, D. & Nath, B.B., 1996, ApJ, **458**, 275.

[4]Nevertheless it is interesting to speculate about the nature of the 4300 $\AA$ feature in the spectrum of van Kerkwijk and Kulkarni (1995). A similar feature in the spectrum of the DQ white dwarf G99-37 is identified as CH in figure 3 of Schmidt et al. (1995).

Fiero, J.M., 1996, P.H.D. Thesis, Stanford University.

Gallant, Y.A. & Arons, J., 1994, ApJ, **435**, 230.

Hester, J.J. & Kulkarni, S.R., 1988, ApJ, **331**, L21.

Hoshino, M., Arons, J., Gallant, Y.A. & Langdon, A.B., 1992, ApJ, **390**, 454.

Kennel, C.F. & Coroniti, F.V., 1984, ApJ, **283**, 710.

van Kerkwijk, M.H. & Kulkarni, S.R., 1995, ApJ, **454**, L141.

Kluzniak, W., Ruderman, M., Shaham, J. & Tavani, M., 1988, *Nature*, **334**, 225.

Kulkarni, S.R. & Hester, J.J., 1988, *Nature*, **335**, 801.

Liebert, J., 1991, IAU Symposium 145, 'Evolution of Stars: The Photospheric Abundance Connection.', eds. G.Michaud & A.Tutukov, p411.

Lynch, W.G., 1987, Ann. Rev. Nuc. Part. Sci., **37**, 493.

Mannheim, K. & Schlickeiser, R., 1994, A&A, **286**, 983.

Meyer, J.P., 1972, A&AS, **7**, 417.

Puget, J.L., Stecker, F.W. & Bredekamp, J.H., 1976, ApJ, **205**, 638.

Phinney, E.S., Evans, C.R., Blandford, R.D. & Kulkarni, S.R., 1988, *Nature*, **333**, 832.

Rosen, L.C. & Cameron, A.G.W., 1972, Ap&SS, **15**, 137.

Rossi, B., 1952, "High Energy Particles", (Prentice-Hall), 81.

Ruderman, M., Shaham, J. & Tavani, M., 1989, ApJ, **336**, 507.

Schatzman, E., 1958, 'White Dwarfs' (Amsterdam: North Holland)

Schmidt, G., Bergeron, P. & Fegley, B, 1995, ApJ, **443**, 274.

Shapiro, S.L. & Teukolsky, S.A., 1983, 'Black Holes, White Dwarfs and Neutron Stars', (Wiley-Interscience).

Tremaine, S. & Żytkow, A., 1986, ApJ, **301**, 155.

Tsao, C.H., Silberberg, R., Barghouty, A.F. & Sihver, L., 1995, ApJ, **451**, 275.

Webber, W.R., Kish, J.C. & Schrier, D.A., 1990, Phys.Rev.C, **41**, 520.

Chapter 6 The Pulsar Planet Production Process

Most plausible scenarios for the formation of planets around pulsars end with a disk of gas around the pulsar. The supplicant author then points to the solar system to bolster faith in the miraculous transfiguration of gas into planets. We here investigate this process of transfiguration. We derive analytic sequences of quasi-static disks which give good approximations to exact solutions of the disk diffusion equation with realistic opacity tables. These allow quick and efficient surveys of parameter space. We discuss the outward transfer of mass in accretion disks and the resulting timescale constraints, the effects of illumination by the central source on the disk and dust within it, and the effects of the widely different elemental compositions of the disks in the various scenarios, and their extensions to globular clusters. We point out where significant uncertainties exist in the appropriate grain opacities, and in the effect of illumination and winds from the neutron star.

6.1 Introduction

Like most things in astronomy, scenarios for the formation of planets and planetary systems around pulsars can be divided into two classes:

1. *Salamander scenarios* (recall that the mythical salamander could survive, even thrive, in fire). In these, the planets were formed as part of the formation of an ordinary main sequence star, and survived its violent transformation to a rapidly spinning neutron star. In this category we may place planets which: survive pre-supernova evolution and the supernova explosion and recoil; spiral into an extended envelope; are the remains of the ablation of a much more massive companion; or are captured from a passing star. These scenarios (reviewed in these proceedings by Podsiadlowski) require unlikely events or physical circumstances of controversial verisimilitude. More importantly, they have nothing new to teach us about planet formation, since such planets would have formed in circumstances similar to the solar system, and the challenge is

to get them to survive, not to make them. We shall thus consider these scenarios no further, as they fall outside the statutory limits of our title.

2. *Memnonides scenarios* (recall that, according to Ovid (8), the Memnonides were birds which annually constructed themselves from the ashes of the warrior Memnon, and circled his funeral pyre). In these the planets are formed from the scattered remains of a disrupted, evaporated, ablated, or otherwise dismembered star (for a comprehensive description of the proposed scenarios, see the review by Podsiadlowski in these proceedings). Neutron stars surrounded by gaseous stellar remains are ubiquitous in standard models of binary evolution, supernovae, and globular cluster pulsar formation. White dwarf analogues are also ubiquitous. Understanding the evolution of such gaseous remnants around degenerate stars is consequently of general importance, whether or not they ultimately transfigure themselves into planets.

6.2 Synopsis of Memnonides Scenarios

In table 6.2, we summarize the Memnonides scenarios which have been proposed, listing for each the physical properties of the initial gaseous disk (our personal favourite, number 5 in the table, a suggestion of C. Thompson, is illustrated in figure 6.1). There are many significant differences between the conditions in the gaseous disks produced by these scenarios and the conditions in the Solar nebula.

1. *The large luminosity of the central source.* In all the scenarios, $\geq 10^{-2} M_{\odot}$ is accreted toward the neutron star. Averaged over a typical planet formation timescale of 10^6 y (see below), this corresponds to an accretion rate of $\geq 10^{-8} \mathrm{M}_{\odot}\,\mathrm{y}^{-1}$, giving a luminosity $\sim 10^{38}\,\mathrm{erg\ s}^{-1}$, about the Eddington luminosity for the neutron star. At 0.4 AU from such a luminosity, the black body temperature is $\sim 6,000$ K, well above the sublimation temperature for even the most refractory solids. To make planets it is therefore crucial either to shield any coagulating dust and planetesimals from this radiation, or more likely, to wait until the rate of accretion onto the central source has dropped below $10^{-10} \mathrm{M}_{\odot}\,\mathrm{yr}^{-1}$. In scenarios 2–5, naïve application of standard disk models (see below) would predict that most of the mass would try to accrete in

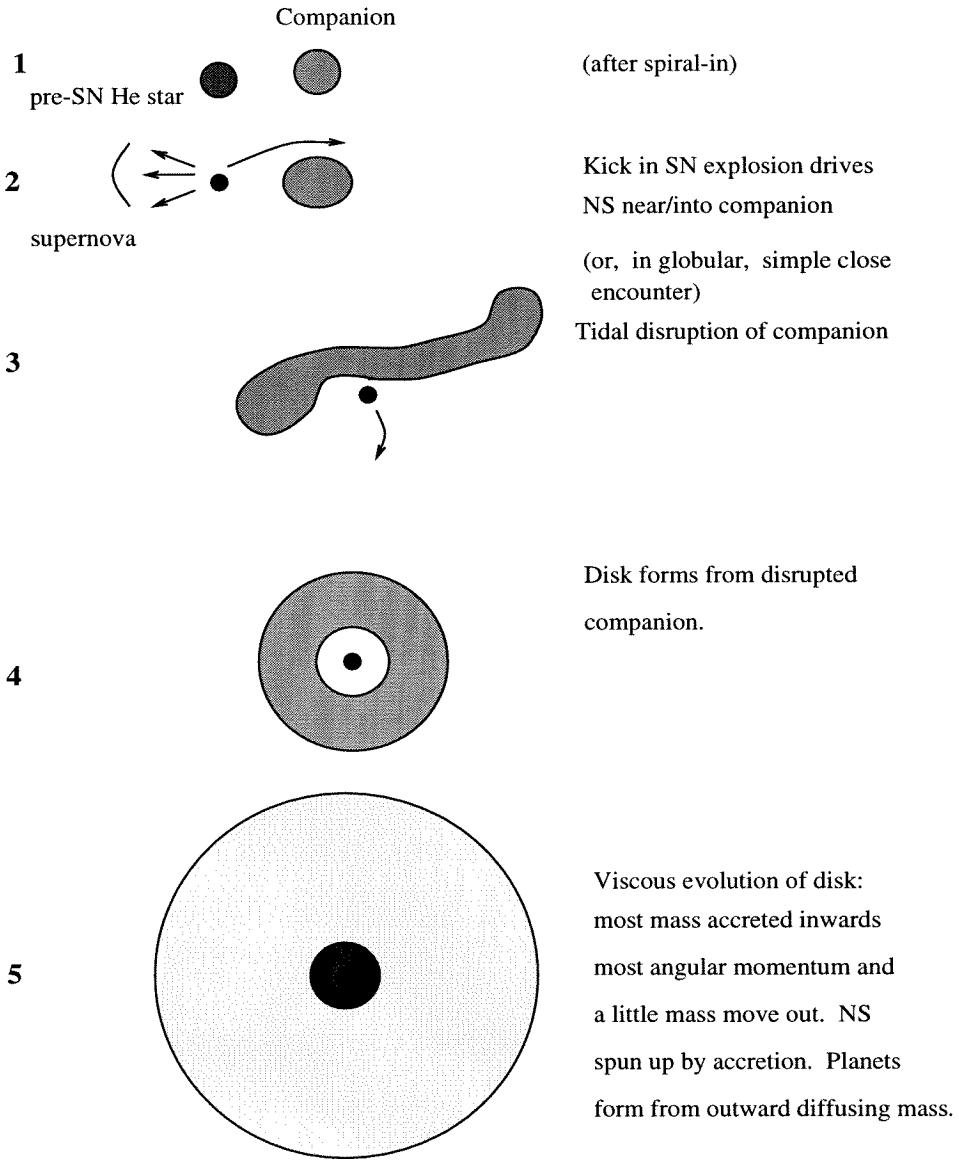

Figure 6.1: **Cartoon of Memnonides Scenario no. 5 of Table 6.2:**. Steps 3–5 could also occur in a globular cluster, during the close encounters which are believed to produce many of the cluster pulsars and X-ray binaries. Steps 3–5 are also representative (with modest changes of scale) of all the other scenarios in Table 6.2.

$\leq 10^4$ y. Since this would lead to an enormously super-Eddington luminosity, the bulk of the mass evidently cannot be accepted by the neutron star, and must be ejected from the system. It is energetically possible for the resulting wind to carry off the incipient outer disk, and thus prevent planet formation altogether.

2. *The planets must be formed from the expanding, not the contracting parts of the nebula* in all the scenarios of table 6.2, except for no. 6. The planets inferred around PSR 1257+12 (Wolszczan & Frail 1992; Wolszczan, these proceedings) lie at radii much larger than the initial radii of the gaseous disk. In standard viscous disk models, this does not present an insuperable difficulty, since the total angular momentum J of the matter in the disk is nearly conserved (negligible angular momentum is accreted onto the point-like neutron star), so $J_d = M_d(t)\sqrt{GMa(t)} = \text{const}$. Since for most reasonable viscosities, the bulk of the mass of the disk is near its outer edge, of radius $r_e(t)$, it follows that

$$r_e(t) \sim r_e(0) \left[\frac{M_d(0)}{M_d(t)}\right]^2 . \qquad (6.1)$$

As the mass of the disk drops through accretion, it must move outwards to conserve angular momentum. The fact that, at most (see worries about super-Eddington winds in (1) above) $\sim [r_e(0)/0.4\,\mathrm{AU}]^{1/2}$ of the total initial disk mass reaches the radii of PSR 1257+12's planets means that in scenarios 1–4 (and to a lesser extent in scenario 5), mass at the desired planetary radii is a dangerously scarce commodity, requiring the planet formation to be quite efficient (see also figure 6.5). In some of the models which have been proposed for the ionized parts of accretion disks in active galactic nuclei (Blandford & Payne 1982, Blandford 1976) and adapted to protostellar disks (Königl 1989), all of the disk's angular momentum is removed in a magnetised wind, and the disk mass simply accretes *without* any outward expansion of the disk. If these models applied to the early evolution of the circumpulsar disks, they would lead to the failure of all of scenarios 1–5 [no. 6 would survive, but in this scenario it is difficult to explain the apparently high proper motion of PSR 1257+12 (Wolszczan, these proceedings)]. Those (including the authors) with an attachment to these scenarios might then take the existence of planets around PSR 1257+12 as an indication

that disks solve their angular momentum problem by viscous transport (e.g., via small-scale magnetic cells), not by angular momentum ejection along a global magnetic field.

3. *The grain opacities could be quite different from those in the ISM and the protosolar nebula.* In Memnonides scenarios there is no dust initially present in the disk. In the solar nebula, aboriginal dust nuclei from the interstellar medium (from the winds of carbon and other extreme giant stars, and perhaps from supernovae) can simply grow by sticking atoms they encounter to their surfaces. In a pulsar nebula, by contrast, the gas must first supercool and nucleate grains. The high densities and long evolution times (respectively thousands of times higher and longer than in red giant photospheric winds —cf. Frenklach *et al.*, 1989*a, b* for discussion of formation of PAHs and silicon carbide grains in red giants) suggest that this should present no difficulty. However, the different environment is likely to yield a different density of nucleation sites and rate of grain growth. Grain radius a grows as $\dot{a} \sim 30\,\mu\mathrm{m\ yr}^{-1}$ in solar metallicity disks with the properties shown in figure 6.4. Consequently, the grain size distribution, and therefore the opacity κ, could be very different from those assumed in the opacity tables used in solar nebula models (and in the rest of this paper). Simple classical nucleation theory (Salpeter 1974; note, however, that this is rarely applicable! —cf. Frenklach *et al.* 1989b) would predict that the density of nucleated grains scales roughly as the inverse of the cooling time, so that the grains in the circumpulsar disk would be $\leq 10^{-3}$ times as numerous as in the protosolar disk, but $\geq 10^3$ times more massive, i.e., ≥ 10 times larger. To see the consequences for the circumpulsar disk, define the viscous stress as αp (hence viscosity $\nu = (2/3)\alpha c_s^2 \Omega^{-1}$ for a Keplerian disk of angular velocity $\Omega = (GM/r^3)^{1/2}$ and isothermal sound speed c_s), and equate the dissipation per unit area of the disk (see 6.4) to the radiation flux diffusing out. This gives an implicit equation for the disk surface density Σ as a function of temperature and radius:

$$\Sigma(T) \simeq \left(\frac{32\sigma_b \mu}{9\alpha k_b}\right)^{1/2} \left[\frac{T^3}{\kappa(\rho, T)}\right]^{1/2} \Omega(r)^{-1/2}, \tag{6.2}$$

where σ_b is the Stefan-Boltzmann constant, T, the temperature at the midplane of the disk, and ρ, the density there, $\rho(r, \Sigma, T) = \Sigma\Omega/(2c_s)$. Since grain opacity is only

weakly dependent on ρ, it follows that $\Sigma(T) \propto a^{1/2}$ (a^1) for $ak_bT/(hc) \gg 1$ ($\ll 1$), where a is the typical grain size, k_b, the Boltzman constant, and h, Planck's constant. The grain size distribution thus determines the structure and evolution of the disk once it cools below $\sim 3000\,K$.

4. *The heavy element abundances may be quite different from solar.* In scenarios 1 and 2, the disk may be formed almost entirely of heavy elements, with a mixture quite different from cosmic (e.g., nearly pure C, O or Si). This dramatically increases the mean mass per particle μ in the neutral gas phase (recall that the thickness of a thermally supported disk $h \propto (T/\mu)^{1/2}$), and the opacity in almost all phases, bottling up the radiation and increasing the midplane temperature of the disk. Scenarios 3–5 can operate in globular clusters which have heavy element abundances as low as 10^{-2} of solar. Over most of their evolution, such disks are much colder at given surface density and radius than the solar nebula. But for the high central source luminosity, these could form planets at smaller radii than Galactic systems.

	$J_{\rm disk}$	$R_{\rm disk}$	$Z_{\rm CO}/Z_\odot$	$Z_{\rm Si,Fe}/Z_\odot$	$V_{\rm sys}$	Age of NS at Planet form.	Occur in glob clust?	WD analogue?
	(g cm^2 s^{-1})	AU			(km s^{-1})	(y)		
Solar nebula	$> 10^{52}$	> 10	1	1	20			
Memnonides Scenario		initial						
1. Supernova fallback	10^{49}	10^{-5}	~ 100?	~ 100?	any	10^6	No	No
2a. NS disrupt WD	10^{50}	10^{-4}	~ 100	1	any	$> 10^8$	Yes	—
2b. WD disrupt WD	10^{50}	10^{-4}	~ 100	1	~ 20(Pop I)	AIC	Yes	Yes
3. Unstable xfer disrupt compan. $M_c \sim 0.1 M_\odot$	10^{50}	10^{-3}	1	1	any	$> 10^9$	Yes	Yes
4. Nonconservative xfer/evap forms circumbinary disk	10^{50}	10^{-2}	1	1	any	any	Yes	No
5. Supernova recoil into companion	10^{51}	$10^{-2.5}$	1	1	> 100	10^6	(tidal cap)	(GC only)
6. Disk captured from Be* wind	10^{52}	1	1	1	~ 20	$< 10^7$	No	Yes
PSR 1257+12	$> 10^{50} \frac{Z_\odot}{Z}$	$a \sim 0.4$	—	—	~ 200?	lo B $\rightarrow >$ 10^7?		

Table 1: Memnonides scenarios for pulsar planet formation

In the particular application to PSR 1257+12, scenarios 1, 2b, 5 and 6 require the pulsar to have evolved in a way which would before 1988 have been considered ridiculous, but is now more fashionable (on phenomenological, not theoretical grounds). PSR 1257+12 belongs to the distinct group of pulsars with low magnetic dipole moments and high spin frequencies which are found (with the sole exception of PSR 1937+21) only in binary systems and in globular clusters (see review by van den Heuvel in these proceedings). These differ from isolated Galactic pulsars both in being much older ($\geq 10^8$y vs. $\leq 10^7$y) and in having accreted from companions. Before 1988, it was generally accepted that the significant difference was the age difference, and that neutron star magnetic fields decayed spontaneously (Narayan & Ostriker 1990). This belief was not hindered by an absence of theoretical justification (cf. review by Goldreich & Reisenegger 1992). More recent data and analyses of pulsar kinematics (Bhattacharya *et al.* 1992) and X-ray binary evolution (Verbunt *et al.* 1990) suggest that the fields may not spontaneously decay. It has thus become fashionable to argue that the significant difference between the high and low field pulsars is not their age, but the fact that the low field pulsars have accreted (cf. Romani 1990). Though the observational and theoretical justification for this view are far from compelling, they would permit a young, high-field neutron star to be turned into a low field pulsar like 1257+12, thus saving scenarios 1, 2b, 5 and 6.

6.3 Vicious Assumptions

In this section, we examine the transfiguration of the hot gas of a dismembered star into a disk of gas large and cool enough to begin forming planetesimals. In doing so, we make three major assumptions whose validity can be questioned.

1. *Neglect self-gravity in the early stages of the disk evolution.* In scenarios 1, 2, 3 and 5, the disrupted companion initially forms (in a few dynamical times) a thick radiation-pressure supported torus with an Eddington-limited luminosity (Evans & Kochanek 1989, Frank 1978, Abramowicz *et al.* 1978), which must last for at least

$$\tau_{\rm KH} \sim \frac{\rm GM_c^2}{\rm R(init)L_{Edd}}, \tag{6.3}$$

which is of order 10 y for a disrupted main sequence star, and of order 10^3 y for a disrupted white dwarf. In scenarios 2 and 5, the resulting torus is massive enough that it is susceptible to the m=1 and 2 fission instability (the I-mode of Christodoulou & Narayan 1992), and may gather itself in a few orbits into a single orbiting lump, rather than an axisymmetric disk. In scenarios 1 and 3, the torus is less massive, but as it loses internal energy and ceases to be supported by internal radiation pressure, it becomes Jeans unstable (the J-mode of Christodoulou & Narayan 1992) and breaks up into many orbiting lumps. Gravitational interactions between these lumps will spread the lumps over a wider range of radii, where on a longer timescale viscosity might be able to smear them back into an axisymmetric disk, now of much wider radial extent, which would then be Jeans stable (see below). We assume that this occurs, and begin our calculations with an axisymmetric disk which has lost its initial internal energy (i.e. we start at $t \gg \tau_{KH}$).

2. *Neglect the effect of radiation from the neutron star and inner disk on the outer disk.* In scenarios 1, 2, 3, 5 and 6, the neutron star initially accretes at a highly super-Eddington rate. As discussed above, the wind from the inner disk could then have a dynamical effect on the outer disk, perhaps blow it away. Even as the luminosity drops below Eddington, the neutron star and inner disk can still affect the evolution of the entire disk. The surface density distribution and rate of radial spreading of the disk are controlled in part by the thermal structure of the disk. If the temperature drops more slowly than $T \propto r^{-1}$, then the disk half-thickness $h \propto T^{1/2} r^{3/2}$ increases faster than r^1, i.e., h/r increases with r. This occurs, for example, in the inner regions of the disk where bound-free ($h/r \propto r^{0.08}$) and electron scattering opacity ($h/r \propto r^{0.05}$) dominate, and in the optically thin outer ice grain regions. When

$$L_c \frac{d\ln(h/r)}{d\ln r} > \frac{3}{2}\frac{GM\dot{M}}{r}\,; \text{i.e.} \quad \frac{d\ln(h/r)}{d\ln r} \geq 15\frac{GM}{rc^2}\,, \tag{6.4}$$

which is satisfied for all the regions mentioned above for $r \geq 10^8$ cm, the flux absorbed from the vicinity of the neutron star exceeds the flux generated locally by viscous dissipation in the disk. The temperature and vertical temperature structure of the disk are then substantially different from those in standard disk models. Even if h/r

decreases with r, radiation scattered down from a wind above the disk can provide significant surface heating. The far infrared spectra of protostellar nebulae appear to require such scattering (or some other means of heating the outer disk far more than standard disk models predict —Kenyon & Hartmann 1987). The most serious effects occur in the outer (ice-coated grain) regions. The surface heating can stabilize the disk against convection, which is sometimes argued to provide the turbulent eddy viscosity justifying an α-viscosity prescription (e.g., Ruden *et al.* 1988; see discussion under (3) below, however). Furthermore, even a small fraction f ($f \sim \max[d\ln(h/r)/d\ln r, \tau_w]$, where τ_w is the scattering optical depth between r and 2r in the wind above the disk) of the central source luminosity L can sublimate the solid grains crucial for planetesimal formation, if incident on the disk. Consider grains with a sublimation temperature $T_{sub} = 10^3 T_{s3}\,K$. Graphite grains sublimate at $T_{s3} \sim 2$ in the solar nebula, and at $T_{s3} \sim 4$ in the denser, C-rich environment of a disrupted white dwarf disk. Ice grains sublimate at $T_{s3} \sim 0.2$ in the solar nebula, and at $T_{s3} \sim 0.25$ in the disk of a disrupted main sequence star. Grains of the given sublimation temperature will not form inside

$$r_{sub} = 2(fL/10^{36}\,erg\ s^{-1})^{1/2} T_{s3}^{-2}\,AU\,. \tag{6.5}$$

Note that grains smaller than $\sim 10\,\mu m$ are transparent to the keV X-rays from the neutron star, but also radiate inefficiently at frequencies $\nu \sim kT/h$, so both heating and cooling rates scale with volume for small grains; for larger grains, they scale with area. Equation 6.5 applies roughly to both. We see that at the ~ 0.4 AU radius of the planets around PSR 1257+12, refractory grains cannot form until $fL \leq 10^{36}\,erg\ s^{-1}$ (i.e., $f\dot{M} \leq 2\times10^{-10} M_\odot\,y^{-1}$), and ice grains until $fL \leq 2\times10^{33}\,erg\ s^{-1}$ ($f\dot{M} \leq 5\times10^{-13}\,M_\odot\,y^{-1}$), less than the current pulsar spin-down luminosity $I\Omega\dot{\Omega} \simeq 2\times10^{34}\,erg\ s^{-1}$ (as we discuss in 6.7, the pulsar wind luminosity is likely to be in such a penetrating form that equation 6.5 does not apply to it). In gas of solar metallicity, the X-rays penetrate only $\sim 0.1\,g\ cm^{-2}$, less than 10^{-5} of the total disk surface density $\geq 10^4\,g\ cm^{-2}$ at 0.4 AU required to make the planets of PSR 1257+12. The shielded inner layers of the disk will then be heated by the inward-diffusing infrared reradiation from the directly heated gas. When the infrared optical depth is high, the temperature of the shielded layers can be somewhat cooler than (6.5) would indicate. Any illuminated

but not sublimated grains with radii $a < 0.4(L/10^{38}\,\mathrm{erg\ s^{-1}})\,\mathrm{cm}$ will feel a radiation pressure force exceeding the force of gravity, and can drive a wind from illuminated dusty surfaces of the disk.

3. *We adopt an α viscosity prescription.* We assume the viscous stress in the disk to be given by αp, with α a constant of order 10^{-2}–10^{-1}, and p the gas pressure. This gives a viscosity

$$\nu = \frac{2}{3}\alpha c_s^2 \Omega^{-1}\,. \tag{6.6}$$

In the ionized portions of the disk this popular prescription has been lent new respectability by the demonstration by Hawley and Balbus (1991) and Balbus and Hawley (1992) that any weak magnetic field in the disk will grow exponentially on the orbital timescale until it becomes dynamically important (forcing reconnection, or rising buoyantly out of the disk).[1] A dynamically important field gives $\alpha \sim B^2/(8\pi p)$, and models of flux loops (Coroniti 1981, Sakimoto and Coroniti 1989) suggest $\alpha \sim 10^{-2}$. In the outer neutral regions of the disk, turbulent convection has been suggested to provide an $\alpha \sim 10^{-2}$ in the optically thick regions of the disk (Ruden *et al.* 1988, though in the linear regime convective modes carry angular momentum *inwards*, not outwards, and thus do not have the characteristics of viscosity —Ryu & Goodman 1992). Ambipolar diffusion through a global magnetic field (Königl 1989) can also remove angular momentum, but as discussed in 6.2, this does not act like a true viscosity, and the disk does not expand outwards as required in scenarios 1–5.

6.4 Viscous Development

A thin viscous accretion disk operates as follows. Relative to disk material at some distance r from the neutron star, matter closer to the neutron star is moving faster, and matter on the outside moving slower. Across the mean free path of the viscosity (e.g., magnetic cell or convection cell size, both of order the disk thickness h if $\alpha \sim 1$), matter on the inner

[1] The objection of Knobloch (1992) that the linear instability is strictly an overstability for non-vertical fields is of purely semantic interest. With *any* realistic seed field expected in a disrupted star, the exponential growth of the "overstability" for any field orientation will have reached the nonlinear phase simulated by Hawley *long* before the linear overstability would have begun oscillating.

fast track and the outer slow track share momentum. Thus the inner matter on average loses momentum (hence angular momentum) and the outer matter gains it. The inner mass, losing angular momentum, spirals inwards, accreting, while the outer matter will move outward, unless there is matter beyond it to which it can in turn transfer its angular momentum.

In the standard model of a neutron star accreting from a companion star orbiting it, mass is lost from the companion at the L1 point, and forms an accretion disk around the neutron star. Initially the disk is quite small (~ 0.1 the Roche lobe size), but as discussed above, the outward transport of the angular momentum lost by matter accreting toward the neutron star makes the disk expand outward until its edge is close enough to the companion that gravitational torques can transfer the angular momentum back to the companion star. The disk thus has a sharp outer edge, close to a resonance (Goldreich & Tremaine 1982, Priedhorsky & Verbunt 1988, Whitehurst & King 1991). In the Memnonides scenarios (save no. 6), there is no outer companion, and the disk is free to expand forever.

The time evolution of a disk of surface density Σ and viscosity ν (given, for our purposes, by equation 6.6) is thus described by a diffusion equation

$$\frac{\partial \Sigma}{\partial t} = \frac{3}{r}\frac{\partial}{\partial r}\left(r^{1/2}\frac{\partial}{\partial r}\left[\nu \Sigma r^{1/2}\right]\right) , \tag{6.7}$$

(cf. Frank, King & Raine 1992) provided that we ignore winds from the disk, and interpret ν as the vertically-averaged viscosity. The energy per unit area produced by viscous dissipation on each side of the disk midplane is

$$F_H = \frac{9}{8}\Sigma \nu \Omega^2 , \tag{6.8}$$

which must be balanced by radiative losses if the disk is to remain thin. Substituting (6.6) and equating to the radiation flux in the diffusion approximation (large optical depth) then gives us equation (6.2), with κ a Rosseland mean opacity. Equations (6.7), (6.6), and (6.2), together with an opacity table $\kappa(\rho, T)$, and $\rho = \Sigma\Omega/(2c_s)$ from vertical hydrostatic equilibrium then give a complete set of equations for the evolution of a disk. Given Σ at some r, (6.2) determines T and hence all the other disk properties, including $\nu(\Sigma, r)$ which can then be substituted into (6.7) and evolved.

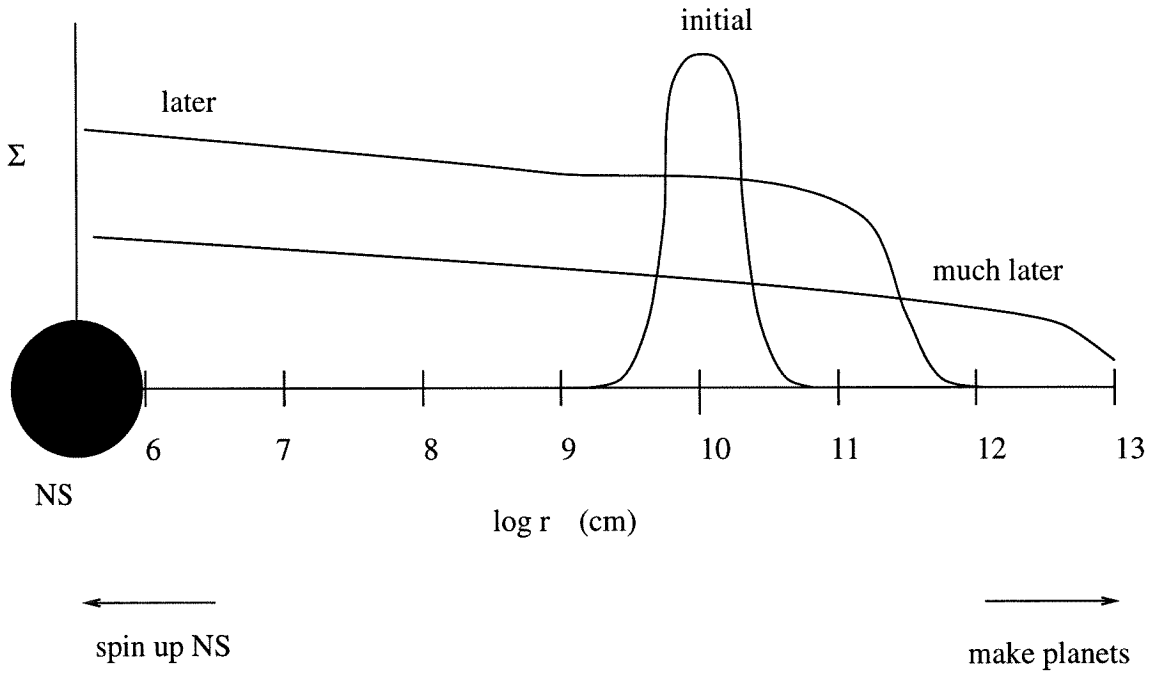

Figure 6.2: **General Features of the Evolution of a Viscous Disk.**

The general character of the evolution from a torus of radius R(init) (see table 6.2) is as follows (see figure 6.2). Most of the mass rapidly accretes inwards, but a small fraction of the mass (usually given by (6.1)) moves outwards to conserve angular momentum. At some particular radius r > R(init), the surface density of the disk will initially rise (as the outer edge of the disk approaches r), and then fall (as the outer edge moves beyond r, and the mass of the disk continues to drop by accretion). The surface density at r > R(init) thus reaches a maximum at a time $t_m(r)$. At this time, the maximum mass is available to form planets near r, provided that the disk is there cool enough to form grains. If it is not, one must wait until it has cooled further, but the surface density and available mass will then be much less.

6.5 Matched Quasi-Static Similarity Solutions

We have integrated the differential equation (6.7) directly (see 6.6), but we have found that its solutions, even for disks with realistic opacities, can be represented well by analytic (algebraic) solutions which we now describe. These allow us to quickly survey parameter

space, and the effects of changes in opacity, composition, etc.

As described following (6.8), using the α prescription, the thermal and vertical hydrostatic equilibrium conditions for a given opacity, determine the midplane temperature T, viscosity ν and disk thickness h all as functions of the surface density and radius. For an opacity law

$$\kappa = \kappa_0 \rho^m T^n , \tag{6.9}$$

we have that

$$T = \left(\frac{9\alpha\kappa_0}{32\sigma_b}\right)^{\frac{2}{6-2n+m}} \left(\frac{k_b}{\mu m_p}\right)^{\frac{2-m}{6-2n+m}} \Sigma^{\frac{2m+4}{6-2n+m}} \Omega^{\frac{2m+2}{6-2n+m}} \tag{6.10}$$

$$\nu = \frac{2}{3}\alpha^{\frac{8-2n+m}{6-2n+m}} \left(\frac{9\kappa_0}{32\sigma_b}\right)^{\frac{2}{6-2n+m}} \left(\frac{k_b}{\mu m_p}\right)^{\frac{8-2n}{6-2n+m}} \Sigma^{\frac{2m+4}{6-2n+m}} \Omega^{\frac{m+2n-4}{6-2n+m}} \tag{6.11}$$

$$h = \left(\frac{k_b}{\mu m_p}\right)^{1/2} \frac{T^{1/2}}{\Omega} \tag{6.12}$$

where $\Omega = (GM/r^3)^{1/2}$ is the Keplerian angular velocity, μ is the mean particle mass in units of m_p and σ_b is the Stefan-Boltzmann constant.

Thus, we have the viscosity in the functional form

$$\nu = \nu_0 \Sigma^q r^p . \tag{6.13}$$

Since for most opacities the viscous timescale (inflow time) decreases inwards, the inner parts of the disk must have reached a quasi-steady state, with $\dot{M} = 3\pi\nu\Sigma$ nearly independent of r. Since even at a maximal spin period ~ 0.7 ms, a neutron star cannot have angular momentum $> 10^{49}$erg s, loss (or gain) of angular momentum to it will not have a significant effect on the total disk angular momentum in any scenario (except possibly no. 1). Thus the total disk angular momentum $J \sim \Sigma(r_e) r_e^4 \Omega(r_e)$ where r_e is ~ 0.7 times the radius of the outer edge of the accretion disk. The viscous timescale there is $t_\nu \sim r_e^2/\nu$, which is also of order the time t for the outer edge of the disk to reach r_e. Combining these equations, we have

$$r_e \propto t^{2/(4-2p+5q)} J^{2q/(4-2p+5q)} , \tag{6.14}$$

$$\dot{M} \propto t^{-1-1/(4-2p+5q)} J^{1-q/(4-2p+5q)} . \tag{6.15}$$

These suggest the existence of more rigorous similarity solutions, which indeed there are. Pringle (1991; see also Cannizzo *et al.* 1990) has shown that similarity solutions of the Zel'dovich-Raizer type can be found for (6.7) when ν is of the form (6.13), i.e. (6.11). Two different types of similarity solution can be found depending on whether the mass or the angular momentum of the accretion disk is conserved. The solution for the angular momentum conserving case is given below.

$$\Sigma = \Sigma_0 x^{-3} \tau^{-2\lambda} \xi^c (1 - k\xi^b)^a , \tag{6.16}$$

where $x = (r/r_0)^{1/2}$, $\tau = \frac{3}{4}\nu_0 r_0^{p-2}\Sigma_0^q t$, $\xi = x\tau^{-\lambda}$ and

$$a = 1/q \tag{6.17}$$

$$b = 1 + c \tag{6.18}$$

$$c = \frac{3q + 3 - 2p}{1 + q} \tag{6.19}$$

$$\lambda = 1/(5q + 4 - 2p) \tag{6.20}$$

$$k = q\lambda/(4q + 4 - 2p) . \tag{6.21}$$

The opacity table used here (all quantities in cgs units) is based on that of Lin & Papaloizou (1985), with an electron scattering opacity added for high densities.

1. Electron scattering: $\kappa = \kappa_1$, where $\kappa_1 = 0.2(1 + X)$, and X is the mass fraction of hydrogen. This opacity is valid for $T \geq 4.55 \times 10^8 \rho^{2/5}$ K.

2. Free-Free/Bound-Free: $\kappa = \kappa_2 \rho T^{-2.5}$, where $\kappa_2 = 1.5 \times 10^{20}$. This opacity is bounded from below by $T = 1.76 \times 10^4 \rho^{1/21}$ K. Instead of the partially ionized opacity favoured by Lin and Papaloizou, we approximate the ionization front as a discontinuous jump into the molecular dissociation and grain evaporation regime, which is characterised by the following two opacities.

3. $\kappa = \kappa_3 \rho^{2/3} T^3$, $\kappa_3 = 2 \times 10^{-8}$. In the temperature and density regime used here, this opacity rarely comes into play, the transition usually taking place from opacity 2 to:

4. $\kappa = \kappa_4 \rho^{2/3} T^{-9}$, $\kappa_4 = 2 \times 10^{34}$. This opacity is bound from above by T = 3000 K, and from below by $T = 4.6 \times 10^3 \rho^{1/15}$

5. The next three opacities are due to various types of grains: $\kappa = \kappa_5 T$, $\kappa_5 = 5 \times 10^{-3}$, and bounded from below by T = 210 K. This is representative of the high-Z refractory grains thought to be important in terrestrial planet formation.

6. $\kappa = \kappa_6 T^{-7}$, $\kappa = 2 \times 10^{16}$. This is bounded below by T = 170K.

7. Below 170 K, the opacity is represented by the ice grain opacity $\kappa = \kappa_7 T^2$, $\kappa_7 = 2 \times 10^{-4}$.

These opacities map out a "phase diagram" in the T-ρ plane, as shown in Figure 6.3.

By associating a single opacity with a given range of density and temperature in the disk, we can build an analytic model of the disk by linking the similarity solutions for different opacities. Each similarity solution has two free parameters, Σ_0 and τ. The τ value of the outermost similarity solution is fixed by the disk outer radius, where $\Sigma = 0$. The τ's of the inner solutions are fixed such that each similarity solution would have its edge at the same place if it were extended to T = 0. The other boundary condition, i.e., that which determines Σ_0, is that the accretion rate $\dot{M}$ remains constant across the boundary between two similarity solutions. The accretion rate at radius r can be calculated from $\dot{M} = \partial g / \partial h$ (Lynden-Bell & Pringle 1974), where g is the torque exerted by the outer annulus on the inner annulus and h is the specific angular momentum at r. This leads to an expression

$$\dot{M} = 6\pi \nu_0 r^{1/2} \frac{\partial}{\partial r} \left[r^{p+1/2} \Sigma^{1+q} \right] . \tag{6.22}$$

Except at the extreme edge of the accretion disk, each similarity solution may be characterised by a power law of the form $\Sigma \propto r^{-p/(1+q)}$, and thus the accretion rate is constant throughout most of the disk. Thus the outer radius and the accretion rate at the inner edge define the patchwork accretion disk completely.

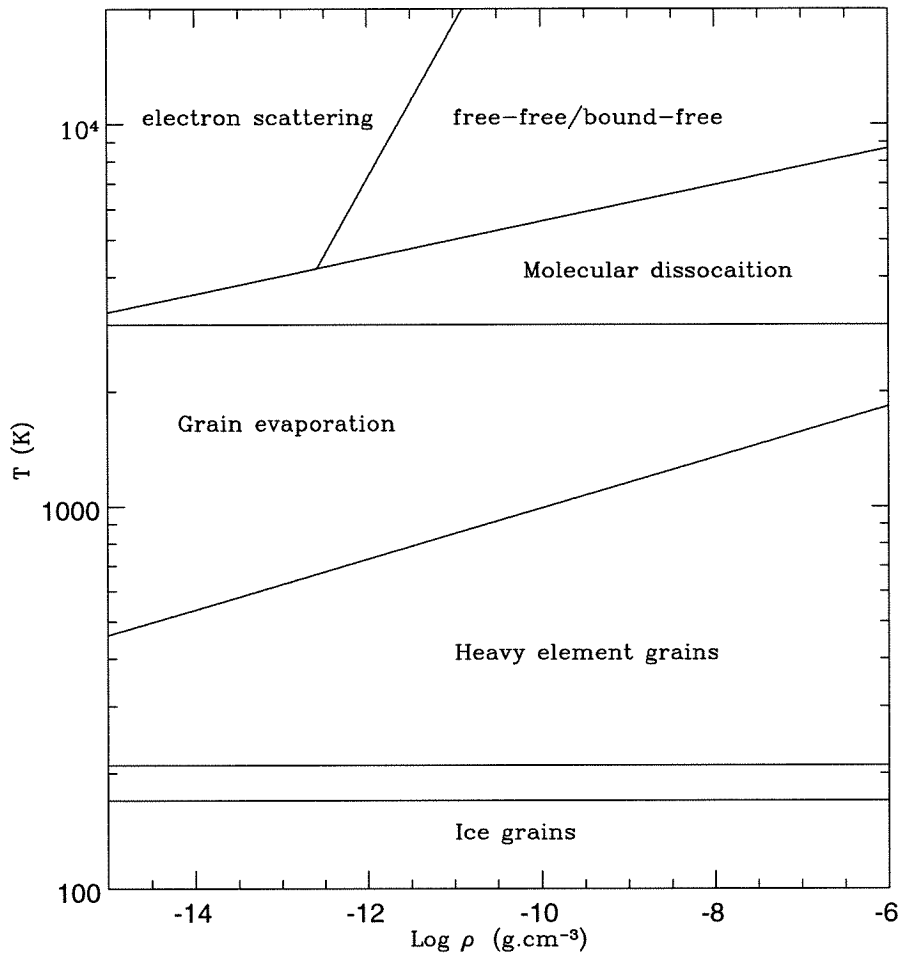

Figure 6.3: **The Phase Diagram:** Here we show the phase diagram in T-ρ space, showing the dominant opacity source in each region. 'e.s.' is electron-scattering. The opacity below the double lines at $T = 170\,\mathrm{K}$ is due to ice-coated grains.

Although a number of opacities are required for a full description, one can obtain an idea of the behaviour of the disk at early and late times by considering just a single opacity. The first practical early time approximation is to assume that the disk is dominated by the free-free/bound-free opacities. The timescales over which this remains valid are of the order of a year. While this is still not applicable to planet formation, one might expect this solution to bear the main characteristics of the disk structure at early times. This solution may also be used to calculate a quick lower bound on the mass in a given disk, since its surface density drops faster at large radii than the properly self-consistent solutions. Using opacity 2 from the above table, we obtain m = 1, n = −2.5, hence q = 0.5, p = 1, and so from (6.14) and (6.15),

$$r_e \propto t^{4/9} J^{2/9}\,; \quad \dot{M} \propto t^{-11/9} J^{7/9} \quad (\mathrm{bf/ff})\,. \tag{6.23}$$

For disks with $r_e \geq 5 \times 10^{13}\,\mathrm{cm}$, other opacities are required for a self-consistent description. Furthermore, to obtain significant disk mass for r_e less than this, one requires super-Eddington accretion rates. This means that matter arrives at the neutron star Alfvén radius more quickly than it can be accepted. Hence there is likely to be a build-up of material at the inner edge of the disk. How much of this is "blown-off" by the pulsar radiation and how much builds up in a thick boundary layer outside the magnetosphere is a matter that can only be decided by detailed modelling. With the magnetic field of PSR 1257+12, the Alfvén radius $r_A \sim 4R_{NS}$. Hence the mass expelled is likely to be only ~ 4 times the mass accreted. Thus, a significant fraction of the mass could pile up in a boundary "shield" outside the magnetosphere.

The analytic solution from which the most concrete conclusions can be drawn is that corresponding to the ice grain opacity, the low temperature regime that dominates the outermost reaches of the disk. The approximation that the disk is dominated by this opacity improves at later times and it is this approximation that is valid on timescales required for planet formation. For this disk, m = 0, n = 2, hence q = 2, p = 0, and

$$r_e \propto t^{1/7} J^{2/7}\,; \quad \dot{M} \propto t^{-15/14} J^{6/7} \quad (\mathrm{ice\ grain})\,. \tag{6.24}$$

$$r_e = 3.0 \times 10^{14}\,\mathrm{cm} \left(\frac{\alpha}{0.1}\right)^{1/3} \left(\frac{\mu}{0.6}\right)^{-1/3} \left(\frac{M_{\mathrm{disk}}}{10^{-3} M_\odot}\right)^{1/2} \left(\frac{\dot{M}}{\dot{M}_{\mathrm{Edd}}}\right)^{-1/6} \tag{6.25}$$

$$J = 3.7 \times 10^{50}\,\mathrm{erg\ s} \left(\frac{\alpha}{0.1}\right)^{1/6} \left(\frac{\mu}{0.6}\right)^{-1/6} \left(\frac{M_{\mathrm{disk}}}{10^{-3}M_{\odot}}\right)^{5/4} \left(\frac{\dot{M}}{\dot{M}_{\mathrm{Edd}}}\right)^{-1/12} \tag{6.26}$$

$$t_{\nu} = 3.6 \times 10^{3}\,\mathrm{yr} \left(\frac{M_{\mathrm{disk}}}{10^{-3}M_{\odot}}\right) \left(\frac{\dot{M}}{\dot{M}_{\mathrm{Edd}}}\right)^{-1} . \tag{6.27}$$

The inner regions of this disk will, of course, be hotter and described by different opacities. Performing matchings at constant $\dot{M}$ as described above equation (6.22), we can derive an evolutionary sequence for the complete disk, shown in figure 6.4. We note that except at their very edges, these disks are stable against self-gravitational instabilities: $Q = \Omega c_s/(\pi G \Sigma) \gg 1$ (cf. Goldreich & Tremaine 1982).

To apply these models to the PSR1257+12 system, we note that the total mass of the two observed planets, $M = 2 \times 10^{-5} M_{\odot}/\sin i$, requires a disk mass $M_{\mathrm{disk}} > 2 \times 10^{-5} M_{\odot}$ and $J \geq 2 \times 10^{48}$ erg s. Since the planets are most likely to be formed from refractory elements (see discussion following (6.5)), more realistic minimum disk mass and angular momentum are larger than these by the reciprocal of the abundance of refractory elements (C, O, Si, Fe).

For a given disk profile, the independent variables are the outer radius, the inner radius and the accretion rate. There are two further parameters, the value of α and the value of μ. The latter parameter will be determined by the composition of the original material. For the following discussion, $\alpha = 10^{-2}$ and the composition of the material is solar (μ will vary with the degree of ionization).

Figure 6.5 shows the distribution of disk properties in the $\dot{M}$–r_e plane, the natural coordinates of the disk model. The solid lines indicate curves of constant total disk angular momentum. These are the evolutionary tracks for disks with a given total angular momentum. The dotted lines are lines of constant inspiral time from the edge of the disk, a rough indication of the disk age. The important curves are the dashed lines. These lines represent contours of mass in the region of the disk where grains have formed, and which lies within 1 AU. This mass was calculated by summing all the mass in that part of the disk dominated by opacity number 5 above and which lay at radii less than 1 AU. This is (a generous estimate of) the mass which would be available for the formation of terrestrial-type planets, the most likely mode of formation for the planets of PSR 1257+12 (see above).

The most favourable region of parameter space is thus that where there is the most mass in grains inside 1 AU. For example, in the evolutionary sequence shown in figure 6.4,

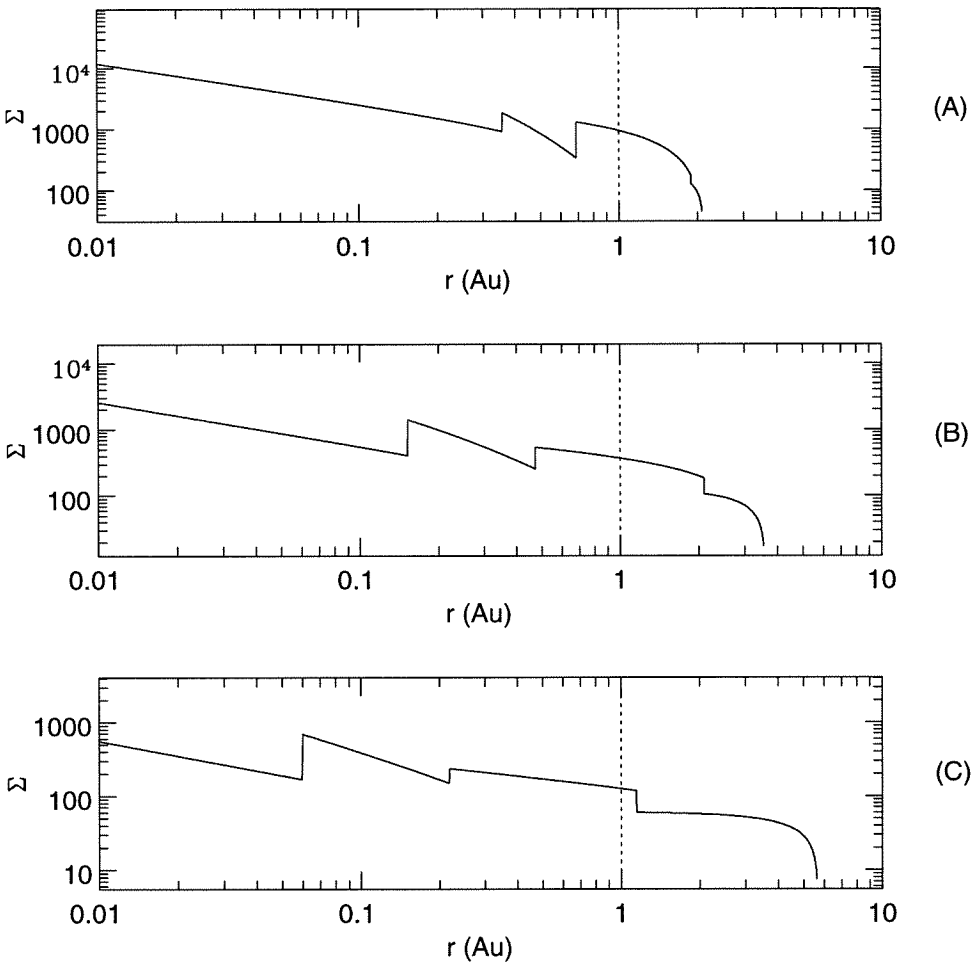

Figure 6.4: **Disk Evolution Sequence:** The sequence of quasi-static disks representing the evolution of a disk with total angular momentum J$\sim 2 \times 10^{50}$ gm cm^2 s^{-1} is shown. The dashed line lies at 1 AU. A: $t = 10^3$ y, B: $t = 10^4$ y, C: $t = 10^5$ y (see figure 6.5). The temperature and physical state at each radius can be estimated by noting that each discontinuity in Σ corresponds to crossing one of the opacity boundaries in figure 6.3, and the temperature increases from right to left (to smaller r). The outermost part of each disk shown here is dominated by the opacity of ice-coated grains.

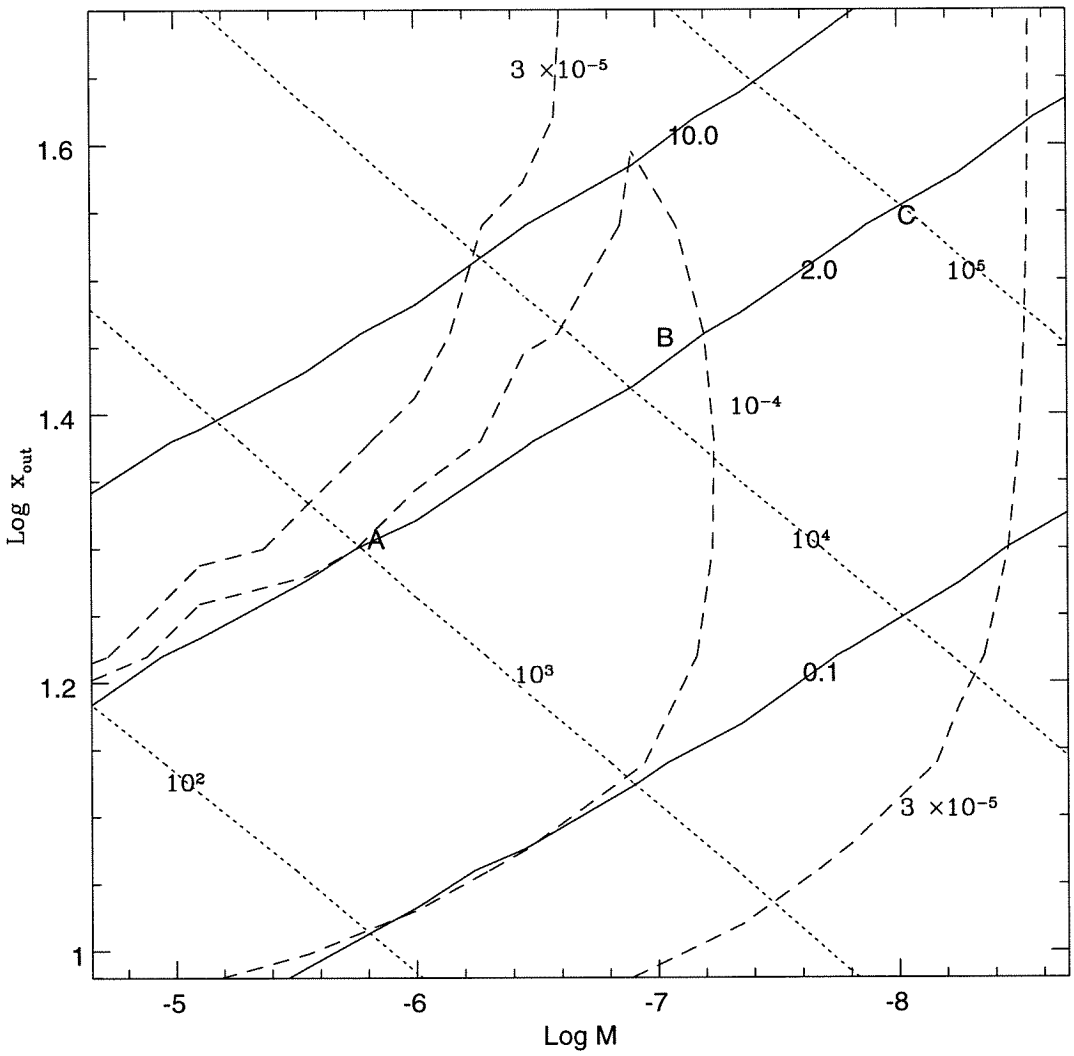

Figure 6.5: **The Parameter Space Spanned by our Quasi-Static Disk Models:** The ordinate $x_{out} = (r_e/10^{11}\,\mathrm{cm})^{1/2}$, where r_e is the radius of the outer edge of the disk. The abscissa is the accretion rate through the inner parts of the disk, in $M_\odot\,yr^{-1}$. To good approximation, a real disk evolves upwards to the right along the solid line of constant total angular momentum $J = 10^{50}J_{50}\,g\,cm^2\,s^{-1}$. The solid lines of constant J are labelled in units of J_{50}. The dotted lines are the viscous time at the edge of the disk, roughly the disk age, and are labelled in years. The dashed lines represent the mass in the cold, refractory grain disk that lies inside 1 AU, and are labelled in $M_\odot$. The letters A, B and C are the positions of the three profiles in figure 6.4.

the point at which the viscous evolution ends will depend on the grain growth in the disk. However, contours of constant mass in the grain region in figure 6.5 show that planetesimal formation would probably have to be completed before 2×10^4 yr, although one could stretch this timescale to 2×10^5 yr if one assumed 100% efficiency in converting disk mass into planets.

Notice that the mass constraint outlined above restricts the amount of disk angular momentum to $J \sim 10^{50}$ erg s. If it is much higher than this, then there is never enough mass in heavy grains to make planets. If it is less than this, then the ice grain disk forms too early, leaving little time for planet formation.

6.6 Validity of the Matching Solutions

As a check on the accuracy of the matched quasi-static solutions described above, we have also calculated the disk evolution using a finite difference scheme. We solve equation (6.7) as transformed defining $x = (r/R(init))^{1/2}$, and $S = x^3\Sigma$, $\tilde{\nu} = \nu/x^2$: $\partial S/\partial\tau = \partial^2/\partial x^2(S\tilde{\nu})$, where $\tau = 3t/(4R^2(init))$. To provide convenient stepsizes, we transform to a new radial variable $y = x^{1/a}$. The following difference scheme conserves both angular momentum and mass explicitly:

$$S_j^{n+1} = S_j^n + \frac{\Delta t}{a\Delta y} y_j^{1-a}\left[\frac{(S\tilde{\nu})_{j+1}^n}{(y_{j+1}^a - y_j^a)} - \frac{(y_{j+1}^a - y_{j-1}^a)(S\tilde{\nu})_j^n}{(y_j^a - y_{j-1}^a)(y_{j+1}^a - y_j^a)} + \frac{(S\tilde{\nu})_{j-1}^n}{(y_j^a - y_{j-1}^a)}\right] . \tag{6.28}$$

This scheme has the stability criterion $\Delta t < (a\Delta y)^2/(2\tilde{\nu}_j)y^{2a-2}$, and thus is second order in space, despite appearances. With a single opacity law, the solutions of our scheme rapidly approach the similarity solution (6.16) to very high precision. With multiple opacity laws, comparison with the results of 6.5 is not quite straightforward, since the definitions for opacities used in 6.5 completely cover the ρ–T plane, but not the Σ-x plane. Thus for the numerical integration, we used a simplified version of the opacity table, with five regions which cover the Σ-x plane. These regions are shown in figure 6.6, along with the corresponding analytical patchwork solution. Such comparisons lead us to believe that the results of 6.5 are reliable to within a factor of two —much better than the uncertainties in the physics!

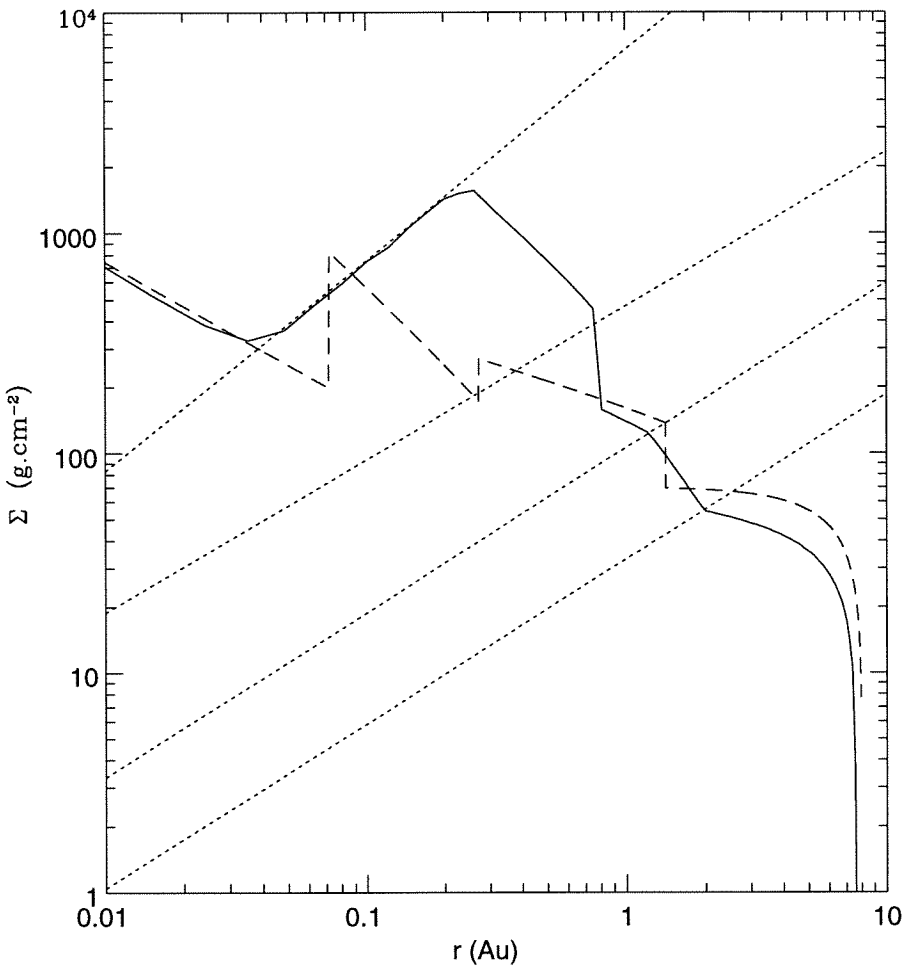

Figure 6.6: **Comparison of Numerical and Analytic Results:** The state at t = 10^6, yr of a J = 2.3×10^{50} erg s disk, started as an annulus at R(init) = 10^{11} cm, is shown. The solid curve is the numerical solution of (6.7). The dashed curve is the quasi-static analytic solution with the same accretion rate. The dotted curves represent the transition boundaries between opacities for the numerical solution. The definitions for opacities in 6.5 completely cover the ρ–T plane, but not the Σ-x plane. Thus for the numerical integration, we used a simplified version of the opacity table, with five regions which cover the Σ-x plane. The modest differences in the opacities used in the two solutions exaggerates their differences. Nevertheless, they track each other well.

6.7 Conclusions

In the particular case of PSR 1257+12, scenarios 1, 2, 5, and 6 are constrained by the requirement that the pulsar be spun up to its present 6 ms period. To spin it up requires accreting

$$\Delta M \geq 0.02 P_{6ms}^{-4/3} I_{45}\, M_\odot\,, \tag{6.29}$$

where the moment of inertia of the neutron star is $10^{45} I_{45}$ g cm^2. This result is insensitive to whether or not the field was initially low, or decayed as a result of accretion, since most of the mass is required to make the last factor of two change in P: $\Delta M \geq I\Omega/j$, where $j = (GMr_A)^{1/2}$ is the specific angular momentum at the Alfvén radius, and $r_A < (GM/\Omega^2)^{1/3}$ as long as spin up continues. The time to spin up to this period is bounded below by the fact that the neutron star cannot accept matter at a super-Eddington rate, so

$$t_{spin-up} \sim 2 \times 10^6 I_{45} P_{6ms}^{-4/3} (\dot{M}_{Edd}/\dot{M})\,\mathrm{yr}\,. \tag{6.30}$$

With standard disk physics, as shown in figure 6.5, only disks with $J > 10^{51}$ erg s maintain the accretion this long. This would favour scenario 5 (or 3 and 4, in which the pulsar could have been spun up at leisure before the disruptive event).

At the other extreme of the evolution, one may enquire what happens as the accretion rate tails off at late times. For a pulsar with magnetic dipole moment $\mu_B = 10^{27}\mu_{27}$ (PSR 1257+12 has $\mu_{27} \sim 1$), the Alfvén radius will be pushed beyond the pulsar's light cylinder when

$$\dot{M} < \dot{M}_* \simeq 10^{-12} \mu_{27}^2 (P/6\,\mathrm{ms})^{-7/2} M_\odot\,\mathrm{yr}^{-1}\,. \tag{6.31}$$

Since beyond the light cylinder, the ram pressure of the pulsar wind falls as r^{-2}, more slowly than the ram pressure of accretion, roughly $\propto r^{-5/2}$ (Illarionov & Sunyaev 1975, Shaham & Tavani 1991), the pulsar wind will then be able to break free, and prevent any further accretion. The pulsar will turn off as an X-ray source, and turn on as a radio pulsar.

In the late stages of evolution of the solar nebula, Poynting-Robertson drag is often invoked to clear dust from the young planetary system (Lin & Papaloizou 1985). In the context of the pulsar nebula, this is much less effective once $\dot{M} < \dot{M}_*$ (6.31). The drag

timescale is

$$t_{PR} \simeq \frac{4\pi c^2 r^2 a_{gr} \rho_{gr}}{f_{abs} L_{psr}} . \tag{6.32}$$

The difference here is that the penetrating part of the pulsar wind, mainly ultrarelativistic ($\gamma \geq 10^5$, Kulkarni *et al.* 1992) electrons and ions, has a stopping column $\geq 10^2\,\mathrm{g\ cm^{-2}}$. Thus grains smaller than baseball size are transparent, and the fraction of the incident pulsar flux absorbed, $f_{abs} \propto (a_{gr}\rho_{gr})$, so all such grains sink at roughly the same rate,

$$t_{PR} \sim 10^9 r_{AU}^2\,\mathrm{y}\,, \tag{6.33}$$

so slowly as to be probably irrelevant.

In conclusion, we find that the scenarios listed in table refTabmem are just barely capable of producing planets of the masses and semi-major axes appropriate to PSR 1257+12, if the disk approximations employed in solar nebula modelling are valid in these circumstances. Such model disks are not capable of producing a massive planet at large radii, as is inferred around the globular cluster PSR 1620–26 in M 4 from its apparently large $\ddot{P}$ (Backer, Sigurdsson, these proceedings). However, the effects of illumination by the central source, its super-Eddington winds, self-gravity in early stages, and the problem of grain nucleation in the nebulae bear investigation beyond our cursory discussion.

ACKNOWLEDGEMENTS

Supported in part by NASA grant NAGW-2394 and the Sloan Foundation.

REFERENCES

Abramowicz, M., Jaroszyński, M. & Sikora, M. 1978, A&A, **63**, 221.

Balbus, S.A. & Hawley, J.F. 1991, ApJ, **376**, 214.

Blandford, R.D. 1976, MNRAS, **176**, 465.

Blandford, R.D. & Payne, D.G. 1982, MNRAS, **199**, 883.

Bhattacharya, D., Wijers, R., Hartman, J. & Verbunt, F. A&A, **254**, 198.

Cannizzo, J.K., Lee, H.M. & Goodman, J. 1990, ApJ, **351**, 38.

Christodoulou, D.M. & Narayan, R. 1992, ApJ, **388**, 451.

Coroniti, F.V. 1981, ApJ, **244**, 587.

Evans, C.R. & Kochanek, C.S. 1989, ApJ, **346**, L13.

Frank, J. 1978, MNRAS, **184**, 87.

Frank, J., King, A.R. & Raine, D.J. *Accretion Power in Astrophysics*, 2nd Ed. Cambridge: Cambridge Univ. Pr., 69.

Frenklach, M., Carmer, C.S. & Feigelson, E.D. 1989a, *Nature*, **339**, 196.

Frenklach, M. & Feigelson, E.D. 1989b, ApJ, **341**, 372.

Goldreich, P. & Reisenegger, A. 1992, ApJ, **395**, 250.

Goldreich, P. & Tremaine, S. 1982, ARA&A, **20**, 249.

Hawley, J.F. & Balbus, S.A. 1992, ApJ, **376**, 223.

Illarionov, A.F. & Sunyaev, R.A. 1975, A&A, **39**, 185.

Kenyon, S.J. & Hartmann, L. 1987, ApJ, **323**, 714.

Knobloch, E. 1992, MNRAS, **255**, 25P.

Königl, A. 1989, ApJ, **342**, 208.

Kulkarni, S.R., Phinney, E.S., Evans, C.R. & Hasinger, G. 1992, *Nature*, **359**, 300.

Lin, D.N.C. & Papaloizou, J. 1985, in *Protostars & Planets II*, D.C. Black & M.S. Matthews, eds, Tucson: Univ. Arizona Pr., 981.

Lynden-Bell, D. & Pringle, J.E. 1974, MNRAS, **168**, 603.

Narayan, R. & Ostriker, J.P. 1990, ApJ, **352**, 222.

Ovidius Naso, P. 8, *Metamorphoses*, book XIII.

Priedhorsky, W.C. & Verbunt, F. 1988, ApJ, **333**, 895.

Pringle, J.E. 1991, MNRAS, **248**, 754.

Romani, R.W. 1990, *Nature*, **347**, 741.

Ruden, S.P., Papaloizou, J.C.B. & Lin, D.N.C. 1988, ApJ, **329**, 739.

Ryu, D. & Goodman, J. 1992, ApJ, **388**, 438.

Sakimoto, P. & Coroniti, F.V. 1989, ApJ, **342**, 49.

Salpeter, E.E. 1974, ApJ, **193**, 579.

Shaham, J. & Tavani, M. 1991, ApJ, **377**, 588.

Verbunt, F., Wijers, R.A.M.J. & Burm, H.M.G. 1990, A&A**234**, 195.

Whitehurst, R. & King, A. 1991, MNRAS, **249**, 25.

Wolszczan, A. & Frail, D.A. 1992, *Nature*, **355**, 145.

Chapter 7 Pulsar Velocities

We analyse the existing proper motion data for pulsars and infer the distribution of birth velocities for pulsars, taking into account the selection effects of the pulsar surveys and treating censored data using survival statistics. We find that the mean birth velocity of a pulsar is $\sim 250 - 300\mathrm{km.s}^{-1}$, rather than the 450 $\mathrm{km.s}^{-1}$ found by Lyne & Lorimer (1995).

7.1 Introduction

The fact that pulsars have velocities much in excess of those of ordinary stars (a subset of whom are presumably the pulsar progenitors) has been known for some time. The origin of these velocities is not so clear. One possibility is that they result from the disruption of a binary population (Gott et al. (1970), Iben and Tutukov (1996)), leaving the pulsar with a velocity characteristic of the orbital velocity of the progenitor in the binary. The problem with this scenario is that it has trouble explaining the largest observed velocities (e.g., Phinney and Kulkarni (1994)). Another possibility is that the pulsar acquired its velocity from an asymmetric supernova collapse, i.e., it received a natal kick.

Lyne and Lorimer (1994) have analysed the known sample of pulsar velocities in the light of recent proper motion studies (Harrison,Lyne and Anderson (1993)) as well as the new pulsar distance scale due to Taylor and Cordes (1993). They conclude that pulsars are born with a mean speed of $\sim 450\,\mathrm{km.s}^{-1}$. Although Lyne and Lorimer restrict their sample to those younger than 4×10^6 years to avoid the selection effect pointed out by Cordes (1986), they did not treat the selection effects that accrue from the flux limits of the pulsar surveys or the limiting accuracy of proper motion determinations. We shall attempt to do that here. Recently, Iben and Tutukov (1996) have also addressed this question, but in a less systematic fashion than what we propose to use in this paper.

In this paper, we will restrict our analysis to those pulsars with velocities determined by proper motion only. While scintillation data have been used to calculate velocities (Cordes (1986), Harrison and Lyne (1993)) to within a factor of 2, we prefer to keep our sample as homogeneous as possible, and so we exclude these data. We use the properties of well-

known pulsar surveys to estimate the V/V_{max} correction for each pulsar, making use of survival statistics (Feigelson and Nelson (1985)) to treat those data with upper bounds (section 7.2). This allows us to estimate the two dimensional velocity distribution of the observed pulsar population and thus the kick velocity distribution taking into account the differential galactic rotation in section 7.3

7.2 The Proper Motion Distribution

7.2.1 Selection Effects

The princeton pulsar database (Taylor et al. (1993)) now contains $\sim$ 800 pulsars, 101 of whom have measured proper motions or upper limits. The number of surveys responsible for this profusion is also gradually increasing in size (in excess of 15). To do a proper treatment of the selection effects for the full proper motion sample would then require modelling the selection effects of a significant number of these surveys. Luckily, we note that most of the proper motion pulsars were detected in the earlier surveys. By restricting ourselves to those pulsars detected in the Molonglo 2 (Manchester et al. (1978)) and Green Bank/NRAO 1,2 and 3 surveys (Damashek et al. (1978), Dewey et al. (1985), Stokes et al. (1985), Stokes et al. (1986)), we are left with 86 out of 101 pulsars. We note that 12 of the 15 pulsars left out have P$<$ 0.1 s (and only one of our restricted sample satisfies this criterion), which is not surprising, since many of the later surveys focussed on finding faster spinning pulsars. In performing this cut, we lose one young pulsar and all but one of the pulsars with spin-down ages greater than 1 Gyr. This also means we are not affected by the possibly different evolutionary histories of millisecond pulsars. We shall omit the one millisecond pulsar (PSR 0655+64) which does fall into our sample as well. Figure 7.1 shows the distribution of the included and excluded pulsars as a function of period and velocity.

The observed pulsar sample suffers from two obvious selection effects, due to flux limits and proper motion limits respectively. Figure 7.2 shows the distribution of inferred luminosities and transverse velocities. The lack of faint, fast pulsars (upper left corner) and bright, slow pulsars (lower right corner) is evident.

To correct for this bias, we need to weight the pulsars according to the maximum volume in which they could have been detected, i.e., using a V_{max} weighting. To do this we need to consider the detection efficiency of the various pulsar surveys. After Narayan (1987) (see

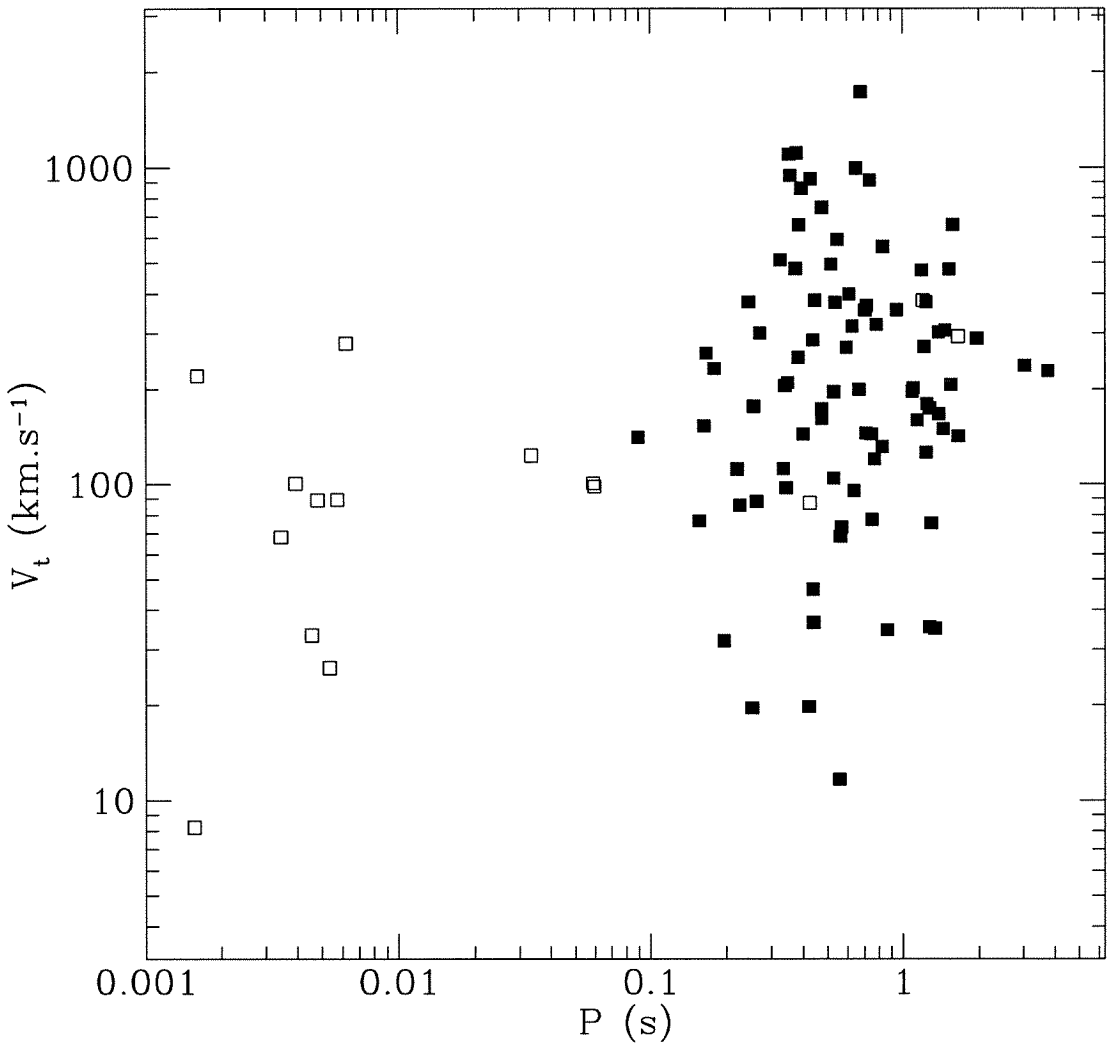

Figure 7.1: **Sample Definition:** The filled squares indicate the pulsars that we include in our analysis. The open squares denote those that are excluded. Since the purpouse here is simply to demonstrate which pulsars are in the sample discussed, we omit any error bars. Of the three excluded pulsars with P $>$ 0.1s, two are recycled binaries, B0655+64 and B0820+02.

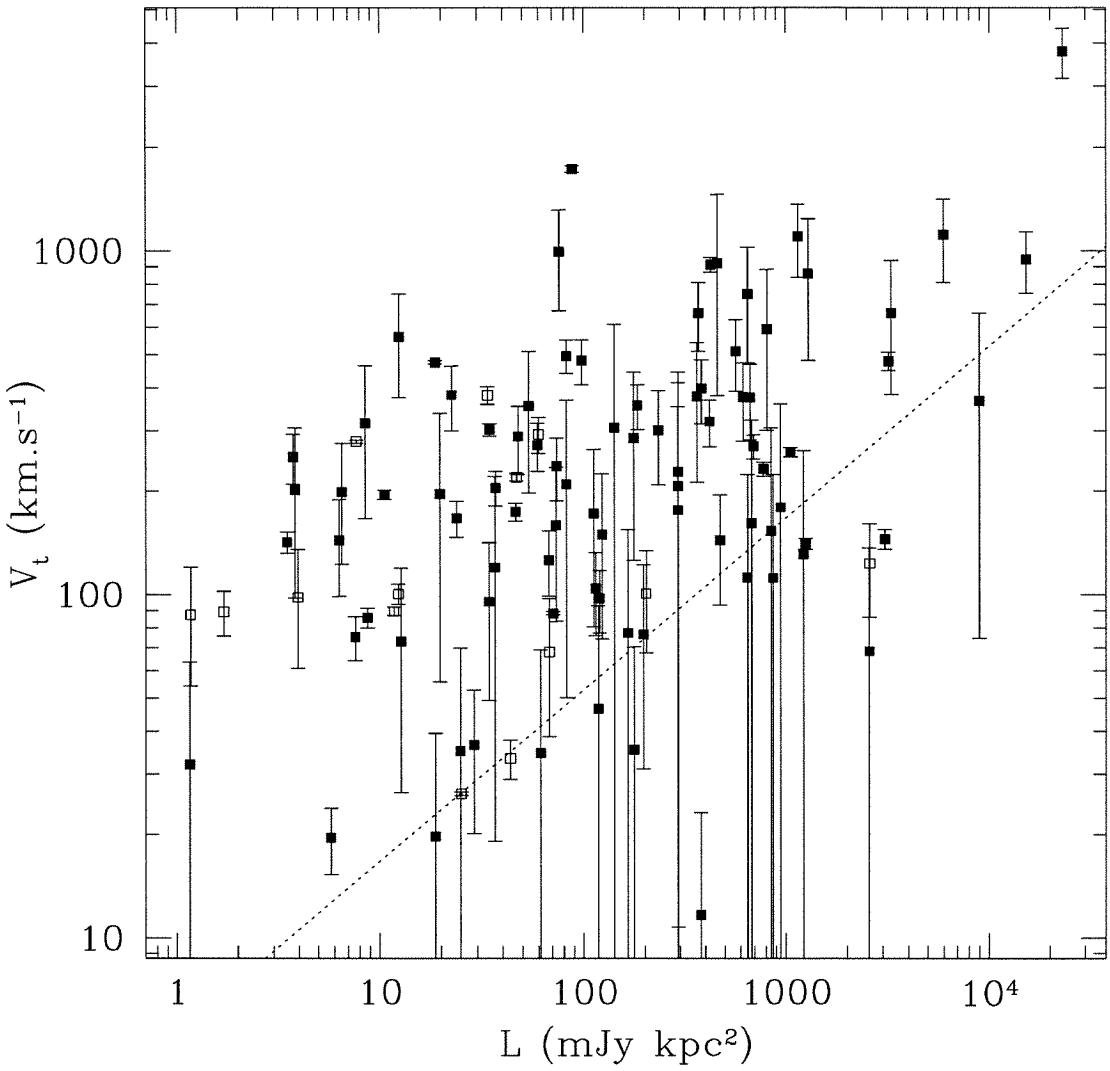

Figure 7.2: **Luminosity and Velocity for the Proper Motion Pulsars:** We again include all the pulsars with proper motions on this plot. The filled squares will be the ones to which our analysis applies. The dotted line indicates a proper motion of 5 mas.yr^{-1} and flux 4 mJy. This line does not represent a cutoff over most of this diagram because making a pulsar brighter at a given distance will move it to the right and making a pulsar faster at a given distance will move it up, thus one can populate both sides of the line with observable pulsars. Nevertheless, at the high luminosity/high velocity end, it should represent the limiting case. It is also noticeable that, on average, higher velocity pulsars have higher luminosities, and so will be overrepresented in an unweighted sample.

also Dewey et al. (1984)), the minimum flux detectable is

$$S_{min} = S_0 \frac{(T_{rec} + T_{sky})}{T_0} \sqrt{\frac{PW}{W_e(P - W)}} \tag{7.1}$$

where T_{rec} and T_{sky} are the system and sky noise temperatures, S_0 is the flux normalization, and W is the measured pulse width, where W_e is the intrinsic pulse width, which is broadened because of sampling, dispersion and scattering

$$W^2 = W_e^2 + \tau_{samp}^2 + \tau_{DM}^2 + \tau_{scatt}^2. \tag{7.2}$$

Thus we calculate the minimum flux for a given survey in a particular direction. The parameters describing each survey were taken from Narayan (1987)[1] and Stokes et al. (1986). We used the updated electron distribution model of Taylor and Cordes (1993) to calculate the dispersion and scatter broadening along a given line of sight. This accounts for the bias due to the flux limits. No such simple model exists for treating the proper motion limits. This is because the accuracy of a given proper motion measurement depends on the vagaries of the distribution of background radio sources near the pulsar position on the sky (Harrison, Lyne and Anderson (1993)). As a crude model of this, we model the distribution of proper motion errors in Harrison et al. using the distribution $p(\mu) = \exp(-\mu/10.5\,\mathrm{mas.yr^{-1}})$. In the V_{max} calculations to follow, the proper motion cutoff is randomly selected from this distribution for each line of sight. We also used simple limits of 5 and 2 $\mathrm{mas.yr^{-1}}$. This introduces a variation of $\sim 10\mathrm{km.s^{-1}}$ in the mean velocity of the young sample and about $30\mathrm{km.s^{-1}}$ in the old sample. Iben and Tutukov (1996) have also taken account of this selection effect.

For each pulsar, we randomly place it in different directions and at different distances with respect to the observer and calculate whether or not it would be detectable in any of the surveys we consider. Thus, using this Monte Carlo integration procedure, we determine the volume within which each pulsar could have been detected. These V_{max} values determine the relative weights of each of the pulsars in the corrected sample.

A possible source of concern with this procedure is illustrated by Figure 7.3. The

[1]The formula for the sky background temperature (3.5) contains an error. The factor $\left[1 + (b/3)^2\right]$ should be in the denominator.

analytic flux limits do not describe the complications of the true detection limits perfectly. In Figure 7.3 we find four pulsars detected by the Molonglo survey that lie below the analytically described detection threshold for that survey. This will reduce the weight accorded to these pulsars. To estimate the impact of this error on our results, we repeated the analysis with these pulsars artificially 'brightened' to meet the flux limit expression. The mean proper motion we infer for the young pulsar sample increases by only 7 km.s^{-1}, so this is not a significant source of error for our analysis here.

The V_{max} correction is not without biases of its own. In particular, weighting pulsars by their V_{max} presupposes that the real distribution is distributed uniformly throughout the galactic volume. However, the pulsars are born from a disk population with a scale height of about 150-450 pc (Narayan and Ostriker (1990)). Thus, a population born with small velocities will not expand to fill as much of the spherical volume as a fast population. The above analysis then overcorrects for the slow pulsars (see Helfand and Tademaru (1977), Cordes (1986), Lyne and Lorimer (1994)). In order to adjust for this, we consider the maximum detectable volume to be limited in the vertical extent by the scale $Z_{max}=V_t t_p$, where t_p is the pulsar timing age. If this is larger than D_{eq}, then there is no change in the weight assigned to that pulsar, but, if $D_{eq} > Z_{max}$, then we assume that we see the edge of the distribution of pulsars of this velocity, and reduce the weight given to that pulsar (see Figure 7.4). Furthermore, for young pulsars, we set a lower limit on Z_{max} of 450 pc, representative of the initial scale height.

In Figure 7.5 we show the distribution of velocities with age and the relative weighting of each pulsar.

7.2.2 Survival Statistics

The V_{max} correction takes care of the selection effects, but we still need to account properly for those data which only have upper limits ('censored' data in the statistical lexicon). Of our 85 pulsars, 20 fall into this category. Using only those data with actual detections will bias our distribution to higher values as we will see below.

Following Feigelson and Nelson (1985), we use survival statistics to treat the effects of our censored data. In particular, we use the Kaplan-Meier estimator (Kaplan and Meier (1958)) to calculate the cumulative probability distribution of the transverse velocities. We have modified this method slightly to take account of our V_{max} correction (see appendix D).

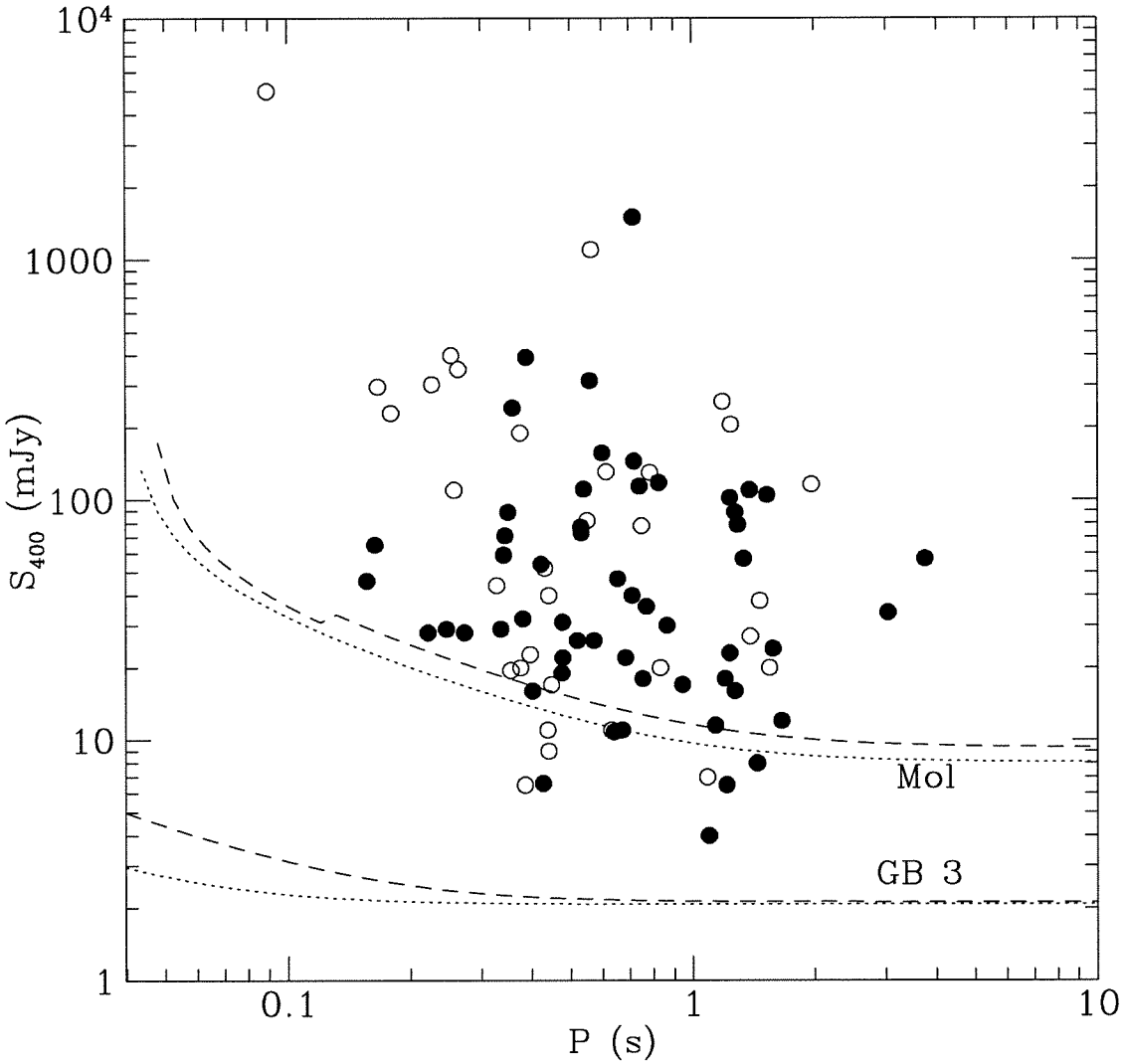

Figure 7.3: **Selection Effects:** The solid circles represent those pulsars detected in the Green Bank surveys. The open circles are the ones detected in the Molonglo surveys. The dotted lines indicate the approximate limiting flux as a function of P for DM=50 cm^{-3}.pc and the most sensitive Molonglo and Green Bank surveys. The dashed lines are for DM=200 cm^{-3}.pc.

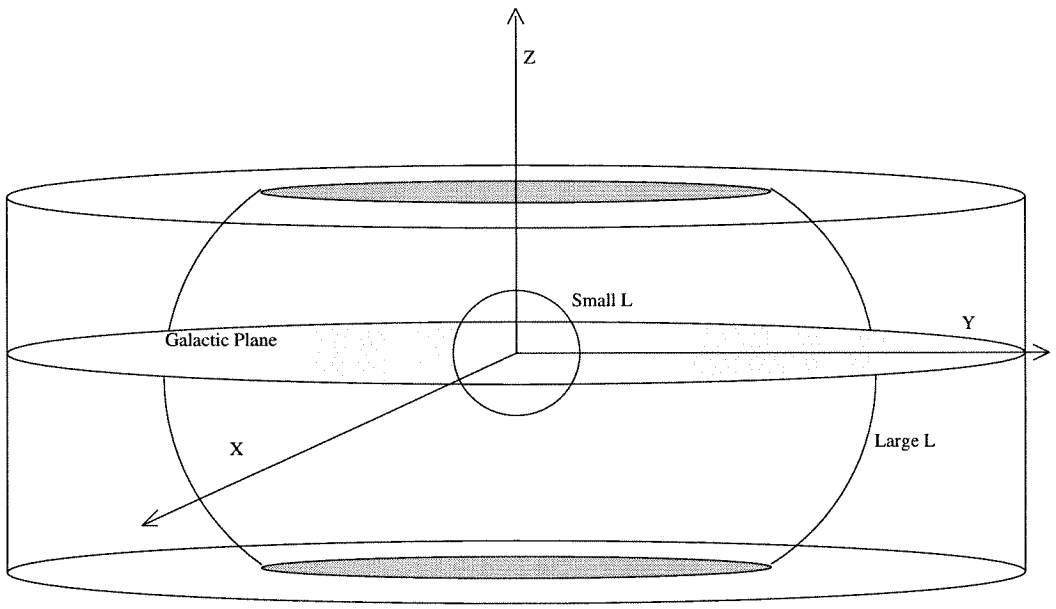

Figure 7.4: **Detectable Volume for Each Pulsar:** Pulsars with small luminosities will only be observable near the galactic plane, so that their V_{max} will be spherical (neglecting other selection effects for the moment). Pulsars with large luminosities will be observable much further away, out to the limits of the disk that such a population, born in the galactic plane, would fill. In this case, the spherical V_{max} will be cut off above the limits of the disk height given by $z = V_z \times t$.

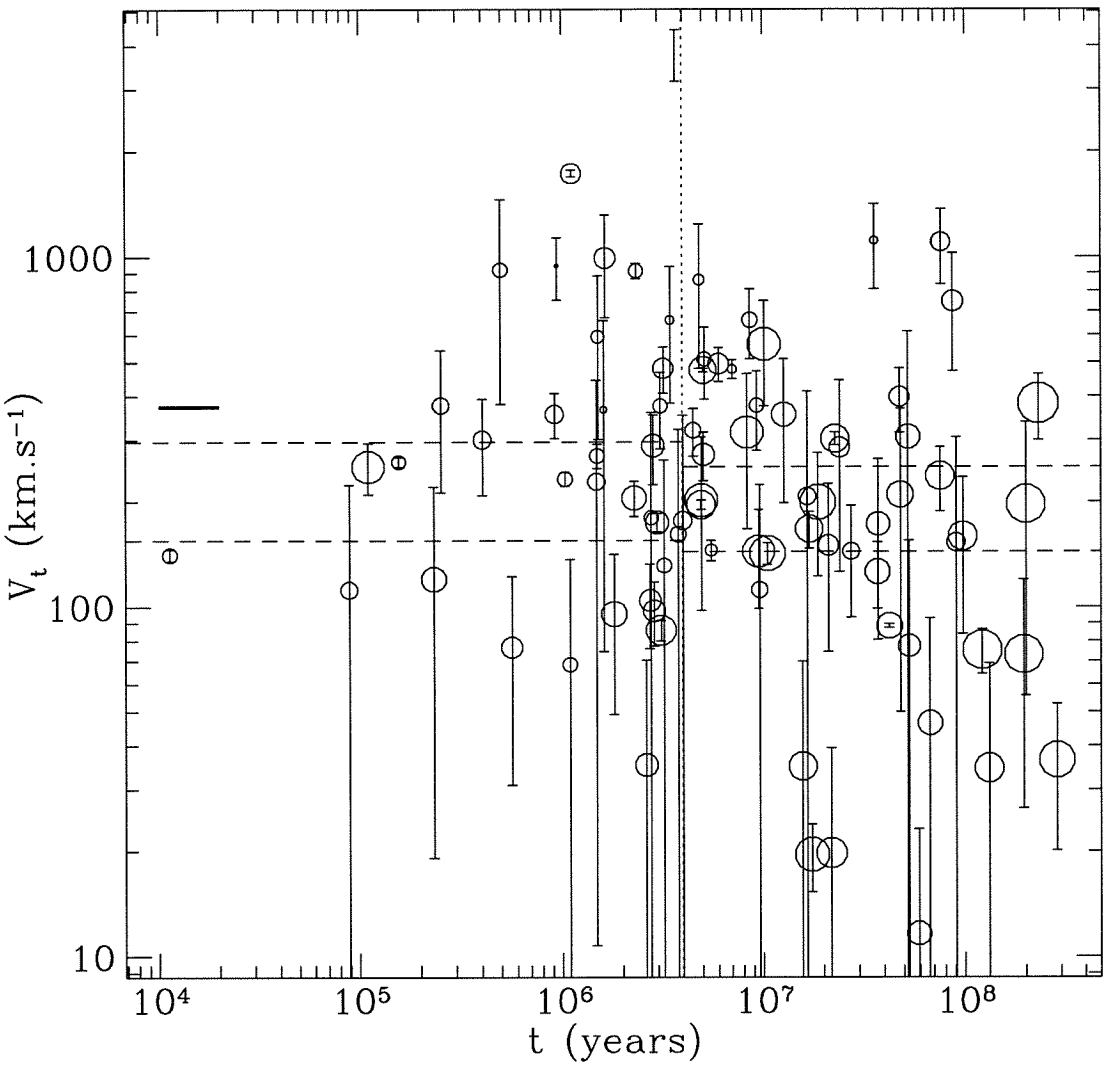

Figure 7.5: **The Weighted Proper Motion Distribution:** The size of each circle is proportional to the logarithm of the weight accorded that pulsar. The vertical dotted line indicates the dividing line between what we consider 'young' and 'old' pulsars. The horizontal dashed lines indicate the range of values we infer for the mean proper motion of the pulsars in each sample. The short horizontal solid line at left indicates the mean proper motion value quoted by Lyne and Lorimer (1995).

7.2.3 The Corrected Distribution

Figure 7.6 shows the cumulative probability distribution of observed transverse velocities taking into account different levels of adjustment. With no adjustments, the mean transverse velocity of the entire sample is 355 km.s^{-1}, in agreement with the analysis of Lyne and Lorimer (1995). The mean of the entire sample including all corrections is 195 km.s^{-1}. However, if we restrict the sample to pulsars with spin-down ages $< 10^7$ years, we obtain a mean transverse velocity of 237 $\pm$ 49 km.s^{-1} (51 pulsars). The mean velocity of the complementary sample with ages $> 10^7$ years is 193 $\pm$50 km.s^{-1} (35 pulsars). In Figure 7.6 we see that the distribution for the old pulsars does have a larger low velocity tail, as one might expect. If we place the velocity cutoff at 4×10^6 years, we find 226 $\pm$ 71 km.s^{-1} for the 36 young pulsars and 198 $\pm$ 53 km.s^{-1} for the older pulsars.

A reduction in the mean velocity for old pulsars has been noted before by several authors (Lyne and Lorimer (1995), Nice and Taylor (1995), Camilo et al. (1995)). We should note, however, that when we refer to "old" pulsars above, we refer to those with spin-down ages less than 10^9 years, i.e., we don't consider millisecond pulsars because of the increased complexity of treating their selection effects. Nevertheless, in a completely model-independent way, we can demonstrate that these pulsars are old in a dynamical sense, because they show the effects of the asymmetric drift (e.g., Mihalas and Binney (1981)). Nice and Taylor (1995) have pointed out that the millisecond pulsar population might possess this property, but it appears to be true for all pulsars with spin down ages $> 10^7$ years. This is shown in Figure 7.7. The effect has its origin in the fact that any population with a significant radial velocity dispersion will rotate about the galactic centre more slowly than the local circular speed (Mihalas and Binney (1981)).

To calculate this we restrict ourselves only to those pulsars with well-determined proper motions (since large enough error bars can reverse the sign of the transverse velocity). However, because we will not treat selection effects in this case, we shall use all the proper motion pulsars that satisfy this and subsequent criteria, including millisecond pulsars. We consider a cartesian coordinate system with origin at the sun, with positive x pointing radially outward and positive y pointing in the direction of $\ell = 270°$. We consider the y-components of the transverse velocity, which measures the approximate azimuthal component of the pulsar velocity with respect to the sun (strictly speaking, this should be done

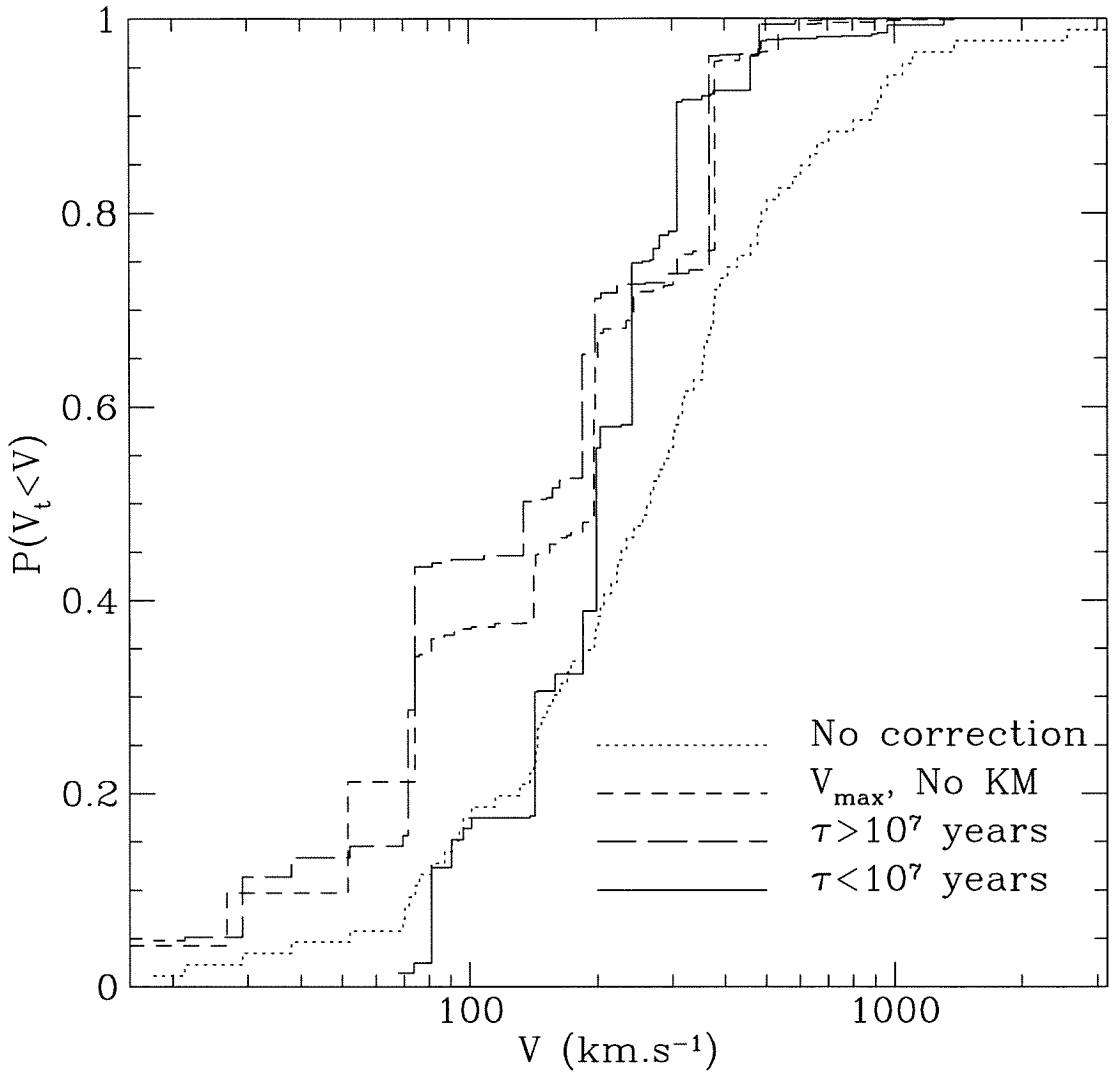

Figure 7.6: **The Inferred Proper Motion Distribution:** The cumulative probability distribution $P(V \leq V_t)$ is shown for different degrees of correction. The dotted line shows the entire sample with no V_{max} weighting and no treatment of upper bounds. The short dashed line is for only the 66 pulsars with detected proper motions corrected using our V_{max} correction (i.e., all those with only upper limits were left out). The long dashed line is the properly corrected sample (with V_{max} corrections and Kaplan-Maier estimator) but only those with spin-down ages greater than 10^7 years. The solid line is the complementary sample of only those pulsars with spin-down ages less than 10^7 years. The 95% confidence levels for the corrected distributions lead to an uncertainty of ~ 0.05 in P for velocities $<$ 300 km.s^{-1}. Above that, the statistics become uncertain and we cannot say much about the distribution.

for each pulsar in its individual local standard of rest, but this rough approach demonstrates our result sufficiently well and remains the same if we reduce the sample radius). We also exclude pulsars with d> 6 kpc and within 20° of ℓ=90 or 270 (where transverse velocities are primarily radial in the galactic frame) and of b = $\pm$90°. This leaves us with 37 pulsars with spin-down ages from 10^3 - 10^{10} years. The signature of the asymmetric drift is thus an excess of positive V_y. Indeed, this is seen to striking effect in figure 7.7, where less than 10% of the pulsars older than 4×10^6 years have negative V_y. The 'raw' data is shown in Figure 7.8.

7.3 The Kick Distribution

In section 7.2, we derived the corrected proper motion distribution appropriate to a volume limited sample. Since pulsars receive their kicks in a rest frame rotating about the galactic centre and we are interested in the low velocity tail, we need to consider the effect of differential galactic rotation.

We consider a pulsar with a given kick speed V_0, with an arbitrary kick direction. Consider a cartesian rest frame in the pulsar progenitor local standard of rest. The component of the kick velocity $V_0 \cos\alpha$ perpendicular to the plane will be unaffected by the differential rotation. However, the two velocity components in the galactic plane, $V_0 \sin\alpha \cos\beta = V_0^* \cos\beta$ and $V_0^* \sin\beta$, will be affected. If we restrict ourselves to distances small with respect to the sun's galactocentric radius (d $\ll$ R_0), then we can describe the effects of differential rotation using the Oort A and B coefficients. If we consider all pulsars to be born in the galactic plane, we obtain the following expression for the 2-D velocity in the galactic plane transverse to the line of sight:

$$V_{T,xy} = V_0^* \cos(\ell - \beta) + \frac{d}{R_0}\left[R_0(B - A) - V_0^* \cos\beta + V_0^* \cos(\ell - \beta)\cos\ell - 2AR_0 \cos^2\ell\right] \tag{7.3}$$

Combining this with $V_{T,z} = V_0 \cos\alpha$, we obtain a proper motion distribution corresponding to the kick distribution. We have also calculated the proper motion distribution using Monte Carlo simulations for various kick distributions.

In Figure 7.9, we see that the low and intermediate range of our proper motion distribution is best fit by a scenario where every pulsar receives a kick of 250 km.s^{-1} in random

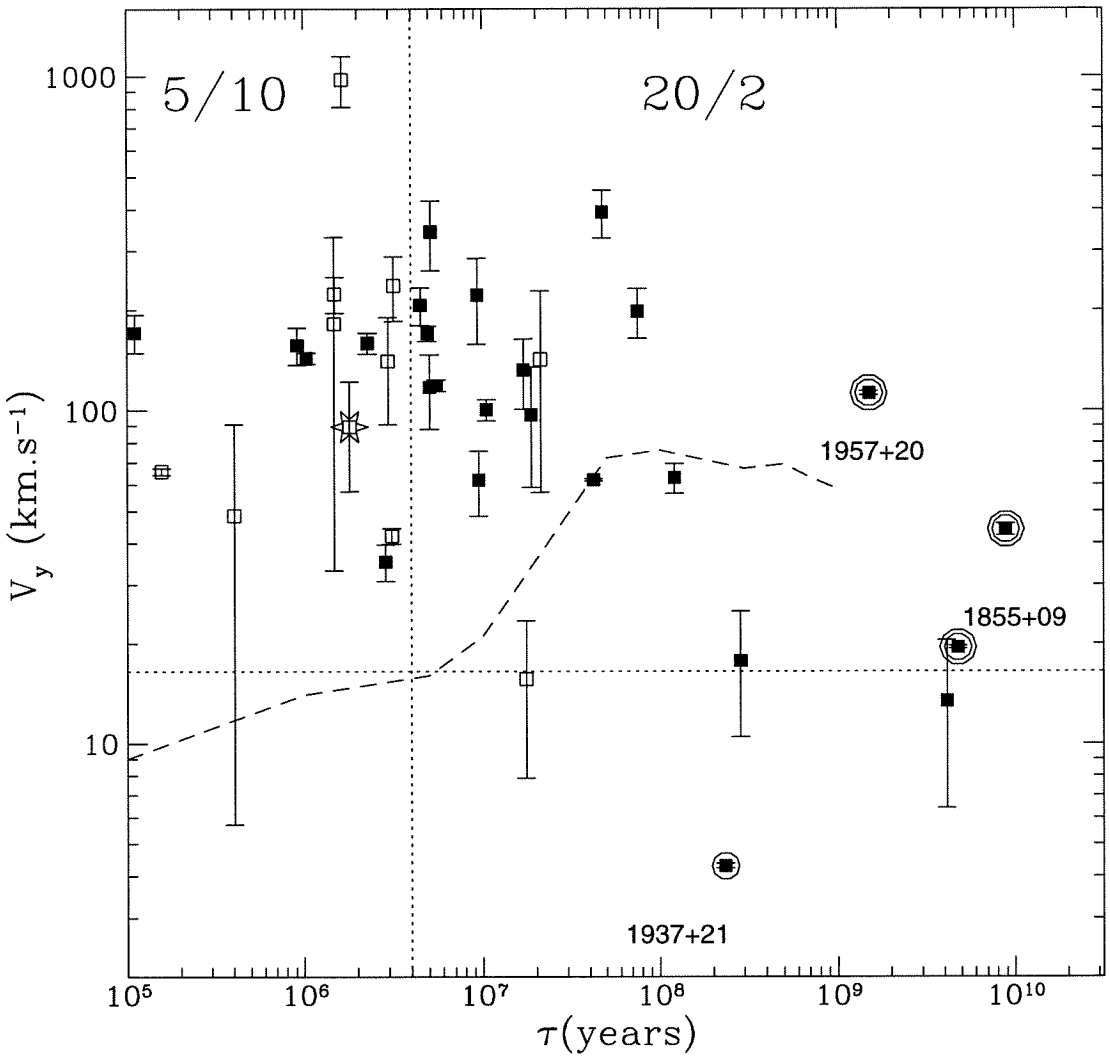

Figure 7.7: **The Asymmetric Drift 1:** The solid squares indicate a positive V_y and open squares indicate a negative V_y. The circled points indicate binaries. The horizontal dashed line indicates the order of magnitude of the sun's motion within its local standard of rest, and velocities below this will experience a contamination of the asymmetric drift. The vertical dashed line is at 4 $\times 10^6$ years, and represents an approximate division between "young" and "old" pulsars, namely those that show the asymmetric drift and those that don't. Of the young pulsars, only 33% have positive V_y, while 91% of the old pulsars have positive V_y. The dashed line indicates the evolution of the mean asymmetric drift velocity obtained from the calculation in section 7.4.

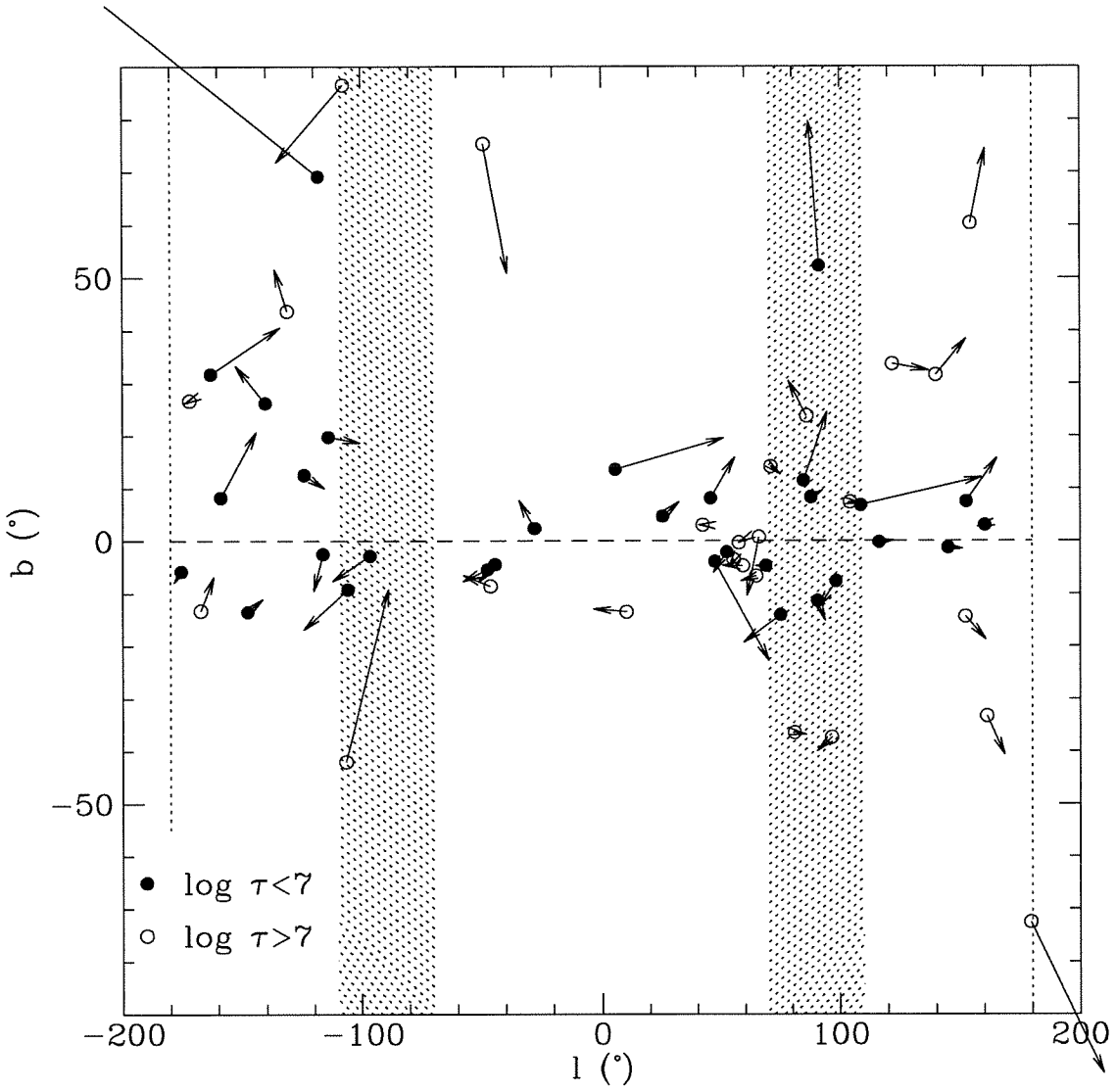

Figure 7.8: **The Asymmetric Drift 2:** We show here the positions in galactic coordinates of those pulsars with well-determined μ_l, i.e., $\Delta\mu_l < 0.5\,|\mu_l|$. The solid circles are 'young' ($\tau < 10^7$ years) and the open circles are old. The arrows indicate the motion of the pulsar in 10^6 years given its current proper motion. The shaded regions around l = -90 and l=90 are excluded from asymmetric drift considerations because the circular motion would be largely along the line of sight. In this diagram the signature of the asymmetric drift is an excess of negative μ_l for $-90 < l < 90$ and positive μ_l otherwise.

directions. This scenario does, however, have a problem producing proper motions larger than about 400 km.s^{-1}. The distribution is also consistent with a Maxwellian distribution of kick velocities with velocity dispersion of $\sim$ 190 km.s^{-1} (corresponding to a 3-D mean of $\sim$ 300 km.s^{-1}). However, it is inconsistent with the Lyne and Lorimer proper motion distribution as well as the earlier form suggested by Paczynski (1990). Neither of these analyses included a discussion of selection effects. Thus, our best estimate for the kick velocity distribution is

$$p(V_k) = \sqrt{\frac{2}{\pi}} \frac{v^2}{\sigma_v^3} e^{-V_k^2/2\sigma_v^2} \tag{7.4}$$

with $\sigma_v = 190$km.s^{-1}.

7.4 Long Term Evolution

Our analysis above is concerned solely with those pulsars with spin-down ages $< 10^7$ years. To do the same for the older pulsar population will require the incorporation of the selection effects of more pulsar surveys, as well as the effect of the death line and recycling of pulsars in binaries. Nevertheless, if we assume that all pulsars originate from a population with the velocity distribution (7.4), we may examine the long-term evolution of this population, in anticipation of comparisons with future analyses. We have performed monte-carlo simulations of such a population using a galactic potential from Paczynski (1990). The potential contains two terms of the form

$$\Phi_i(R,z) = \frac{GM_i}{\left[R^2 + \left(a_i + (z^2 + b_i^2)^{1/2}\right)^2\right]^{1/2}} \tag{7.5}$$

where i=1,2 represent the disk and bulge respectively. A third component, the halo, is represented by

$$\Phi_3(R,Z) = -\frac{GM_c}{r_c}\left[\frac{1}{2}\ln\left(1+\frac{r^2}{r_c^2}\right) + \frac{r_c}{r}\mathrm{atan}\left(\frac{r}{r_c}\right)\right]. \tag{7.6}$$

The various parameter values are given in table 7.1. The birth positions of the pulsars are distributed exponentially in both galactocentric radius (R) and disk height (z), with scale lenghts of 4.5 and 0.075 kpc respectively. The integration is performed using the Burlisch-Stoer integration algorithm from Press et al. (1992).

To recreate the observations we 'observe' the pulsars from a galactocentric radius of 8

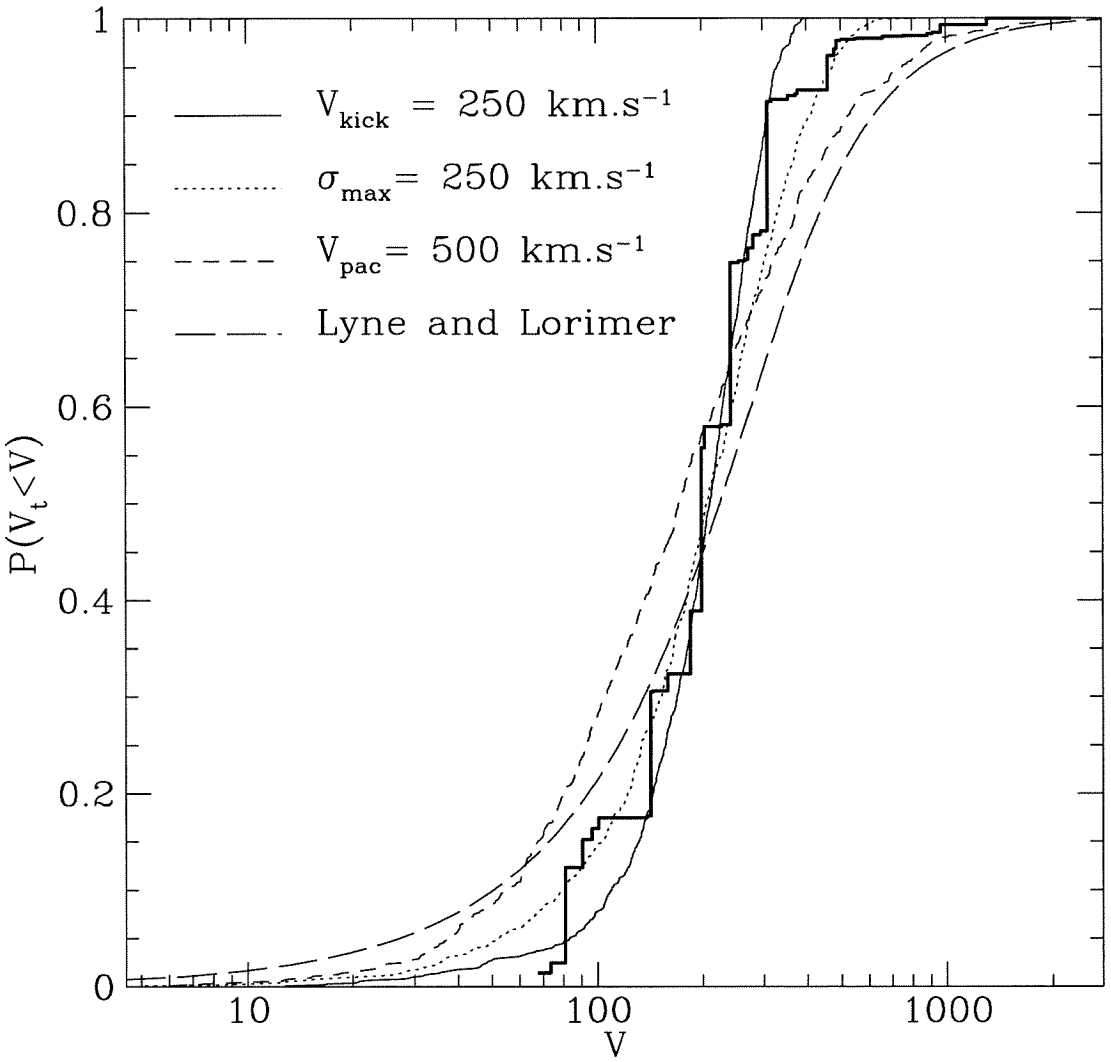

Figure 7.9: **Determining the Birth Velocity Distribution:** The heavy solid line is the corrected proper motion distribution. The light solid line is the proper motion distribution obtained for a single kick speed of 250 km.s^{-1} in random directions. The dotted line is for a maxwellian and is also consistent. The short and long dashed lines represent the results of Paczynski (1990) and Lyne and Lorimer (1995) and are both inconsistent.

	a (kpc)	b (kpc)	r_c (kpc)	M ($M_\odot$)
Bulge	0	0.277		1.12×10^{10}
Disk	3.7	0.20		8.07×10^{10}
Halo			6.0	5.0×10^{10}

Table 7.1: The parameters of our Galactic Model

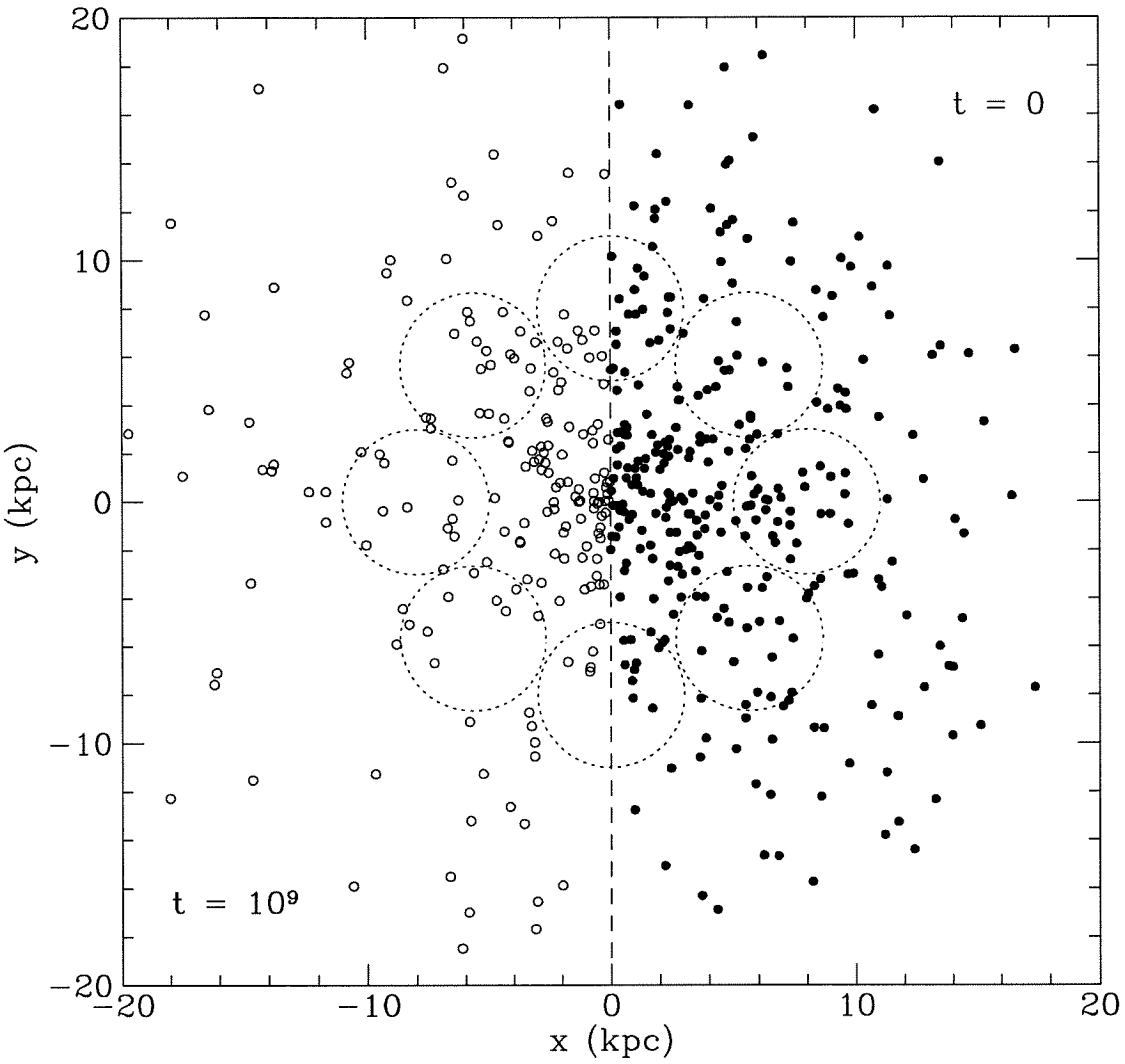

Figure 7.10: **Monte Carlo Pulsars:** The right half of this projection onto the galactic plane is for the initial positions of the pulsars. The mirror images of the positions of the same pulsars after 10^9 years is shown on the left hand side. The circles indicate the volumes sampled by the 'observations'.

kpc, using a volume of radius 3 kpc about the observer (this distance is chosen to approximately recreate the volume sampled by Harrison, Lyne and Anderson (1993)). To make more efficient use of our simulations we can use 8 simultaneous observers spread equidistantly around the circle R = 8 kpc (see Figure 7.10). As long as the observing volumes don't overlap, the observations from all volumes can be added together. We calculate the transverse velocities after subtracting the circular velocity of the observer and derive the observed velocity distribution as a function of time.

Figure 7.11 shows the evolution of the transverse velocity distribution with time. We can compare it to our corrected observed distributions, both for $t < 10^7$ years[2] and for $t > 10^7$ years. Our older distribution here does not include the millisecond pulsars and has a mean age of $\sim 2 \times 10^7$ years. Hence this curve should not be interpreted as representing the truly dynamically old population. Indeed, the high velocity end of the distribution agrees well with the 10^7 year curve, although a low velocity excess has begun to develope. To properly constrain the evolved distribution will require modelling the selection effects of all the pulsars with proper motions.

An additional constraint on the evolved distribution is the magnitude of the asymmetric drift. For the kick distribution (7.4) the magnitude is small ($V_\ell < 10\,\mathrm{km.s^{-1}}$) to begin with, reaching a maximum of ~ 80 km.s^{-1} after 10^8 years and then reaching an asymptotic value of ~ 60 km.s^{-1} after 10^9 years. The evolution of this quantity is shown in Figure 7.7. Again, we see we have the correct order of magnitude.

As we have noted before, a proper comparison of our results with the older pulsars will require an analysis of the millisecond pulsar distribution. However, many of these pulsars are in binaries (see, for example, Figure 7.7). Thus, we also need to calculate the distribution of kick velocities for the binaries. Similar calculations have been performed by numerous authors for different kick distributions (e.g. Dewey and Cordes (1986), Brandt and Podsiadlowski (1995)) and we shan't go into details here. This calculation introduces further uncertainties into the problem through the initial distribution in orbital period, companion masses and pre-supernova helium star masses. Figure 7.12 shows a representative calculation for a binary that initially had a 1 day orbital period, a companion of 1 $M_\odot$ and a Helium star of 3.5 $M_\odot$ which then exploded in a supernova, leaving a 1.4 $M_\odot$ neutron

[2]We see that the 10^5 year distribution confirms our analysis of section 7.3

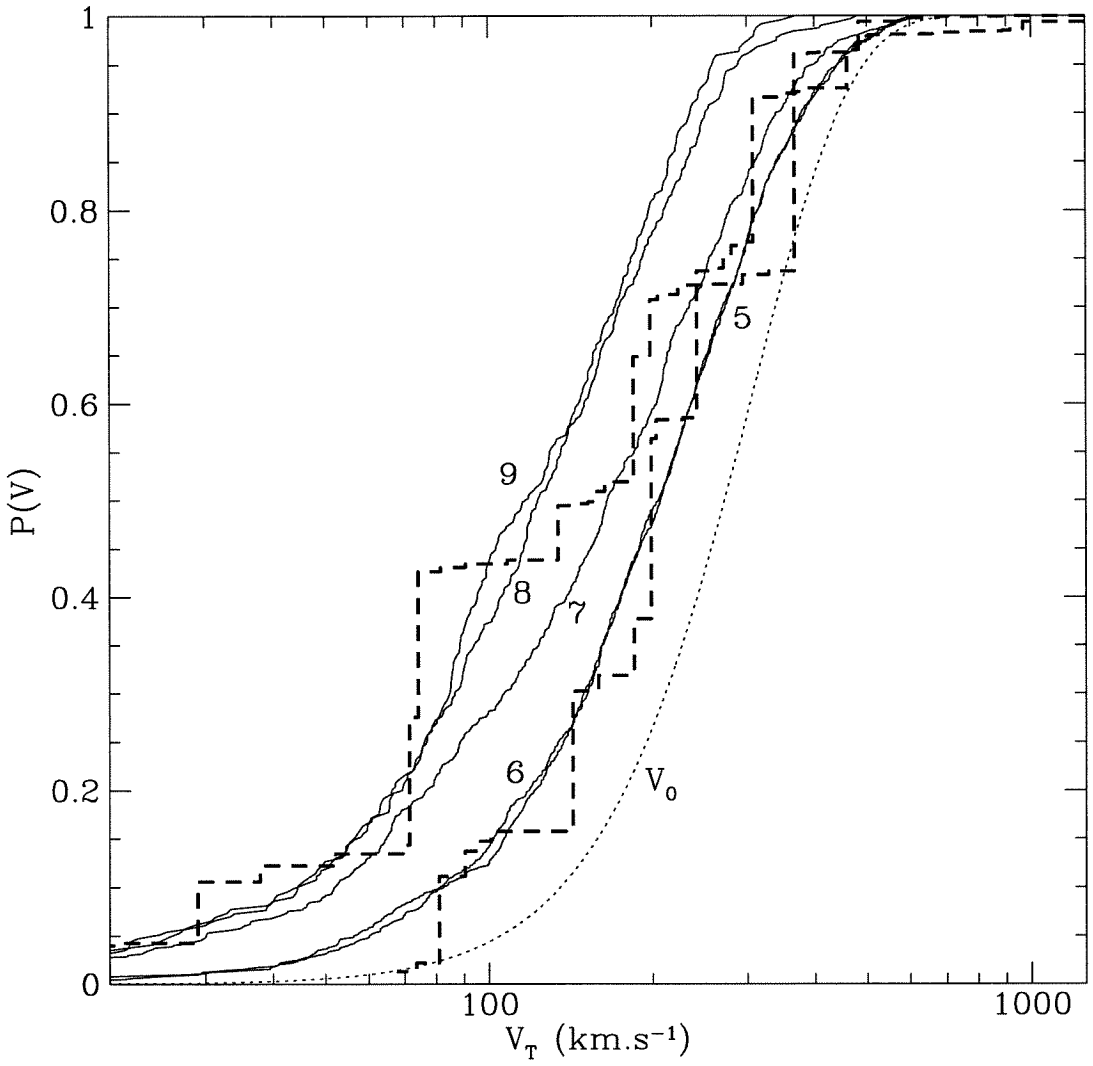

Figure 7.11: **Velocity Distribution Evolution:** The solid lines, labelled by log(age), are the time-dependant transverse velocity distributions produced by the initial three dimensional distribution labelled V_0 (dotted line). The dashed lines indicate the observed 'young' (lower) and 'old' (upper) distributions.

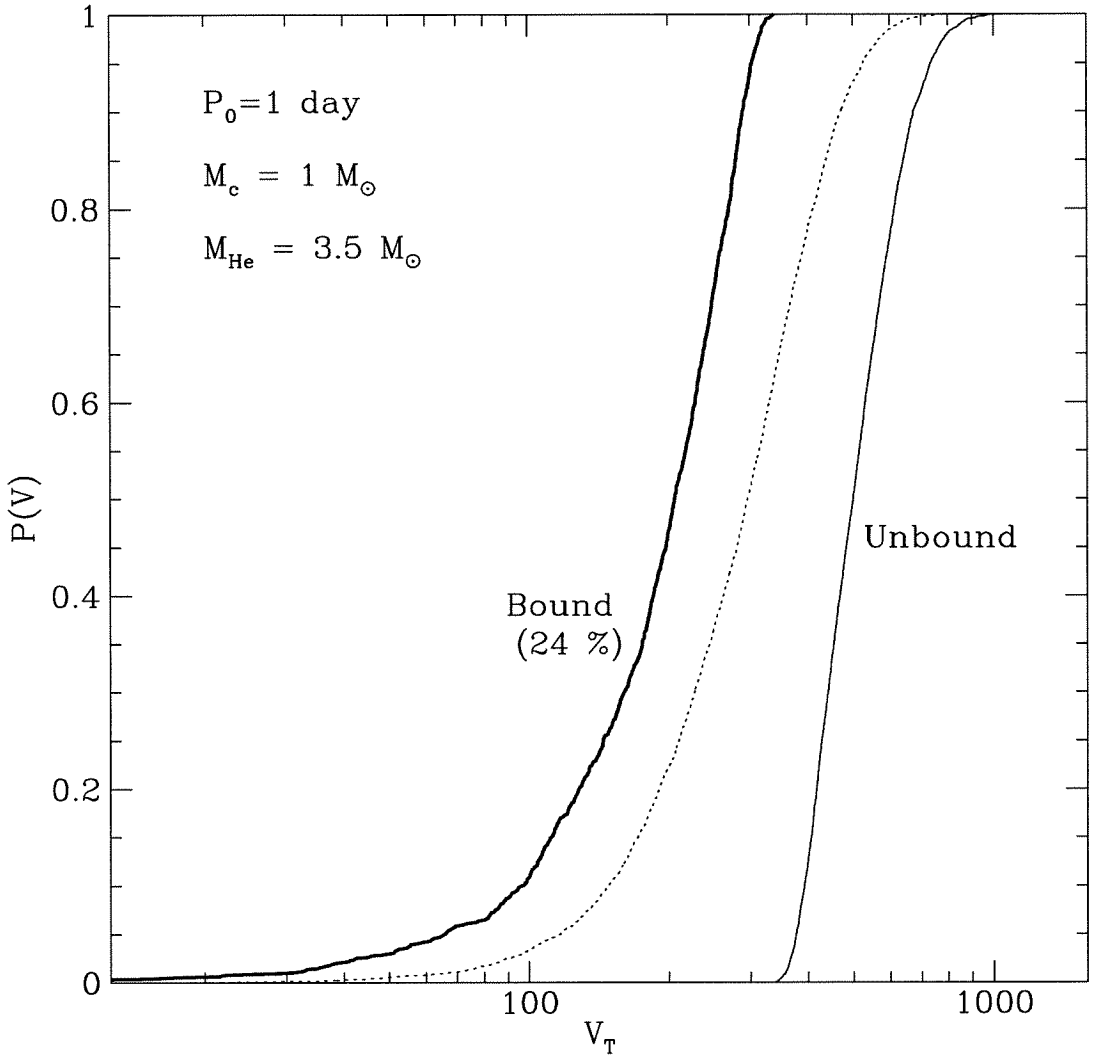

Figure 7.12: **Kicks in Binaries:** The dotted line is the three-dimensional kick the neutron star in the binary acquires at birth. 24 % of the binaries survive this, acquiring centre-of-mass velocities given by the thick solid line. The rest of the binaries are unbound, with the neutron star acquiring a velocity given by the thin solid line. The final orbital periods of the bound systems range from 0.5 days to 10^4 days.

star which also acquired a kick chosen from the distribution (7.4).

7.5 Discussion

Our approach above is designed to provide a robust, largely model-independent estimate of the characteristic velocities of pulsars. We have tested the procedure with simple Monte Carlo simulations using known distributions. We find that we can reproduce the mean velocities to within $\sim 30 - 50$ km.s^{-1}, although the exact shape of the distribution at the high velocity (> 300km.s^{-1}) is not well constrained. To better estimate the shape of the distribution will require more detailed modelling and the use of more of the pulsar population information, such as was done by Narayan and Ostriker (1991) or Bhattacharya et al. (1991).

Another recent analysis by Iben and Tutukov (1996) finds a large birthrate of very slow (< 10km.s^{-1}) pulsars. Their treatment neglects flux limits (although some inferences are made on the basis of a nearby sample only, their full analysis uses pulsars at all distances), and treated the proper motion limits using various ad hoc analytic cutoffs. They also used no upper age cutoffs, so that their large birthrate of slow pulsars was due to 3 old ($t > 10^7$ years) pulsars, which acquired significant weight because of the small likelihood of seeing them. When restricting ourselves to ages $< 10^7$ years, we do not find any such low velocity tail. Furthermore, we find that the flux cutoff is responsible for the detection limit of more pulsars than the proper motion limit.

Some constraints on the nature of pulsar kicks can be obtained by analysing the properties of binaries containing neutron stars. Recently, in the light of the results of Lorimer and Lyne (1995), Brandt and Podsiadlowski (1995) analysed the effect of the revised kick distribution on the post-supernova orbital parameters of neutron star binaries. Their analysis indicated that an isotropically distributed kick velocity of 450 km.s^{-1} was inconsistent with the eccentricity-orbital period distribution of the observed binary population. However, a kick velocity of 200 km.s^{-1} was perfectly consistent. Similarly, Wijers et al. (1992) obtained an upper limit of 400 km.s^{-1} for a characteristic kick velocity from an analysis of the eccentricities of the known double neutron star binaries. Both of these results are in good agreement with our analysis.

The most direct test of the pulsar kick velocities is to find the supernova remnant

associated with the birth of a given pulsar. If the pulsar was born at the centre of a circularly symmetric supernova remnant, we may infer a proper motion and thus a velocity. Much work has been devoted to this (Caraveo (1993), Frail et al. (1994)), and the results indicate velocities significantly larger than the mean velocity derived by other methods. In fact, the mean velocity of the Frail et al. sample is 990 km.s^{-1}, with a median of 480 km.s^{-1}. Whether or not this discrepancy with respect to our results is real depends on the veracity of the various assumptions used to infer a proper motion from a supernova association. Some of the problematic assumptions discussed by Frail et al. include the difficulty of defining the shape of a remnant and the possible displacement of the supernova blast centre with respect to the geometric centre of the remnant (possibly caused by expansion into an inhomogeneous surrounding medium). It is illuminating, although not conclusive, to note that the two pulsars associated with supernova remnants which have measured proper motions are the Crab and Vela pulsars, with transverse velocities of 150 and 120 km.s^{-1} respectively (In particular, Frail et al. note that the methods used on other pulsar-remnant associations would imply a velocity of 800 km.s^{-1} for the Vela pulsar!)

A revised velocity distribution can possibly affect the results of statistical analyses of the pulsar population as a whole. Indeed, it may even contribute to an explanation for the conflicting claims concerning magnetic field decay. Narayan and Ostriker (1990) used a Maxwellian distribution for their paper on the pulsar population as a whole. They used two different populations of pulsars and their kick distribution was a function of magnetic field. Their two populations had velocities that varied from 80-250 km.s^{-1} for their S population and from 20-100 km.s^{-1} for their F population. The analysis of Bhattacharya et al. (1991) also used a Maxwellian, but with a somewhat lower dispersion of 110 km.s^{-1}. Our value lies a little above these characteristic values, consistent with the fact that the dispersion measure distances are now thought to be larger than those used in the above analyses.

One possible problem with our result lies with the lack of a pronounced low velocity tail. This has implications for the retention fraction of neutron stars in globular clusters, as well as the existence of some obviously low velocity pulsars with ages $> 10^7$ years (see section 7.2.3). Globular cluster central escape velocities are ≤ 50 km.s^{-1} (and frequently $\sim$ 10 km.s^{-1}). If all kick velocities are ~ 250 km.s^{-1}, then no pulsars born from isolated stars are retained! If the distribution is maxwellian, then the fraction retained is about 0.2%, which is still extremely low! Yet, the retention fraction of neutron stars is claimed to be

of the order of 10% (Phinney (1993)) or higher (Hut and Verbunt (1983)). However, it is possible that pulsars born in binaries, either primordial or dynamically formed, could be responsible for the pulsars found in globular clusters (see Hut et al. (1992)). Brandt and Podsiadlowski (1995) find that $\sim$ 17% of binaries remain bound if the kick velocity is 200 km.s^{-1}, which is the right order of magnitude to explain the required mass in dark massive remnants. However, this is likely to be an upper limit on the retention fraction because even systems which remain bound can receive significant centre-of-mass velocities. In the light of this, we should point out that the lack of a low velocity tail in our distribution is not a result of the V_{max} weighting. Of the 51 pulsars in our sample with ages less than 10^7 years, the lowest transverse velocity is 70 km.s^{-1}. If there are young pulsars with very small velocities, then they have not been measured yet. Another possible complication is the creation of fast (P $<$ 0.1 s) pulsars with initial timing ages $> 10^7$ years. The birthrate of such pulsars is not constrained by our analysis because of both our age cutoff and the restriction of our analysis to the early Molonglo and Green Bank surveys.

In conclusion, we have shown that the distribution of pulsar proper motions, corrected for selection effects, is consistent with a characteristic kick velocity at birth of $\sim$ 250-300 km.s^{-1}. We find little evidence for a significant low velocity tail to the distribution. Our method is largely model-independent, and hence robust in its reproduction of the mean velocity and low velocity shape of the distribution. However, the shape of the distribution at velocities $>$ 300 km.s^{-1} is not well constrained by this method. Our results are in good agreement with the properties of binaries containing neutron stars and pleasantly close to the value expected from numerical supernova simulations. However, our results may be in conflict with the estimates for the retention of pulsars in globular clusters.

REFERENCES

Bhattacharya, D. et al., 1991, A&A, **254**, 198.

Brandt, N. & Podsiadlowski, P., 1995, MNRAS, **274**, 461.

Camilo, F., Nice, D.J. & Taylor, J.H., 1995, preprint

Caraveo, P.A., 1993, ApJ, **415**, L111.

Cordes, J., 1986, ApJ, **311**, 183.

Dewey, R.J., et al., 1984 in *Millisecond Pulsars*, ed. S.P.Reynolds & D.R.Stinebring (NRAO), p. 234.

Dewey, R.J., et al., 1985, ApJ, **294**, L25.

Feigelson, E.D. & Nelson, P.I., 1985, ApJ, **293**, 192.

Frail, D.A., Goss, W.M. & Whiteoak, J.B.Z., 1994, ApJ, **437**, 781.

Gott, J.R., Gunn, J.E. & Ostriker, J.P., 1970, ApJ, **160**, L91.

Harrison, P.A. & Lyne, A.G., 1993, MNRAS, **265**, 778.

Helfand, D.J. & Tademaru, E., 1977, ApJ, **216**, 842.

Hut, P. & Verbunt, F., 1983, Nature, **301**, 587.

Hut, P., et al., 1992, PASP, **104**, 981.

Iben, I. & Tutukov, A.V., 1996, ApJ, **456**, 738.

Kaplan, E.L. & Meier, P., 1958, *J.Am.Statistical Ass.*, **53**, 457.

Lyne, A.G. & Lorimer, D.R., 1994, Nature, **369**, 127.

Manchester, R.N., et al., 1978, MNRAS, **185**, 409.

Mihalas, D. & Binney, J., 1981, 'Galactic Astronomy', (W.H.Freeman and Company)

Narayan, R., 1987, ApJ, **319**, 162.

Narayan, R. & Ostriker, J.P., 1990, ApJ, **352**, 222.

Nice, D.J. & Taylor, J.H., 1995, ApJ, **441**, 429.

Paczynski, B., 1990, ApJ, **348**, 485.

Phinney, E.S., 1993, in *Structure & Dynamics of Globular Clusters*, ed. S.G.Djorgovski & G.Meylan, (ASP), **50**, 141.

Phinney, E.S. & Kulkarni, S.R., 1994, ARA&A, **32**, 591.

Press, W.H., Teukolsky, S.A., Vetterling, W.T. & Flannery, B.P., 1992, *Numerical Recipes*, Cambridge University Press

Harrison, P.A. & Lyne, A.G., 1993, MNRAS, **265**, 778.

Harrison, P.A., Lyne, A.G. & Anderson, B., 1993, MNRAS, **261**, 113.

Stokes, G.H., Segelstein, D.J., Taylor, J.H. & Dewey, R.J. , 1986, ApJ, **311**, 694.

Stokes, G.H., Taylor, J.H., Weisberg, J.M. & Dewey, R.J., 1985, Nature, **317**, 787.

Taylor, J.H. & Cordes, J.M., 1993, ApJ, **411**, 674.

Taylor, J.H., Manchester, R.N. & Lyne, A.G., 1993, ApJS, **88**, 529.

Wijers, R.A.M.J., van Paradijs, J. & van den Heuvel, E.P.J., 1992, A&A, **261**, 145.

Appendix A Low Temperature H and He Opacities

Much of the following calculation is essentially a recapitulation of the work of Lenzuni, Chernoff and Salpeter (1991), but with a variety of different compositions and, in a few places, slightly updated physical inputs. We undertook this calculation to fill in the gap in the opacity table left by the restriction of OPAL opacity calculations to temperatures larger than 6000 K. This is because OPAL does not include the contribution of molecular opacities, which becomes important for hydrogen at temperatures below 6000 K.

We calculate the opacity of a gas containing the atomic, ionic and molecular species H, He, H_2, H^-, He−, H_2^+, H_3^+ and He^+ as well as electrons. We assume that the equation of state is that of an ideal gas (comparison with the Saumon et al. calculations show that this is a good approximation for $\rho \leq 10^{-2}\mathrm{g.cm}^{-3}$) and that LTE holds. Most of our partition functions and cross-sections come from Lenzuni et al. (1991), although we have recalculated some of the molecular absorption coefficients as described below.

A.1 Ionization Balance

The assumption of LTE means that we use the Saha equation throughout this calculation. For the case of hydrogen atmospheres, this is sufficient because the region of parameter space where pressure ionization occurs is not probed by the atmospheric models we require. For a pure helium atmosphere, the opacity is low enough that pressure ionization can become important. Where necessary we treat this using an abrupt transition from radiative to conductive opacity. The use of the assumptions of ideal gas and LTE up to this point are not terribly important because the helium radiative opacity is low enough that the atmosphere remains approximately isothermal. The important factor is the density at which we begin pressure ionization. We choose this to be $\rho \sim 1 - 3\,\mathrm{g.cm}^{-3}$.

Table A.1 shows the dissociation/ionization potentials used for each important reaction.

In Figures A.1 and A.2, we see the change in the equilibrium concentration of different

Reaction	χ_I (eV)
$H_2 \rightarrow 2H$	4.478
$H \rightarrow H^+ + e^-$	13.598
$H_2^+ \rightarrow H + H^+$	2.643
$H_3^+ \rightarrow H_2 + H^+$	4.355
$H^- \rightarrow H + e^-$	0.755
$He \rightarrow He^+ + e^-$	24.586

Table A.1: The Ionization potentials for the important reactions in an H-He plasma at temperatures $< 10^4$ K.

species with temperature. The figures are for a mixture that is equal mass helium and hydrogen. The basic trend shows that molecular hydrogen dominates at low temperatures and high densities, while atomic hydrogen dominates at higher temperatures and lower densities, eventually becoming ionized hydrogen. The minor species of ions never become important for the equation of state, but are nevertheless important for the opacity, as we shall see. The intermediate density case of 10^{-4}g.cm^{-3} corresponds to optical depths of order unity in the white dwarf atmospheres.

A.2 Collisionally Induced Molecular Absorption

The ground electronic state of the H_2 molecule has no electric dipole moment, so any absorption of photons has to take place via electric quadropole transitions. Thus, at low densities, molecular hydrogen is transparent to visible and infrared light.

At higher densities, however, collisions between an H_2 molecule and a helium atom (or H atom or another H_2 molecule) form a temporary 'supermolecule' with a non-zero electric dipole and can thus absorb photons much more efficiently. The collision times are (Borysow, Frommhold and Dore (1987))

$$\Delta t \sim 3 \times 10^{-13} \left(\frac{T}{3000K}\right)^{-1/2} \tag{A.1}$$

which implies broad absorption with a characteristic frequency width

$$\Delta\nu \sim (c\Delta t)^{-1} \sim 111 cm^{-1} \left(\frac{T}{3000K}\right)^{1/2}. \tag{A.2}$$

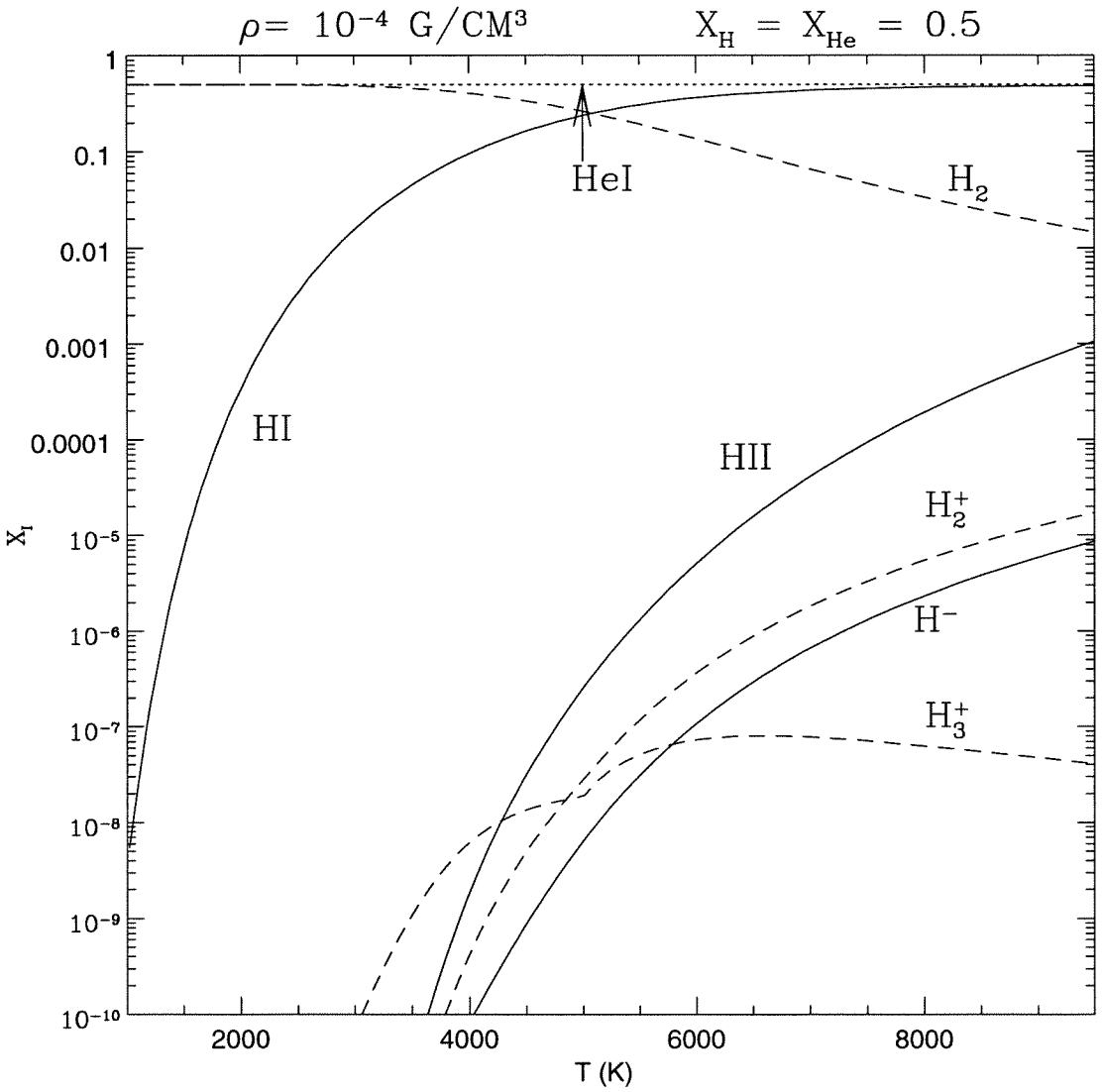

Figure A.1: **Ionization Balance 1:** The solid lines refer to the various ionization states of atomic hydrogen. The dashed lines refer to the various ions of molecular hydrogen. The dotted line corresponds to helium. For these temperatures, helium remains completely neutral. The curves represent the mass fraction of each species as a function of temperature.

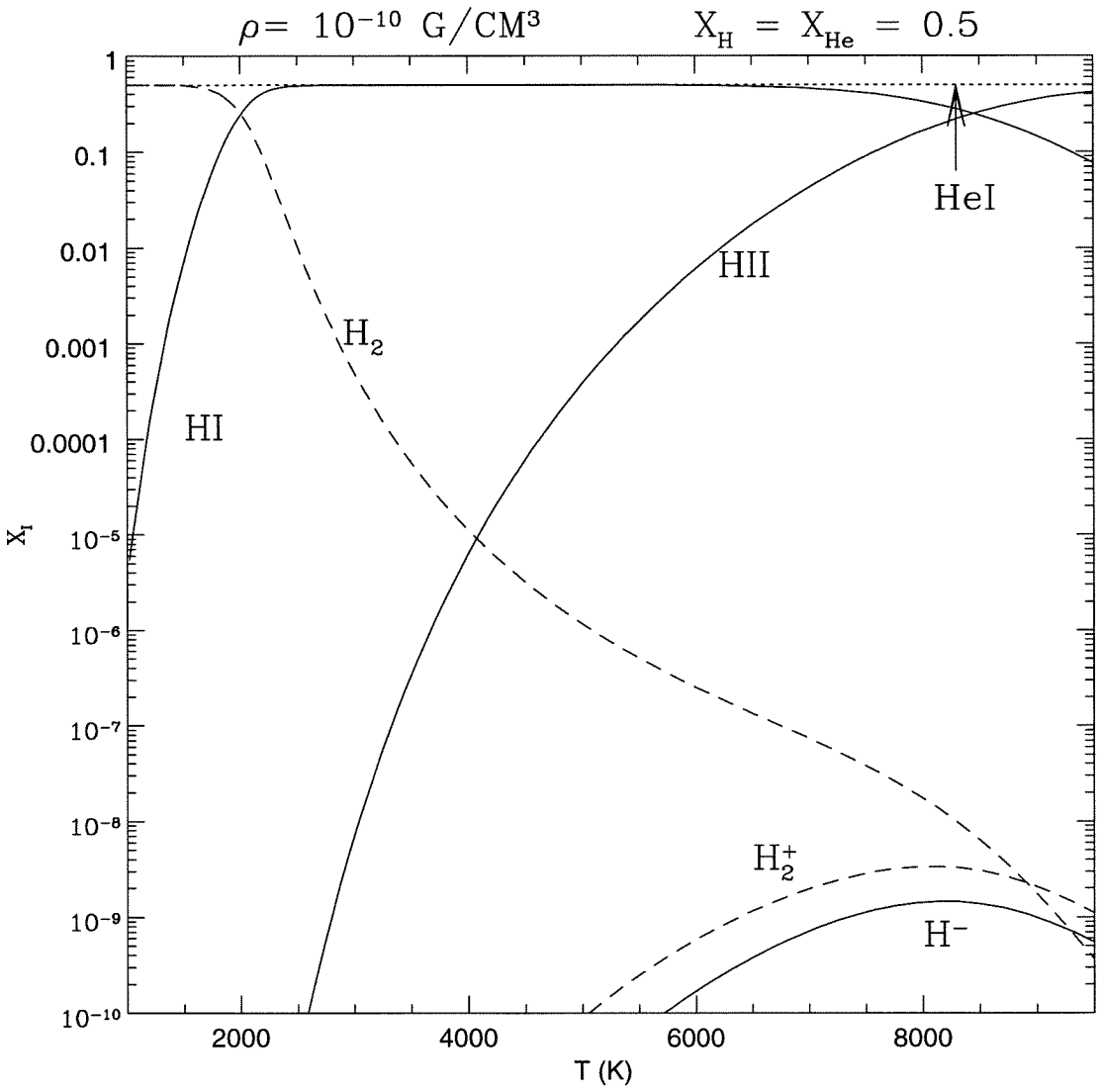

Figure A.2: **Ionization Balance 2:** The low density case clearly shows the transition from molecular to atomic to ionized hydrogen.

This line width is broader than the characteristic energy difference between rotational levels $\sim h/2\pi m_p c(1\text{Å})^2 \sim 70\,cm^{-1}$, but smaller than that between vibrational levels ($\sim (m_p/m_e)^{1/2}\,\nu_{rot} \sim 2900\,cm^{-1}$). Thus, the absorption occurs in broad bands centred around the rotational-vibrational transition frequencies of the H_2 molecule. For $H_2 - H_2$ collisions, simultaneous transitions can occur in both colliding partners, which leads to absorption at the sums and differences of these transition frequencies as well.

The opacity in the rototranslational (RT) and rotovibrational (RV) transitions due to H_2 – He collisions is given by the expression

$$\kappa(\omega, T) = \frac{4\pi^2}{3hc} n(H_2) n(He) \omega \left(1 - e^{-\hbar\omega/kT}\right) G(\omega, T) cm^{-1} \tag{A.3}$$

where G is the spectral density given by

$$G(\omega, T) = \sum_{vv'} \sum_{JJ'} \sum_{L\lambda} P_{vJ}(T) C(J\lambda J'; 00)^2 g_{L\lambda}^{vv'}(\omega - \omega_{vJv'J'}; T) \tag{A.4}$$

where C is the Clebsch-Gordon coefficient linking the two levels involved in each transition, P is the thermal Boltzmann factor

$$P_{vJ}(T) = \frac{g_J\, e^{-E_{vJ}/kT}}{Z_{H_2}} \tag{A.5}$$

and $g_{L\lambda}^{vv'}$ is the absorption line profile for each transition. The quantum numbers v and J label the vibrational and rotational energy levels respectively. The quantum numbers L and λ are the quantum numbers that result from an expansion of the vector separation of the two colliding molecules/atoms (L) and the two nuclei of the molecule (λ) in terms of spherical harmonics. The reflection symmetry of the H_2 molecule restricts λ to even values[1]. The absorption processes are linked by a selection rule $L = \lambda \pm 1$. This is because the absorption or emission of a photon requires a change in the angular momentum of the system. λ and L represent the components of the orbital angular momentum along the H_2 axis and the H_2 – He axis respectively, so that the absorption of a photon changes the configuration. The spectral density for the $H_2 - H_2$ interaction is somewhat more complicated due to the possibility of double transitions.

[1] $Y_\ell^m(\pi + \theta, \phi) = (-1)^\ell Y_\ell^m(\theta, \phi)$

The dominant contributions to the opacity come from the transitions with low L and λ. We calculate the RT contributions for $H_2 - H_2$ using the code of Zheng and Borysow (1995), which accounts for all v=v′ transitions for v=0-3. Our calculations of the $H_2 - H_2$ RV transitions use the results of Borysow and Frommhold (1990) supplemented by the estimates of Lenzuni et al. (1991) for the overtones (e.g., $v = 0 \rightarrow 2$) and double transitions ($v_1 = 0 \rightarrow 1, v_2 = 0 \rightarrow 1$). The $H_2 - He$ results are similarly obtained from the results of Borysow and Frommhold (1989) and Borysow, Frommhold and Birnbaum (1988). An example of the CIA spectra at 1000 K is shown in Figure A.3.

All our calculations assume binary interactions. At high densities, many-body effects can alter the opacities. Lenzuni et al. determined that higher order effects are only important for $\rho \geq 10^{-2}$g.cm^{-3}. This is not important because the hydrogen opacity is sufficiently large that this region lies in the optically thick part of the atmosphere and the energy transport is driven by convection for the atmospheres we calculate.

A.3 The Opacity Table

Now that we have an ionization equilibrium, we need to calculate all the possible opacity sources, both from absorption and from scattering. We include molecular CIA absorption as described in the previous section for $H_2 - H_2$ and $H_2 - He$. We also include bound-free absorption from both neutral hydrogen and H^-. We include the free-free absorption from H, H^-, H_2, H_2^-,H_3, He and He^-. We also include Rayleigh scattering from H, H_2 and He, as well as Thomson scattering. Finally, we also include the dissociation reactions for H_2 and H_2^+. The cross-sections for these processes were taken from Lenzuni et al. (1991) and references therein.

Figures A.4 and A.5 show the dominant opacity sources for a low density and intermediate density environment. We see that molecular absorption becomes important for high density and low temperature, while H^- dominates the opacity at higher temperatures, despite its low abundance by mass.

Once we have monochromatic opacities, we need to calculate the Planck and Rosseland mean opacities which will be used in our calculations and for comparison to other opacity compilations.

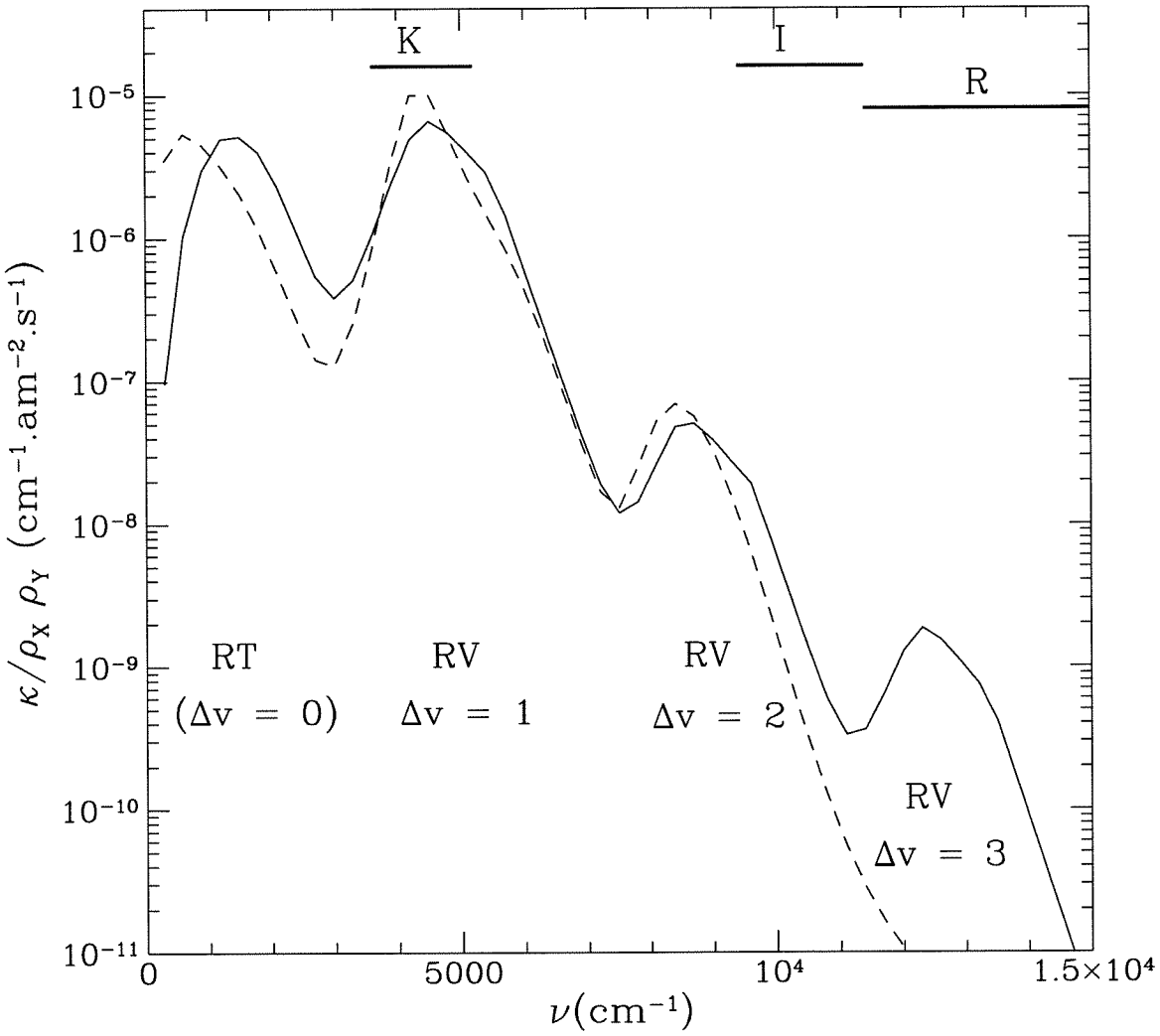

Figure A.3: **The Collisionally Induced Opacity of Hydrogen:** The solid line shows the $H_2 - H_2$ CIA opacity, and the dashed line shows the $H_2 - He$ opacity. In both cases the density dependence has been removed. The temperature for this case is T=1000 K. The approximate positions of important infrared passbands are shown at the top, and the various broad peaks are labelled according to the various transitions. The abbreviation am stands for amagat = $c^{1/2}$/Loschmidts number = 6.45×10^{-15} cm$^{7/2}$s$^{-1/2}$.

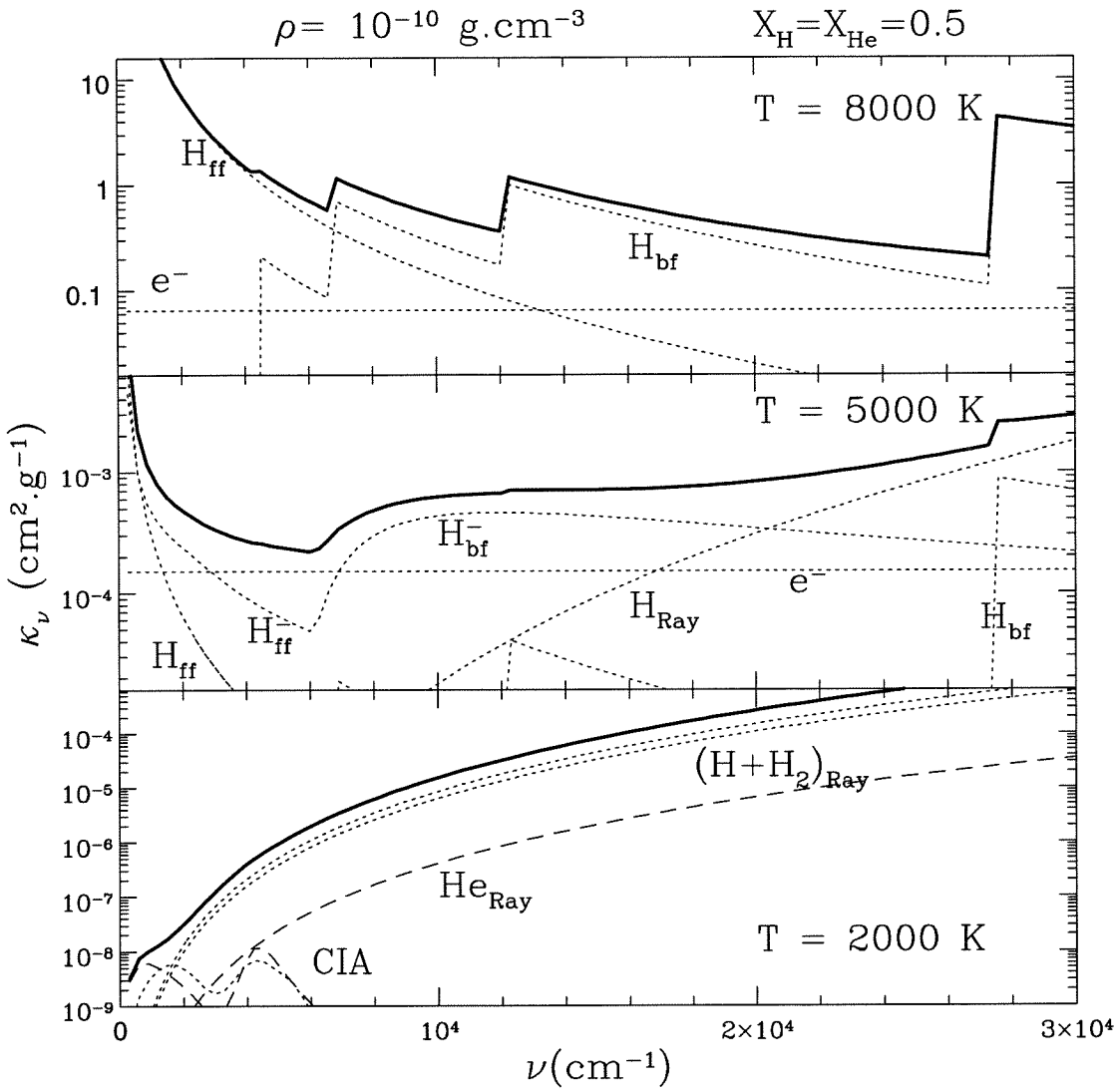

Figure A.4: **The Low Density Opacity:** This figure shows the monochromatic opacity at three different temperatures for a low density, equal parts by mass H-He plasma. We see that, at low temperatures, the opacity is dominated by Rayleigh scattering, and then at intermediate temperatures by the H^- ion and finally atomic H bound-free and free-free opacities at higher temperatures. The heavy solid line indicates the total monochromatic opacity in each panel. The dotted lines are H opacities and the dashed lines are He opacities.

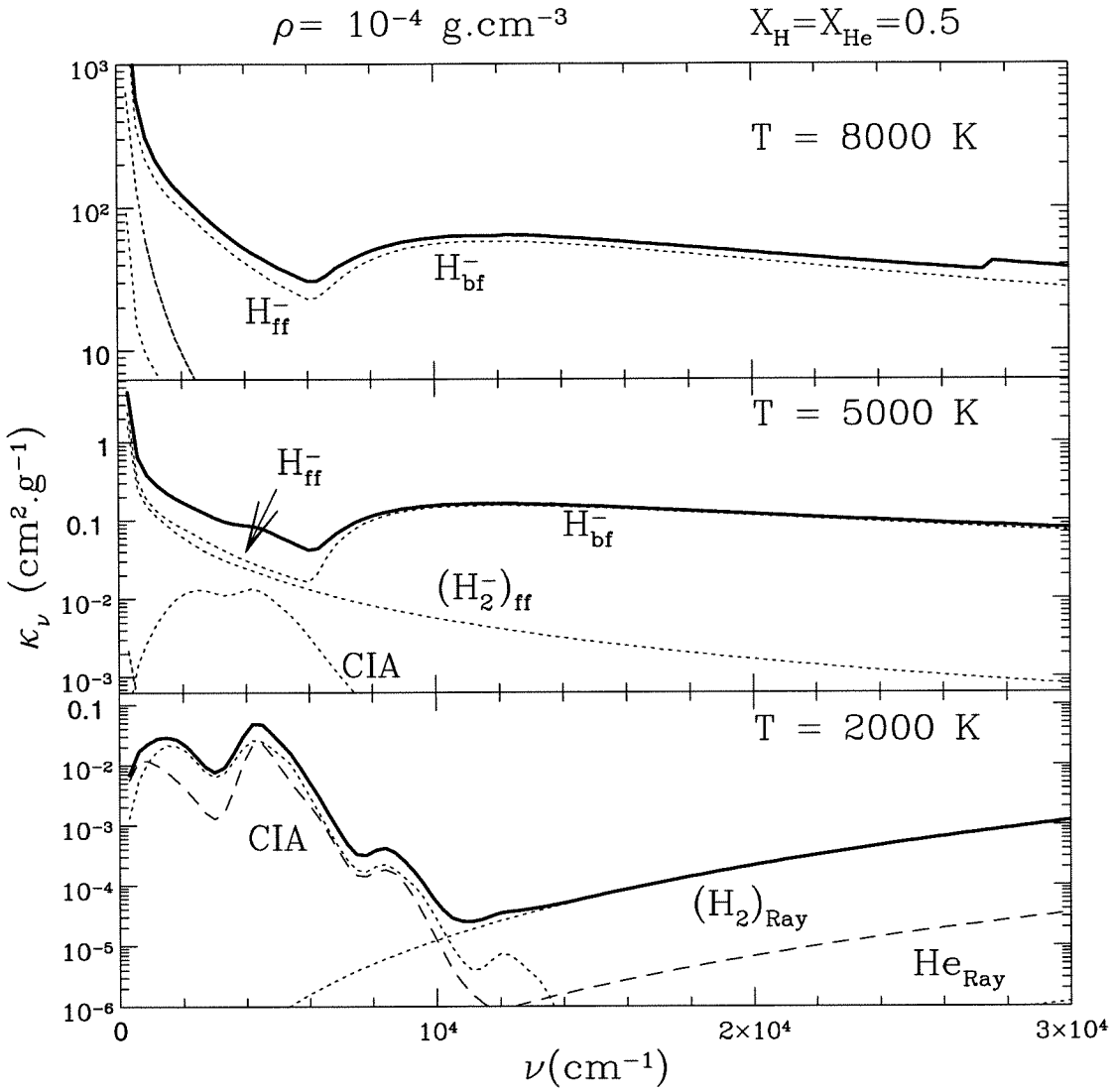

Figure A.5: **The Intermediate Density Opacity:** This figure shows the monochromatic opacity at three different temperatures for an intermediate density, equal parts by mass, H-He plasma. We see that, at low temperatures, the opacity is dominated by Rayleigh scattering at short wavelengths, but that collisionally induced molecular absorption dominates at longer wavelengths. As the temperature increases, the contribution from the molecules drops away and the H^- and H_2^- opacities take over (middle panel) until the opacity is dominated by the H^- absorption.

1. The Rosseland mean opacity is defined by

$$\frac{1}{\kappa_R} = \frac{\int_0^\infty \frac{1}{\kappa_\nu}\frac{\partial B_\nu}{\partial T} d\nu}{\int_0^\infty \frac{\partial B_\nu}{\partial T} d\nu} \tag{A.6}$$

and is used in the optically thick limit. It results from averaging the radiative diffusion equation (which is valid at large optical depths) over frequency.

2. The Planck mean opacity is defined by

$$\kappa_P = \frac{\int_0^\infty \kappa_\nu B_\nu d\nu}{\int_0^\infty B_\nu d\nu} \tag{A.7}$$

and is used in the optically thin limit. This results from the frequency average of the emissivity and Kirchoff's law.

Figure A.6 shows the comparison between the Rosseland and Planck means calculated above and the OPAL opacities of Rogers and Iglesias (1992). The curves join smoothly onto one another in the region of common validity. At lower temperatures, the Planck and Rosseland means start to differ significantly from one another as the dominant opacity source shifts from H^- to Rayleigh scattering. The two means will differ when the monochromatic opacity varies significantly in the frequency range of interest. This is because the Rosseland mean calculation gives extra weighting to those frequencies which have small opacities. The transition is shown by Figures A.7 and A.8. The density in both cases is $\rho = 10^{-9}$g.cm^{-3}, so that they can be compared with Figure A.6. In Figure A.7, where the temperature is 6000 K, we see that the Planck and Rosseland means stress the same frequency range, and thus the resulting mean values are similar. However, in Figure A.8, where the temperature is 3000 K, the opacity at the peak of the two integrands differs by more than two orders of magnitude, which is why the mean values differ significantly. For temperatures lower than 3000 K at this density, the deviation decreases again, because the dip at low frequencies is filled in by the increase in molecular CIA opacities (at higher densities this will occur at even higher temperatures). However, at higher densities, the strong molecular CIA opacities can also lead to deviations between Rosseland and Planck means.

This is demonstrated in Figure A.9, where we have taken the ratio of Planck and Rosseland mean opacities. We see that at low densities and temperatures, the Rayleigh scattering

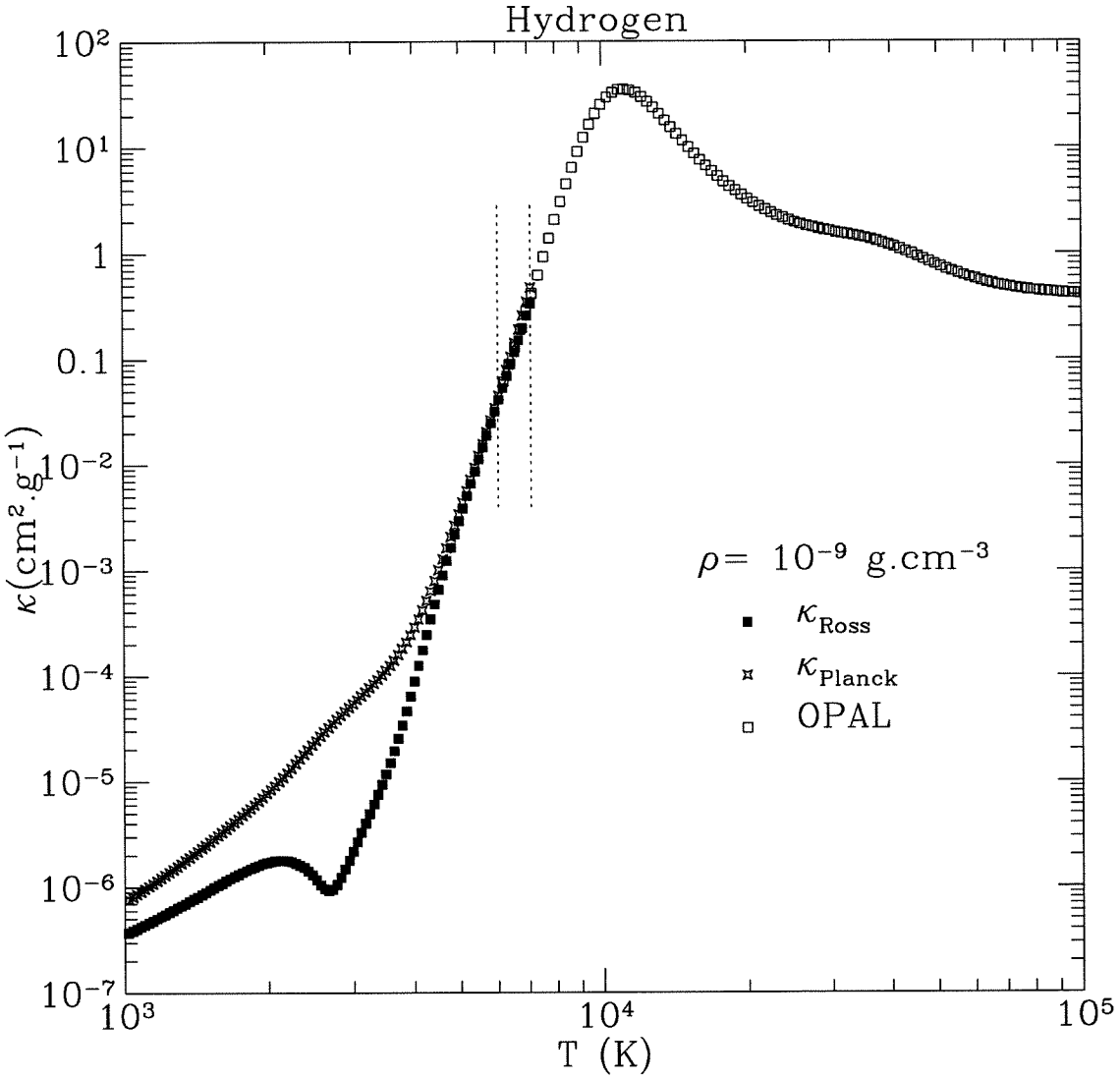

Figure A.6: **Matched Opacities:** The solid squares are the Rosseland means we calculate and the open squares are the result of the OPAL calculation. We see that there is excellent agreement at these low densities. The Planck opacity starts to deviate for T $\leq$ 4000 K, due to the formation of molecules and the influence of CIA.

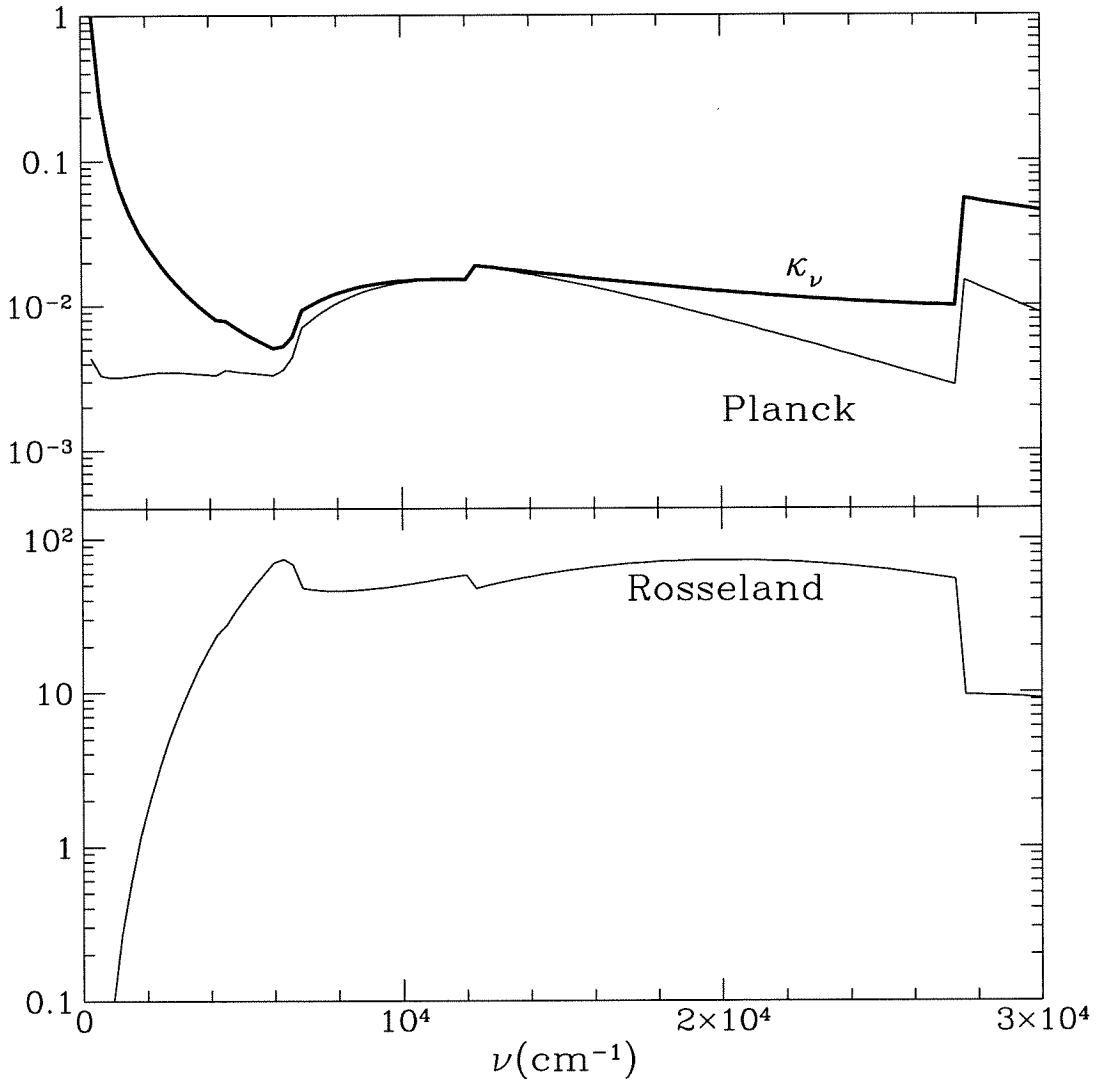

Figure A.7: **Planck/Rosseland Mean 1:** The bottom panel shows the integrand of the integral in the numerator of equation (A.6). The top panel shows the integrand for the integral in the numerator of equation (A.7) (thin line) and the true monochromatic opacity (thick line). The density in this case is 10^{-9}g.cm^{-3} and the temperature is 6000 K.

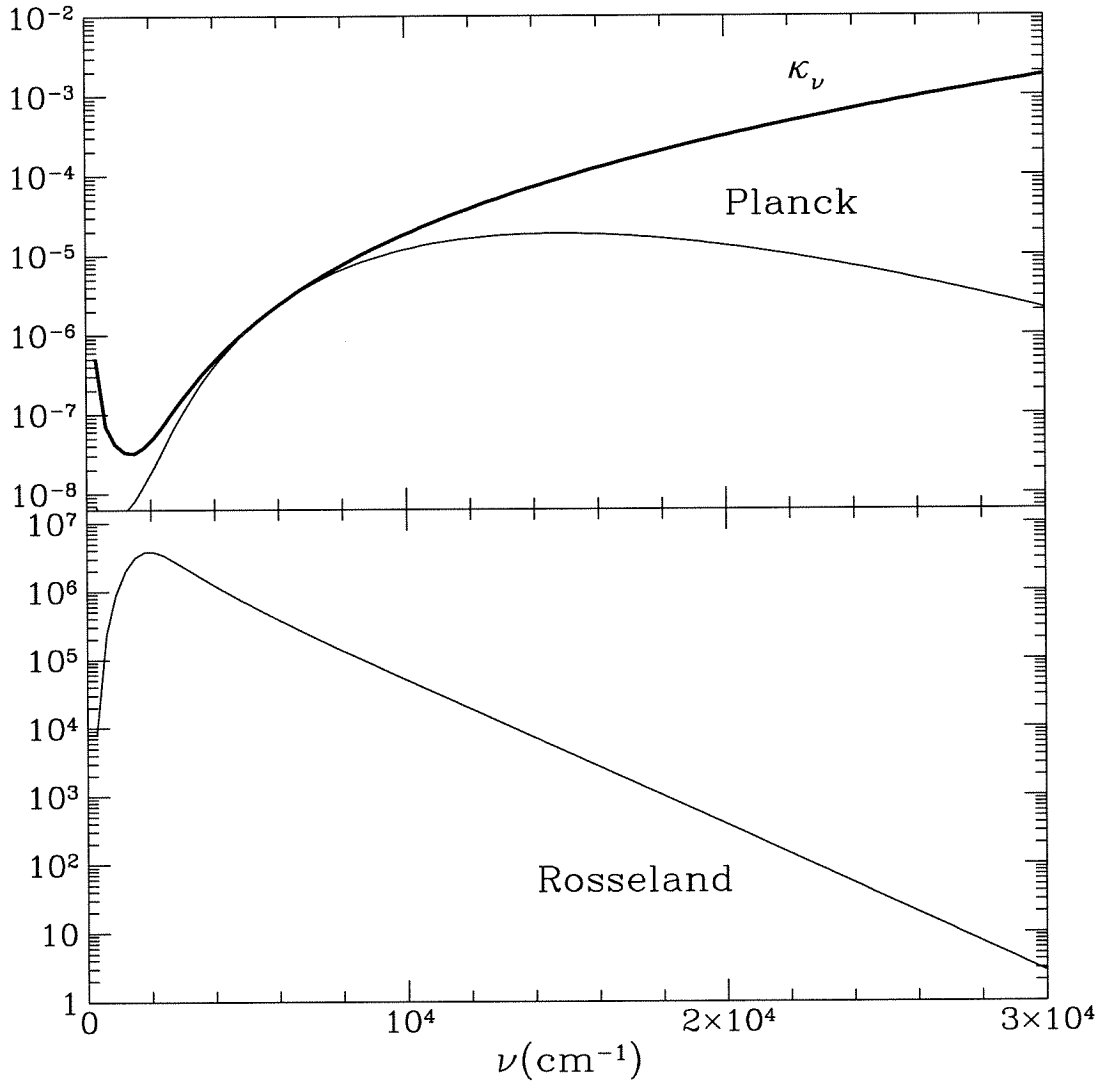

Figure A.8: **Planck/Rosseland Mean 2:** As before, but this time the temperature is 3000 K and the disparity in the Rosseland and Planck means is large.

leads to a significant difference while at high densities the CIA also leads to a large ratio. At temperatures above 4000 K, the two mean opacities are in reasonable agreement. Thus, we can calculate tables of Rosseland and Planck opacities for any hydrogen/helium plasma. Figure A.10 shows some results for the two extreme compositions. The lack of molecules results in a very low opacity for the helium atmosphere.

REFERENCES

Borysow, A. & Frommhold, L., 1989, ApJ, **341**, 549.

Borysow, A. & Frommhold, L., 1990, ApJ, **348**, L41.

Borysow, J. Frommhold, L., & Birnbaum, G., 1988, ApJ, **326**, 509.

Lenzuni, P. Chernoff, D.F., & Salpeter, E.E., 1991, ApJS, **76**, 759.

Rogers, F.J. & Iglesias, C.A., 1992, ApJS, **79**, 507.

Zheng, C. & Borysow, A., 1995, ApJ, **441**, 960.

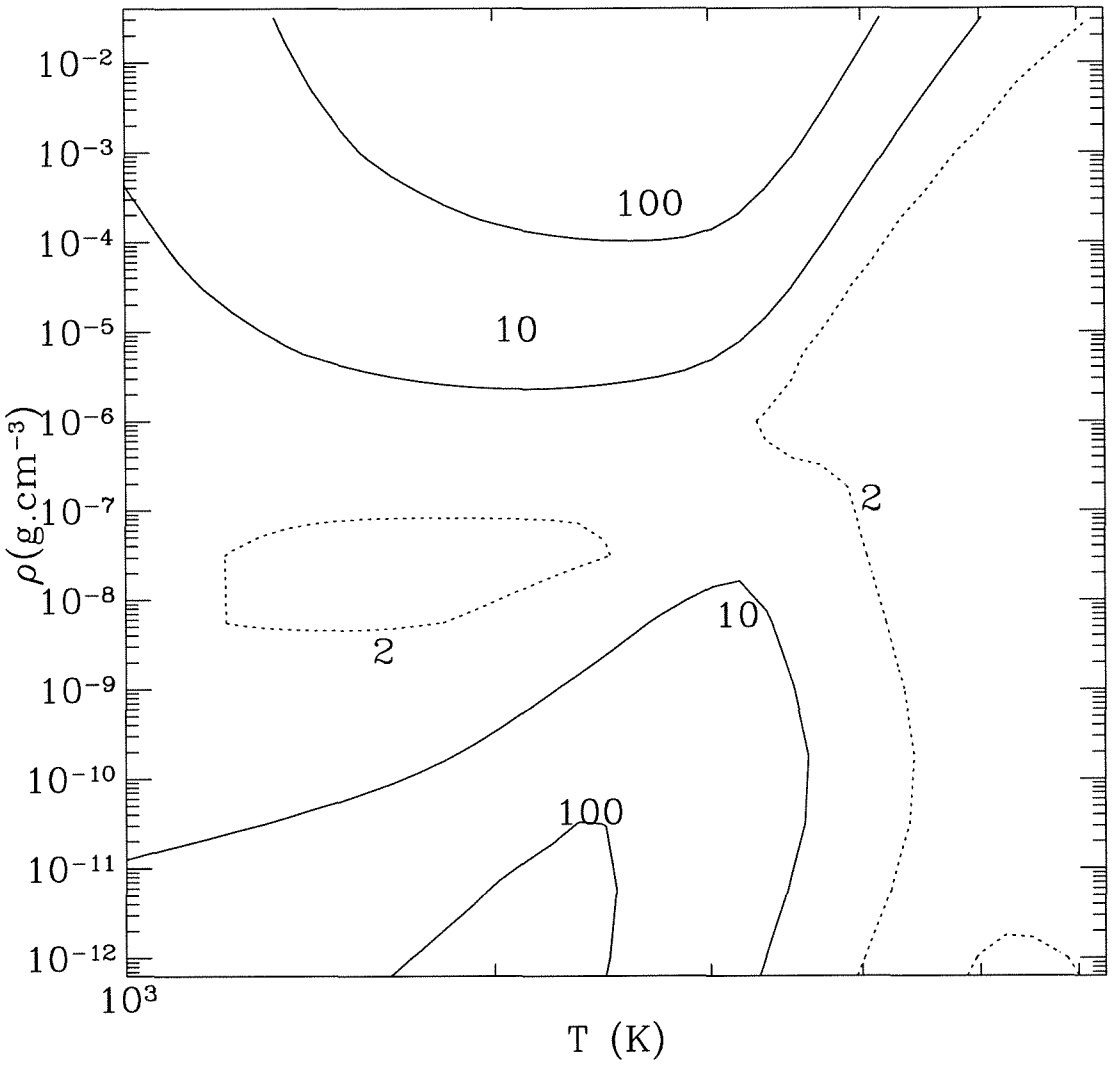

Figure A.9: **Planck/Rosseland Mean 3:** The contours represent constant values of $\kappa_{\rm Planck}/\kappa_{\rm Ross}$. The dotted contour has a value of 2, and the solid contours, of 10 and 100. Thus, we see that below 4000 K, there is a large difference between Planck and Rosseland mean opacities, and we must use the former for the optically thin regions.

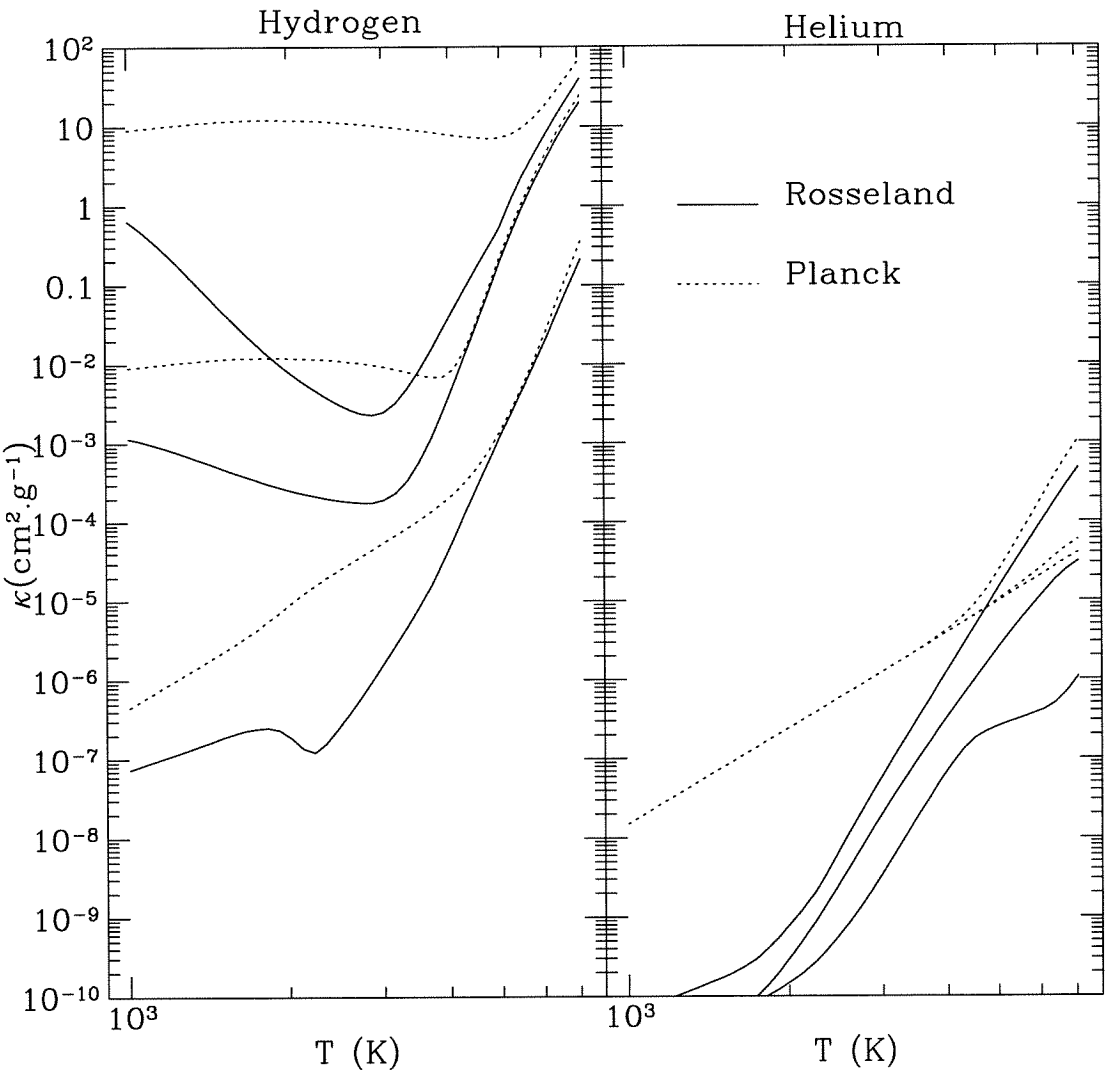

Figure A.10: **Planck/Rosseland Mean 4:** The left panel shows hydrogen Rosseland (solid lines) and Planck (dotted lines) mean opacities as a function of temperature for densities of 10^{-11}, 10^{-5} and 10^{-2} g.cm^{-3} respectively (going from bottom to top). The right panel shows the same quantities but for a pure helium atmosphere.

Appendix B The Thomas-Fermi Model of High Density Matter

In calculating our models, we found that the Fontaine et al. (1977) or Saumon et al. (1995) tables did not extend to the highest densities we required. Thus, to obtain complete coverage of the pressure-density plane, we calculated the equation of state in the high density limit using the Thomas-Fermi model described here.

B.1 The Basic Physics

The Thomas-Fermi model incorporates the effects of a non-uniform electron distribution about each ion by considering the material to be constructed out of identical cells (similar to Wigner-Seitz cells) in which the electron motions are described by a degenerate Fermi gas in an electric potential. This is equivalent to assuming the electron interaction energy is much weaker than the kinetic or potential energies of the individual electrons (since the degenerate gas describes non-interacting particles). The electron distribution is described by

$$n_e = \frac{2}{h^3}\int_0^\infty 4\pi p^2 f(E)dp \tag{B.1}$$

where f is the Fermi-Dirac probability distribution function. In the non-relativistic case, $E = p^2/2m_e$ and so

$$n_e = \frac{8\pi}{h^3}\left(2m_e^3\right)^{1/2}\int_0^\infty E^{1/2} f(E)dE \tag{B.2}$$

Casting this in normalized terms and using $\lambda_e = \hbar/m_e c$, we get

$$n_e = \frac{\sqrt{2}}{\pi^2\lambda_e^3}\left(\frac{kT}{m_e c^2}\right)^{3/2}\int_0^\infty \frac{z^{1/2}dz}{e^{z-z_f}+1} \tag{B.3}$$

where $z_f = p_f^2/2m_e kT$. This is related to the Fermi energy by

$$E_f = \frac{p_f^2}{2m_e} - e\phi(r) \tag{B.4}$$

where $\phi(r)$ is the electrostatic potential in which the electrons move, generated by the Poisson equation

$$\nabla^2\phi = -4\pi\left[Z\,e\delta(0) - e\,n_e(r)\right] \tag{B.5}$$

The Fermi energy itself, E_f, is constant with radius (otherwise electrons would move to radii with lower E_f). Normally E_f is the argument of the Fermi-Dirac function, and the change can be considered as simply a transformation of variables due to the fact that we integrate over the kinetic energy $p_f^2/2m_e$ rather than the full energy E_f. (This is perfectly valid because we do an integral over momentum at fixed position (see equation (B.4).)) We will also denote from now on

$$I_n(z_f) = \int_0^\infty \frac{z^n dz}{e^{z-z_f}+1}. \tag{B.6}$$

The delta function in Poisson's equation can be incorporated into an inner boundary condition and combined with the result that the cell should be charge neutral at its boundary to provide the well defined problem

$$\nabla^2\phi = \frac{4\sqrt{2}e}{\pi\lambda_e^3}\left(\frac{kT}{m_ec^2}\right)^{3/2} I_{1/2}\left(\eta + \frac{e\phi(r)}{kT}\right) \tag{B.7}$$

subject to

$$\lim_{r\to 0} r\phi(r) = Z\,e \tag{B.8}$$

$$\left.\frac{\partial\phi}{\partial r}\right|_a = 0 \tag{B.9}$$

where a is the cell radius and $\eta = E_f/kT$. With the assumption of spherical symmetry, this is a one dimensional problem and $\nabla^2\phi = \frac{1}{r}\frac{\partial^2}{\partial r^2} r\phi$. We define a new variable Ψ via

$$E_f + e\phi(r) = \frac{Ze^2}{r}\Psi \tag{B.10}$$

and rescale the radial variable using $r = R\,x$, where

$$R = \left(\frac{\pi Z}{4\sqrt{2}}\right)^{1/3}\left(\frac{m_ec^2}{kT}\right)^{1/2}\lambda_e \tag{B.11}$$

leading to the equation

$$\frac{1}{x}\frac{\partial^2}{\partial x^2}\Psi(x) = I_{1/2}\left(\alpha\frac{\Psi(x)}{x}\right) \tag{B.12}$$

with

$$\Psi(0) = 1 \tag{B.13}$$

$$\left.\frac{\partial\Psi}{\partial x}\right|_{x_0} = \left.\frac{\Psi(x)}{x}\right|_{x_0} \tag{B.14}$$

where

$$\alpha = \left(\frac{4\sqrt{2}}{\pi}\right)^{1/3} \frac{Z^{2/3}}{\lambda_e} \frac{e^2}{\sqrt{m_e c^2 kT}} \tag{B.15}$$

and $x_0 = a/R$. Since the mass per cell is that of an ion, we can relate the cell volume to the mass density, $\frac{4}{3}\pi a^3 = \frac{Am_p}{\rho}$, and thus

$$\rho = \frac{3\sqrt{2}}{\pi^2}\left(\frac{kT}{m_e c^2}\right)^{3/2} \frac{Am_p}{Z\lambda_e^3 x_0^3}. \tag{B.16}$$

The pressure is calculated from the momentum transfer across the cell boundary, i.e.,

$$P = \frac{2}{h^3}\int_0^\infty 4\pi p^2 \frac{pv}{3} f(E)dp \tag{B.17}$$

at r=a. This becomes

$$P = \frac{2\sqrt{2}}{3\pi^2}\frac{kT}{\lambda_e^3}\left(\frac{kT}{m_e c^2}\right)^{3/2} I_{3/2}\left(\eta + \frac{e\phi(r)}{kT}\right) \tag{B.18}$$

or, cast in more familiar terms,

$$P = \frac{2}{3}\frac{I_{3/2}(\alpha\Psi'(x_0))}{I_{1/2}(\alpha\Psi'(x_0))} n_e kT \tag{B.19}$$

(note that we have applied the boundary condition in the arguments). This is just the electron contribution to the pressure. There is also a contribution from the thermal motions of the ideal ion gas, so that we have

$$P = \frac{\rho kT}{Am_p} + \frac{2\sqrt{2}}{3\pi^2}\frac{kT}{\lambda_e^3}\left(\frac{kT}{m_e c^2}\right)^{3/2} I_{3/2}\left(\alpha\Psi'(x_0)\right) \tag{B.20}$$

To calculate all the thermodynamic quantities, we need to calculate the internal energy of each cell as well. We start by calculating the total energy. The total kinetic energy of all

the electrons is

$$E_k = \int_0^a 4\pi r^2 dr \int_0^\infty 4\pi p^2 \frac{p^2}{2m_e} \frac{2}{h^3} f(E) dp \tag{B.21}$$

which can be reduced to

$$E_k = \int_0^a 4\pi r^2 n_e(r) kT \frac{I_{3/2}(z_f)}{I_{1/2}(z_f)} \tag{B.22}$$

The electrostatic potential energy is given by

$$E_p = -\frac{e}{2} \int_0^a 4\pi r^2 dr n_e(r) \phi_e(r) - e \int_0^a 4\pi r^2 dr n_e(r) \frac{Ze}{r} \tag{B.23}$$

where the first term is the electron-electron contribution (note the factor 1/2 to take care of double summation over each interaction) and the second is the electron-ion contribution. The electronic potential is $\phi_e = \phi - Ze^2/r$. Combining E_k and E_p (and adding in the ionic thermal motion contribution) we get

$$E_{tot} = \frac{3}{2} kT + \int_0^a 4\pi r^2 dr n_e(r) \left(kT \frac{I_{3/2}(\eta + \frac{e\phi}{kT})}{I_{1/2}(\eta + \frac{e\phi}{kT})} - \frac{e}{2} \left(\frac{Ze}{r} + e\phi(r) \right) \right) \tag{B.24}$$

Casting this in terms of our calculating variables (and making it per unit mass rather than per particle), this becomes

$$E_{tot} = 3.099 \times 10^{13} T_6 (1 + f) \tag{B.25}$$

where

$$f = 1.333 \int_0^{x_0} x^2 dx \left[I_{3/2} \left(\alpha \frac{\Psi}{x} \right) - \frac{0.5398}{T_6^{1/2}} \left[\frac{1 + \Psi}{x} - \frac{\Psi(x_0)}{x_0} \right] I_{1/2} \left(\alpha \frac{\Psi}{x} \right) \right]. \tag{B.26}$$

We have used Helium (Z=2, A=4) and denoted $T/10^6 K = T_6$.

A further problem is that we really want the energy relative to the T=0, P=0 state, which is not zero in equation (B.24). Thus $U = E_{tot}(T, P) - E_{tot}(0, 0)$. The calculation of this will be deferred to the next section.

B.2 Mathematical Asides

We need to calculate the functions $I_n(z_f)$. We use Gauss-Laguerre quadrature, which calculates integrals of the form

$$\int_0^\infty z^n e^{-z} f(z) dz \tag{B.27}$$

We can cast our functions in such a form by integrating the function

$$f(z) = \frac{e^{z_f}}{1 + e^{z_f - z}} \tag{B.28}$$

We can derive some useful limits.

1. $z_f \gg 1$

$$I_n(z_f) \sim \frac{1}{n+1} z_f^{n+1} \tag{B.29}$$

2. $z_f \sim 0$

$$I_n(z_f) \sim (1 - 2^{-n}) \Gamma(1+n) \zeta(1+n) \tag{B.30}$$

3. $z_f \ll -1$

$$I_n(z_f) \sim \Gamma(1+n) e^{z_f}. \tag{B.31}$$

The limit (1) is important, because it applies for $x \ll 1$, so that our equation becomes

$$\frac{1}{x} \Psi''(x) \sim \frac{2}{3} \left(\frac{\alpha \Psi(x)}{x} \right)^{3/2} \tag{B.32}$$

This still yields a non-linear equation

$$\Psi'' = \frac{2\alpha^{3/2}}{3} \frac{\Psi^{3/2}}{x^{1/2}} \tag{B.33}$$

In the limit of small x, however, $\Psi(x) \sim \Psi(0) \sim 1$, so that we get the solution

$$\Psi(x) = 1 + \Psi'(0)x + \frac{8}{9}\alpha^{3/2}x^{3/2} \tag{B.34}$$

which we can use to generate initial values at finite x values, as long as we maintain the constraint that the second and third terms remain much less than 1. Our method of solution is to choose a value of $\Psi'(0)$ and then integrate outwards until the boundary condition is satisfied. In this way, for a given α, we can generate x_0 as a function of $\Psi'(0)$.

It turns out that we require a fairly large dynamic range in x to get good accuracy (i.e., small x to get good initial conditions and x of order unity or larger at the outer boundary). Thus, we find it more convenient to transform to a logarithmic variable $z = \ln x$. This leads to the equation

$$\Psi'' - \Psi' = e^{3z} I_{1/2}\left(\alpha e^{-z}\Psi\right) \tag{B.35}$$

with the boundary conditions

$$\Psi(-\infty) = 1 \tag{B.36}$$

$$\Psi'(z_0) = \Psi(z_0) \tag{B.37}$$

Solving the above problem is not quite sufficient, as we must also perform the integral over r to calculate the energy. Since we solve the above differential equations using adaptive stepsize ODE integrators, it is inconvenient to try to then use the solution (whose solution values are not guaranteed to be in any regular stepsize order) to calculate an integral. It far easier to cast our integral in terms of a differential equation which we can then solve simultaneously with the same ODE integrator. Actually, because the integral contains a term $\Psi(x_0)/x_0$, which depends on the outer boundary (which isn't known until the end of the calculation), we have to split the integral into two differential equations

$$f = 1.333\left(f_1 + f_2\frac{\Psi x_0}{x_0}\right) \tag{B.38}$$

where

$$\frac{\partial f_1}{\partial z} = e^{3z}\left[I_{3/2}\left(\alpha e^{-z}\Psi\right) - \frac{0.5398}{T_6^{1/2}}(1+\Psi)e^{-z}I_{1/2}\left(\alpha e^{-z}\Psi\right)\right] \tag{B.39}$$

$$\frac{\partial f_2}{\partial z} = e^{3z}\frac{0.5398}{T_6^{1/2}} I_{1/2}\left(\alpha e^{-z}\Psi\right) \tag{B.40}$$

In addition, as a check of our numerical accuracy, we can also calculate the integral

$$\int_0^a 4\pi r^2 n_e(r) dr \tag{B.41}$$

which should yield Z (=2 for Helium), the ionic charge. This can also be cast in the form of a differential equation

$$\frac{\partial Z_e}{\partial x} = Z x^2 I_{1/2}\left(\frac{\alpha\Psi}{x}\right) \tag{B.42}$$

where $Z_e(a) = Z$. Figure B.1 shows an example of our cell calculation.

We need the T=0, P=0 limit to calculate the internal energy. Since $\alpha \propto T_6^{1/2}$, we once again reduce our equation to

$$\Psi'' = \frac{\Psi^{3/2}}{x^{1/2}} \tag{B.43}$$

This equation is analysed by Shapiro and Teukolsky (1983), pg. 34. The P=0 (corresponding to the $x_0 \to \infty$) limit is given by $\Psi'(0) = -1.5880710$. Thus, a solution of this equation with this initial value will yield our limit.

If we consider now the energy integral in the same limit, we get (ionic part drops away when T=0)

$$E_{tot} = \frac{4\sqrt{2}}{\pi\lambda_e^3}\frac{(Ze^2)^{5/2}}{(m_e c^2)^{3/2}}\int_0^a r^2 dr\left[\left(\frac{2}{5}-\frac{1}{3}\right)\left(\frac{\Psi}{r}\right)^{5/2} - \frac{1}{3}\frac{\Psi^{3/2}}{r^{5/2}} + \frac{1}{3}\frac{\Psi(a)}{a}\left(\frac{\Psi}{r}\right)^{3/2}\right] \tag{B.44}$$

There are three different integrals to be performed here. Since we have expressed things in terms of r, consider $\Psi'' = A\Psi^{3/2}/x^{1/2}$. The integrals become (using integration by parts and the equation for Ψ''),

$$\int_0^a r^2 dr\left(\frac{\Psi}{r}\right)^{5/2} = \frac{5}{7}\left[\frac{4}{5}a^{1/2}\Psi(a)^{5/2} - \frac{\Psi'(0)}{A}\right] \tag{B.45}$$

$$\int_0^a r^2 dr\frac{\Psi^{3/2}}{r^{5/2}} = \frac{1}{A}\left(\frac{\Psi(a)}{a} - \Psi'(0)\right) \tag{B.46}$$

$$\int_0^a r^2 dr\left(\frac{\Psi}{r}\right)^{3/2} = \frac{1}{A} \tag{B.47}$$

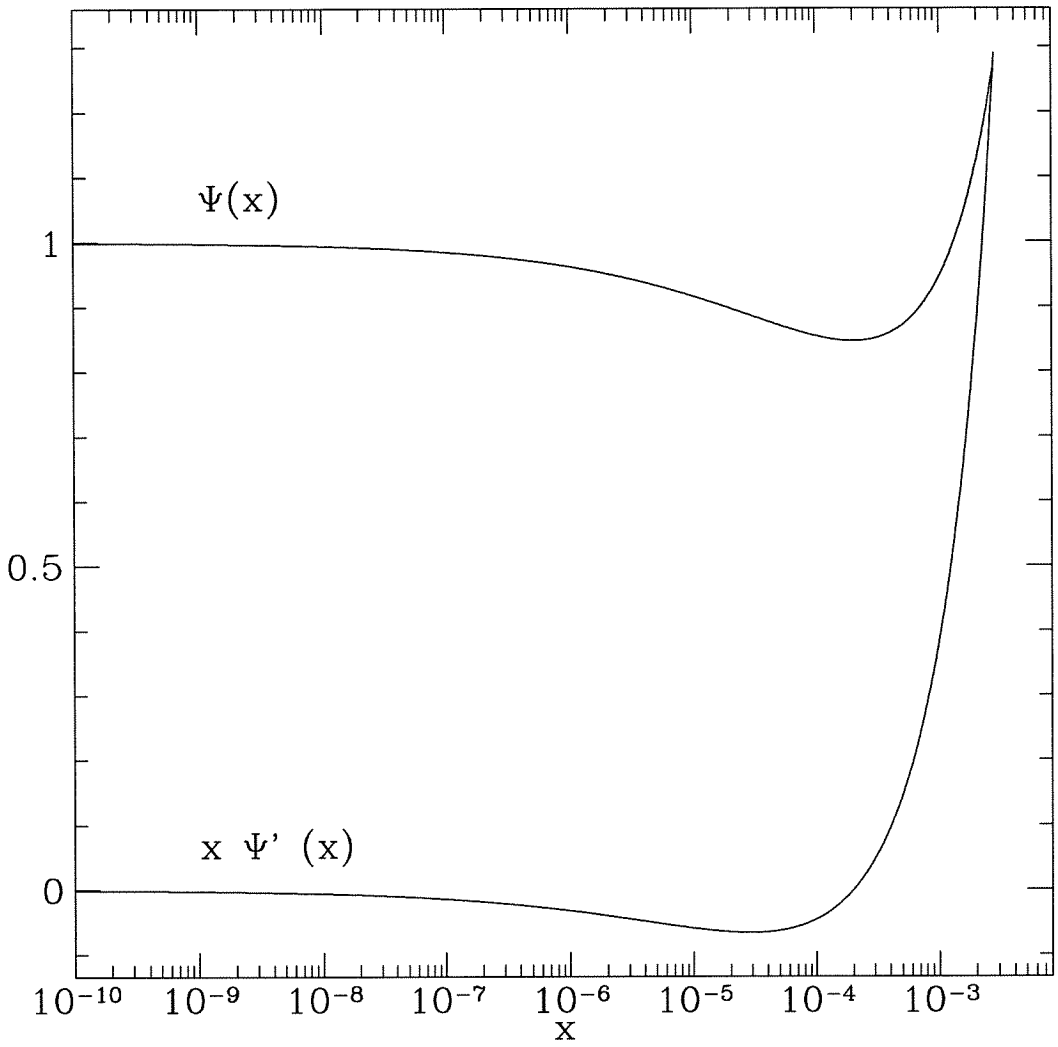

Figure B.1: **A Sample Solution:** This shows $\Psi(x)$ and $x\Psi'(x)$ for the case of $T = 10^4$ K and initial condition $\Psi'(0) = -20.0$, which corresponds to a density of $\rho = 2 \times 10^6 \text{g.cm}^{-3}$. The global solution is accurate to within 5%, based on the calculation of Z_e.

In the end, this all reduces to

$$E_{tot} = \frac{3}{7}A^{2/3}Z^2e^2\left[\frac{2}{15}x_0^{1/2}\Psi(x_0)^{5/2} + \Psi'(0)\right] \tag{B.48}$$

where A is not the atomic number but the normalization constant in our equation. Thus we get

$$E_{tot} = 1.0505 \times 10^{-10}\left(\frac{Z}{2}\right)^3\left[\frac{2}{15}x_0^{1/2}\Psi(x_0)^{5/2} + \Psi'(0)\right] \tag{B.49}$$

for the energy per particle, which has to be converted into energy per unit mass. The equation has a power law solution $\Psi \sim x^{-3}$ which does not satisfy $\Psi(0) = 1$, but to which the solution will tend at large radii. Thus $x^{1/2}\Psi^{5/2} \rightarrow x^{-7}$ and so the first term in the integral tends to zero. Finally, we get

$$E_{tot} = -2.497 \times 10^{13} \tag{B.50}$$

Thus,

$$U = E_{tot} + 2.497 \times 10^{13}. \tag{B.51}$$

We also expect to recover a couple of limits for our equation of state. For T=0, $I_{3/2}(x)/I_{1/2}(x) \propto x$ and $n_e \propto (T\Psi'(x_0))^{3/2}$ which means that

$$P \propto n_eT\psi'(x_0) \propto n_eTn_e^{2/3}T^{-1} \propto n_e^{5/3} \tag{B.52}$$

which is the completely degenerate electron gas equation of state. Similarly, for $T \rightarrow \infty$, $I_n \rightarrow$ constant, and so

$$P \propto n_eT \tag{B.53}$$

which is the ideal gas limit.

B.3 Thermodynamics

With the information provided by P and U, we can calculate the other thermodynamic quantities we may require. We collect the formulae here for further information.

The first important quantity is

$$\nabla_{\rm ad} = \left(\frac{\partial \ln {\rm T}}{\partial \ln {\rm P}}\right)_{\rm S} \tag{B.54}$$

We consider

$$\begin{aligned}\frac{1}{\nabla_{\rm ad}} &= \left(\frac{\partial \ln {\rm P}}{\partial \ln {\rm T}}\right)_{\rm S} \\ &= \left(\frac{\partial \ln {\rm P}}{\partial \ln {\rm T}}\right)_{\rho} + \left(\frac{\partial \ln {\rm P}}{\partial \ln \rho}\right)_{\rm T}\left(\frac{\partial \ln \rho}{\partial \ln {\rm T}}\right)_{\rm S} \\ &= \chi_{\rm T} + \chi_{\rho}\left(\frac{\partial \ln \rho}{\partial \ln {\rm T}}\right)_{\rm S}\end{aligned} \tag{B.55}$$

We can use one of Maxwell's relations to show that

$$\left(\frac{\partial \ln \rho}{\partial \ln {\rm T}}\right)_{\rm S} = \rho {\rm T}\left(\frac{\partial {\rm S}}{\partial {\rm P}}\right)_{\rho} \tag{B.56}$$

and using the Thermodynamic identity,

$${\rm T}\left(\frac{\partial {\rm S}}{\partial {\rm P}}\right)_{\rho} = \frac{\rm U}{{\rm P}\chi_{\rm T}}\left(\frac{\partial \ln {\rm U}}{\partial \ln {\rm T}}\right)_{\rho} \tag{B.57}$$

and thus

$$\frac{1}{\nabla_{\rm ad}} = \chi_{\rm T} + \frac{\rho {\rm U}\chi_{\rho}}{{\rm P}\chi_{\rm T}}\left(\frac{\partial \ln {\rm U}}{\partial \ln {\rm T}}\right)_{\rho} \tag{B.58}$$

The heat capacities can be derived as follows:

$${\rm C_V} = \left(\frac{\partial {\rm Q}}{\partial {\rm T}}\right)_{\rm V} = \left(\frac{\partial {\rm U}}{\partial {\rm T}}\right)_{\rho} = \frac{\rm P}{\rho {\rm T}}\frac{\chi_{\rm T}}{\chi_{\rho}}\left(\frac{1}{\nabla_{\rm ad}} - \chi_{\rm T}\right) \tag{B.59}$$

and

$$\begin{aligned}{\rm C_P} &= \left(\frac{\partial {\rm Q}}{\partial {\rm T}}\right)_{\rm P} = {\rm T}\left(\frac{\partial {\rm S}}{\partial {\rm T}}\right)_{\rho} = {\rm T}\left(\frac{\partial {\rm S}}{\partial \rho}\right)_{\rm P}\left(\frac{\partial \rho}{\partial {\rm T}}\right)_{\rm P} = \rho\left(\frac{\partial \ln \rho}{\partial \ln {\rm T}}\right)_{\rm P}\left(-\frac{1}{\rho^2}\right)\left(\frac{\partial {\rm P}}{\partial {\rm T}}\right)_{\rm S} \\ &= \frac{\rm PQ}{\rho {\rm T}\nabla_{\rm ad}}\end{aligned} \tag{B.60}$$

where ${\rm Q} = \chi_{\rm T}/\chi_{\rho}$. Thus we get

$${\rm C_P} = \frac{\rm PQ}{\rho {\rm T}\nabla_{\rm ad}} \tag{B.61}$$

$$C_V = C_P - \frac{PQ}{\rho T}\chi_T \tag{B.62}$$

$$\gamma = \frac{C_P}{C_V} = \frac{1}{1 - \chi_T \nabla_{ad}} \tag{B.63}$$

REFERENCES

Fontaine, G., Graboske, H.C. & Van Horn, H.M., (1977), ApJS, **35**, 293.

Saumon, D., Chabrier, G. & Van Horn, H.M., 1995, ApJS, **99**, 713.

Shapiro, S.L. & Teukolsky,S.A. , *Black Holes, White Dwarfs and Neutron Stars*, John Wiley & Sons (1983)

Appendix C Secondary Energy Distribution

For a beam particle of mass m_1 and lorentz factor γ_1 and a target particle of mass m_2, the lorentz boost to the centre of mass frame and the centre of mass frame energy are

$$\gamma_b = \frac{m_2 + m_1\gamma_1}{E_0/c^2} \tag{C.1}$$

$$\frac{E_0}{c^2} = \left(m_1^2 + m_2^2 + 2m_1m_2\gamma_1\right)^{1/2} \tag{C.2}$$

For the purposes of our calculations here, the γ_1 is the beam lorentz factor after the removal of pion losses in each collision. The product particles have masses m_3 and m_4. The energy available to them (E_*) is E_0 minus the rest mass energy of the wounded nucleus, $\sim \gamma_b\,(m_1 + m_2 - m_3 - m_4)\,c^2$. It is well known that the centre of mass energy of the products is uniquely determined to be

$$\gamma_3' = \frac{(E_*/c^2) + m_3^2 - m_4^2}{2m_3E_*/c^2} \tag{C.3}$$

$$\gamma_4' = \left[1 + \left(\frac{m_3}{m_4}\right)^2 \left[(\gamma_3')^2 - 1\right]\right]^{1/2} \tag{C.4}$$

However, the products emerge at an arbitrary angle θ' to the beam direction in the centre of mass frame and the transformation back to the laboratory frame yields

$$\gamma_3 = \gamma_3'\gamma_b\left[1 + \beta_b\beta_3'\cos\theta'\right] \tag{C.5}$$

yielding the distribution

$$P(\gamma_3) = \frac{1}{\pi}\left[(\gamma_3'\gamma_b\beta_b\beta_3')^2 - (\gamma_3 - \gamma_3'\gamma_b)^2\right]^{-1/2} \tag{C.6}$$

Appendix D The Kaplan-Meier Estimator

We describe here the formalism set out in Feigelson and Nelson (1985).

Consider our data to be the set of n distinct values $\{x_i\}_{i=1}^n$, where the x_i are ordered in the manner $x_1 > x_2 > \cdots > x_n$, where x_i can be either a detected value or an upper bound. Now, for a given value t, let

$$P_i = P\left[t \leq x_{i+1} \,|t \leq x_i\right]$$

i.e., the conditional probability that t is less than x_{i+1} given that it is less than x_i.

Using this, we can calculate the probability that t is less than any given x_i by

$$P\left[t \leq x_i\right] = \Pi_{j=0}^{i-1} P\left[t \leq x_{j+1} \,|t \leq x_j\right]$$

To calculate this, we need to estimate the P_j. To start, $P_1 = 1$, since all values are at most as big as x_1. For any other x_j, if it is a detection, then there are $n - j + 1$ values at most as large as x_j, and all except x_j are also at least as large as x_{j+1}. Thus, we estimate

$$P_j = \frac{n-j}{n-j+1} = 1 - \frac{1}{n-j+1}.$$

If x_j is an upper bound, then $P_j = 1$ by following similar reasoning as above. Thus, we have that

$$P\left[t \leq x_i\right] = \Pi_{j=1}^{i-1} \left(1 - \frac{1}{n-j+1}\right)^{\delta_j}$$

where $\delta_j = 1$ if x_j is a detection, and $\delta(j) = 0$ if x_j is an upper limit. This is the Kaplan-Meier (1958) estimator of the distribution function. In the case where we have ties in our data (i.e., more than one measurement at the same value), this becomes

$$P\left[t\right] = \Pi_{j, x_j > t} \left(1 - \frac{d_j}{n_j}\right)^{\delta_j}$$

where n_j = number of measurements $\leq x_j$, and d_j is the number of measurements at the

value x_j.

We also want to calculate the mean of velocities. Since p(x) dx = ΔP, the mean of a quantity x is given by

$$< x >= \int_0^\infty x dP = \int_0^\infty P dx$$

where we have integrated by parts. Thus we estimate the mean by

$$< V_t >= \sum_{i=1}^{N} P\left[x_i\right]\left(x_i - x_{i-1}\right)$$

and we take $x_0 = 0$.

To include a V/V_{max} weighting, we adjust the number of "counts" at each value according to the weights w(j), and thus we have

$$\frac{d_j}{n_j} = \sum_{i \leq j} \frac{w_j}{w_i}$$

In calculating the error on this new estimator, we note that we have artificially increased the total number of observations fed into the sum and thus have reduced the error by a factor $\sqrt{N}$. We remove this artificial error but lose some of the rigour of the confidence limits quoted in Feigelson and Nelson.